Driving rain on building envelopes

Fabien J.R. van Mook

Copyright © 2002 Fabien J.R. van Mook.

Cover photograph © 1999 Ben Elfrink.

Cover design by Bert Lammers.

Printed by the Eindhoven University Press, in Eindhoven, the Netherlands.

Published as issue 69 in the *Bouwstenen* series of the Faculty of Architecture, Planning and Building of the Eindhoven University of Technology.

ISBN 90-6814-569-X

Measurement data are available at http://sts.bwk.tue.nl/drivingrain/

Driving rain on building envelopes

proefschrift

ter verkrijging van de graad van doctor aan de Technische Universiteit Eindhoven,
op gezag van de Rector Magnificus, prof.dr. R.A. van Santen, voor een commissie
aangewezen door het College voor Promoties in het openbaar te verdedigen op
maandag 17 februari 2003 om 16.00 uur

door

Fabien J.R. van Mook

geboren te 's-Hertogenbosch

Dit proefschrift is goedgekeurd door de promotoren:

prof.ir. J.A. Wisse
en
prof.dr.ir. K. Kopinga

Copromotor:
prof.dr.ir. M.H. de Wit

Contents

Acknowledgements **9**

1 Introduction **11**

1.1 Problem definition 12

1.2 Outline 13

1.3 Literature survey 14

2 Theory **21**

2.1 Wind 21

2.1.1 Mean wind speed in the a.s.l. 22

2.1.2 Change of terrain roughness 23

2.1.3 Turbulence in the a.s.l. 25

2.1.4 Flow near buildings and urban canopy 25

2.1.5 Axis system definitions 27

2.2 Rain 28

2.2.1 Raindrop size 28

2.2.2 Drop velocity 29

2.2.3 Stopping distance and dispersion 31

2.2.4 Raindrop spectrum and rain intensity 33

2.3 Driving rain 37
2.3.1 Theoretical model 38
2.3.2 Empirical model 40

3 Site and measurement set-up **43**
3.1 Geography and surroundings 44
3.2 Instrumentation 50
3.2.1 Ultrasonic anemometers 53
3.2.2 Tipping-bucket rain gauges 55
3.2.3 Rain indicator 55
3.2.4 Disdrometer 56
3.2.5 Driving rain gauges TUE-I and TUE-II 58
3.2.6 Driving rain gauges CTH and DTU 63
3.3 Data acquisition 66
3.4 Methods of data processing 67
3.4.1 Reference wind data 68
3.4.2 Façade wind data 68
3.4.3 Horizontal rain data 68
3.4.4 Raindrop spectrum data 69
3.4.5 Driving rain data of the TUE-I and TUE-II gauges 70
3.4.6 Driving rain data of the CTH and DTU gauges 71

4 Driving rain gauges **73**
4.1 Overview of the measurements 73
4.2 The TUE-I and TUE-II gauges 81
4.3 The CTH and DTU gauges 84
4.4 Summary 85

5 Measurements **89**

5.1 Data processing and selection 90

5.2 General presentation of the measured data 93

5.2.1 Wind 93

5.2.2 Horizontal rain amounts and intensities 96

5.2.3 Horizontal rain measurements by two gauges and a disdrometer 101

5.2.4 Rain spells 104

5.2.5 Driving rain amounts and intensities 105

5.2.6 Driving rain at two positions 106

5.2.7 Example of rainfall with high driving rain intensities 111

5.2.8 Maximum horizontal rain and driving rain 113

5.2.9 Raindrop spectra 116

5.3 Driving rain models 119

5.3.1 Model definitions 119

5.3.2 Parameterisation 121

5.3.3 Estimations and measurements 125

5.4 Summary 130

6 CFD simulations **133**

6.1 Wind calculation method 133

6.2 Driving rain calculation method 137

6.3 Results of wind calculations 142

6.4 Results of driving rain calculations 148

6.5 Summary 164

7 Conclusions **167**

Samenvatting **175**

References **181**

Symbols **191**

Curriculum vitae **195**

Stellingen — Theses **197**

Acknowledgements

The research reported in this booklet was not possible without the help of many persons, to whom the author is very grateful. During the first half of the 1990s, prof.ir. Jacob Wisse became more and more aware that a further study on driving rain was necessary, and possible due to the recent improvements in computers and CFD. He is acknowledged for the initiative of such a research at the university and I am very grateful for his wise advice and enthusiastic support during the course of my research. Profs. dr.ir. Klaas Kopinga and dr.ir. Martin de Wit are also thanked very much for their continuous advice and support. The latter was so kind to tolerate the noise which the wiper of the driving rain gauge in one of the windows of his office room (position P6, figure 3.6) produced. Dr. Hans Kuerten and prof.dr.ir. Jan Carmeliet kindly commented the manuscript of this thesis.

Thanks to the collaboration with dr. Mikkel Kragh (Technical University of Denmark) and dr. Anneli Högberg (Chalmers University of Technology), interesting ideas were exchanged and a full-scale comparison test of driving rain gauges from different countries was achieved. Since the end of 1998, Bert Blocken (Katholieke Universiteit Leuven) enforced our international collaboration even more. In April 2000, Bert Blocken and I did driving rain tests in the Jules Vernes Wind Tunnel of the Centre Scientifique et Technique du Bâtiment (CSTB) in Nantes. This was made possible by the kind collaboration with the CSTB researchers Jean-Paul Flori, Philippe Delpech and Marc Dufresne De Virel.

I thank dr. Marcel Bottema, dr.ir. Chris Geurts, dr. Suresh Kumar and prof.dr. Ted Stathopoulos for their comments and discussions during different stages of the research. I thank the four students who brought the research forward. The first CFD calculations of wind around the Main Building of the TUE were performed by Ivo Baten for his master's thesis. Stan Bollen and Gert Eerdekens investigated the measurements and CFD calculations of driving rain at the VLIET building at their Katholieke Universiteit Leuven. Kjell Bijsterbosch developed a driving rain gauge with a drop-counting device.

The facility services of the TUE and the facility management of the Faculty of Architecture, Building and Planning are acknowledged for allowing the full-scale measurements on the Main Building and Auditorium of the TUE and for realising a part of the measurement set-up. I thank Sip Overdijk, head of the laboratories of the Structural Engineering

group of the Faculty, for allowing the use of their ultrasonic anemometer and PhyDAS for the wind measurements.

I thank the following persons for their technical support and aid (in random order): Wim van der Ven, Jan Vermeulen, Jos van Schijndel, Jan Diepens, Guus Theuws, Harrie Smulders and Wout van Bommel (laboratories of the Building Physics group), Marc Frencken (power supply for the driving rain wiper motor), Eric Wijen (Structural Engineering group), Stan van Asten (Building Production group), Nol Peeters, Henk Weel and Joep v.d. Weijden (Faculty's workshop), Ben Elfrink (Faculty's photographer), Tom Flesch, Arno Vervest, P. Peters and M. Theeuwes (University's electronic workshop).

Without making a long list of names, I thank the colleagues and the other staff members at the Building Physics group for support and interesting discussions, and finally all the other persons not mentioned who gave me advice, literature etc.

The research was a joint project of the Faculty of Architecture, Planning and Building and of the Faculty of Technical Physics, and was partly funded by the common TUE commission on « Technology for Sustainable Development ».

Chapter 1

Introduction

Building envelopes deteriorate due to many factors. The exposure of building envelopes to the in- and outdoor climate is the inevitable factor, while the quality of their design, building and maintenance determines the durability as well. To which extent deterioration should be prevented, depends on requirements such as safety, aesthetics, use, life time, building costs and maintenance costs. Anyhow, the first step in minimising the deterioration is better design, for which knowledge of the local outdoor climate is primordial. In the present thesis, one facet of the local climate is studied, namely driving rain. *Driving rain* is rain that is carried by wind and driven onto building envelopes.

Deterioration problems related to driving rain are many and often linked to each other. Moisture in an exterior wall due to driving rain may cause for example reduction of the thermal insulation, corrosion to metal fixtures, cracks in porous masonry during freezing, efflorescence of salts, expansion or shrinkage (and thus damaging stresses), or it may cause fungal growth on the façade or on the indoor side. Direct rain water leakage into a building can also make the building less useful. Other examples for which driving rain directly determines the functionality of a building or building parts, are canopies over entrances and bus shelters. Together with pollutants (by wet and dry deposition), driving rain causes staining and weathering of the surface of building envelopes.

Deterioration of façades was described comprehensively in e.g. Schaffer (1972, reproduction of the 1931 edition), Simpson and Horrobin (1970), Grunau (1973, 1975), and Winkler (1997). These references are also instructive because they contain many pictures of weathered building parts. In literature one finds also more specialised studies relating to the issues mentioned in the previous paragraph, for example: Couper (1974) (splashing and run-off from differently shaped projections), El-Shimi et al. (1980) (weathering on precast concrete panel façades), Newman et al. (1982) (rain penetration through cavity fills in masonry walls), Flori (1990) (wetting and drying of a façade), Mulvin

and Lewis (1994) (weathering of a classical 18th-century building), and Brocken (1998) (moisture transport in masonry).

Although many decisions at designing buiding envelopes imply knowledge of (driving) rain and its statistics, much is still unclear (see also the survey on driving rain research in section 1.3). The general motivation of this research is to develop tools to estimate driving rain amounts on building envelopes, which are useful for (1) the design of façades and roofs, (2) the testing of building materials and elements in laboratories, and (3) research on moisture transfer in building envelopes.

1.1 Problem definition

The modelling of driving rain will be presented in detail in section 2.3, but here we will simply state that the driving rain amount on a particular position on the envelope of a particular building is determined by the wind flow around the building, and the rainfall. Estimations of driving rain amounts thus rely on data of wind and rain. Unfortunately, such data, especially driving rain data for the building in question, is almost always lacking. If a building is designed (and not yet built), such data can simply not be acquired. Therefore one tries to estimate driving rain with wind and rain data available from weather stations. These data are then 'translated' to driving rain data. Two translation steps are often taken: (1) from the weather station to an intermediate reference, and (2) from the intermediate reference to the building. This two-step approach follows —so to speak— changes in wind due to the topography: the wind blows from the countryside (where the weather station often resides), over the town to the site and eventually to the building. « Site » is here understood as the vicinity of the building in question. The intermediate reference wind speed is obtained at the site where the wind is not disturbed (influenced) by the building. If the site is densely built, the exact position where the intermediate reference has to be measured, is not determinable because the

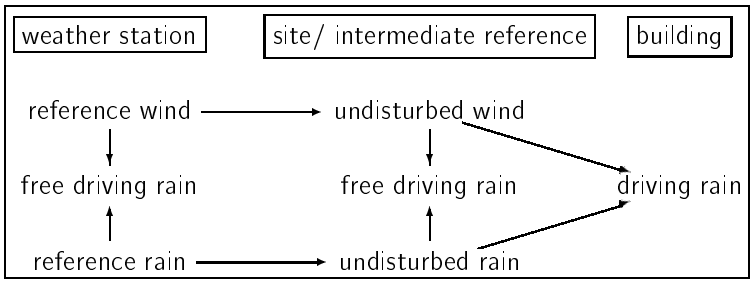

Figure 1.1: Two-step approach for translation of weather station data to driving rain data on an building envelope.

wind flow is influenced by both the building and its surroundings. In such cases the intermediate reference is hypothetical.

Figure 1.1 illustrates the two-step approach. Not always one will clearly find these steps in literature; sometimes even the first step or the second step is left out. For example in the British standard on the estimation of driving rain quantities (BSI 1992) one can find features of the two-step approach, as each step can be identified by the one or several coefficients in the formulae. Figure 1.1 introduces the term « free driving rain », which is defined as rain through the vertical.

To elaborate on the problem one has to (1) select and define the considered quantities and the kind of relationships, (2) select topographies and building types and (3) gather in situ measurements. As we will see in the literature survey (section 1.3), much knowledge is lacking or insufficient, namely:

- detailed full-scale measurements of driving rain with reference measurements of wind and rain,
- design rules for driving rain gauges,
- comparisons between driving rain measurements and model results (including more sophisticated modelling with computational fluid dynamics, CFD),
- the comprehension of the huge variation in weather, topography and building forms.

The present study is intended to contribute to these items, although one particular building and topography will be considered.

1.2 Outline

In this section the research set-up and goals are explained along the outline of the present study.

Chapter 2 (*Theory*) introduces definitions of the considered quantities and the models on driving rain. There are two (though closely related) models described in the chapter. The so-called theoretical model is about the calculation of individual raindrop trajectories. This model is applied for driving rain calculations with CFD, and its details are presented in chapter 6 (*CFD simulations*). The second model is an empirical model, and is rather based on over-all rain quantities (i.e. no individual raindrops are considered but their volumes are taken together). The empirical model serves mainly the full-scale measurements, as measurement techniques detect over-all rain quantities.

The Main Building of the Eindhoven University of Technology (TUE) is used as test object for the full-scale measurements of wind and (driving) rain. This building, its surroundings, the instrumentation and the data processing techniques are described in chapter 3. The site is interesting because the Main Building has an relatively simple geometry and is much higher than the average surroundings. Moreover, an intermediate reference position is easily defined. Much attention is paid to the design of the driving rain gauges. Two driving rain gauges were developed at the TUE and, thanks to collaboration with the Chalmers University of Technology (CTH) and the Technical University of Denmark (DTU), two other driving rain gauges were included in a full-scale comparison test. We did not expose the driving rain gauges to artificial driving rain, because preliminarily we did not have real driving rain data with corresponding raindrop spectra, rain intensities and wind speeds. Moreover, realistic artificial driving rain is probably very difficult to generate.

Chapter 4 presents results of the full-scale comparison test of the driving rain gauges on a façade of the Main Building. The experiences from this test contribute to the formulation of design rules for driving rain gauges. Questions which are addressed in the chapter, are among others: which principle for the measurement of the collected driving rain water works best in practice, what is the influence of the shape, size and surface finish of the driving rain gauge on the readings, in which direction should further development of the designing and testing of driving rain gauges go.

The full-scale measurement set-up functioned for twenty-four months. Chapter 5 presents the measured data. The presentation and analysis include statistics (average and variation) of wind, rain and driving rain, correlations between intermediate reference wind and rain data and driving rain data, correlations between weather station wind data and intermediate reference wind data, parameterisations of the empirical driving rain model with the measured data. An improved driving rain model is also presented.

In chapter 6 we describe the model for the CFD calculations of wind and raindrop trajectories at the site of the Main Building. Results of the calculations are compared to the full-scale measurements. The main goal in the chapter is the investigation of the suitability of CFD for driving rain calculations, especially the aspects which should be dealt with to obtain reliable results.

Chapter 7 reports the main conclusions and suggestions for further research.

1.3 Literature survey

Driving rain has been the subject of research for many years. Main surveys can be found in Lacy (1965), Frank (1973), Prior (1985) and Flori (1988). We must note that many references in these surveys are not easily available and sometimes not available at all.

Towards a standard The oldest instrument (according to Middleton 1969) which determined the direction from which rain is coming, was made in 1816. It was a so-called « vectopluviometer » and had a horizontal opening and a vertical opening which faced into the wind by a vane. Note that it measured the *free* driving rain as we define it in this thesis (figure 1.1), because the vectopluviometer is not mounted on a façade. Holmgren was probably the first who performed measurements of driving rain on a façade of a building in Trondheim in 1937 (Lacy 1965). According to Lacy (1965) Holmgren's gauge looked very much like the left gauge of figure 1.2a. Driving rain water was collected by a shallow square tray fixed to the wall and the collected water was guided into a bottle. Similar gauges are still used today, and we will call them « traditional ».

During the second World War Chr. Nell measured driving rain on houses in a street in Voorschoten (NL). Basart (1946) reported the findings of Nell who compared the driving rain data measured by two different methods: by a traditional gauge and by regular weighting of a plate made of very absorbent bricks. Differences were attributed to measurement anomalies and to the variation in the raindrop size distributions, changing from one storm to another. The report of Basart is the only one with results of a comparison test of driving rain gauges which we found.

Hoppestad of the Norwegian Building Research Institute (Lacy 1965) assumed that the free driving rain intensity (R_v, i.e. rain intensity through the vertical) is proportional to the product of rain intensity through the horizontal (R_h) and the local wind speed (U):

$$R_\mathrm{v} = \alpha R_\mathrm{h} U, \tag{1.1}$$

where α is assumed to be the reciprocal of the 'average' falling velocity of raindrops. An assumed average falling velocity of 4.5 m s^{-1} yields $\alpha = 0.2$ s m^{-1}.

The idea behind equation 1.1 is that the motion of a rain drop is affected by the horizontal wind speed and the vertical falling velocity, and that the ratio of rain intensities approximates the ratio between the mentioned two velocities. The reader should bear in mind that R_v is not the driving rain intensity on a building envelope, but some kind of intermediate reference, as indicated in section 1.1.

In 1955 Hoppestad was the first to publish maps of free driving rain (Flori 1988). The maps were based on calculated annual and monthly free driving rain amounts of all the meteorological stations in Norway. The (average) coefficient α was obtained by measurements of R_v at four stations. While the maps gave a first quantitive overview of vertical rain (and indirectly of driving rain), Hoppestad underlined that the calculations did not take the variability of α, nor corrections for the local environment (topography, terrain roughness, etc.) into account.

Lacy and Shellard introduced the « driving rain index » in 1962 (Lacy 1965). The index was defined as the product of the annual mean wind speed (in m s^{-1}) and the annual rainfall (in m, i.e. precipitation height on the horizontal). Maps with driving rain indices

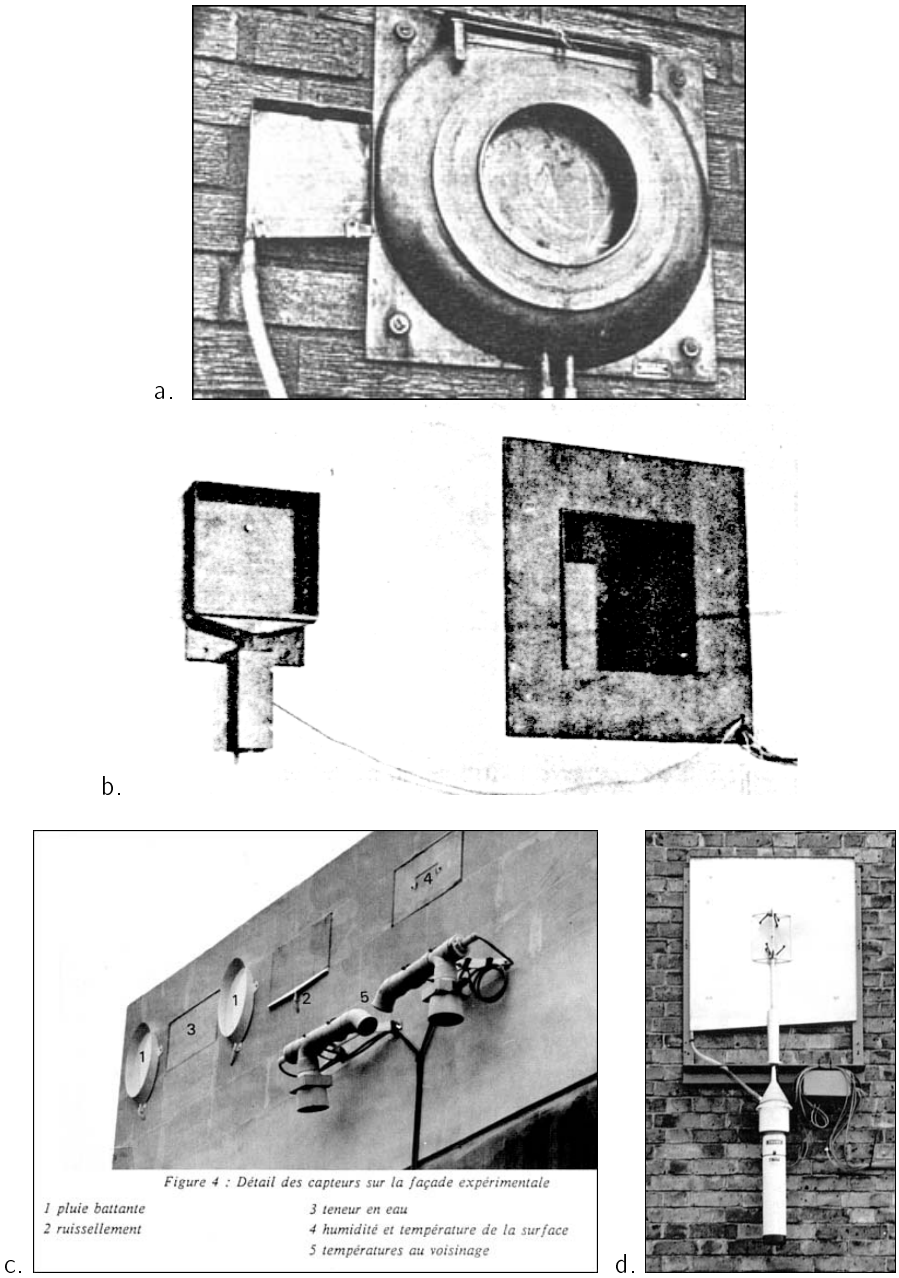

Figure 1.2: Driving rain gauges from (a, left) BRE (UK) (Lacy 1965), (a, right) TNO (NL), (b) Künzel (Frank 1973), (c) Flori (1990) and (d) Osmond (1995).

(d.r.i.) were produced for the United Kingdom. A meeting of the working commission on rain penetration in Madrid 1966 at the Commission Internationale du Bâtiment promoted the elaboration of driving rain index maps for different countries to investigate whether this approach to estimate free driving rain amounts could be widely used (Frank 1973). The idea was to classify areas of potentially low (index < 3), moderate (index 3–7) and high (index > 7) free driving rain onsets. By the end of the 1960s, d.r.i. data had been collected for the United Kingdom, Norway, Canada, Denmark, Poland, Rumania, Spain, West Germany and East Germany.

Künzel evaluated the maps of these countries in 1968 (Frank 1973). He observed that the driving rain index maps gave reasonable indications for driving rain amounts in the UK and parts of Scandinavia. However, the mentioned classification did not hold for other parts of Europe: in many areas, low driving rain indices corresponded with high driving rain amounts in reality. So it seemed that the meaning of the index depended on topography and climate, and was not universal as intended by Lacy and Shellard. A reason for this discrepancy was that on average in some regions the wind speed during rain differs from the wind speed during dry periods. The annual wind speed averaged over all hours (as used for the d.r.i. by Lacy and Shellard) did thus not everywhere represent well the wind speed during rainfall.

Prior (1985) reported that in the beginning of the 1970s Caton of the Meteorological Office noted that also in the UK the ratio of the mean wind speed during rain to that of all hours varied so much, that Lacy's index could significantly under- or overestimate free driving rain amounts. Caton prepared d.r.i. maps based on hourly products of rainfall and wind speed, taking into account wind direction. Caton also investigated a « driving rain spell index », which represented driving rain amounts associated with rain spells having a specified average frequency of occurrence. A rain spell has a variable duration and can consist of a series of rainfalls interspersed with periods up to 96 h without rain. For the development of a standard on the assessment of driving rain exposure of buildings by the British Standards Institution, Prior was asked to continue Caton's investigations. The results were reported in Prior (1985) and were eventually integrated in BS 8104 (BSI 1992).

So, the British standard is based on data from 1959 to 1991, of 52 weather stations throughout the UK. Hourly wind speed data were corrected and translated to corresponding values for wind speed at 10 m height on an open level country. Hourly rainfall data was not available for every weather station; a procedure for 'filling in' missing data points was applied (Prior 1985). Two indices were calculated for every location and every of the 12 wind directions: (a) an average annual driving rain index and (b) a driving rain spell index associated with a frequency of once in three years. The first index was thought relevant for the weathering of building envelopes and the latter for assessing the risk of rain penetration through masonry walls. The standard gives a method for the assessment of the annual driving rain amount —or the worst likely spell amount in any three year period respectively— on a wall of an particular orientation, calculated

from directional indices (plotted on maps) corrected for terrain roughness, topography, obstruction by nearby buildings, building type and position on the building envelope. The British standard is still the only standard on driving rain estimations; in the Comité Européen de Normalisation a European version of this standard is in preparation.

It is not clear to us on which studies the correction factors in BS 8104 were based. Perhaps they are, among others, based on Brown (1988) who measured « catch ratios » on different buildings and at different façade positions in Dorset (UK). Brown defined the catch ratio as the quotient of the driving rain amount on a position on a façade and the free driving rain amount. Other sources for measurements of catch ratios could have been Lacy (1965, 1977) and Frank (1973).

In the 1990s, full-scale driving rain measurements were carried out by Flori (1990), Henriques (1992), Hens and Mohamed (1994), Fraunhofer-Institut für Bauphysik (see e.g. Künzel 1994), Sankaran and Paterson (1995b) (free driving rain only), Osmond (1996, 1996), Kerr et al. (1997), Straube (1998), Kragh (1998), Högberg (1998), Högberg (1999), Blocken and Carmeliet (2000b), and Choi (2001) (only free driving rain and raindrop spectrum). Driving rain measurements presented in Högberg et al. (1999), van Mook (1999a) and van Mook (1999b) relate to work for this thesis and are presented in more detail in chapters 4, 5 and 6.

An original approach is developed by Snape and Atkinson (1999), who investigated driving rain intensity patterns by comparing photos of stains and other surface depositions on a façade.

Computer simulations Perhaps the first computer simulations of driving rain were done by Sandberg (1974) and Rodgers et al. (1974). In both articles only raindrop trajectories were calculated by computer; the wind speed fields around a (two-dimensional) building were obtained from wind tunnel experiments. At the end of the 1980s and beginning of the 1990s, new possibilities of computational fluid dynamics and new possibilities offered by improved hardware were exploited. Choi (1993) presented simulations in which firstly the wind flow around a high-rise building was calculated by a K-ϵ model, and secondly, for a given mean wind field, trajectories of drops were calculated. Considered wind speeds were 5, 10 and 20 m s^{-1}, and also the considered rain intensities were extreme (at least compared to the north-west European climate): 10, 30 and 50 mm h^{-1}. In Choi (1994b) it becomes clear that he was interested in extreme driving rain onsets for a building in Sydney. Other articles of the same author are: Choi (1994c) (parametric study), Choi (1994a, 1999b) (driving rain index), Choi (1995) (gust effects on driving rain) and Choi (1999a) (tropical thunderstorms). The method of Choi (1993) is used by almost every other researcher.

Two-dimensional simulations of driving rain on a building of moderate height (5.5 and 11 m) in a moderate climate (reference wind speed of 10 m s^{-1} and rain intensity of 1.3 mm h^{-1}) were presented by Bookelmann and Wisse (1992) and Wisse (1994).

Contrary to the method of Choi, Sankaran and Paterson (1995a) took dispersion of raindrops due to wind turbulence into account for a simulation of driving rain on a very tall building of 183 m height (and 45×31 m^2 cross section). The wind flow with its standard deviation was calculated using a standard K-ϵ model. For a rainstorm with 30 mm h^{-1} and 17 m s^{-1}, the driving rain intensity on the front face simulated by taking raindrop dispersion into account, was approximately two times the driving rain intensity simulated without raindrop dispersion. Hangan and Surry (1998) also included turbulent raindrop dispersion in their driving rain simulations; they also compared their results with wind tunnel experiments. Lakehal et al. (1995) studied different turbulence models (based on the K-ϵ model) for the calculation of turbulent dispersion of raindrops and applied them to calculate driving rain intensities on façades in a two-dimensional street-canyon. They could not conclude which was the most accurate model because the full-scale measurements were insufficient. This article is also interesting for a historical review on driving rain simulations.

Other articles on driving rain simulations are Karagiozis and Hadjisophocleous (1996), Karagiozis et al. (1997), Blocken et al. (1999), Blocken and Carmeliet (2000a) and Etyemezian et al. (2000).

Windtunnel experiments Surry et al. (1994) and the associated report of Inculet and Surry (1995) described wind tunnel experiments in which driving rain on a reduced-scale building was studied qualitatively. Driving rain distributions were measured by water-sensitive paper. Full-scale driving rain tests in (boundary-layer) wind tunnels have not yet been published, as far as we know. The large wind tunnels (with cross sections of 10 m and more) at the CSTB in Nantes (FR) (Gandemer and Barnaud 1995) may be useful for full-scale driving rain experiments.

Summary Overviewing the literature on driving rain, we conclude that:

- there is only one official standard on the estimation of driving rain quantities, namely BS 8104:1992,
- only few detailed measurements, for example on hourly basis or less, are available,
- references on comparisons of driving rain gauges have not been found,
- CFD simulations of driving rain are all based on the standard K-ϵ model. Only in a few cases turbulent dispersion of raindrops is taken into account,
- simulations on driving rain are not compared to full-scale measurements of driving rain on the same building. Only recently, such comparisons are published by van Mook (1999a) and Blocken et al. (2001),

- raindrop size distributions used in simulations are based on quite old measurements (e.g. Marshall and Palmer 1948 and Best 1950) in which the distributions were idealised by simple logarithmic functions, although measurements show much climatic and temporal variations (e.g. Wessels 1972, Joss and Gori 1978, Uijlenhoet 1999).

Chapter 2

Theory

A study on driving rain on building envelopes is based on boundary layer meteorology, bluff body aerodynamics, computational fluid dynamics, meteorology and building technology. This chapter presents various quantities which will be used in the following chapters.

2.1 Wind

Wind around a building causes driving rain on the envelope of the building. Without wind there is no driving rain. The atmospheric boundary layer (a.b.l.) is the layer close to the Earth's surface, in which wind is directly influenced by friction with the Earth's surface. Its height ranges from hundreds of metres to a few kilometres and depends on the intensity of thermal mixing (convection), terrain roughness and latitude. The atmospheric surface layer (a.s.l.) is the lowest 10-20% of the a.b.l., where shear is approximately constant with height and production of turbulence is high. The a.s.l. over a uniform flat terrain in a neutral boundary layer is characterised by a wind velocity increasing with height and a wind direction being nearly constant with height.

Due to spatial changes in surface roughness, internal boundary layers (i.b.l.) develop, in which wind speed and direction are modified by the properties of the surface (obstacles), while the top of the i.b.l. flow is the wind velocity adjusted to the terrain conditions before the roughness change. The thickness of the i.b.l. increases downstream of the roughness change.

In the following we will only pay attention to a neutral boundary layer, i.e. an atmospheric situation in which vertical heat transfer is negligible.

2.1.1 Mean wind speed in the a.s.l.

The mean wind speed in the a.s.l. as a function of height is expressed by the so-called « logarithmic law »:

$$\bar{u}(z) = \frac{u_*}{k} \ln\left(\frac{z-d}{z_0}\right), \tag{2.1}$$

where $\bar{u}(z)$ is the mean horizontal wind speed [m s^{-1}] at z [m] height from ground level, u_* the friction velocity [m s^{-1}], k the von Kármán constant (0.4), d the displacement height [m], and z_0 the aerodynamic roughness length [m].

The friction velocity u_* is defined by:

$$\tau_0 = \rho u_*^2, \tag{2.2}$$

and can be measured in the a.s.l. from:

$$u_* = -\sqrt{\overline{u'w'}}, \tag{2.3}$$

where τ_0 is the surface shear stress [N m^{-2}] (i.e. drag force per unit of area), ρ the air density [kg m^{-3}], and u' and w' are the fluctuating components of the longitudinal and vertical wind velocities, respectively.

Displacement height and roughness length are measures for the roughness of a terrain. A classification of typical z_0 values is presented in Wieringa (1992, 1996). Some typical values are listed here:

z_0 [m]	landscape
0.0002	open sea or lake
0.03	flat terrain with grass, airport runways
0.10	moderately open country with low vegetation and occasional obstacles separated by more than 20 obstacle heights $\mathcal{H}$ (e.g. low hedges, single rows of trees)
1.0	closed and regularly covered terrain; open spaces up to $\mathcal{H}$ (e.g. city, mature forests)

The logarithmic law (eq. 2.1) applies only for:

- homogeneous and stationary flow. The fetch with a homogeneous surface roughness should be at least 10 to 20 km,
- neutrally stable atmospheric conditions,
- heights z in the ranges

- $z > 20z_0 + d$,
- $z < z_{\text{a.s.l.}}$, where $z_{\text{a.s.l.}}$ is the height of the a.s.l., and

- positions far from buildings, i.e. at distances $> 2.5\mathcal{H}$ above the building, $> 12\mathcal{H}$ in the wake of the building, and $> 3\mathcal{H}$ upstream (with $\mathcal{H}$ denoting building height).

2.1.2 Change of terrain roughness

In the literature one finds several approaches for a relation between wind above two adjacent terrains with different roughness properties. Here, we investigate an abrupt roughness change according to two models. Figure 2.1 sketches the situation. The quantities on the terrain upwind from the change will be denoted by index 1, downwind by index 2.

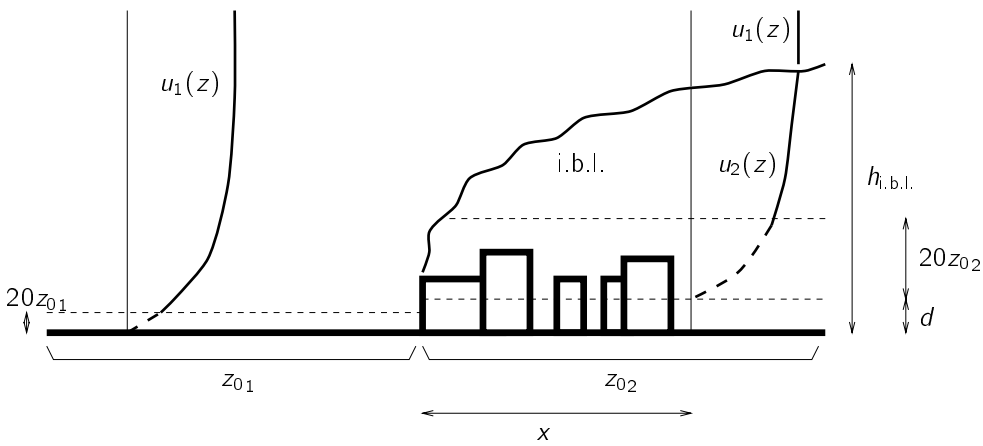

Figure 2.1: Development of a internal boundary layer (i.b.l.) and change of mean wind profiles due to a roughness change. Wind is coming from the left.

Internal boundary layer model According to the internal boundary layer model described in Simiu and Scanlan (1996), it is suggested that the wind velocity at the top of the i.b.l. ($h_{\text{i.b.l.}}$) on the second terrain equals the velocity at the same height on the first terrain.

The height of the i.b.l. at a distance x [m] from the roughness change is (Simiu and Scanlan 1996, p. 73):

$$h_{\text{i.b.l.}}(x) = 0.28 z_{0\max} \left(\frac{x}{z_{0\max}} \right)^{0.8}, \tag{2.4}$$

with $z_{0\,\mathrm{max}}$ = the largest value of z_{01} and z_{02}.

An example is given to calculate the wind speed at a position A at 45 m above ground level in a town (denoted by $u_2(45)$) with a known wind speed at 10 m height at a weather station outside the town ($u_1(10)$). The distance from A to the town border is $x = 5$ km. The weather station is on grass covered terrain, so $z_{01} = 0.03$ m. The roughness of the town is $z_{02} = 1$ m and the displacement height is $d_2 = 10$ m. So, position A at 45 m height is above $20z_{02} + d_2$. According to equation 2.4, $h_{\mathrm{i.b.l.}}$ equals 250 m. The relationship between the mean wind speeds at 10 m and 250 m height at the weather station is calculated from the logarithmic law:

$$u_1(250) = \frac{u_{*1}}{k} \ln\left(\frac{250}{z_{01}}\right), \quad \text{and} \quad u_1(10) = \frac{u_{*1}}{k} \ln\left(\frac{10}{z_{01}}\right).$$

This yields $u_1(250) = 1.6u_1(10)$.

According to the i.b.l. model the wind velocity at A at i.b.l. height $h_{\mathrm{i.b.l.}}(250)$ approximates the wind velocity at the weather station at the same height, so:

$$u_2(250) = u_1(250), \quad \text{and} \quad u_2(250) = \frac{u_{*2}}{k} \ln\left(\frac{250}{z_{02}}\right).$$

The wind speed at 45 m height at A is:

$$u_2(45) = \frac{u_{*2}}{k} \ln\left(\frac{45}{z_{02}}\right),$$

which yields in this example: $u_2(45) = 1.08u_1(10)$.

Similarity model The second approach is referred to as the similarity model (Simiu and Scanlan 1996, p. 48); the ratio of friction velocities is empirically estimated from the ratio of roughness lengths:

$$\frac{u_{*2}}{u_{*1}} = \left(\frac{z_{02}}{z_{01}}\right)^{0.0706}. \tag{2.5}$$

For the above example, this approach yields $u_2(45) = 0.78u_1(10)$.

The present example shows that the two methods yield different results. The example reflects the site used in the study reported in this thesis. Measurements at this site yield $u_2(45) = 1.13u_1(10)$ according to Geurts (1997) and $u_2(45) = 0.90u_1(10)$ according to our own measurements (see section 5.2.1). These values differ ~20% from each other and the estimations differ to a similar extent. This is an indication of the error that has to be taken into account when estimating weather station vs. local wind speed ratios. (Note that for this example changing z_{02} into 1.5 m and/or z_{02} into 0.1 m will yield a difference of 3–10% in the estimated ratios.) The ratio $u_2(45)/u_1(10)$ at our site is discussed in de Wit et al. (2002) too.

Table 2.1: Typical values of standard deviations of wind velocity and mean turbulent kinetic energy in the a.s.l., obtained by measurements.

	Panofsky and Dutton (1984)	Geurts (1997)
σ_u/u_*	2.4	2.41
σ_v/u_*	1.9	1.91
σ_w/u_*	1.25	1.37
K/u_*^2	5.5	

2.1.3 Turbulence in the a.s.l.

Turbulence in wind causes variation of wind velocity in time and space. Turbulence is often considered as a superposition of eddies with different sizes transported by the mean flow. The simplest characterisation of turbulence is by turbulence intensity, defined as the ratio of the root-mean-square of the fluctuating component of the longitudinal wind velocity and its time-averaged value:

$$I_u(z) = \frac{\sqrt{\overline{u'^2(z)}}}{\bar{u}(z)} = \frac{\sigma_u}{\bar{u}(z)}, \tag{2.6}$$

where $I_u(z)$ is the longitudinal turbulence intensity [-] at elevation z m, $u'(z)$ the fluctuating component of the longitudinal wind velocity [m s^{-1}], i.e. $u(z) = \bar{u}(z) + u'(z)$.

Similarly one defines lateral and vertical turbulent intensities $I_v(z)$ and $I_w(z)$, respectively.

The total mean turbulent kinetic energy K (per unit of mass) is defined as:

$$K = 0.5\left(\sigma_u^2 + \sigma_v^2 + \sigma_w^2\right). \tag{2.7}$$

As shear is approximately constant with height in the a.s.l., the friction velocity u_* is also approximately constant. The standard deviation of wind speed normalised by u_* is therefore also a measure of turbulence in the a.s.l. Typical values, obtained by measurements, are presented in table 2.1.

2.1.4 Flow near buildings and urban canopy

In the previous subsections we focussed on undisturbed wind. Describing wind patterns nearby buildings and in urban canopies (i.e. beneath the average roof height in towns) is quite difficult because many parameters and especially topography and building geometry

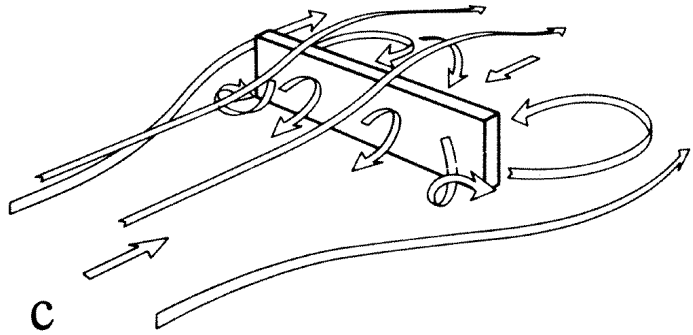

Figure 2.2: Wind near a wide building (Beranek 1994b).

are involved. Beranek (1994b, 1994a) and Bottema (1993b) discuss this topic. We will first discuss the most important characteristics of the flow nearby a free standing building, bearing in mind that these characteristics should be useful for the evaluation of CFD simulations and that for a study on driving rain the lee side of a building is less interesting. Figure 2.2 shows a sketch of the time averaged wind pattern nearby a wide building in the atmospheric boundary layer. Its characteristics are (for more details, see e.g. Bottema (1993b, p. 80 and further)):

- a frontal vortex, i.e. recirculating flow at the windward side of a building. Its size depends mainly on the building height ($\mathcal{H}$), building width ($\mathcal{W}$) and the approach flow angle, and is of the order of $\mathcal{L}_g$, i.e. the smaller of $2\mathcal{H}$ and $\mathcal{W}$, for wind approaching perpendicularly to the façade. For buildings with $\mathcal{W}/\mathcal{H} \gg 3$, however, its size is about $\mathcal{H}$.
- corner streams are the zones near corners with higher wind speeds (higher than the approach wind speed at building height) and lower turbulence intensities.
- separation at corners occurs at the lateral faces of a building. The separation starts on the edge itself, if the corner is sharp. Downstream of the separation the flow can reattach to the lateral face.
- recirculation zones at the lee side are characterised by turbulent and very unsteady flow. They extend to approximately $4\mathcal{L}_g$ behind the building.

The complexity of flows in building groups is of course larger than near a single building on an unbuilt plane. Yet three typical flow regimes are distinguished, depending on the ratio of building height and distance between the buildings. Figure 2.3 shows these for a two dimensional configuration.

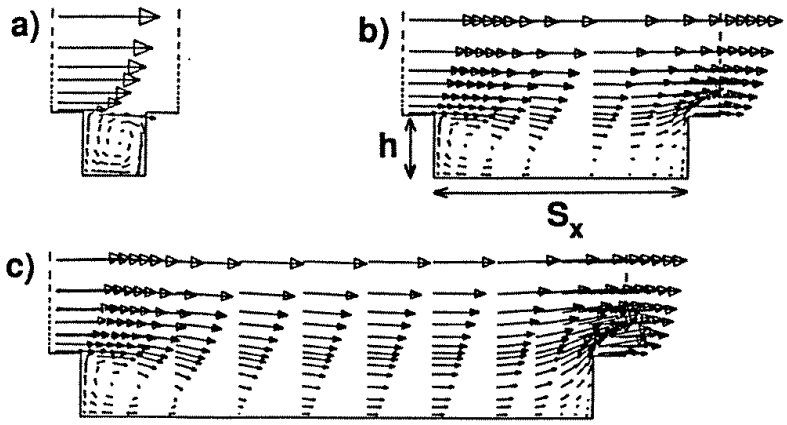

Figure 2.3: Computed 2-dimensional flow patterns which are typical flow regimes in building groups (Bottema 1993b): a. $S_x/h = 1$ skimming flow, b. $S_x/h = 4$ wake interference flow, c. $S_x/h = 8$ isolated roughness flow.

2.1.5 Axis system definitions

We use two definitions for the wind velocity vector. The first one, which we will use most frequently, is a globally defined axis system, i.e. relative to north (see figure 2.4):

- the positive velocity components U_x and U_y are due north and due west, respectively. The positive component U_z is directed upwards;
- the wind direction Φ is the angle in a horizontal plane from which the wind comes, expressed in degrees clockwise from north.

The following quantities are derived from the wind velocity components:

- the horizontal wind speed:

$$U_{\mathrm{h}} = \sqrt{U_x^2 + U_y^2}; \tag{2.8}$$

- the (absolute) wind speed:

$$U = \sqrt{U_x^2 + U_y^2 + U_z^2}. \tag{2.9}$$

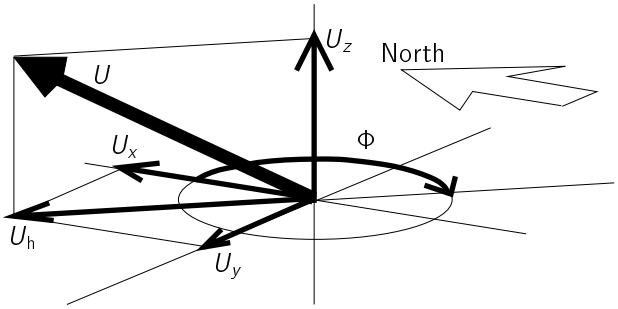

Figure 2.4: Global wind axis system: the definition of wind velocity components U_x, U_y, U_z, horizontal wind speed U_h and horizontal wind direction Φ.

The second definition is related to the mean wind direction:

- the longitudinal wind velocity u is parallel to the mean horizontal wind direction (thus: $u = U_h$);
- the lateral wind velocity v is perpendicular to the mean horizontal wind direction (thus: $\bar{v} = 0$);
- the vertical wind velocity w is directed upwards (thus: $w = U_z$).

2.2 Rain

Precipitation occurs when cloud particles, which grow in complex processes like condensation and aggregation, reach such a size that their falling velocity is larger than the upward wind speed in the air. Precipitation is called rain when its particles are liquid water at ground level. Apart from its complex formation in clouds, rain is basically a population of falling drops interacting with each other (collision, breakup) and with their environment (wind, evaporation).

General literature on rain can be found in for example Pruppacher and Klett (1978). For climatological information on rain one can refer to Buishand and Velds (1980) for the Netherlands.

2.2.1 Raindrop size

In a first approximation, the minimum size of raindrops falling on the ground depends on vertical wind speeds in clouds. In clouds with updraughts of less than 50 cm s^{-1}, drops

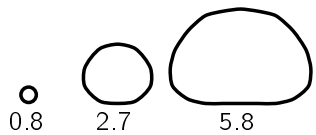

Figure 2.5: Shape of falling raindrops obtained from wind tunnel experiments, after Pruppacher and Klett (1978, p. 22). To scale. Equivalent diameters in mm.

of 0.2 mm (terminal velocity of 70 cm s^{-1}) and more will fall out. In air of 90% humidity such a drop can fall 150 m before total evaporation and thus reach the ground. A drop of 1 mm can fall 40 km. Rain which mainly consists of drops of 0.1 mm diameter, is called drizzle, and is produced by low layer clouds.

The maximum diameter of raindrops is about 7 mm, because larger drops will break apart during the fall.

Only drops of diameters of less than 0.3 mm are nearly perfect spheres at terminal (falling) velocity. Therefore for larger drops one can not unambiguously describe the shape by one length. This problem is solved by the definition of a equivalent diameter: the diameter of a sphere with the same volume as the deformed drop.

Falling drops of (equivalent) diameters of 0.3 to 1 mm resemble oblate spheroids. Drops larger than 1 mm resemble oblate spheroids with flat bases (figure 2.5).

In the following sections and chapters, the term « diameter » should be understood as the « equivalent diameter ». Moreover, one should keep in mind that raindrop diameters range from 0.1 mm to 7 mm. The number of raindrops per drop size in rainfall (« raindrop spectrum ») is discussed in section 2.2.4.

2.2.2 Drop velocity

The velocity of a drop depends on gravitation and drag due to wind speed. The motion of a drop can be described by:

$$m_{\mathrm{D}} \frac{d\vec{u}_{\mathrm{D}}}{dt} = m_{\mathrm{D}}\vec{g} - \frac{\pi}{8}\,\mu\, Re\, C_d(Re)\, D\,(\vec{u}_{\mathrm{D}} - \vec{u}), \tag{2.10}$$

with m_{D} = mass [kg] of a raindrop ($= \rho_{\mathrm{D}}\pi D^3/6$), D = drop diameter [m], $\vec{u}_{\mathrm{D}}$ = drop velocity vector [m s^{-1}], $\vec{u}$ = wind velocity vector [m s^{-1}], $\vec{g}$ = gravitational acceleration [m s^{-2}], C_d = drag coefficient [-] depending on the Reynolds number, Re = Reynolds number ($= \rho D|\vec{u}_{\mathrm{D}} - \vec{u}|/\mu$), ρ_{D} = density [kg m^{-3}] of water, ρ = density [kg m^{-3}] of air, and μ = dynamic viscosity [kg m^{-1} s^{-1}] of air.

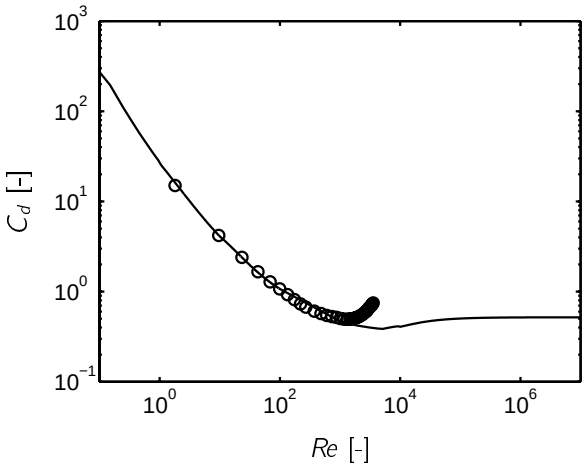

Figure 2.6: Drag coefficient C_d as function of the Reynolds number Re, for particles in general (——, Morsi and Alexander 1972), and falling water drops (o, Gunn and Kinzer 1949).

Figure 2.6 shows the drag coefficient C_d as function of the Reynolds number. The function of Morsi and Alexander (1972) was obtained from fitting a large amount of laboratory data for different kinds of particles, from different references. Data on falling water drops in still air obtained by Gunn and Kinzer (1949) have been included in the graph. For falling drops $D > 5$ mm ($Re > 3\times10^3$), the drag coefficient is underestimated by Morsi and Alexander (1972).

The terminal velocity is the maximum vertical velocity which a drop reaches. It is, in other words, the velocity when the gravitational force equals the drag force. The usual assumption that the vertical velocity approximately equals the terminal velocity, is thus only valid in wind flow with zero vertical wind velocity. Generally this is a good approximation for the undisturbed wind flow far from obstacles; near buildings vertical wind velocity influences the drop velocity. Strictly speaking, the horizontal wind component could also influence the falling velocity because it can deform the shape of a raindrop and thus the drag.

Gunn and Kinzer (1949) presented a table with terminal velocity data as a function of drop diameter, measured in laboratory. We fitted these data with the following function:

$$w_{\text{term}} = 9.40\left(1 - \exp\left(-1.57 \times 10^3 D^{1.15}\right)\right) . \tag{2.11}$$

with w_{term} = terminal velocity [m s^{-1}], and D = equivalent raindrop diameter [m].

Often one applies such a relation obtained from laboratory experiments in still air at an air pressure of 760 mm Hg, a temperature of 20°C and a relative humidity of 50%. In figure

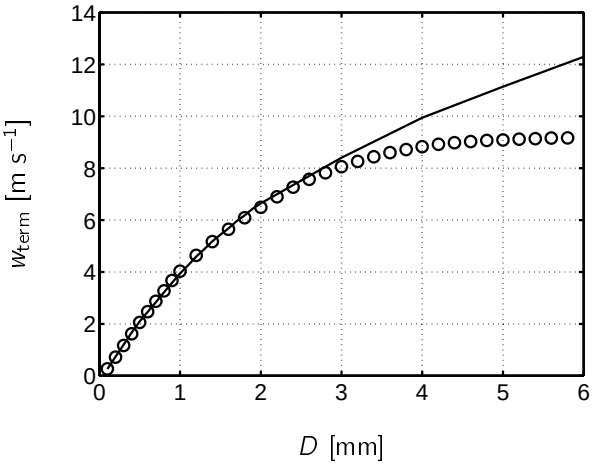

Figure 2.7: Terminal drop velocity as function of raindrop diameter: according to eq. 2.10 with C_d of Morsi and Alexander (1972) (——), and according to the measurements of Gunn and Kinzer (1949) (o).

2.7 the relation given by eq. 2.11 is plotted, with terminal velocities calculated directly from the equation of motion (eq. 2.10) and drag coefficients of Morsi and Alexander (1972). The latter method overestimates the terminal velocity of bigger drops ($D > 3$ mm), because the used drag coefficient function does not take drop deformation into account.

2.2.3 Stopping distance and dispersion

The stopping distance ℓ_{stop} is the distance travelled by a drop as a result of its inertia, after the driving force is suddenly taken away (Fuchs 1964). In our case, the driving force is the wind speed. The stopping distance is a function of the drop diameter D and the initial speed u_i of the drop and can be calculated by use of equation 2.10 with the conditions $\vec{g} = 0$, $u(t < 0) = u_i$ and $u(t \geq 0) = 0$. The solution is:

$$\ell_{\text{stop}} = \frac{4}{3}\, D\, \frac{\rho_D}{\rho} \int_0^{Re_i} \frac{dRe}{Re\; C_d(Re)}, \tag{2.12}$$

with $Re_i = \rho D u_i / \mu$.

Figure 2.8a shows the stopping distance for various initial speeds (cf. wind speeds) and various drop diameters, calculated with values of C_d given by Morsi and Alexander (1972). The same figure gives results calculated with C_d values of Gunn and Kinzer (1949), as far as the limited range of Reynolds numbers allowed for (cf. figure 2.6).

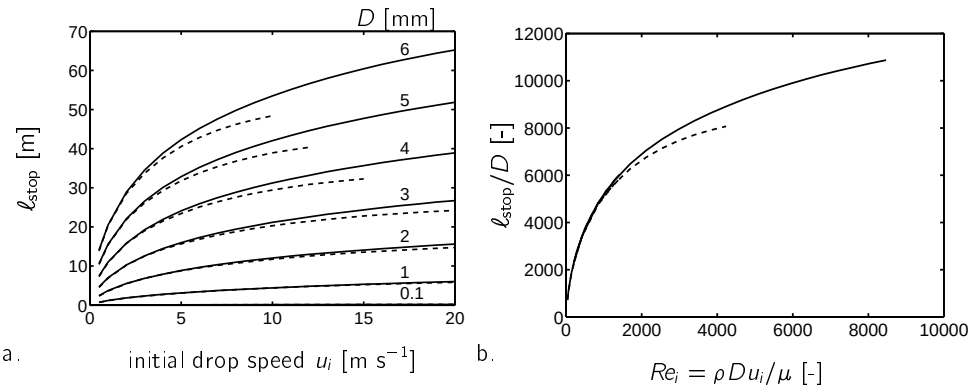

Figure 2.8: Stopping distance of rain drops, calculated with values of C_d given by Morsi and Alexander (1972) (——), and Gunn and Kinzer (1949) (----).

Figure 2.8b shows the same information as figure 2.8a, but now condensed into two lines, as is obvious from eq. 2.12.

The stopping distance is a measure for the ability of raindrops to follow changes in wind speed and direction. In general, in eddies where wind flow is curved and accelerated, the stopping distance can characterise the dispersion of raindrops, i.e. the raindrop trajectory deviations from the wind pattern. Raindrops with a certain ℓ_{stop} will follow eddies with a certain minimum dimension, say $\mathcal{L}_{\text{min}}$, but eddies with a dimension smaller than $\mathcal{L}_{\text{min}}$ will hardly or not effect the raindrop trajectory. We will assume here that $\mathcal{L}_{\text{min}}$ approximately equals ℓ_{stop}.

The integral length scale, L_u, is an estimate of the dimensions of the largest eddies in a neutral homogeneous boundary layer. Estimates range from 50 to 200 m (Geurts 1997). Figure 2.8 shows that for wind speeds up to 10 m s^{-1} the stopping distance is less than L_u, and that the drops will follow such eddies. Close to buildings we will find smaller eddies, for example a frontal vortex with the dimension of the building height (see section 2.1.4 for other typical values).

Without a numerical model it is not easy to estimate how the raindrops will be dispersed by eddies other than L_u or a frontal vortex. Crowe et al. (1998, p. 201) cite an estimation for the length scale of a turbulent eddy within the framework of the K-ϵ turbulence model for the fluid:

$$\mathcal{L}_{\text{turb. eddy}} = C_\mu \frac{K^{\frac{3}{2}}}{\epsilon}, \tag{2.13}$$

with C_μ = an empirical constant (in our case, 0.032) and ϵ = the dissipation rate [m^2 s^{-3}]. Details of the model will be given in chapter 6, but for now we simply refer to equations 6.3 and 6.4 for K and ϵ in the a.s.l, respectively. Substituting these two equations in eq. 2.13, we obtain:

$$\mathcal{L}_{\text{turb. eddy}} = C_\mu^{\frac{1}{4}} kz, \tag{2.14}$$

with $k =$ the von Kármán constant (0.4). For example at $z = 50$ m, the length scale of the turbulent eddy is estimated to be approximately 8 m. According to figure 2.8, this would e.g. mean that raindrops with diameters up to 2 mm are strongly influenced by these turbulent eddies at wind speeds of 5 m s^{-1}.

Although the relation $\mathcal{L}_{\text{min}} \approx \ell_{\text{stop}}$ is only a crude approximation, we conclude that dispersion of raindrops due to the turbulence of the wind is very likely an important factor.

2.2.4 Raindrop spectrum and rain intensity

Rain is characterised by raindrop spectra. In meteorology raindrop spectra (also called « raindrop distributions ») are often expressed in a number of drops per (volume) unit of air per (equivalent) drop diameter. It is here called « raindrop number concentration spectrum », denoted by $n(D)$ and its unit is m^{-3} m^{-1}.

For our purposes, it is more practical to express raindrop spectra in terms of mass fluxes on or through a certain area. First we define a raindrop mass concentration spectrum $m(D)$ [kg m^{-3} m^{-1}]:

$$m(D) = n(D)\ \rho_{\text{D}} \frac{\pi}{6} D^3, \tag{2.15}$$

with $D =$ raindrop diameter [m] and $\rho_{\text{D}} =$ density [kg m^{-3}] of water.

Subsequently, a raindrop mass flux spectrum $\varphi_{\text{h}}(D)$ [kg m^{-2} s^{-1} m^{-1}] through the horizontal is defined by:

$$\varphi_{\text{h}}(D) = m(D)\ w_{\text{term}}(D), \tag{2.16}$$

with $w_{\text{term}}(D) =$ terminal velocity [m s^{-1}] of a drop with diameter D.

Relation 2.16 is only valid (1) if the vertical velocity of every drop equals the terminal velocity (and is not affected by vertical wind, turbulence and raindrop interaction), and (2) if the raindrop spectrum does not depend on time and location (i.e. in stationary rainfall). Uijlenhoet and Stricker (1999) gave an extensive overview of different definitions of raindrop spectra and their integral quantities.

Raindrop mass flux spectra give a better impression of the contribution of every drop size to the total rain amount. This amount is expressed by the horizontal rain intensity R_{h} [mm h^{-1}] and is defined by the amount of rain water falling through a horizontal plane per hour in the undisturbed wind flow, and equals the summation of the mass fluxes of all drops falling through the plane:

$$R_{\text{h}} = 3600 \int_0^\infty \varphi_{\text{h}}(D) dD. \tag{2.17}$$

Note that rain amounts are usually expressed in a height of a layer of water, so that a rain amount of 1 mm equals 1 kg m^{-2}. Note also that rain intensities are often expressed in mm h^{-1}.

Three other quantities are sometimes used, namely (1) the liquid water content W [kg m^{-3}], i.e. the amount of liquid water per unit of air:

$$W = \int_0^\infty m(D)dD, \tag{2.18}$$

(2) the fraction $F(D)$ [-] of liquid water in the air comprised by drops with diameter less than D [m]:

$$F(D) = \frac{\int_0^D m(\Delta)d\Delta}{\int_0^\infty m(\Delta)d\Delta}, \tag{2.19}$$

and (3) the median drop size D_{50} [m]:

$$F(D_{50}) = \frac{1}{2}. \tag{2.20}$$

Three frequently used empirical formulae for raindrop spectra are presented in the following.

Marshall and Palmer (1948) spectra Probably the most widely used empirical description of raindrop spectra is that of Marshall and Palmer (1948):

$$n(D) = n_0 e^{-\Lambda D}, \tag{2.21}$$

with $n(D)dD$ = the number of drops per cubic metre in the drop diameter range (D, $D+dD$) and D = the equivalent drop diameter.

Marshall and Palmer (1948) obtained n_0 and Λ from measurements amongst others by Laws and Parsons (1943), who describe in detail the measurement and averaging methods used at that time:

$$n_0 = 8 \times 10^3 \quad \text{and} \quad \Lambda = 4.1 R_\mathrm{h}^{-0.21}. \tag{2.22}$$

with n_0 in m^{-3} mm^{-1}, Λ in mm^{-1} and R_h in mm h^{-1}. Note that D in eq. 2.21 is in mm.

Examples of Marshall and Palmer (1948) spectra are plotted in figure 2.9a. We converted these raindrop size spectra into raindrop mass flux spectra and the result is plotted in figure 2.9b. Comparison of figures a and b shows that a mass flux spectrum gives a

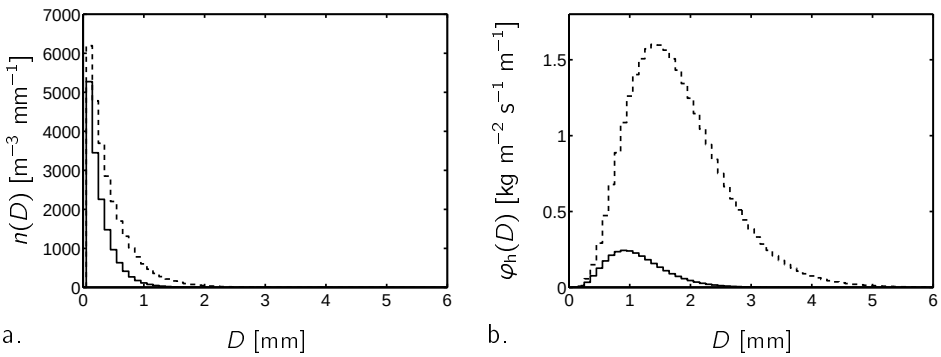

Figure 2.9: Raindrop spectra according to Marshall and Palmer (1948), for two rain intensities R_h: —— 1 mm h^{-1}, ---- 10 mm h^{-1}. Graph a shows raindrop number concentration spectra $n(D)$; graph b shows raindrop mass flux spectra $\varphi_h(D)$. $\Delta D =$ 0.1 mm.

better impression of the contribution of every drop size to the total rain amount on the horizontal.

Subsequent studies pointed out that the parameters n_0 and Λ vary widely (and even during rainfall). One has tried to classify these parameters by the type of rain, as e.g. in Joss and Waldvogel (1969) (table 2.2).

Marshall and Palmer (1948) obtained the parameterisation 2.22 by analysing rainfall with drops of 1 to 3.5 mm diameter and with rain intensities of 1 to 23 mm h^{-1}. It is therefore often assumed that this parameterisation overestimates of the number of drops below 1 mm diameter. Therefore, other spectra (e.g. gamma distributions) were proposed. An overview is given in Sempere Torres and Porrà (1994).

Table 2.2: Parameters n_0 and Λ of the Marshall and Palmer (1948) raindrop spectrum, for various types of rainfall (Joss and Waldvogel 1969).

type of rainfall	N_0 [m^{-3} mm^{-1}]	Λ-R_h relationship [Λ mm^{-1}, R_h mm h^{-1}]
drizzle	30 000	$\Lambda = 5.7 R_h^{-0.21}$
widespread	7 000	$\Lambda = 4.1 R_h^{-0.21}$
thunderstorm	1 400	$\Lambda = 3.0 R_h^{-0.21}$

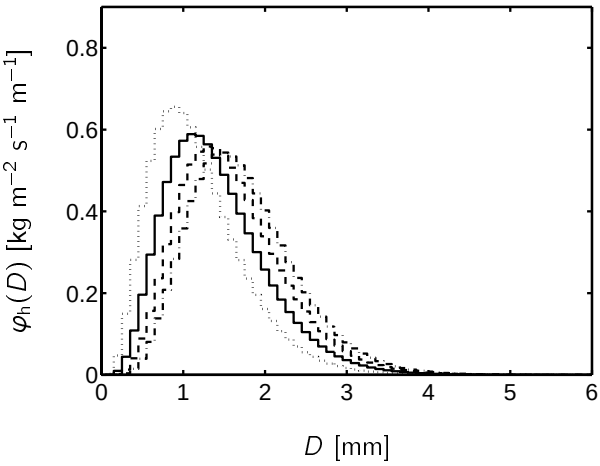

Figure 2.10: Raindrop mass flux spectra with a rain intensity of 3 mm h^{-1}, according to Marshall and Palmer (1948) (——), and Ulbrich (1983) (.....: $\mu = -1$, ----: $\mu = 1$, -.-.-.: $\mu = 2$). $\Delta D = 0.1$ mm.

Ulbrich (1983) spectra The raindrop spectrum of Ulbrich (1983) is defined as:

$$n(D) = n_0 D^{\mu} e^{-\Lambda D}, \tag{2.23}$$

with μ = a parameterisation constant [-] (realistic values from -1 to 6), n_0 and Λ according to eq. 2.22, and D in mm.

The Ulbrich spectrum includes an extra parameter (μ), which should take variations in n_0 (of eq. 2.21) into account. E.g. Waldvogel (1974) showed that large and sudden changes in n_0 can occur from moment to moment within a given rainfall type. Figure 2.10 shows examples of Ulbrich spectra. Note that for $\mu = 0$ the Ulbrich spectrum equals the Marshall-Palmer spectrum.

Best (1950) spectra The third type of raindrop spectrum presented here, was proposed by Best (1950). The spectrum is expressed by:

$$m(D) = \frac{dF}{dD} W, \tag{2.24}$$

where

$$1 - F(D) = \exp\left(-\left(\frac{D}{AR_h^a}\right)^b\right) \quad \text{and} \quad W = CR_h^q,$$

with $F(D)$ = the fraction of liquid water in the air comprised by drops with diameter less than D [mm], R_h = the horizontal rain intensity in mm h^{-1}, and W = the amount of liquid water per unit of air in mm^3 m^{-3}.

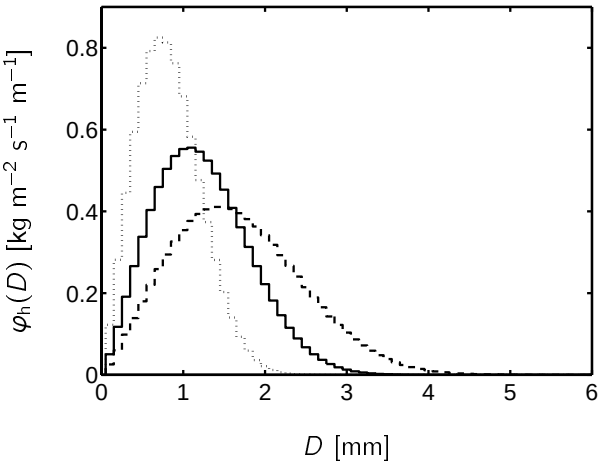

Figure 2.11: Raindrop mass flux spectra with a rain intensity of 3 mm h^{-1}, according to Best (1950). ——: $A = 1.30$, $a = 0.232$, $b = 2.25$, $C = 67$, $q = 0.846$. Similar spectra, according to the measurements of Wessels (1972): .....: $A = 0.88$, $a = 0.21$, ----: $A = 1.77$, $a = 0.21$. $\Delta D = 0.1$ mm. Cf. figure 2.10.

The values of the constants A, a, b, C and q were obtained from results of measurements in Great-Britain and eight papers (e.g. Laws and Parsons 1943 and Marshall and Palmer 1948), and amount to 1.30, 0.232, 2.25, 67 and 0.846, respectively. The Best spectrum is used in Wessels (1972) to analyse raindrop spectra measured at De Bilt (NL) during 1968 and 1969. The best regression of the 533 observations was found with $A = 1.21$ and $a = 0.21$. 90% of the observations had a constant A ranging from 0.88 to 1.77 (with $a = 0.21$). Individual raindrop spectra can thus vary widely in shape, as is illustrated in figure 2.11.

Summary The three presented raindrop spectra can be summarised by the following formula for the raindrop mass concentration spectrum:

$$m(D) = C_1 \; D^{C_2} \; \exp\left(-C_3 D^{C_4}\right) . \tag{2.25}$$

The expressions for the parameters C_1, C_2, C_3 and C_4 are listed in table 2.3.

2.3 Driving rain

Generally one considers « driving rain » as rain that is carried (driven) by wind. A synonym is « wind-driven rain ». Here, we will use a more restricted definition: driving rain (or wind-driven rain) is rain that is carried by wind and driven onto building envelopes. Usually we

Table 2.3: Parameters C_1, C_2, C_3 and C_4 of eq. 2.25 for Marshall and Palmer (1948) spectra, Ulbrich (1983) spectra and Best (1950) spectra. In equation 2.25 and the equations below, the units of D, $m(D)$ and ρ_D are [m], [kg m^{-3} m^{-1}] and [kg m^{-3}], respectively. The units of n_0, Λ, A, a, b, C and q are the same as in the equations 2.22, 2.23 and 2.24.

Marshall and Palmer:	$C_1 =$	$10^3 \frac{\pi}{6} \rho_D n_0$ [kg m^{-3} m^{-1}]
	$C_2 =$	3
	$C_3 =$	$10^3 \Lambda$
	$C_4 =$	1
Ulbrich:	$C_1 =$	$10^{3+3\mu} \frac{\pi}{6} \rho_D n_0$ [kg m^{-3} m^{-1}]
	$C_2 =$	$\mu + 3$
	$C_3 =$	$10^3 \Lambda$
	$C_4 =$	1
Best:	$C_1 =$	$10^{-9+3b} \rho_D \frac{bCR_h^{q-ab}}{A^b}$ [kg m^{-3} m^{-1}]
	$C_2 =$	$b - 1$
	$C_3 =$	$\frac{10^{3b}}{A^b R_h^{ab}}$
	$C_4 =$	b
	Note that in eq. 2.24: $W = 10^{-9} \rho_D C R_h^q$ [kg m^{-3}].	

will look at building envelopes which are vertical, although rain distribution on roofs is affected by wind too.

Because wind always plays a role in formation and distribution of rain, the quantities and physical concepts described in the previous section 2.2 also apply for driving rain (yet sometimes slightly adapted).

2.3.1 Theoretical model

The general model of driving rain used in this study takes the trajectories of raindrops into account. In reality, every individual drop has its individual drop trajectory. Moreover, the lifetime of a drop is affected by drop interaction (collision and breakup) and the environment (wind and evaporation). The model takes only the influence of the wind into account. This is sketched in figure 2.12 for raindrops of one particular size. From the discussion in section 2.2.3 we expect that the trajectories of raindrops will also be affected by the turbulence in the wind. The turbulent dispersion of raindrops will imply that raindrops starting at the same point will follow different paths (figure 2.12).

The driving rain amount per drop size in relation to the reference rain amount per drop

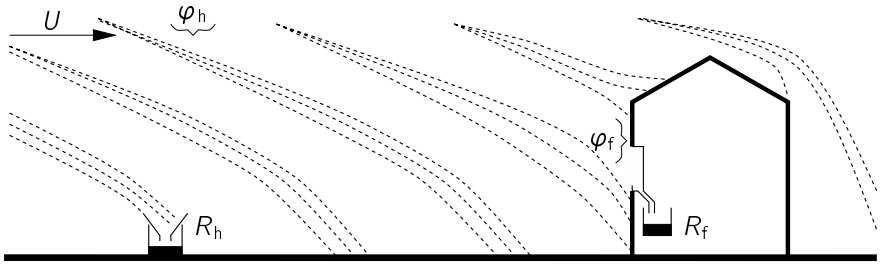

Figure 2.12: Sketch of trajectories of raindrops with the same diameter. The wind is from left to right. The trajectories disperse due to the turbulence of the wind.

size is characterised by a catch ratio $\eta(D)$:

$$\eta(D) = \frac{\varphi_f(D)}{\varphi_h(D)}, \tag{2.26}$$

with $\varphi_f(D)$ = the raindrop mass flux spectrum on the façade surface, and $\varphi_h(D)$ = the raindrop mass flux spectrum through the horizontal in the undisturbed wind flow (calculated using eq. 2.16).

The reference of $\varphi_f(D)$ in eq. 2.26 is taken in the wind flow undisturbed by individual buildings or other obstacles. The reference is preferably taken at the site itself and then the model applies for the second step in our general two-step approach (figure 1.1).

The driving rain intensity R_f on the building envelope is:

$$R_f = 3600 \int_0^\infty \varphi_f(D) dD = 3600 \int_0^\infty \eta(D) \varphi_h(D) dD. \tag{2.27}$$

The catch ratio $\eta(D)$ (and eventually the driving rain intensity) depends on the following factors:

- raindrop size —the driving rain intensity depends on the raindrop spectrum,
- wind field,
- building geometry and topology of the surroundings,
- position on the building envelope.

The model can be elaborated into a numerical model. This will be done in chapter 6 (CFD simulations). Similar numerical models were described in the literature, e.g.:

Bookelmann and Wisse (1992), Choi (1993), Karagiozis and Hadjisophocleous (1996), van Mook et al. (1997), Sankaran and Paterson (1995a), Hangan and Surry (1998) and Blocken and Carmeliet (2000a). However, the cited authors (except for Sankaran and Paterson 1995a) did not take the turbulent dispersion of raindrops into account: the trajectories were calculated according to the mean wind field. In chapter 6 we will study the differences resulting from calculations with or without turbulent drop dispersion.

2.3.2 Empirical model

In the practice of driving rain measurements, raindrop spectra have never been measured, and raindrop trajectories are not determined. Based on the integral rain quantities, one correlates the driving rain intensity with the horizontal rain intensity, i.e. the reference in the undisturbed wind flow, by means of their ratio:

$$k = \frac{R_\mathrm{f}}{R_\mathrm{h}}. \tag{2.28}$$

k is here called « driving rain ratio ». Measured values of k can be found e.g. in Hens and Mohamed (1994), Osmond (1996) and Kragh (1998).

1. Vertical rain intensity Some authors try to distinguish several factors in the driving rain ratio. The first step is to define a vertical rain intensity R_v [mm h^{-1}], i.e. the rain intensity through a vertical plane in the undisturbed wind flow. It is assumed to be related to the reference wind speed and horizontal rain intensity in the following way:

$$R_\mathrm{v} = \alpha\, U_\mathrm{r}\, R_\mathrm{h}^{\beta}, \tag{2.29}$$

with U_r = the reference wind speed [m s^{-1}], and α and β are empirical constants.

Lacy (1965) calculated α and β as follows: he assumed that the ratio of vertical and horizontal rain intensities is equal to the ratio of wind speed and terminal velocity of drops of median size (D_{50}):

$$R_\mathrm{v} = R_\mathrm{h} \frac{U_\mathrm{r}}{w_\mathrm{term}(D_{50})}. \tag{2.30}$$

He gives an empirical relationship between R_h and D_{50} which he deducted from data presented by Laws and Parsons (1943):

$$D_{50} = 1.238 R_\mathrm{h}^{0.182}, \tag{2.31}$$

and by combining this with the $w_\mathrm{term}(D)$ relation deduced from Best (1950) he obtains:

$$w_\mathrm{term}(D_{50}) = 4.505 R_\mathrm{h}^{0.123}. \tag{2.32}$$

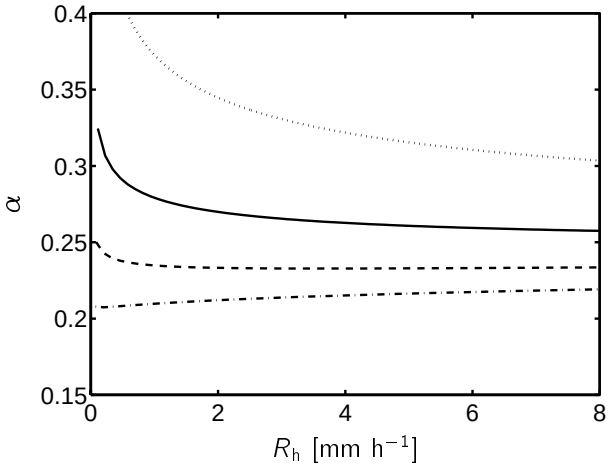

Figure 2.13: Lacy's parameter α (with $\beta = 0.88$) as function of horizontal rain intensity, for raindrop spectra of Marshall and Palmer (1948) (——), and Ulbrich (1983) (.....: $\mu = -1$, ----: $\mu = 1$, -·-·-: $\mu = 2$). Cf. figure 2.10.

Substituting eq. 2.32 in eq. 2.30 yields the desired relation:

$$R_v = 0.222\, U_r\, R_h^{0.88}, \tag{2.33}$$

so that $\alpha = 0.222$ and $\beta = 0.88$.

Lacy (1965) showed also that calculated values of R_v (eq. 2.33) agree quite well with measurements of R_v for 75 storms with driving rain that occurred during 1948–1963 in Garston (UK). Only rain storms of more than 10 hours were taken into account; the time interval of the measurements was not specified. Measurements of Künzel (1994) at Holtzkirchen (DE) yielded a value for α of about 0.2.

With the quantities defined in section 2.2.4, one can express the vertical rain intensity R_v [mm h^{-1}] in terms of the reference wind speed U_r [m s^{-1}] and the integral of the raindrop mass concentration spectrum (i.e. the liquid water content W [kg m^{-3}]):

$$R_v = 3600\, U_r \int_0^\infty m(D)dD = 3600\, U_r\, W. \tag{2.34}$$

To investigate the validity of the model of Lacy (eq. 2.29) for several given raindrop spectra, we combine equations 2.29 and 2.34, yielding $3600 U_r W = \alpha U_r R_h^\beta$, and plot $\alpha = 3600 W/R_h^\beta$ for $\beta = 0.88$. Figure 2.13 shows this plot for raindrop spectra of Marshall and Palmer (1948) and Ulbrich (1983) (compare with figure 2.10). In figure

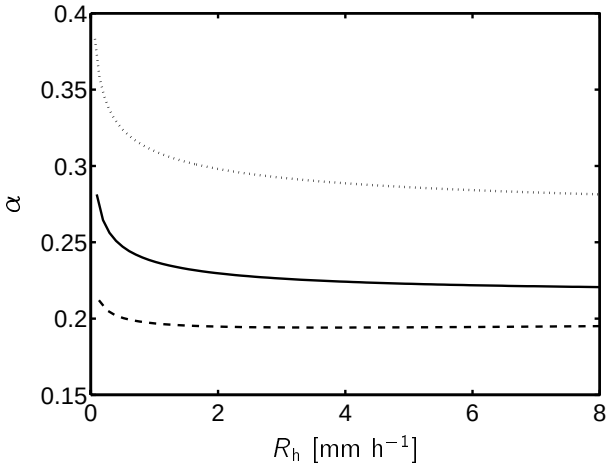

Figure 2.14: Lacy's parameter α (with $\beta = 0.88$) as function of horizontal rain intensity, for raindrop spectra of Best (1950). ——: $A = 1.30$, $a = 0.232$, $b = 2.25$, $C = 67$, $q = 0.846$. Variation of α calculated from the measurements of Wessels (1972): .....: $A = 0.88$, $a = 0.21$, - - - -: $A = 1.77$, $a = 0.21$. Cf. figure 2.11.

2.14 α is plotted for Best spectra according to parameters given by Best (1950) and according to the measurements in the Netherlands of Wessels (1972) (cf. figure 2.11). These figures show that parameter α becomes constant for larger R_h, but for rain intensities below 1 mm h^{-1} α can increase up to 0.4. Moreover, rainfall with larger drops will yield a lower value of α. Applying the data of Wessels (1972), we find that α ranges from 0.2 to 0.35. The generally measured value 0.22 (i.e. at the lower part of the mentioned range) might originate from the sensitivity of free-standing driving rain gauges, which is often low for low rain intensities and for rainfall with mainly small drops.

2. Driving rain intensity The second step is to relate vertical rain intensity to driving rain intensity:

$$R_f = \kappa \, R_v. \tag{2.35}$$

The obstruction factor κ is meant to reflect the building geometry, surrounding topology and façade position. It ranges from 0.1 to 2. Examples for values of κ are found in Lacy (1965), Frank (1973), Lacy (1977), Brown (1988), Henriques (1992) and Künzel (1994).

Finally, we conclude that both the coefficient α and the obstruction factor κ depend on the raindrop spectrum. So, they are interdependent. It is probably better to merge the two coefficients into one coefficient ($\kappa \times \alpha$).

Chapter 3

Site and measurement set-up

In this chapter the site and instrumentation for the full-scale experiments are described. The objectives of the experiments are the following:

- development and testing of driving rain gauges. Driving rain gauges are not commercially available and no standard for their design does exist. Therefore several types of driving rain gauges were designed, tested and compared in practice.
- acquisition of driving rain data simultaneously with relevant weather data (in real circumstances, in full scale) for the development of models for driving rain and for studies on heat, air and moisture transport in building envelopes.
- verification of CFD simulations of wind and driving rain for the same situation.

The Main Building of the TUE was found to be a practical choice for the experiments, because of the following reasons:

- The Main Building is oriented north-south and has a large west façade. The prevailing direction for wind and rain is between south and west. Therefore the west façade is suited for driving rain measurements.
- There are no significant obstacles up to 400-500 m from the Main Building in south-west to westward direction. The fetch in this direction is rough and consists mainly of trees. Moreover, the Main Building is a large building (45 m high, 169 m wide, 20 m deep) and its height is much larger than $20z_0$.
- A suitable location for reference measurements of wind and rain from the mentioned directions was found at the west side of the Main Building.

- Moreover, an ultrasonic anemometer on top of a mast placed west from the Main Building has been operational for reference wind measurements since April 1994. It was part of the measurement set-up of Geurts (1997) and useful information on the wind characteristics on the site has been obtained.
- A meteorological station of the Royal Netherlands Meteorological Institute (KNMI) is located at Eindhoven Airport (approximately 7.5 km westwards to the TUE site). The data of this station is useful for comparison with our data.
- During the measurements, the Building Physics group was situated at the two top floors of the Main Building. This and the general fact that the measurements are done at the university campus, facilitate the installation, accessibility and maintenance of the instruments. Moreover, the façade elements of the Main Building are easily removable, because the façade is a curtain wall, consisting of glass windows in frames of steel columns.

The following sections deal with the site, instrumentation and data processing. Details have already been reported in van Mook (1998a) and van Mook (1998b). Högberg et al. (1999) describe the full-scale comparison test of driving rain gauges at the west façade of the Main Building. For this test, the Chalmers University of Technology (CTH), the Technical University of Denmark (DTU) and TUE compared driving rain gauges which they use.

3.1 Geography and surroundings

The Main Building of the TUE is situated on the campus of the TUE, which is located near the centre of the town of Eindhoven (figure 3.1). The town has approximately 200.000 inhabitants. The latitude and longitude coordinates are 51.45° N and 5.48° E. The height above sea level is approximately 16 m. Eindhoven is situated in the south of the Netherlands: 110 km from Amsterdam, 100 km from Rotterdam, 105 km from Brussels and 120 km from Cologne. The North-Sea coast is more than 110 km westwards and hills can only be found some 70 km south-east- and southwards.

The region around Eindhoven is characterised by a quite flat topography. The surrounding villages do not have high-rise buildings; also in Eindhoven the number of high-rise buildings is quite small. The distance between the meteorological station at Eindhoven Airport and the experiment site is approximately 7.5 km. The two locations lie on the same latitude (figure 3.1). Oemraw (1982) and Verkaik (1999) described the meteorological station.

Figures 3.2 and 3.3, respectively, show a plan and an areal view of the direct surroundings of the Main Building. A more detailed plan of the site and elevations of the test building are drawn in figures 3.4, 3.5 and 3.6.

Figure 3.1: Eindhoven and its surroundings. « TUE » denotes the location of the Auditorium of the university; « EA » the location of weather station at the Eindhoven Airport. The light grey areas consist mainly of trees, the dark grey areas represent built areas.

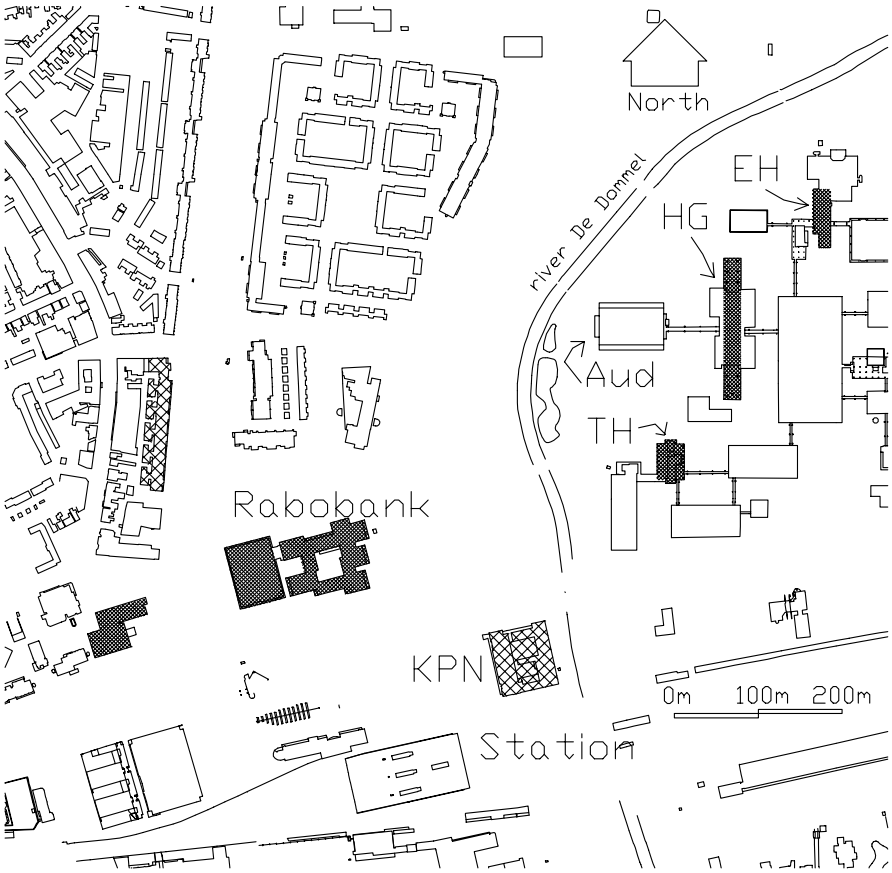

Figure 3.2: Plan of the site and westward fetch. The Main Building is denoted by « HG », the Auditorium by « Aud », and Building T by « TH ». Other buildings with height up to 50 m are hatched. Buildings with heights from 15 to 35 m are indicated with a lighter hatch.

Figure 3.3: Areal view from west. The three high-rise buildings are (from left to right): Building EH, Main Building and Building T.

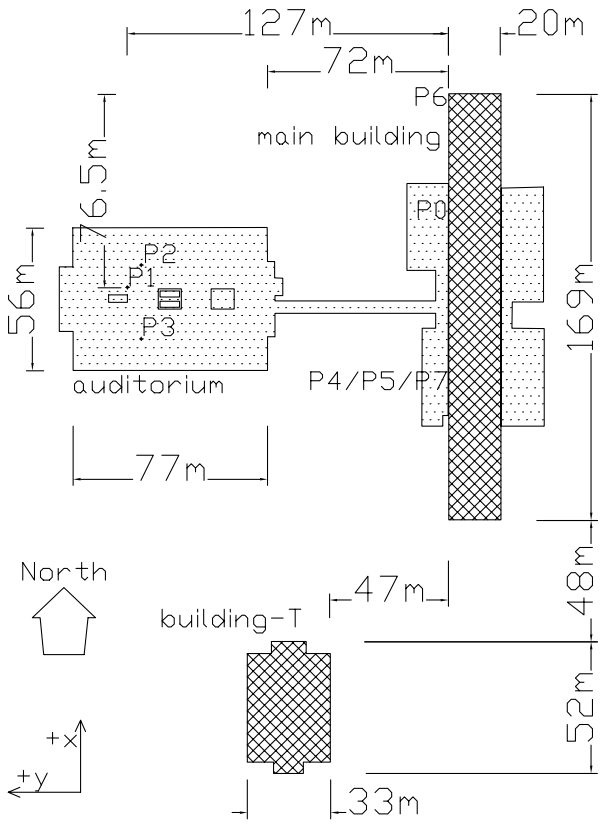

Figure 3.4: Measurement positions, plan.

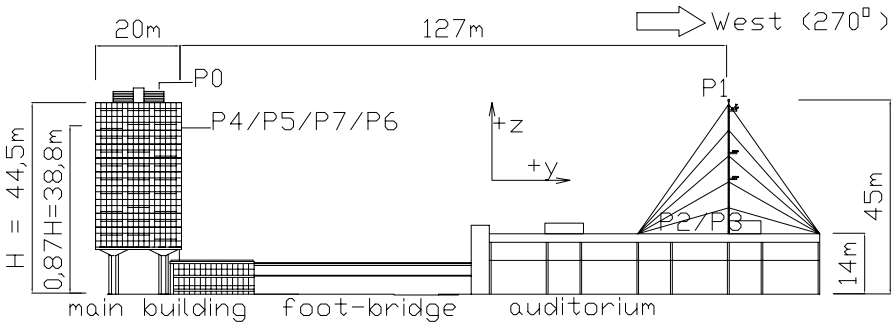

Figure 3.5: Measurement positions, view from north.

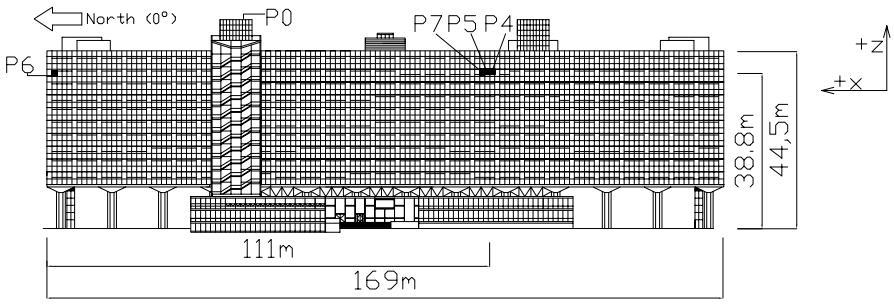

Figure 3.6: Measurement positions, view from west.

The dimensions of the Main Building are: (height) 45 m, (width) 169 m and (depth) 20 m. The reference location is at the Auditorium, i.e. for the measurement of reference wind and rain quantities. The Auditorium is 14 m high and is located at 72 m from the west façade of the Main Building. The Auditorium is surrounded by a park with trees with a height of approximately 15 m. The park extends to the west where mainly residence buildings are located. On the roof of the Auditorium a mast is mounted, which holds an ultrasonic anemometer on top. The anemometer is located at 45 m height, which is the roof height of the Main Building. The mast is 127 m west from the west façade of the Main Building.

Buildings T and EH are the high-rise buildings (50 m height) in the vicinity of the Main Building (figure 3.2). The Rabobank building is approximately 500 m south-eastwards from the Main Building, and has a height of 50 m. Angles of obstruction due to these high-rise buildings, seen from the centres of the Main Building and the Auditorium, respectively, are listed in table 3.1.

The surroundings and the mast were reported in detail by Geurts (1994). Since then several buildings were renovated. The Auditorium was renovated during the latter half of 1995; a lift house, kettle house and cooling fan block were installed on its roof.

Table 3.1: Angles of obstruction due to other buildings, seen from the centres of the Auditorium and the west façade of the Main Building. Expressed in degrees clockwise from north. Also the respective distances are listed.

	from Main Building		from Auditorium	
Main Building	—	—	59°–125°	110 m
Building EH	32°–53°	250 m	55°–70°	150 m
Building T	195°–210°	150 m	150°–163°	140 m
Rabobank	235°–248°	∼500 m	225°–243°	∼380 m

Table 3.2: Instrumentation for reference measurements at the Auditorium.

position	quantity	instrument	sampling
P1	wind velocity (3d)	Solent Research Ultrasonic Anemometer	21 / s ⋆
P2	horizontal rain intensity	Young tipping-bucket rain gauge 52202	2 / min
P3	horizontal rain intensity	Young tipping-bucket rain gauge 52202	2 / min
P3	duration of hor. rain	rain indicator	2 / min
P3 ⋆⋆	raindrop spectrum	disdrometer (Parsivel M300 by PMTech)	2 / min

⋆ One-minute averages of 21 samples per second are logged.
⋆⋆ Operational from October 1999.

The south-west substructure (floors 0 and 1) of the Main Building was renovated from summer 1998 to spring 1999. Everything but roof, floors and columns was removed; the building volume was remained during and after the renovation. In April 1999 the cladding, inner walls and top floor of Building T were removed. Its renovation for the new housing of the faculty of Architecture, Building and Planning started in February 2001.

3.2 Instrumentation

Figures 3.4, 3.5 and 3.6 show in detail the measurement positions which have been arranged for this study. They are numbered P1 to P7. Table 3.2 lists the applied instrumentation for the reference measurements.

Reference quantities are measured at positions P1, P2 and P3, i.e. above or on the roof of the Auditorium of the TUE. The reference wind velocity is measured on the mast on the Auditorium at 45 m height (position P1). The reference horizontal rain intensity is measured on two locations on the roof of the Auditorium: a position at the north side (P2) and one at the south side (P3) of the Auditorium roof were selected to investigate possible spatial differences of horizontal rain intensities. At position P3 a rain indicator was also installed in order to measure the duration of horizontal rain and to switch the wiper of the TUE-II driving rain gauges (see section 3.2.5).

Driving rain is measured at positions P4, P5, P6 and P7. Positions P4, P5 and P7 are adjacent to each other, at (approximately) the centre of the west façade of the Main Building. Position P6 is at the north edge of the façade (its centre is at 1.88 m from the edge). All façade positions are situated 39 m from ground level (87% of the building

Table 3.3: Instrumentation for measurements at the west façade of the Main Building.

From 11 December 1997 to 7 July 1998

position	quantity	instrument	sampling
P4	wind velocity (3d) at 75 cm from façade surface	Solent Windmaster 1086M Ultrasonic Anemometer	1 / s
P4 ⋆	driving rain intensity	driving rain collector TUE-I	2 / min
P5	driving rain intensity	driving rain collector TUE-II	2 / min
P6 ⋆⋆	driving rain intensity	driving rain collector TUE-II	2 / min

⋆ Rectangular catchment area of TUE-I: $A_{\text{catch}} = 0.830 \times 0.635 = 0.527$ m^2.
⋆⋆ Operational from 2 March 1998.

From 17 July 1998 to 16 September 1998

position	quantity	instrument	sampling
P4	wind velocity (3d) at 125 cm from façade surface	Solent Windmaster 1086M Ultrasonic Anemometer	1 / s
P4	driving rain intensity	driving rain collector CTH	2 / min
P4	driving rain intensity	driving rain collector DTU	6 / min
P5	driving rain intensity	driving rain collector TUE-II	2 / min
P6	driving rain intensity	driving rain collector TUE-II	2 / min

From 16 September 1998 to 31 December 1999

position	quantity	instrument	sampling
P4 ⋆⋆	wind velocity (3d) at 50 cm from façade surface	Solent Windmaster 1086M Ultrasonic Anemometer	1 / s
P4	driving rain intensity	driving rain collector TUE-II	2 / min
P5 ⋆	driving rain intensity	driving rain collector TUE-I	2 / min
P7	driving rain intensity	driving rain collector CTH	2 / min
P7	driving rain intensity	driving rain collector DTU	6 / min
P6	driving rain intensity	driving rain collector TUE-II	2 / min

⋆ Till 25 February 1999, the catchment area of TUE-I was circular: $A_{\text{catch}} = 0.444$ m^2. After that, its catchment area was reduced to $0.250 \times 0.250 = 0.0625$ m^2.
⋆⋆ From 14 September 1999 onwards the anemometer distance is 124 cm.

Figure 3.7: The two driving rain gauges on the west façade of the Main Building during the first measurement period from 11 December 1997 to 7 July 1998. From left to right: TUE-II (position P5) and TUE-I (P4). The ultrasonic anemometer has been mounted below TUE-I. Photograph by Ben Elfrink.

height). The driving rain gauges were placed behind specially arranged openings in the façade. These openings were formed by removing the original glass windows and replacing them by a plywood board with an opening of 827 × 735 mm^2.

At position P4 an anemometer was mounted on a boom, fixed to the façade. The length of the boom is variable. This enables measurements of wind velocities at a distance of 0.25–1.5 m from the façade, which will be useful for comparison with CFD simulations.

Table 3.3 shows the instrumentation applied on the west façade of the Main Building. The instrumentation at the central façade position changed over time. Three periods are distinguished. During the first period (December 1997 to July 1998) the driving rain gauges TUE-I and TUE-II were installed at positions P4 and P5 respectively (figure 3.7). The second period was a short period during which two new driving rain gauges were tested. One of them came from the Chalmers University of Technology (CTH) and the other was developed at the Technical University of Denmark (DTU). In the third period (from September 1998 onwards, figure 3.8), the positions of the TUE-I and TUE-II gauges were interchanged with respect to the first period. The shape of the catchment area of TUE-I was changed from a rectangle into a circle. The distance between the anemometer and the façade was reduced to 50 cm (figure 3.8). During the third period, the CTH and DTU gauges were located at position P7 (i.e. next to P4 and P5), so that their readings could be compared with those of the TUE-I and TUE-II gauges for the full-scale comparison test of driving rain gauges.

The driving rain gauge at the north façade edge (P6) was operational since March 1998,

Figure 3.8: The four driving rain gauges on the west façade of the Main Building during the third measurement period from 16 September 1998 to 25 February 1999. From left to right: DTU (position P7), CTH (P7), TUE-I (P5) and TUE-II (P4). The ultrasonic anemometer has been mounted near TUE-II. Photograph by Ben Elfrink.

and was always of the TUE-II type.

The disdrometer became operational on 1 October 1999. Its measurements went on till 7 January 2000. Except for analyses of the disdrometer data, we will not take the other data after December 1999 into account.

Altogether, the full-scale measurements comprised a period of two years (December 1997 to December 1999) and resulted in an almost complete set of data on reference horizontal rain, reference wind velocity and driving rain obtained by the TUE-II gauges at P4/P5 and P6.

In the following subsections the used instruments will be discussed briefly. See van Mook (1998a) for details.

3.2.1 Ultrasonic anemometers

The ultrasonic anemometer on the mast on the Auditorium (position P1) is suited for measurements of wind speed spectra. The sample rate is 168 per second; the output sample rate is 21 per s. From this data 1-min averages of the three velocity components U_1, U_2 and U_3 (figure 3.10) are calculated and logged. The ultrasonic anemometer at the façade position P4 is a simpler version. It can sample with a rate of 9 per second, but it is configured so that every second a sample is taken and logged. Major advantages of

Figure 3.9: The driving rain gauge (type TUE-II) on the north edge of the west façade of the Main Building (position P6). Situation from 2 March 1998.

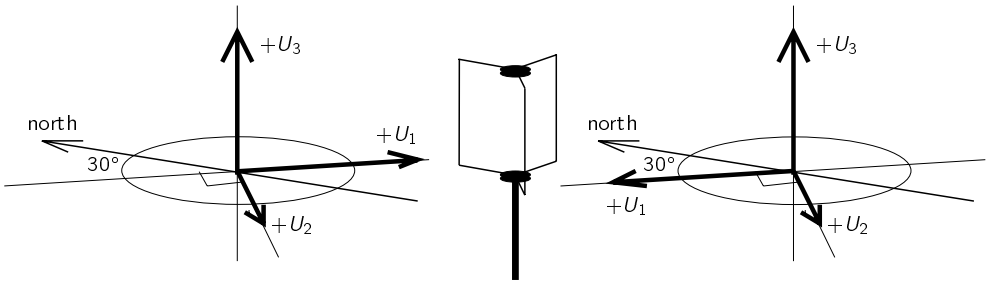

Figure 3.10: Anemometer axis systems of the Solent Research at position P1 (left) and the Solent Windmaster at position P4 (right).

the used anemometers are: no moving parts (and thus no maintenance), accurate (error ~3%), no calibration, and easy communication via an RS232 serial line.

3.2.2 Tipping-bucket rain gauges

For the horizontal rain intensities two standard rain gauges of the tipping-bucket type are applied. Figure 3.11 shows one of the two tipping buckets. The horizontal catchment area is circular and equals 200 cm^2. The typical resolution V_{tip} is 2 ml per tip, which corresponds to a rain amount of 0.1 mm with the given catchment area. Their calibration was done by ourselves, yielding:

series number	V_{tip} [ml]	position
#413	1.90 ± 0.14	P2
#414	2.21 ± 0.11	P3

3.2.3 Rain indicator

The rain indicator is a device which only indicates whether there is precipitation or not. It consists of 6 sensor boards on which electrodes were deposited in a grid. A drop or snowflake which is lying on a board and touches the electrodes, is sensed by an electronic circuitry. In that case, heating resistors mounted on the rear of the sensor board are switched on in order to facilitate evaporation. We did not investigate the rate of evaporation. The sensor boards were manufactured by Conrad Electronics. Their size is 4 × 4 cm^2 and the distance between the electrodes is 1.5 mm. Note that the rain indicator can not distinguish between dew, rain, snow and other forms of precipitation.

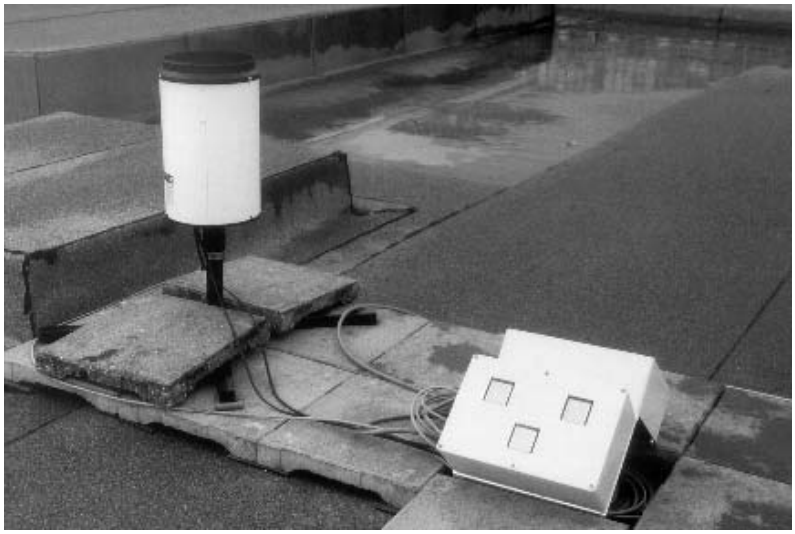

Figure 3.11: Rain gauge (left) and rain indicator (right) at position P3 (roof of the Auditorium). Photograph by Ben Elfrink.

The rain indicator was installed on the roof of the Auditorium (position P3, figure 3.11), and therefore it detects horizontal rain. It serves two purposes: (1) it switches the wiper of driving rain gauges of type TUE-II on when it rains (see section 3.2.5), (2) it is used to measure the duration of rain events. The measurement of the rain duration by a rain indicator is more direct and more accurate than by a tipping-bucket rain gauge, which gives only a signal after a time when the bucket is full. The rain duration measurements will be used to obtain corrected horizontal rain intensity data from the tipping-bucket rain gauge data (see section 3.4.3).

3.2.4 Disdrometer

We call every device which measures raindrop spectra, a disdrometer. In literature one finds alternatives, like the spelling « distrometer » and the terms « spectrometer » and « spectropluviometer »; sometimes « disdrometer » is restricted to the device developed by Joss and Waldvogel (1967). The following modern measurement methods exist (see Laws and Parsons (1943) and Wessels (1967) for the older filter-paper and flour methods):

- Joss-Waldvogel disdrometer (Joss and Waldvogel 1967). This device consists of a sensor head with a catchment area of 50 cm^2. Drops impinging on the head cause

a downward displacement which is sensed by a coil. The amplitude of the voltage pulse from the coil is a measure for the size of a drop. The signal-processing electronics classifies the pulses into 20 channels which correspond to 20 raindrop diameter ranges, as calibrated and specified by the manufacturer. The Joss-Waldvogel disdrometer is often used as a reference, because it was the first electronic instrument which was (and still is) commercially available,

- shadowgraph or imaging method. A laser beam, optically shaped into a rectangular or elliptical cross section with a relatively small height, illuminates a CCD or an array of photodiodes. Drops passing through the beam are sized by the shadow created on the light sensor. The principle was applied e.g. by Knollenberg (1970) (with an array of photodiodes). The two-dimensional video-disdrometer of Schönhuber et al. (1994) is equipped with two video cameras. In fact, the video cameras take pictures of the front and the side of each single raindrop, snowflake or other hydrometeor passing through the light sheet. This produces detailed information on size, shape and speed of hydrometeors,

- light attenuation method. Instead of sensing the whole shadow image of a raindrop, a single photodiode senses the total attenuation of the detected light. Salles et al. (1998) describe a disdrometer (originally from 1969) which uses this principle and which was improved by them. Other such devices were developed by Grossklaus et al. (1998) and by Löffler-Mang and Joss (2000),

- Doppler radar method. In contrast to conventional weather radars, Doppler radars suited for raindrop spectrum measurements measure the spectral radar reflectivity in a relatively small air volume. The Doppler radar points vertically and therefore measures the falling velocity of the raindrops. With help of an assumed relation between drop size and terminal (falling) velocity (e.g. eq. 2.11), the raindrop mass flux spectrum through the horizontal can be calculated. Applications of this principle were described e.g. by Sheppard (1990) and Richter and Hagen (1997).

In our choice for a disdrometer, the directness of the drop size measurement principle, the (in)sensitivity to wind, the resolution in time and space, the easiness of use and the price were the most important criteria. The two-dimensional video-disdrometer of Schönhuber et al. (1994) would have been the most ideal instrument, because it measures the sizes and velocities of the raindrops in the most direct way. It can even be used on a façade to measure the raindrop spectrum of driving rain. Unfortunately, its price exceeded far too much our budget. The Doppler radar by METEK (2000) has the advantage of measuring in a relatively large air volume (50–250 m^3) which improves the resolution, but at the time it was being improved so that it could measure vertical wind velocities (to correct the falling drop velocities). We chose the optical disdrometer of Löffler-Mang and Joss (2000) (manufactured as « Parsivel M300 » by PMTech), although its development was not yet totally finished. Its main advantages are the direct measurement principle and its easiness of use.

The characteristics of the disdrometer are the following (PMTech 1999, Löffler-Mang and Joss 2000):

- A 780 nm laser diode is the source of a horizontal light sheet, 27 mm wide, 1 mm high and 180 mm long. In the receiver the light sheet is focussed on a single photodiode. The decrease of the output voltage, due to a passing drop, depends linearly on the fraction of the light sheet blocked. The amplitude of the signal is a measure of the drop size; the duration allows an estimation of the drop velocity.
- After signal conditioning and A/D conversion, the data processing unit determines the amplitude and duration of every signal (i.e. of every particle). By the manufacturer, an empirical relation between amplitude and particle size was determined. With help of this relation, the data processing unit determines the size of the detected particle. The combination of the detected particle size and velocity is used to determine whether it is a raindrop or an other hydrometeor (e.g. snowflakes fall much slower than raindrops and have larger sizes).
- Every 30 s, the data processing unit reports the measurements by outputting (a) the mean particle velocity in each size class, (b) the particle number concentration per size class ($n(D_j)$ in m^{-3} mm^{-1}), (c) a code for the precipitation classification, (d) the horizontal rain intensity, and (e) several control parameters. The applied size classes are tabulated in table 3.4. The codes for the precipitation classification are explained in the manual (PMTech 1999). Data of approximately a month can be stored in the data processing unit.
- A correction (Raasch and Umhauer 1984) is applied to estimate the real particle number concentration spectrum when coincidence of particles in the light sheet occurs at higher rain intensities. Löffler-Mang and Joss (2000) calculated that an intensive drizzle with $R_h = 30$ mm h^{-1} would yield an error of 9% due to coincidence; a convective shower with $R_h = 300$ mm h^{-1} would yield 5%. Thus, errors due to coincidences are unimportant for normal rain.

The disdrometer was delivered in December 1998, but it took a year of testing and improvements (by the manufacturer) before the disdrometer became really operational on 1 October 1999. It was installed approximately 1.8 m from position P3 (figure 3.12). We did not do any calibration or adjustments; we will compare the rain intensity calculated from the disdrometer data with those of the tipping-bucket rain gauges in chapter 5.

3.2.5 Driving rain gauges TUE-I and TUE-II

There is no standard for the design of driving rain gauges. In literature details of used driving rain gauges are rarely given; Frank (1973), Flori (1990) and Osmond (1995)

Table 3.4: The 25 particle size classes of the Parsivel M300 (PMTech 1999), indicated by the centre diameter, D_j, and the interval, ΔD_j.

D_j [mm]	ΔD_j [mm]	D_j [mm]	ΔD_j [mm]
0.146	0.146	3.942	0.730
0.292	0.146	4.745	0.876
0.438	0.146	5.767	1.168
0.584	0.146	7.008	1.314
0.730	0.146	8.468	1.606
0.876	0.146	10.293	2.044
1.022	0.146	12.556	2.628
1.214	0.292	15.330	3.066
1.533	0.292	18.688	3.650
1.825	0.292	22.776	4.526
2.190	0.438	27.813	5.548
2.701	0.548	33.945	6.716
3.285	0.548		

Figure 3.12: Disdrometer (Parsivel M300) at position P3 (roof of the Auditorium).

are the exceptions known to us. No references on a comparison of different types of driving rain gauges were found, and hence no reference dealing with the systematical error of a given driving rain gauge type. This subsection deals with the design of driving rain gauges which were developed at the TUE. Details of the gauges were previously reported in van Mook (1998a).

The most widely used driving rain gauges consist of:

- a collector (a shallow tray) fixed to the wall of a building. The drops hit the tray, drip downwards and are collected by:
- a drainage channel, which leads the collected rain water to:
- a reservoir or a water flux gauge. A water flux gauge enables the measurement of the instantaneous driving rain intensity.

It is obvious that the catch efficiency (and thus the measurement error) of a gauge depends on size, shape and finish of the gauge surfaces. One should prevent that drops remain on the collector or in the drainage channel and evaporate, that drops splash out of the gauge, and that the shape of the gauge causes extra wind disturbances.

It is very difficult, sometimes practically impossible, to imagine realistic tests for evaluation of every error. The main concern though was the reduction of remaining and evaporating drops. This idea was brought about by observations at the façade of the Main Building of the TUE that much of the drops simply remain on the window glass, and do not drip downwards during many driving rains.

The following requirements were considered for the design of the TUE driving rain gauges:

1. estimated driving rain intensity range: 0.05 to 2.0 mm h^{-1} at least,
2. sampling rate: 1 per min,
3. practical catchment area limited by the window size of the Main Building: approx. 0.5 m^2,
4. estimated maximum collected driving rain sum during 3 consecutive days: 5 mm,
5. short and straight drainage path to direct the collected raindrops into the water flux gauge,
6. hydrophobic coating to decrease the number of drops remaining on the collector or in the drainage path,

7. provisions preventing that the wind blows into the reservoir and preventing that the wind affects the desired flow of the drops into the reservoir (e.g. due to wind suction).

The first and fourth requirement are estimations obtained from hourly meteorological data of De Bilt (KNMI). The driving rain intensity range was calculated according to the principle of Lacy (1965) and BS 8104 (1992). The estimations appear to be quite good, as was confirmed by our measurements (see section 5.2.5; only two times in two years the 3-day driving rain sum exceeded 5 mm).

The first three requirements imply that the minimum amount of water, measurable within a minute for a driving rain intensity of 0.05 mm h^{-1} and through a catchment area of 0.5 m^2 will be 0.5 ml. We use a balance, which can easily and accurately measure such small amounts of water.

The fourth requirement implies that, if the catchment area is 0.5 m^2, the driving rain gauge reservoir will collect at most 2.5 litres in three consecutive days.

Figures 3.13 and 3.14 show the two types of driving rain gauges. Both types consist of a collector, a so-called wind deflector (to satisfy requirement 5 and 7, see figure 3.15), a reservoir and a balance (for the actual detection of the amount of water). Also for both types, all the inner sides have been coated with PTFE (teflon) to comply with requirement 6. The main difference is that driving rain gauge TUE-II is equipped with a wiper and driving rain gauge TUE-I is not. The wiper is basically a standard

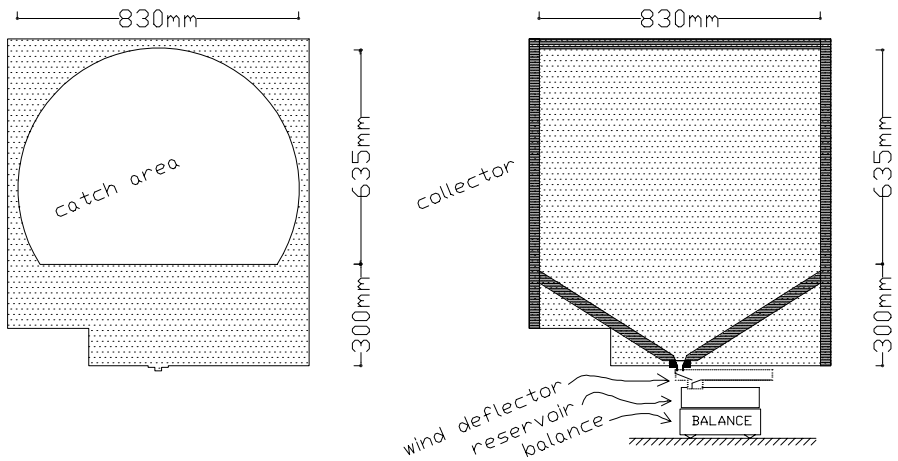

Figure 3.13: Driving rain gauge TUE-I, with driving rain collector, wind deflector, reservoir (2 l) and balance. Left: front plate with the circular catchment area (0.444 m^2). Right: back plate and the inside.

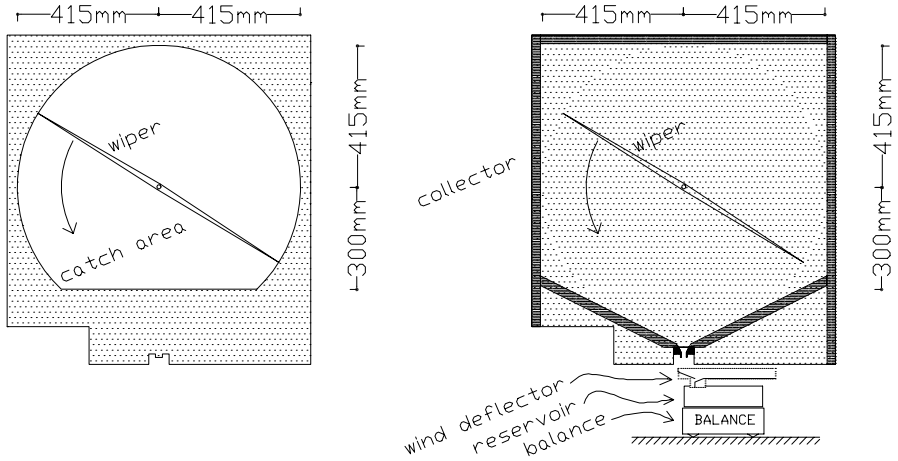

Figure 3.14: Driving rain gauge TUE-II, with driving rain collector, wind deflector, reservoir (3 l) and balance. Left: front plate with the circular catchment area (0.492 m^2). Right: back plate and the inside. (See figure 3.15 for a detail of the wind deflector.)

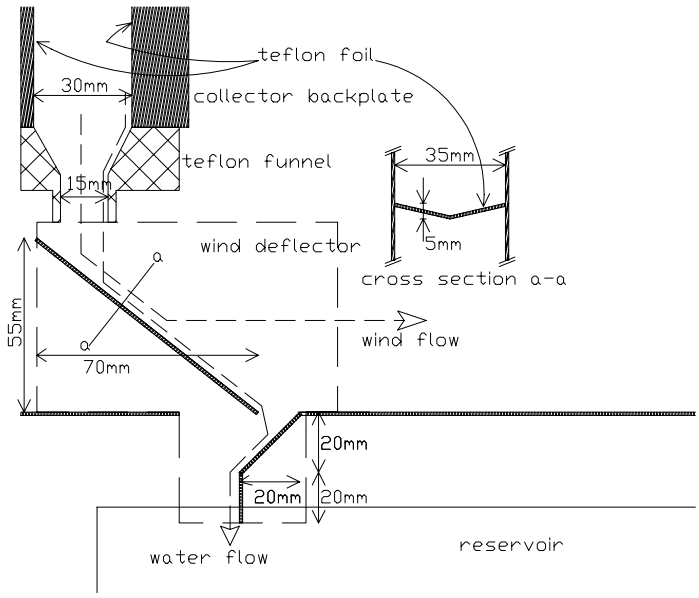

Figure 3.15: Detail of the wind deflector of driving rain gauge TUE-II.

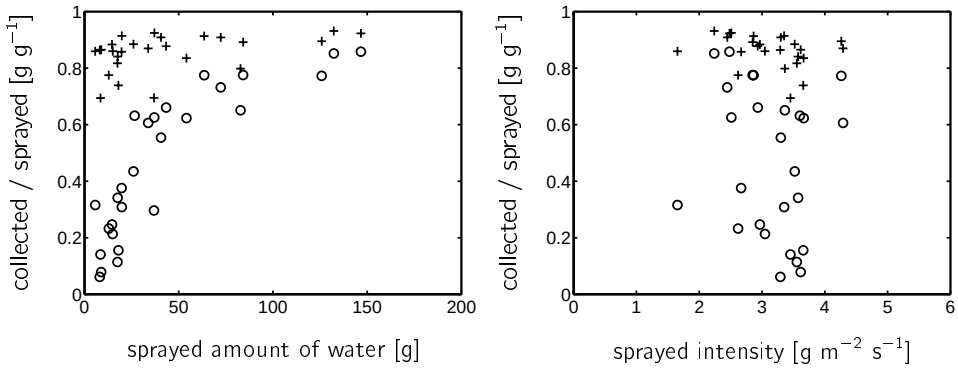

Figure 3.16: Spray test on driving rain collector TUE-II: o without wiping and + with wiping. The tested collector was not yet exposed to the outdoor climate. A spray intensity of 1 g m^{-2} s^{-1} equals to 3.6 mm h^{-1}.

windscreen wiper for cars, and is automatically switched on by a rain indicator. The speed is approximately 1 rotation per 3 seconds; after every 5 seconds the wiper rests during 5 s to reduce wear and tear.

The wiper serves to improve the driving rain intensity measurement: drops on the collector are forced to coagulate and drip down. Furthermore, the wiper keeps the surface of the driving rain gauge clean. In the laboratory the driving rain collectors were tested for their collection efficiency. By a plant sprayer drops were sprayed onto the collector and the collected amount of water and the sprayed amount of water were measured. Also the time of spraying was measured. Results of this test (figure 3.16) show that wiping significantly decreases the dependence of the collection efficiency on the total sprayed amount *and* the spray intensity. The real effect of wiping can only be found by full-scale measurements, because the drop spectrum and the intensity of the used spray is different from real rain.

3.2.6 Driving rain gauges CTH and DTU

Apart from the TUE-I and TUE-II gauges the full-scale comparison test of driving rain gauges included two additional gauges, one provided by the Chalmers University of Technology (CTH) and another one by the Technical University of Denmark (DTU).

Gauge CTH (figure 3.17) can be considered as a traditional driving rain gauge. It has a small catchment area (0.032 m^2), is made out of perspex and the collected rain flux is measured by a tipping bucket with a tipping volume of 1 ml. One tipping in 20 min represents a driving rain intensity of 0.09 mm/h. The gauge is described in Högberg (1998) and Högberg (2002).

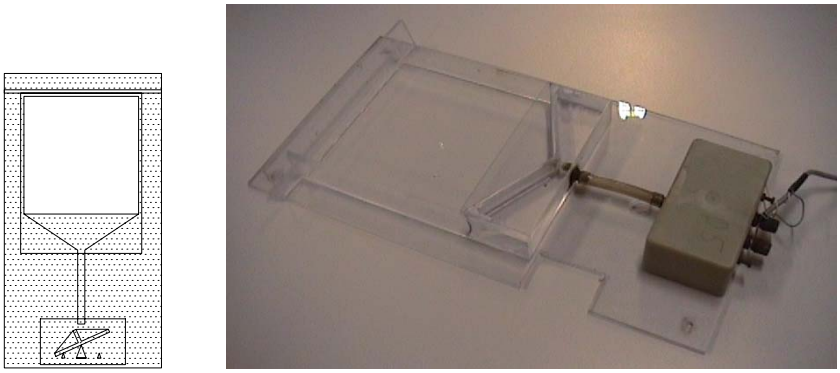

Figure 3.17: Driving rain gauge CTH. The catchment area is $0.18 \times 0.18 = 0.032$ m^2.

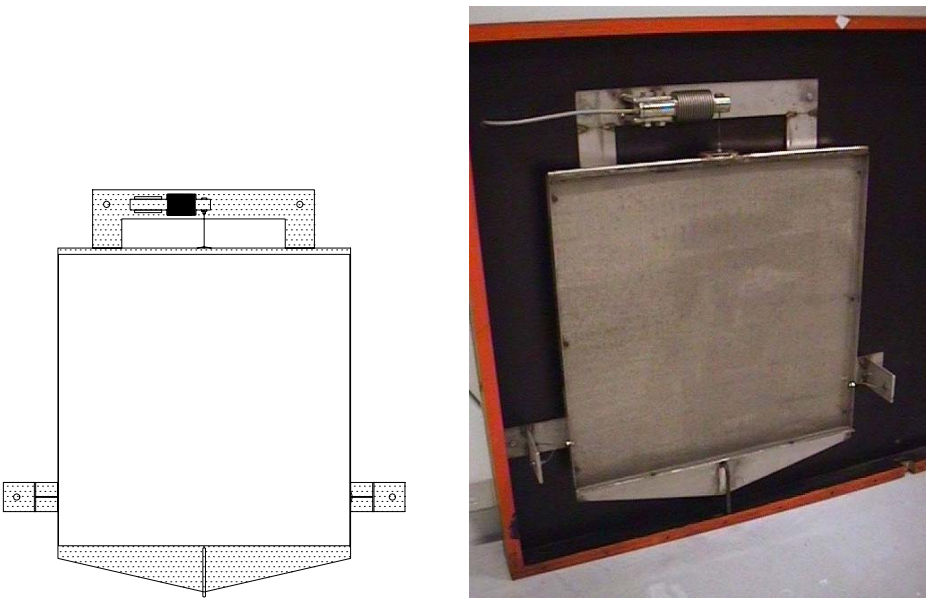

Figure 3.18: Driving rain gauge DTU. The catchment area is $0.46 \times 0.46 = 0.21$ m^2.

The DTU gauge (figure 3.18) was designed as an improved driving rain gauge. As for the design of TUE-II, the main concern was reduction of measurement errors due to raindrops which remain stuck on the collector surface and subsequently are not measured in a flux gauge. The solution of the DTU gauge is weighting the whole collector, i.e. including the drops on the collector. The collector of gauge DTU is suspended freely from a strain gauge (though horizontal movements are prohibited). The collector consists of a stainless steel tray with a net mounted on the tray to reduce raindrop bouncing. A reservoir is integrated in the collector and is self-siphoning with a capacity of approximately 300 ml. Details are described in Kragh (1998). Obviously, the reading of the strain gauge is sensitive to wind fluctuations. This is partially compensated by averaging the reading during each 10-min period. The driving rain sum over a 10-min period is calculated by the difference of the mass of the collector in two subsequent 10-min periods. Only positive differences exceeding a threshold value of 1.3 g and during periods of rain according to a rain indicator, are taken into account. The mentioned threshold value approximates the resolution of the strain gauge and A/D converter.

In table 3.5 the main characteristics of the driving rain gauges are summarised.

Table 3.5: Overview of the applied driving rain gauges.

type	principle min. intensity	material	catch area
CTH	traditional collector with tipping bucket (V_{tip} = 1 ml) $\frac{1tip}{10min}$ = 0.19 mm h^{-1}	perspex	0.18 × 0.18 = 0.032 m^2
DTU	collector weighted by a strain gauge ($\Delta m \approx 1.3$ g) $\frac{1.3g}{10min} \approx 0.04$ mm h^{-1}	stainless steel	0.46 × 0.46 = 0.21 m^2
TUE-I	traditional collector with reservoir (2 l) and balance ($\Delta m = 0.1$ g) $\frac{0.1g}{10min}$ = 0.001 mm h^{-1}	teflon coating	0.444 m^2
TUE-II	as TUE-I but with a rotating wiper and a reservoir of 3 l $\frac{0.1g}{10min}$ = 0.001 mm h^{-1}	teflon coating	0.492 m^2

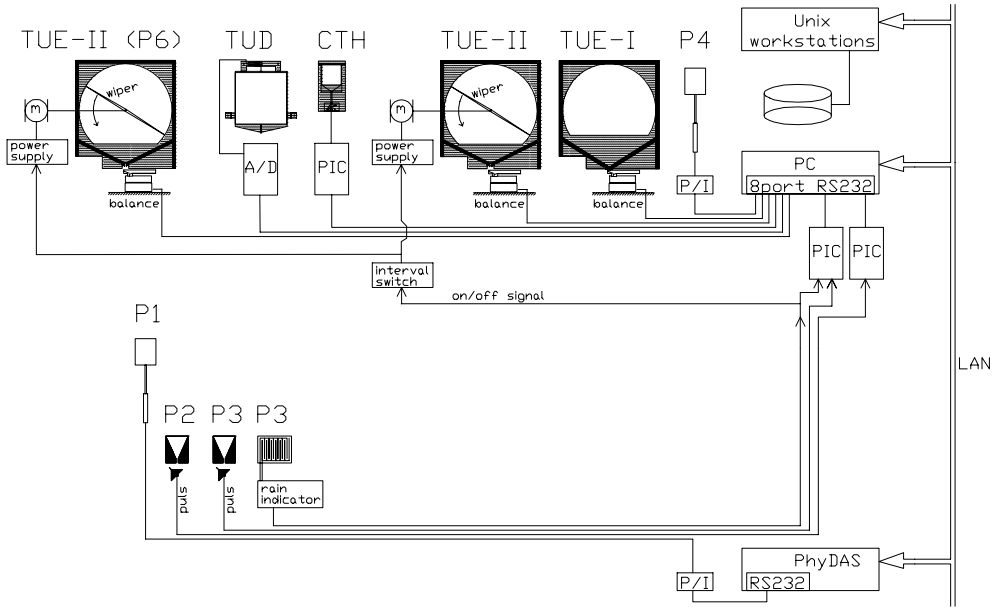

Figure 3.19: Data acquisition systems. The abbreviations appear in the text, except for PIC, A/D and P/I, which are interfaces.

3.3 Data acquisition

The whole data acquisition system is depicted in figure 3.19. The data of the anemometer above the roof of the Auditorium is registered by *PhyDAS*, a high-performance data acquisition system (d.a.s.) developed at the faculty of Physics of the TUE. At the time of installation for the study of Geurts (1997) such a system was needed to handle large data flows. For the present study such a d.a.s. is not strictly needed. Therefore, the data of all the other instruments are registered by a personal computer (486DX66, Windows 95). It has been equipped with a special card which enables data transmission via 8 ports according to the RS232 standard. Most applied instruments can communicate via RS232; if not (like for the tipping-bucket rain gauges), an interface was built to enable the reading of the instrument via RS232. Data were logged by 'polling': this means that after every time interval the PC 'asks' for the reading of an instrument. The readings are directly logged, so that the polling rate equals the sampling rate. The sampling rates for every instrument are listed in tables 3.2 and 3.3.

The time of the clocks of the PhyDAS and the PC is the local winter time. This means that the logged time equals UTC + 1 hour, and that the extra hour for daylight saving during summer is not applied. The computer clocks are manually adjusted to the time

with a precision of 1 to 6 seconds. Important is that the clocks of the two computers are synchronised. Given our application, a larger precision is not needed.

All data of the PhyDAS and PC are collected and stored on hard disks of Unix workstations. Backups are stored on tape and cd-rom. Data processing and analysis are done on Unix workstations, with help of basic Unix commands and the Matlab package.

3.4 Methods of data processing

The first step of the data processing is to convert the raw (logged) data into a time series according to a particular averaging or summing period. The second step is to use these time series for further calculations. Conversion and calculation methods are summarised in this section.

The average of a finite sequence of samples $x_1, x_2, x_3, ..., x_N$ is commonly defined as:

$$\overline{x} = \frac{1}{N} \sum_{i=1}^{N} x_i. \tag{3.1}$$

The standard deviation of a finite sequence of samples is defined as:

$$\sigma_x = \sqrt{\frac{1}{N-1} \sum_{i=1}^{N} (x_i - \overline{x})^2}. \tag{3.2}$$

The standard deviation can also be calculated from the sum of the squared sample values ($\sum_{i=1}^{N}(x_i^2)$):

$$\sigma_x = \sqrt{\frac{\sum_{i=1}^{N}(x_i^2) - N\overline{x}^2}{N-1}}. \tag{3.3}$$

The coefficient of determination r^2, or correlation coefficient, of estimated values $x_{\mathrm{e},i}$ in relation to their measured values $x_{\mathrm{m},i}$ is calculated by eq. 3.4 (Montgomery and Runger 1999, p. 464).

$$r^2 = \frac{\sum_{i=1}^{N} \left(x_{\mathrm{e},i} - \overline{x_{\mathrm{m}}}\right)^2}{\sum_{i=1}^{N} \left(x_{\mathrm{m},i} - \overline{x_{\mathrm{m}}}\right)^2}. \tag{3.4}$$

The averaging or summation period is denoted by t_{cl}, and called 'clock period'. The start and end of each period are synchronised with clock and calendar. The first clock period of a day starts at 0h00.

3.4.1 Reference wind data

The output of the ultrasonic anemometers is directly given in a standard unit of velocity, for every component (U_1, U_2, U_3) (figure 3.10). One-minute averages and sums of squared output values of the anemometer on the mast of the Auditorium are calculated and form the raw data. For a chosen period t_{cl}, the mean wind speed components $\overline{U_1}$, $\overline{U_2}$ and $\overline{U_3}$ are calculated from the one-minute data.

Next, these mean wind speed components are transformed into the global axis system (figure 2.4): U_x, U_y, U_z. Furthermore, the quantities U, U_{h}, Φ, u, v and w can be calculated with the definitions given in section 2.1.5.

3.4.2 Façade wind data

The raw data of the ultrasonic anemometer mounted on the boom at façade position P4 consists of 1 second values (U_1, U_2, U_3) (figure 3.10). From these, the t_{cl}-averaged quantities U_x, U_y, U_z, U, U_{h} and Φ are calculated.

3.4.3 Horizontal rain data

Horizontal rain data are obtained by three devices, two tipping-bucket rain gauges and a rain indicator. The horizontal rain intensity during a clock period t_{cl} is calculated from the number of tippings during this period:

$$R_{\mathrm{h,u}} = \frac{3.6}{t_{\mathrm{cl}}} \frac{N V_{\mathrm{tip}}}{A_{\mathrm{catch}}}, \tag{3.5}$$

with $R_{\mathrm{h,u}}$ = the (uncorrected) horizontal rain intensity [mm h^{-1}], N = the number of tips during t_{cl} [s], V_{tip} = the effective volume [ml] of a bucket, and A_{catch} = the catchment area [m^2] of the rain gauge.

In fact the horizontal rain intensity $R_{\mathrm{h,u}}$ is an average during t_{cl}.

If the sample rate of the rain indicator is denoted by t_{s}, the rain duration during a clock period t_{cl} is calculated by:

$$t_{\mathrm{prec}} = N t_{\mathrm{s}}, \tag{3.6}$$

with t_{prec} = the rain or precipitation duration [s] during t_{cl}, and N = the number of samples at which the rain indicator senses rain or other forms of precipitation during the clock period.

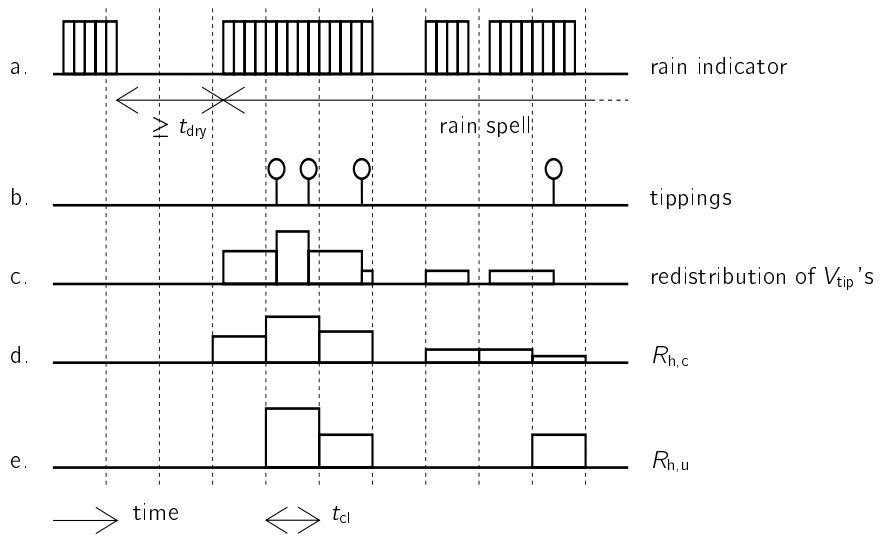

Figure 3.20: Correction of rain intensity R_h by combination of rain indicator data and tipping-bucket data. See section 3.4.3 for an explanation.

Corrected horizontal rain intensity $R_{h,c}$ The data of the rain indicator and one of the rain gauges can be combined to correct rain intensity data, especially during shorter averaging periods t_{cl}. A method is presented in this section. The upper two graphs of figure 3.20 are sketches of rain indicator and rain gauge readings as a function of time. The rain amount registered by the first tipping in a period t_{cl}, could have been collected during previous clock periods. The reading of the rain indicator can be of help to estimate how to 'redistribute' this amount over the previous periods. To prevent that rain is distributed over too many previous periods, a minimum time t_{dry} is defined. This minimum time divides time into dry periods and periods with more or less continuous rain (i.e. rain spells). The result of the redistribution of rain amounts of the registered tippings is sketched in figure 3.20c. The redistribution is done in proportion to the precipitation times measured by the rain indicator. Summing up the redistributed rain amounts per clock period t_{cl} yields the so-called corrected rain intensity $R_{h,c}$ (figure 3.20d). For comparison, the uncorrected rain intensity $R_{h,u}$ calculated with eq. 3.5 is sketched in figure 3.20e.

3.4.4 Raindrop spectrum data

Every 30 s, the disdrometer reports the mean particle velocity in every size class and the particle number concentration in every size class. We will denote these quantities with $u(D_j)$ [m s^{-1}] and $n(D_j)$ [m^{-3} m^{-1}], respectively. The raindrop mass flux per drop size

class per 30 s ($\varphi(D_j)$ [kg m^{-2} (30 s)$^{-1}$]) can be calculated from these two quantities by (cf. eq. 2.15 and 2.16):

$$\varphi(D_j) = \rho_{\mathrm{D}} \, \frac{\pi}{6} \, D_j^3 \, u(D_j) \, n(D_j) \, \Delta D_j, \tag{3.7}$$

with D_j and ΔD_j = the centre and interval of the drop size class in m (table 3.4), and ρ_{D} = density [kg m^{-3}] of water.

The reported spectra are only taken into account if the disdrometer indicates that the precipitation is drizzle or rain. So, spectra of snow, hail and mixtures are discarded.

The disdrometer output has two disadvantages for our purposes. Firstly, the disdrometer gives the raindrop number concentration spectrum, which is calculated from the quantity which we are interested in, namely the raindrop mass flux spectrum. We have to 'recalculate' the raindrop mass flux spectrum by use of the given averaged particle velocities $u(D_j)$. Secondly, the interval of the size classes increases with the centre diameter, which results in larger absolute errors of the real mass flux at larger diameters. The two disadvantages can be solved by outputting every detected raindrop with its diameter and velocity, but it was not possible to us to adapt the software in the data processing unit of the disdrometer.

3.4.5 Driving rain data of the TUE-I and TUE-II gauges

In gauges TUE-I and TUE-II, the driving rain collected in a reservoir is measured by a balance, of which simply the weight values are logged. The (mean) driving rain intensity R_{f} during a clock period t_{cl} is calculated from the difference between begin and end values of the logged mass:

$$\Delta m = m_{t+t_{\mathrm{cl}}} - m_t, \tag{3.8}$$

$$\begin{aligned} R_{\mathrm{f}} = \; & \Delta m/(A_{\mathrm{catch}} t_{\mathrm{cl}}) && \text{if} \quad \Delta m \geq m_{\mathrm{min}}, \\ = \; & 0 && \text{if} \quad \Delta m < m_{\mathrm{min}}, \end{aligned} \tag{3.9}$$

with m_{min} = a threshold value [kg] for the minimum detectable mass difference during a clock period, A_{catch} = the catchment area [m^2] of the driving rain gauge, and t_{cl} = the clock period in h.

By the threshold value m_{min} one suppresses variations of the measured mass value due to e.g. temperature changes. It depends on the resolution of the balance (m_{min} = 0.105 g was found suitable for the applied balances with a resolution of 0.1 g).

3.4.6 Driving rain data of the CTH and DTU gauges

The number of tippings of the CTH driving rain gauge is logged two times per second. The driving rain intensity $R_{\mathrm{f,CTH}}$ can be calculated similar to R_{h}, eq. 3.5.

The raw data of the DTU gauge consists of voltage values of the strain gauge. The data processing method was already mentioned in section 3.2.6. The resulting driving rain intensity is calculated from the difference of the 10-min averaged masses, of two subsequent 10-min clock periods, similar to eq. 3.9. Driving rain intensities for larger clock periods are calculated from the obtained 10-min driving rain intensities.

Chapter 4

Driving rain gauges

In this chapter, results of the full-scale comparison test of the driving rain gauges are presented. Two driving rain gauges were developed at the TUE (called TUE-I and TUE-II) and, thanks to collaboration with the Chalmers University of Technology (CTH) and the Technical University of Denmark (DTU), two other driving rain gauges were included in the test. The gauges are described in sections 3.2.5 and 3.2.6.

Section 4.1 gives an overview of the driving rain measurements. Whereas the full-scale measurements at the Main Building comprised a period from December 1997 to November 1999, the period during which all four driving rain gauges were simultaneously operational, lasted only from October 1998 to January 1999. In sections 4.2 and 4.3 the measurement readings of the gauges and their differences are discussed in detail. Section 4.4 summarises the observations.

A full presentation of the measurements of wind, rain and driving rain is given in chapter 5. It is inevitable to refer to chapter 5 from time to time in the present chapter, as some results in the present chapter are related to the reference wind and rain measurements. Data processing and selection criteria and the definition of the quantities used are explained in section 5.1.

4.1 Overview of the measurements

The idea behind the full-scale comparison test of the driving rain gauges is to register the readings of the different driving rain gauges while they are exposed to the same, natural driving rain for a reasonable period of time. In order to expose the gauges to the same driving rain, they were mounted together as closely as possible on the west

façade of the Main Building of the TUE (positions P4, P5 and P7; P4/5/7 for short). Figure 3.8 shows a photograph of the situation. The spatial positions of the gauges are within 2.5 m horizontally and within 0.7 m vertically. The exact operation periods and the exact positions of the mounted driving rain gauges are listed in table 3.3 and described in section 3.2. The periods during which the gauges were operational, are also visible at a glance in table 4.1, in which monthly driving rain amounts of each gauge at P4/5/7 are listed. This table also lists the percentage of clock periods with available data (i.e. when the installed devices worked properly).

The TUE-II gauge will often be used as a reference for the comparisons. It is the gauge which was operational for the whole 24-month measurement period. Moreover, as we will see in the following, it is one of the gauges which functions well. As monthly driving rain amounts do not give many conclusive details on the performance of the different gauges, we mention the monthly results of a gauge compared to the TUE-II gauge only concisely here:

- CTH ↔ TUE-II. The CTH gauge functioned from 17 July 1998 to 31 November 1999. For this period, its total driving rain amount was 85% of that of the TUE-II gauge.
- DTU ↔ TUE-II. The DTU gauge functioned during the same period as the CTH gauge. The total driving rain amount of the DTU gauge during that period was 116% of that of the TUE-II gauge.
- TUE-I ↔ TUE-II. From 1-12-1997 to 7-7-1998 and from 16-9-1998 to 25-2-1999, the driving rain gauges TUE-I and TUE-II were both operational. They were mounted close to each other at façade positions P4 and P5; after 16 September 1998 the gauges were interchanged. Evidently, the TUE-II gauge registered more driving rain than the TUE-I gauge. The total driving rain amount of the TUE-I gauge during the mentioned period was 47% of that of the TUE-II gauge.
- TUE-Ib ↔ TUE-II. In February 1999 the TUE-I gauge was adapted, i.e. its catchment area was reduced. It was (fully) operational from April to 31 November 1999. Its total driving rain amount was 32% of that of the TUE-II gauge.

In Högberg et al. (1999), the readings of the four gauges CTH, DTU, TUE-I and TUE-II were compared for the period of 1-10-1998 to 28-2-1999. For these five months, the CTH, DTU and TUE-I gauges, respectively, measured 94%, 84% and 51% of the driving rain amount registered by the TUE-II gauge. Compared to the TUE-II gauge the DTU gauge measured less during this five-month period (84%) than during the 16-month period (115%). Also the CTH gauge seems to have a different performance after February 1999. It is impossible to check whether the performance of the gauges really changed over time. In the following two sections (sections 4.2 and 4.3) we will therefore compare the driving rain registrations on a smaller time basis, namely 10-min clock

Table 4.1: Monthly driving rain amounts [mm] at position P4/5/7 of four different driving rain gauges: TUE-I (and TUEIb with a reduced catchment area), TUE-II, CTH and DTU. The last column shows the percentage of clock periods with available data. An asterisk indicates that the device was not operational during the whole month, but (un)installed during the month.

	TUE-I	TUE-Ib	TUE-II	CTH	DTU	% avail.
1997 12	1.06	-	2.78	-	-	99
1998 01	2.88	-	5.77	-	-	97
1998 02	0.49	-	0.83	-	-	98
1998 03	2.06	-	4.87	-	-	82
1998 04	0.29	-	1.11	-	-	79
1998 05	0.37	-	0.94	-	-	98
1998 06	1.52	-	3.92	-	-	70
1998 07	∗ 0.00	-	1.93	∗ 1.69	∗ 1.80	90
1998 08	-	-	3.35	4.31	4.47	99
1998 09	∗ 0.17	-	9.61	10.93	9.37	99
1998 10	6.40	-	11.70	10.93	8.96	88
1998 11	0.12	-	0.59	0.81	1.19	82
1998 12	1.88	-	3.43	3.40	3.78	99
1999 01	1.38	-	3.30	2.76	4.68	99
1999 02	∗ 1.95	∗ 0.00	4.06	1.59	4.06	98
1999 03	-	∗ 0.97	4.31	0.45	5.07	99
1999 04	-	0.27	1.49	1.10	2.22	98
1999 05	-	0.01	0.12	0.29	0.56	99
1999 06	-	0.98	2.43	2.66	3.75	99
1999 07	-	0.77	2.25	1.62	3.47	90
1999 08	-	1.08	1.70	1.20	2.88	89
1999 09	-	0.12	0.76	0.52	1.45	96
1999 10	-	0.14	0.82	0.19	1.30	99
1999 11	-	0.04	0.80	0.26	1.39	94

periods. On these results our explanation of the differences will be based. In general, differences in reading arise from:

a. aerodynamic disturbance, by which raindrop trajectories deviate from those without the gauge. The cause may be protruding rims or other projections, or even a collector sunk into the wall,

b. run-off water flowing from other parts of the façade into the collector,

c. raindrops splashing out of the collector,

d. size and shape of the catchment area,

e. hydrophobicity and smoothness of the collector. This is particularly important if the collected raindrops have to find their way to the water flux gauge. This aspect is also related to whether and how raindrops coagulate before rolling downwards,

f. drainage path. The length and 'straightness' of the path which drops have to follow from impingement to the point where they are measured,

g. influence of wind on the path of the drops. In extreme cases the wind may blow drops out of the collector, or prevent drops from getting into the water flux gauge,

h. influence of wind on the reading of the DTU gauge (its collector is suspended freely from a strain gauge),

i. evaporation of raindrops or collected rain water. Depending on the finish of the collector surface and the actual number of drops (raindrop spectrum and rain intensity), smaller drops remain stuck on the collector surface and are not measured,

j. principle of the rain flux measurement. Important is its resolution, i.e. the minimum measurable amount of water during a clock period,

k. spatial differences, because the gauges are not exactly mounted on the same position.

Aspects a, b and c were not investigated during the comparison test, although at designing and mounting of the gauges these aspects were taken into account. Aspects e, f and g were also taken into account at the design, whereas during the test, cleanness of the collector surface and the motion of drops through the drainage system of the gauges were inspected visually whenever possible. Differences due to aspects d, e and h–k are investigated by correlating the readings of the different gauges to each other, and by relating them with the reference rain intensity ($R_{\mathrm{h,c}}$) and wind speed (U_y). Of course, the raindrop spectrum is an important factor for all the mentioned aspects where rain intensity plays a role. Raindrop spectra were measured from October 1999 to January 2000. However, they are not included in this chapter, because during this period the amount of driving rain was unfortunately unsufficient for a meaningful correlation between raindrop spectrum data and driving rain data.

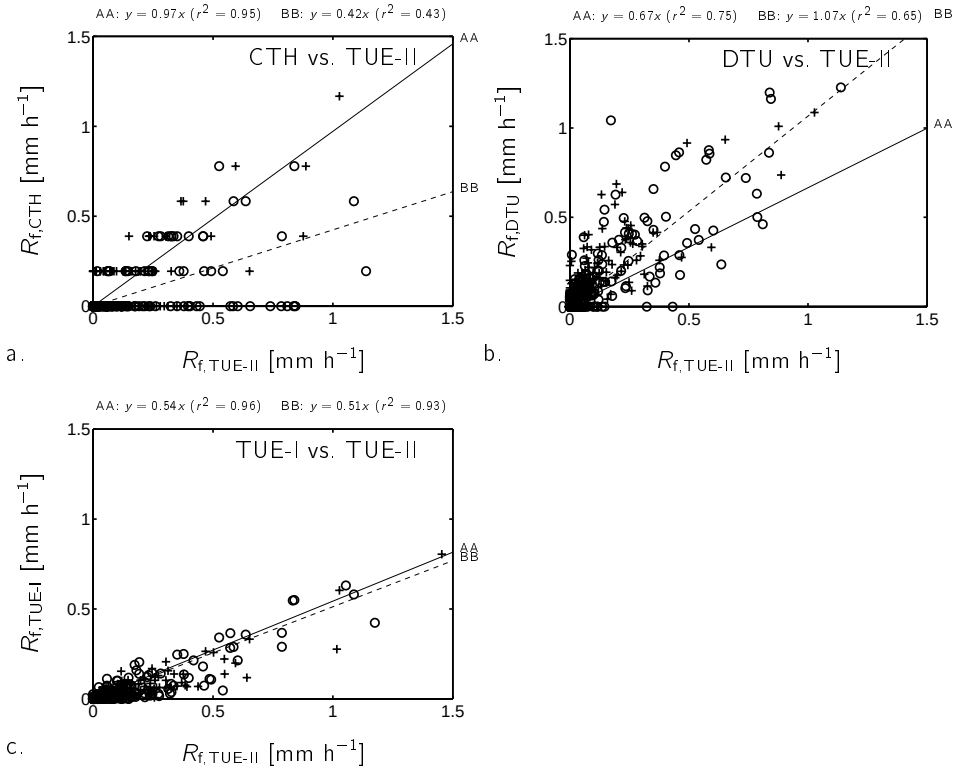

Figure 4.1: Correlations of 10-min driving rain intensities R_f of gauge CTH, DTU and TUE-I with gauge TUE-II, for selected reference wind velocity components perpendicular to the façade U_y of 4–5 m s^{-1} (measurement points + and correlation ——) and 6–7 m s^{-1} (o and ----). Period: 1-12-1997 to 30-11-1999.

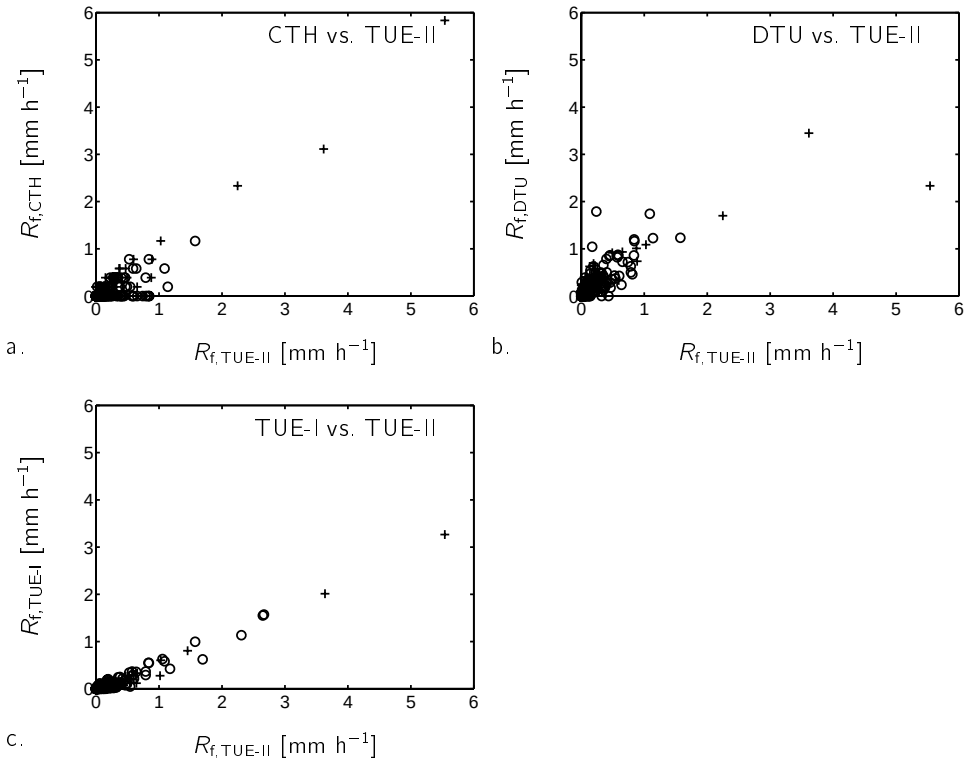

Figure 4.2: As figure 4.1, but with extended axes.

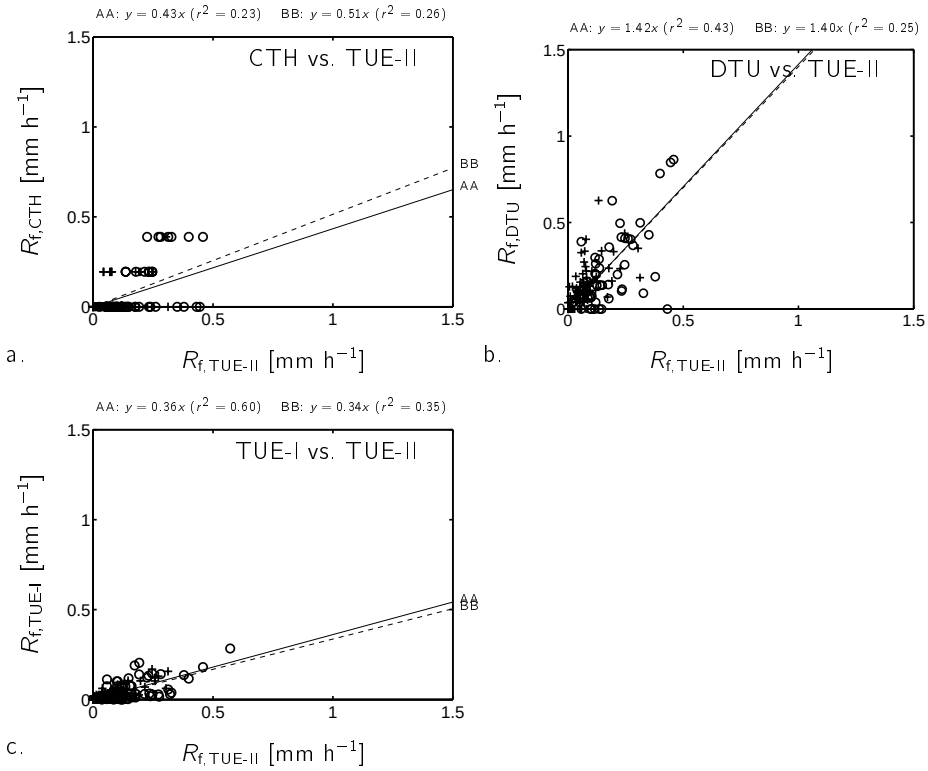

Figure 4.3: As figure 4.1, but for reference rain intensities $R_{h,c,P2}$ of 1.0–2.5 mm h^{-1}.

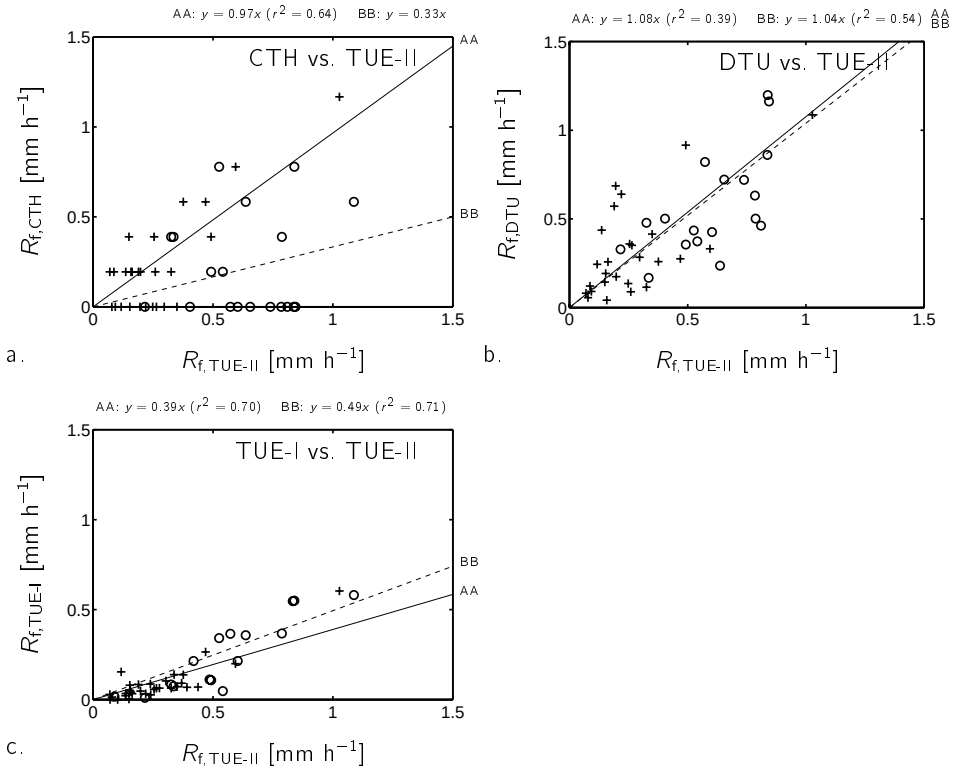

Figure 4.4: As figure 4.1, but for reference rain intensities $R_{h,c,P2}$ of 3.0–5.5 mm h^{-1}.

4.2 The TUE-I and TUE-II gauges

The two driving rain gauges TUE-I and TUE-II are almost identical. Gauge TUE-II is equipped with a wiper, gauge TUE-I is not.

In the previous section 4.1 it was shown that on a monthly basis the TUE-I gauge registers only approximately half of the rain amount measured by the TUE-II gauge. This is also valid for 10-min periods, as is shown in figure 4.1c. This figure shows correlations of 10-min driving rain intensities measured by the TUE-I gauge with the TUE-II readings. To visualise the possible influence of wind, the data points were selected for certain wind velocities U_y, and put into two sets, i.e. a set with 4–5 m s^{-1} and a set with 6–7 m s^{-1}. The measurement points were also fitted by a linear function $y = cx$. The slopes are $c = 0.54$ for U_y = 4–5 m s^{-1}, and $c = 0.51$ for U_y = 6–7 m s^{-1}. The correlation coefficients are quite satisfactory: $r^2 = 0.96$ and 0.93, respectively. Figures 4.3c and 4.4c show the data of figure 4.1c separated into measurement points with reference rain intensities $R_{\mathrm{h,c}}$ of 1.0–2.5 mm h^{-1} and 3.0–5.5 mm h^{-1}, respectively. Comparing these three figures, one observes that higher wind speeds and higher horizontal rain intensities (in other words: the measurement points indicated by **o** in figure 4.4c) yield more data through which a 'nicer' fit can be obtained, although the correlation coefficient is not better than that of figure 4.1c. The correlation between the TUE-I and TUE-II gauges is more systematic (less scatter) at higher driving rain intensities. For lower driving rain intensities (figure 4.3c) the scatter is larger, but the slopes of the correlation for U_y = 4–5 m s^{-1} and 6–7 m s^{-1} are approximately the same.

During the summer of 1998 we interchanged the positions of the gauges TUE-I and TUE-II. Figure 4.6a shows the correlation when TUE-I was at position P4 and TUE-II at P5. Figure 4.6b shows the situation after TUE-II was installed at P4 and TUE-I at P5. The correlation before and after the exchange is approximately the same: $R_{\text{TUE-I}}/R_{\text{TUE-II}}$ equals 0.48 (with $r^2 = 0.89$) in the first case, and 0.51 (with $r^2 = 0.88$) in the latter case. This indicates that the measurement positions P4 and P5 are close enough to have the same driving rain onslaught.

Without changing something else, the catchment area of TUE-I was reduced from 0.444 m^2 to 0.0625 m^2 in February 1999. This new version is called TUE-Ib (figure 4.5). The catchment area was reduced to investigate its influence on the reading of the driving rain gauge. Initially it was thought that a smaller catchment area would suffer less from evaporation of drops remaining on its surface, and/or that drops on a smaller collector would have shorter paths to the water flux gauge. The TUE-Ib/TUE-II correlation is depicted in figure 4.6c. Note that the correlation between TUE-Ib and TUE-II is 0.27 with a poor correlation coefficient (r^2) of 0.48. These values have been obtained for driving rain intensities up to 1.5 mm h^{-1}. When higher driving rain intensities are considered (see figure 4.6d), the reading of TUE-Ib is closer to the reading of TUE-II. A second degree polynomial fits well through the measurement points ($r^2 = 0.87$), although there is no theoretical argument for choosing such a polynomial. Of course, we expect that

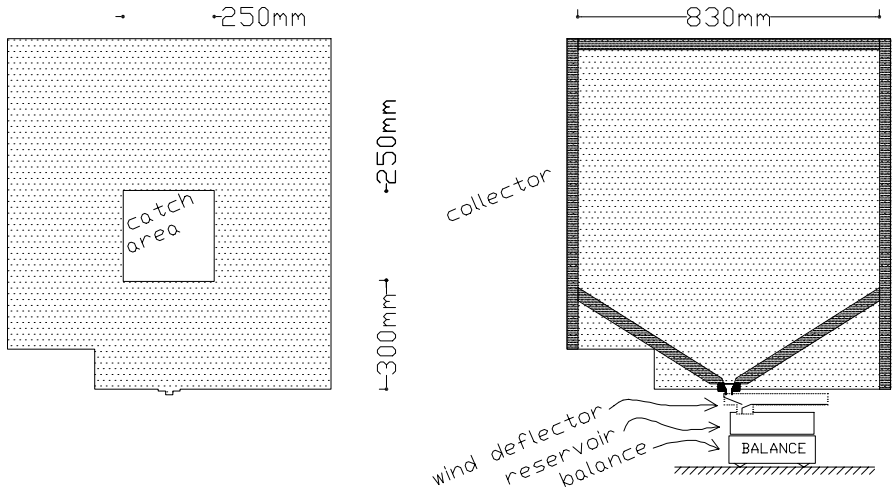

Figure 4.5: Driving rain gauge TUE-Ib (i.e. the TUE-I gauge with the reduced catchment area). Left: front plate with the catchment area ($0.250 \times 0.250 = 0.0625$ m^2). Right: back plate and the inside. Cf. figure 3.13.

above a certain (high) level of driving rain onslaught, the readings of TUE-Ib and TUE-II will become the same, so the correlation should somehow change into a correlation $y = cx$ with $c = 1$ (at driving rain intensities higher than shown in the figure). Figure 4.7 shows the reading of gauge TUE-Ib as a function of driving rain intensity measured by the TUE-II gauge for several wind speed ranges. It reveals that TUE-Ib yields only responses at relatively high rain intensities ($R_{\mathrm{f,\ TUE\text{-}II}} \gtrsim 0.2$ mm h^{-1}) or wind speeds ($U_y \gtrsim 6$ m s^{-1}). Contrary to the initial expectation, a smaller catchment area for the gauge without wiper did not yield better readings. An explanation may be that the drainage path length of the TUE-Ib gauge is too long (the drainage path from the collector to the water flux gauge is approximately 30 cm and did not change compared to the original TUE-I gauge).

Probably a model for the simulation of raindrop sticking, coagulating and running off on a driving rain collector as mentioned in Blocken et al. (2001), will give a better understanding why the reading of the TUE-Ib gauge is worse than the TUE-I gauge. The same model can be used to study the differences between the TUE-I and the TUE-II gauges. For assumed raindrop spectra, it will give the relationship between the shape and size of the collector and the amount of collected rain water remaining on its surface and running off. The effect of the development of the raindrop spectrum during a rain event on the driving gauge readings with respect to the process of running-off can be investigated too.

Altogether one can conclude that the differences in reading between the TUE-I and

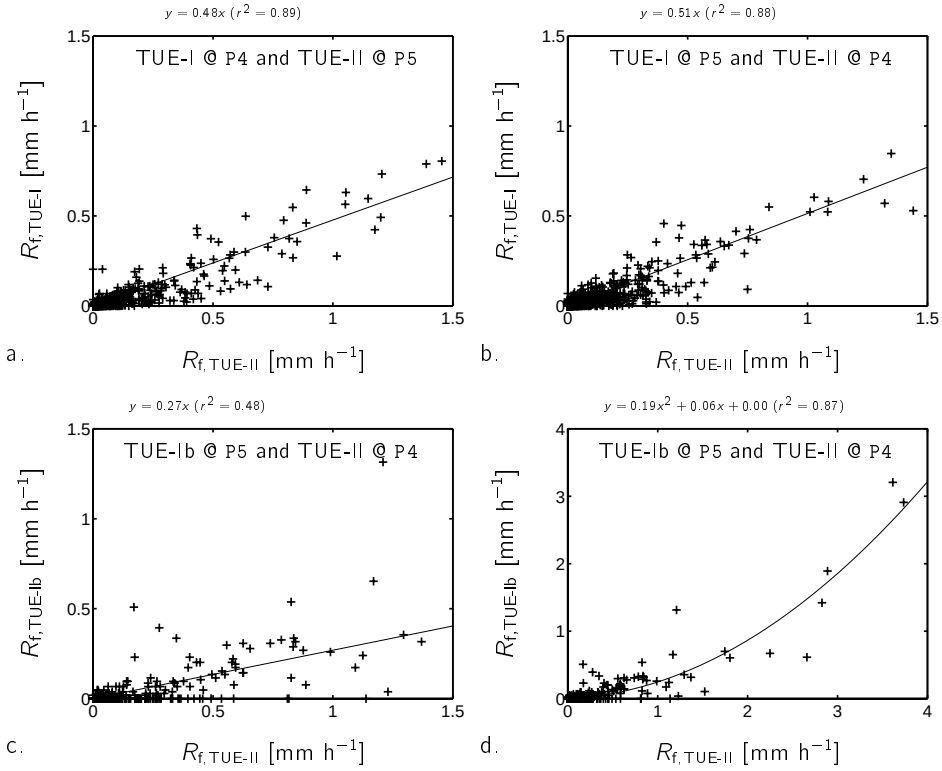

Figure 4.6: Correlations of 10-min driving rain intensities R_f of gauge TUE-I with gauge TUE-II, when (a.) TUE-I and TUE-II were at positions P4 and P5 respectively, from December 1997 to June 1998, (b.) after swapping the positions from September 1998 to February 1999, and (c.) the catchment area of TUE-I was reduced to 0.063 m^2, from February 1999 to November 1999. Figure d is the same as c, but with extended axes.

TUE-II gauges are quite systematic. They can be explained by the evaporation of the collected raindrops remaining stuck on the collector of the TUE-I gauge. Raindrops are less likely to remain stuck on the collector of the TUE-II gauge —and subsequently evaporate— because of its wiper. When the collectors were unmounted for inspection and cleaning, TUE-II was always significantly cleaner and its surface was smoother, whereas the surface of the collector of the TUE-I gauge was covered with a thin layer of dirt.

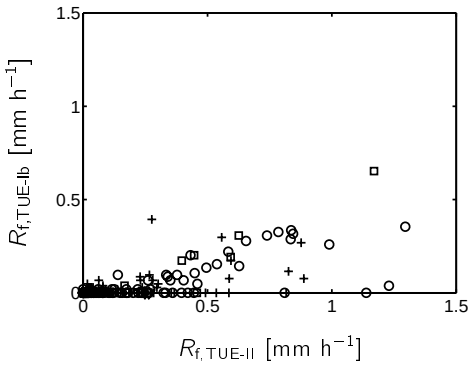

Figure 4.7: Correlations of 10-min driving rain intensities R_f of gauge TUE-Ib with gauge TUE-II, for selected reference wind velocity components perpendicular to the façade U_y of 4–6 m s^{-1} (+), 6–8 m s^{-1} (o), 8–10 m s^{-1} (□) and 10–12 m s^{-1} (◇). Cf. figure 4.1c. Period: 26-2-1999 to 30-11-1999.

4.3 The CTH and DTU gauges

In section 4.1 it was already shown that during a period of 16 months the CTH and DTU gauges register about 85% and 115% of the driving rain amount measured by the TUE-II gauge, respectively. Correlations of 10-min driving rain intensities of gauges CTH and DTU with gauge TUE-II are depicted in figures 4.1a and b. For these graphs, the measurement points have been selected into sets with wind speeds U_y of 4–5 m s^{-1} and with 6–7 m s^{-1}. The many measurement points on the x axis in figure 4.1a indicate that the CTH gauge often measures no rain while the TUE-II gauge measures a positive driving rain amount. Because of this, the linear fit is not successful; the slope tends to be smaller than in case the points on the x axis are left out. The linear fit through the measurement points with U_y = 4–5 m s^{-1} in figure 4.1a has a slope of 0.97 and a correlation coefficient (r^2) of 0.97. This ideal correlation is caused by three measurement points with very high driving rain amounts (between 2 and 6 mm h^{-1}, see figure 4.2a) for which the readings of CTH and TUE-II were almost the same. Figures 4.3a and 4.4a, where the measurement points have been additionally selected according to horizontal rain intensity, show much scatter and poor correlations.

Given the similarities in monthly driving rain amounts of the CTH gauge compared to those of the TUE-II gauge, and given the large scatter in the 10-min driving rain amount correlations between the two gauges, one is inclined to attribute the observed differences to differences in time response between the two gauges. Because the tipping bucket of the CTH gauge has to be filled completely before it can tip and give a reading, the reading of the CTH gauge can have only certain discrete values (properly said: the intervals are much larger than those of the TUE-II gauge readings). Figure 4.1a

(and consequently also figures 4.3a and 4.4a) shows this. One tipping of gauge CTH in 10 minutes represents a driving rain intensity of approximately 0.18 mm h^{-1}. No measurement point can exist between a horizontal line at 0.18 mm h^{-1} (one tipping) and the x axis (zero tippings). Measurement points with two, three and more tippings are also forming horizontal lines at equal distances from each other. Compare the CTH results with those of the TUE-II gauge, which has a much lower threshold for 10-min periods (figure 4.1c).

The correlation of 10-min driving rain amounts of the DTU gauge with those of the TUE-II gauge is plotted in figure 4.1b. The slope of the linear fit is about 1, which is quite good. However, the fit through the measurement points with 4–5 m s^{-1} (+) yields a slope of only 0.67. This is due to one measurement point for which a driving rain amount of 5.5 mm h^{-1} according to gauge TUE-II corresponds with 2.3 mm h^{-1} according to gauge DTU (figure 4.2b). Selections of the measurement points in figure 4.1b, according to driving rain intensities, are plotted in figures 4.3b and 4.4b. The latter figure shows quite good correlations between DTU and TUE-II: the slopes are 1.04–1.08, although due to the scatter the correlation coefficients are poor ($r^2 = 0.39$–0.54). The large scatter is probably due to the noise caused by the wind acting on the freely suspended collector. This noise is filtered out by simply averaging the signal over each 10-min clock period (section 3.4.6), which may be too simple a method. Figure 4.3b (selection with $R_{h,c} = 1.0$–2.5 mm h^{-1}) shows fits with a slope of about 1.40, which indicates that lower driving rain intensities yield higher relatively readings of DTU. It seems therefore that the reading of DTU is now sensitive to the driving rain intensity.

4.4 Summary

The conclusions of the full-scale driving rain gauge comparison test are listed here (and were partially presented in Högberg et al. 1999):

- Driving rain intensities on façade positions P4 and P5 are considered to be identical (figures 4.6a and 4.6b). Temporal fluctuations between these positions were not investigated, because the test did not include measurements with identical driving rain gauges at P4, P5 and P7, which are located adjacent to each other. We suggest such an experiment for a further study.

- The monthly driving rain amounts of the CTH, DTU and TUE-II gauges deviate within 30% from each other (table 4.1). Gauge TUE-I registers approximately half of the monthly driving rain amount.

  On much smaller time bases, such as 10-min intervals, gauge responses can deviate significantly (figures 4.1–4.4). This applies especially to small time bases of the used tipping-bucket driving rain gauge (CTH): during a 10 min period it tips only

once at a driving rain intensity of 0.18 mm h^{-1}. Therefore we suggest that for short-time intervals one should apply a continuous measuring principle instead of the tipping-bucket principle.

- The effect of size and shape of the catchment area cannot clearly be deduced from the experiments. A comparison of the CTH gauge (0.032 m^2) and the TUE-I gauge (0.5 m^2) does not give a straightforward conclusion, because of the difference in measuring principle of the collected rain flux, as pointed out in the previous item. However, the results of gauges TUE-I and TUE-II suggest that for large catchment areas (e.g. 0.5 m^2) a wiper is necessary.

  Another difficulty in interpreting the effect of the size of the catchment area results from a comparison between the TUE-I, TUE-Ib, TUE-II and CTH gauges. While the CTH and TUE-II gauges (two very different catchment areas and measurement principles) yield comparable results (at least over long periods of time), the TUE-I and TUE-Ib gauges (same measurement principle but very different catchment areas) register about 47% and 32% of the driving rain amount of the TUE-II gauge, respectively. One would expect that the TUE-Ib gauge would suffer less from raindrop evaporation than the TUE-I gauge because of its smaller catchment area, and consequently measure higher driving rain intensities. An explanation may be the fact that the drainage path length of the TUE-Ib gauge is much larger than the CTH gauge.

- Teflon coating for a smooth, hydrophobic collector surface is on itself not completely satisfactory. This has also been concluded from laboratory tests at the CTH. Teflon gets dirty, like other finishes (e.g. perspex). A wiper can serve to keep the surface clean, and to improve coagulation and dripping-down of collected raindrops.

- Readings of the DTU gauge (compared to the TUE-II readings) are sensitive to driving rain intensity (figures 4.1b–4.4b). Lower driving rain intensities are overestimated by the DTU gauge. The scatter in the DTU/TUE-II correlations is larger than in the TUE-I/TUE-II correlations. This is probably due to the noise caused by the wind acting on the freely suspended collector. The applied signal-processing method (see section 3.4.6) was kept simple and can perhaps be improved.

- Given every aspect of the driving rain comparison test, one concludes that the TUE-II gauge registers driving rain intensities well. It has a good resolution for shorter time intervals (e.g. 10-min periods). Its wiper keeps the surface clean and forces impinged raindrops to coagulate and drip down (hence less evaporation). Moreover, it is not sensitive to wind.

The comparison test gives the following design rules for driving rain gauges:

- a large catchment area ($\sim$0.5 m^2) is useful for a better resolution for the water flux gauge,

- one should prevent drops from remaining stuck onto the collector surface. A rotating wiper is a simple solution for this problem,
- the water flux gauge, which measures the water flux coming from the collector, should be adapted to the desired time basis and the catchment area of the collector. For a resolution of R mm h^{-1} in t min, a water flux gauge with a collector of A_{catch} m^2 should be able to detect $(RtA_{\text{catch}})/60$ kg. When designing a driving rain gauge it is important to have a fairly good estimate of R. As an example of full-scale driving rain measurements, one can consider the distribution of 5-min driving rain intensities measured at the Main Building in the next chapter (figure 5.15). Maximum values of R_{f} at the Main Building are listed in tables 5.5 and 5.6,
- a smooth surface (e.g. of perspex or teflon) will enable easy cleaning of the driving rain gauge. A rotating wiper also helps in this respect.

Some problems were not solved by the full-scale experiments:

- the influence of shape and size of the collector on the reading of the driving rain gauge is still unclear,
- the possibility of splashing and the effects of protruding rims and other projections were not investigated,
- the influence of the raindrop spectrum on the readings of the gauges was not investigated due to lack of sufficient data.

Chapter 5

Measurements

The full-scale measurements of wind, rain and driving rain are presented in this chapter. The measurements span 24 months, i.e. from December 1997 to November 1999. In chapter 4, the results of the full-scale comparison test of the driving rain gauges were presented. Hence, in this chapter we will deal only with the data of the TUE-II type driving rain gauges, and will not pay attention to the data of the other driving rain gauges (the CTH and DTU types).

Section 5.1 deals with data processing and selection criteria and with the identification of the quantities which will be used in the subsequent sections of the chapter. Also, the source of the data of the weather station at Eindhoven Airport will be given. The data are presented in section 5.2, which includes statistics of wind, rain and driving rain, correlations between intermediate reference wind and rain data and driving rain data, correlations between weather station wind data and intermediate reference wind data, an analysis of the spatial differences of horizontal and driving rain between two positions, and measurements of raindrop spectra. In section 5.3, we will define two empirical driving rain models, which estimate driving rain intensity as a function of the (intermediate) reference quantities. They will be parameterised and evaluated with the measured driving rain intensities. As the present chapter is rather extensive, it will be concluded with a summary (section 5.4).

The measurement data are available on internet at

http://sts.bwk.tue.nl/drivingrain/

5.1 Data processing and selection

In section 3.4 methods for data processing were presented. In some methods parameters have to be set. The values of the parameters which only depend on characteristics of the devices were already defined in that section. In this section, the remaining parameter, the clock period t_{cl}, and data selection criteria are defined.

The clock period which we will use in this chapter, is $t_{\mathrm{cl}} = 5$ min. This value is more than twice as large as the minimum clock period of 1–2 min allowed by the applied sampling times of both the wind and rain measurements. A shorter clock period would be an advantage for detailed analyses of rain data, but 5 min is the smallest unit of time generally used for analyses of wind data over years (as e.g. in KNMI 1992). The effect of the clock period value on the calculated values of the rain intensities is addressed later in this section.

The following quantities are used for the analyses of the measured wind, rain and driving rain data:

- reference quantities, measured at the Auditorium (i.e. at positions P1, P2 and P3):
  - horizontal wind velocity U_{h},
  - horizontal wind direction Φ,
  - wind velocity component perpendicular to the west façade U_{y},
  - horizontal rain intensity $R_{\mathrm{h,c}}$ at positions P2 and P3,
- quantities at the west façade (i.e. positions P4/5 and P6):
  - driving rain intensity $R_{\mathrm{f,P4/5}}$, measured by the TUE-II gauge either at position P4 or P5,
  - driving rain intensity $R_{\mathrm{f,P6}}$, measured by the TUE-II gauge at position P6 from 2-3-1998 onwards.

The wind velocities measured at several distances from the façade at P4 are not used in the analyses in the present chapter, but will be used for comparison with the CFD results in chapter 6. Note that the reference horizontal rain intensity which we will use in this chapter is the corrected rain intensity $R_{\mathrm{h,c}}$ (defined in section 3.4.3). Later in this section, the choice of $R_{\mathrm{h,c}}$ is explained.

Since in chapter 4 it was concluded that the driving rain gauge of the TUE-II type is very suitable, the measurements of the other types of driving rain gauges are not considered in the present chapter. We will focus on the spatial differences between the horizontal rain intensities at the two positions on the roof of the Auditorium (P2 versus P3, see

Table 5.1: Monthly percentage of available clock periods. A clock period is « available » when all installed devices (at the Auditorium and at the west façade of the Main Building) were well functioning. Based on 5 min clock periods.

year	month	% avail.	year	month	% avail.
1997	12	99	1998	12	99
1998	1	97	1999	1	99
1998	2	98	1999	2	98
1998	3	82	1999	3	99
1998	4	79	1999	4	98
1998	5	98	1999	5	99
1998	6	70	1999	6	99
1998	7	90	1999	7	90
1998	8	99	1999	8	89
1998	9	99	1999	9	96
1998	10	88	1999	10	99
1998	11	82	1999	11	94

figure 3.4) and between the driving rain intensities at the two positions at the west façade of the Main Building (P4/5 versus P6, figure 3.6).

The measurement data are put in a table in which every row represents a clock period and gives the corresponding values of the above mentioned quantities. A clock period is said to be « available » if every device, yielding one or two of the above mentioned quantities, is working properly. A device which is simply not installed (operational), does not cause a clock period to be unavailable. Tables 3.2 and 3.3 show the periods during which the devices were operational. An out-of-order due to maintenance, power failure or other malfunction when a device was operational, causes a clock period to be unavailable. A clock period is also unavailable when a device produced less than 90% of the readings which it should have produced during a clock period given its sample time.

The over-all period of the full-scale measurements started on 1-12-1997 and ended on 30-11-1999. Table 5.1 shows the percentage of available clock periods per month. The presence of months with availability percentages lower than 90% is explained in the following. The months of March and April 1998 have relatively low availability figures, due to the reprogramming of the PhyDAS data acquisition system. In June 1998, the data acquisition system was down during 6 days due to a power failure, which could not be fixed immediately. The driving rain collected during these days (the reservoirs were found to be almost full after this period) was not registered. During in total three days of October 1998 the data acquisition systems were out-of-order due to a probable power failure. During November 1998 the PhyDAS data acquisition system was again reprogrammed.

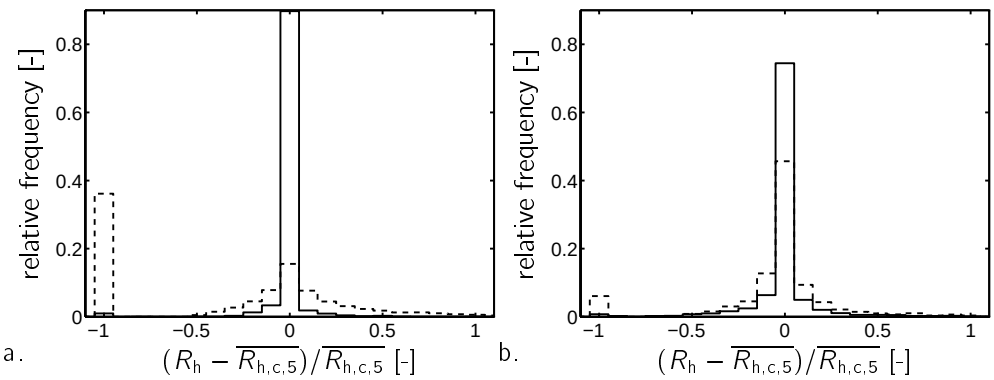

Figure 5.1: Histogram of $(R_h - \overline{R_{h,c,5}})/\overline{R_{h,c,5}}$ with $R_h = R_{h,c,10}$ (——— in figure a), $R_h = R_{h,u,10}$ (----, fig. a), $R_h = R_{h,c,60}$ (———, fig. b), $R_h = R_{h,u,60}$ (----, fig. b). Based on horizontal rain measurements at position P2 from 1-12-1997 to 30-11-1999.

The correction of horizontal rain intensity data and the effect of clock period duration For the analysis of rain quantities, the corrected rain intensity $R_{h,c}$ is used instead of a rain intensity calculated directly from the number of tippings during a clock period ($R_{h,u}$). These two quantities were defined in section 3.4.3. Figure 5.1 shows histograms of the relative difference:

$$\frac{R_h - \overline{R_{h,c,5}}}{\overline{R_{h,c,5}}}, \tag{5.1}$$

where R_h can either mean $R_{h,c,10}$ (corrected 10-min values), $R_{h,u,10}$ (uncorrected 10-min values), $R_{h,c,60}$ (corrected 1-h values) or $R_{h,u,60}$ (uncorrected 1-h values).

$\overline{R_{h,c,5}}$ is the average of the corrected 5-min horizontal rain intensities $R_{h,c,5}$ during a corresponding 10-min or 1-h clock period. A good correspondence between 5-min and 10-min (or 1-h) rain intensity values should result in a 'high peak' at zero relative difference (formula 5.1) in the histogram.

Two important conclusions are drawn from the histograms in figure 5.1. The first conclusion is that the correction is indeed an improvement and yields more realistic rain intensity data. This is supported by two observations. The first observation is that figure 5.1a shows that the corrected 10-min rain intensities correspond better with the averaged corrected 5-min rain intensities than the uncorrected 10-min rain intensities. Approximately 90% of the corrected 10-min rain intensities deviate less than ±5% from the corresponding corrected 5-min averages (figure 5.1a), whereas hardly 20% of the uncorrected 10-min rain intensities deviate less than ±5% from the corresponding corrected 5-min averages. The second observation is that peaks occur at a relative difference

of -1 in the histograms with the uncorrected rain intensities (figures 5.1a and 5.1b). A relative difference of -1 means zero R_h and non-zero $\overline{R_{h,c,5}}$ (eq. 5.1), and occurs more often in the case of uncorrected $R_{h,u}$. Note that the errors in the uncorrected rain intensity values result from the principle of the tipping bucket of the rain gauges (see section 3.4.3).

The second conclusion is drawn from the relatively poor correspondence between the averaged 5-min rain intensities and the 1-h rain intensities. Figure 5.1b shows that only 75% of the 1-h rain intensities deviate less than ±5% from the corresponding 5-min averages. Hence, hourly rain intensity data should be applied with care, because they will give a poor indication of the actual rain intensities, especially maxima. Five-minute data (or possibly 10-min) are thus preferred for our purposes.

KNMI data Data of the weather station at Eindhoven Airport were obtained from reports of the Royal Netherlands Meteorological Institute (KNMI). Thirty-year averages of monthly wind speeds based on data of 1961-1990 were presented in an official report on climatological data of 15 principal weather stations (KNMI 1992). Every month, the KNMI issues a bulletin with (among other parameters) precipitation amount and monthly averaged wind speed (KNMI 1997–99).

On internet, the KNMI presents wind data of 51 weather stations (KNMI 2000). The data consist of hourly averaged wind speeds and consist of averages of wind directions of the last 10 minutes of every clock hour. The actual wind speeds were averaged and subsequently corrected to obtain the so-called potential wind speed, which corresponds to a hypothetical wind that would blow a particular location from any direction at 10 m height over a terrain with $z_0 = 0.03$ m (Wieringa 1996 and Verkaik 2000). The potential wind speed of every clock hour at the Airport are thus given by the KNMI. The available Eindhoven Airport data span from 1-1-1960 to 31-12-1999.

5.2 General presentation of the measured data

In the previous section 5.1, the data (sub)set of the full-scale measurements at the TUE site was defined by specifying the clock period and the quantities of interest. In this section, this data set, along with weather data from the weather station at Eindhoven Airport, is presented.

5.2.1 Wind

Figure 5.2 shows monthly wind speed averages obtained from measurements at the Auditorium and at the meteorological station at Eindhoven Airport. For the airport wind

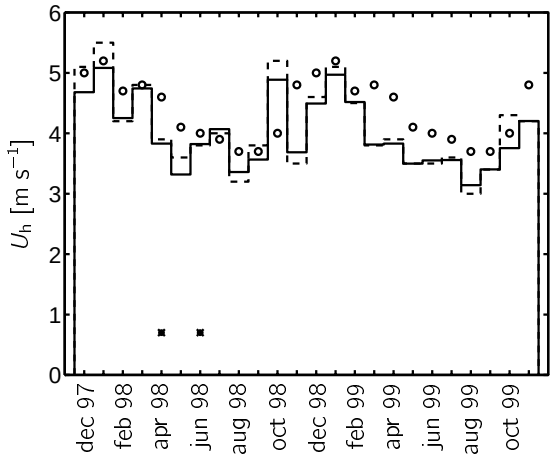

Figure 5.2: Monthly mean wind speeds at Eindhoven Airport (30-year normal: o, measured (KNMI 1997–99): ----) and at the Auditorium (based on 5-min averages: ——). Period: 1-12-1997 to 30-11-1999. An asterisk indicates that the monthly percentage of available clock periods at the TUE site is below 80%.

speeds, 30-year normals and the actual monthly averages were obtained from KNMI (1997–99). The figure also shows the averaged wind speed on top of the mast on the Auditorium. These data are based on 5-min averages, and only wind speeds of 0.1 m s^{-1} or more were taken into account. An asterisk in the graph indicates that the monthly percentage of available clock periods is below 80%. Inspection of figure 5.2 reveals that the actual monthly averages of wind speeds at Eindhoven Airport and at the Auditorium are very similar; both data sets have generally lower wind speeds than the 30-year normals. Since a comparison of hourly averages is more informative than monthly averages, this will be the subject of the following part of this section 5.2.1.

Figure 5.3 shows correlations of hourly wind speeds at Eindhoven Airport $U_{h,EA}$ and the Auditorium $U_{h,P1}$, selected for four wind direction intervals at Eindhoven Airport (Φ_{EA}). The data for Eindhoven Airport, published in KNMI (2000), consists of hourly wind speeds and hourly wind directions. The wind speeds published were obtained by rounding off to 0.5 m s^{-1} and subsequently by the exposure correction to obtain U_h at 10 m height on a terrain with $z_0 = 0.03$ m (Wieringa 1996 and Verkaik 2000). This explains the vertical alignment of the measurement points in figure 5.3. Only wind data with $U_{h,EA} \geq 0.5$ m s^{-1} are taken into account. The data of the Auditorium are simply based on our measurements (uncorrected wind speeds). The correlations in figures 5.3a, c and d (i.e. for wind from the north, south and west) are similar: $U_{h,P1}/U_{h,EA} = 0.90$. This value is lower than the value of 1.13 reported by Geurts (1997). He used 30-min averages of the wind speeds which he measured at the Auditorium during wind exceeding

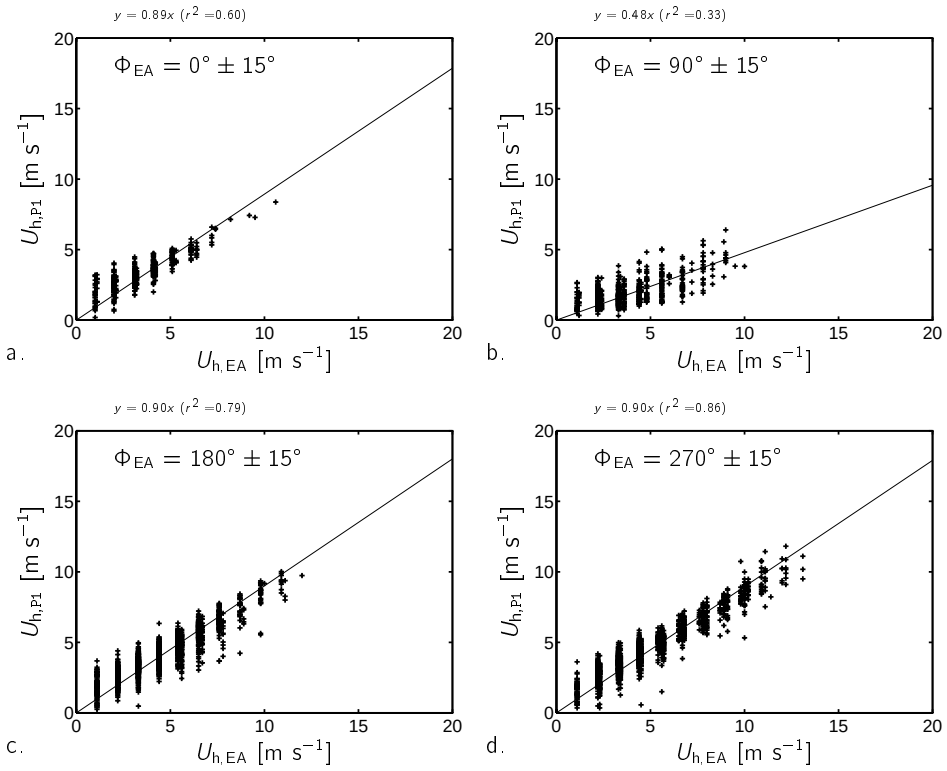

Figure 5.3: Correlations of hourly horizontal wind speeds at Eindhoven Airport (EA) (KNMI 2000) and the Auditorium (P1), for four wind directions Φ_{EA}. Period: 1-12-1997 to 30-11-1999.

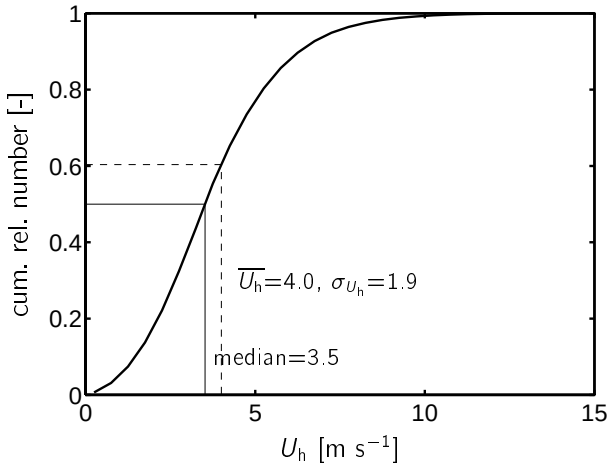

Figure 5.4: Cumulative relative distribution of wind speeds U_h. Based on 5-min data measured at the Auditorium from 1-12-1997 to 30-11-1999. Mean and median 5-min wind speeds are also indicated.

a predefined speed (5–8 m s^{-1}) and he used wind speed averages of the last 10 min of every clock hour at the Airport. This difference between his and our data processing may explain the difference in the values of $U_{h,P1}/U_{h,EA}$. The statistics of this correlation is discussed in more detail by de Wit et al. (2002).

The correlation $U_{h,P1}/U_{h,EA}$ for eastern wind is smaller (0.48, figure 5.3b). This is most likely due to the position of the measurement point at the Auditorium (P1), which is located west of the Main Building. The anemometer at P1 is measuring in the wake of the Main Building when wind is blowing from the east. In the case of eastern wind, there is also an influence of the town on the wind measurements at Eindhoven Airport (located west of the town). However, the airport data were already corrected to compensate for such influences.

Finally, for illustrative purposes, the cumulative relative number distribution of the 5-min wind speeds at the Auditorium is depicted in figure 5.4. The mean wind speed for the whole 24 month period is 4.0 m s^{-1} (the standard deviation equals 1.9 m s^{-1}).

5.2.2 Horizontal rain amounts and intensities

Table 5.2 lists monthly precipitation amounts measured at Eindhoven Airport (KNMI 1997–99) and at the Auditorium. One should bear in mind that the precipitation data include rain, snow and other types of precipitation. However, according to the monthly

Table 5.2: Monthly horizontal precipitation amounts [mm] at positions P2 and P3 at the Auditorium, at Eindhoven Airport (EA) (KNMI 1997–99), and monthly driving rain amounts at P4/5 and P6 (TUE-II type gauges in both cases). Asterisks indicate that the monthly percentage of available clock periods of the TUE data is below 80%.

	horizontal rain amounts			dr. r. amounts	
year month	P2	P3	EA	P4/5	P6
1997 12	64.5	57.8	53.1	2.78	—
1998 01	67.7	62.8	58.2	5.77	—
1998 02	12.9	11.8	10.8	0.83	—
1998 03	85.2	76.3	80.3	4.87	5.25
1998 04 *	77.6	74.4	74.7	1.11	2.46
1998 05	32.5	21.5	26.5	0.94	2.03
1998 06 *	64.5	63.9	148.2	3.92	8.38
1998 07	56.2	54.8	50.3	1.93	2.75
1998 08	48.3	47.1	47.8	3.35	5.36
1998 09	131.8	132.6	167.7	9.61	14.21
1998 10	143.2	138.7	158.5	11.70	13.36
1998 11	80.1	75.4	80.4	0.59	1.17
1998 12	57.2	50.1	51.7	3.43	5.07
1999 01	85.8	79.1	102.6	3.30	6.20
1999 02	65.7	56.8	71.0	4.06	10.21
1999 03	73.1	66.4	68.2	4.31	5.74
1999 04	38.4	36.2	41.5	1.49	2.51
1999 05	53.4	52.8	71.6	0.12	0.52
1999 06	63.4	60.6	53.8	2.43	3.10
1999 07	46.9	44.2	68.8	2.25	4.54
1999 08	95.8	89.6	92.1	1.70	2.44
1999 09	29.8	25.6	38.0	0.76	1.23
1999 10	28.2	27.5	27.5	0.82	1.86
1999 11	34.2	35.6	43.2	0.80	1.72
totals	1536.6	1441.7	1686.5	72.90	100.13

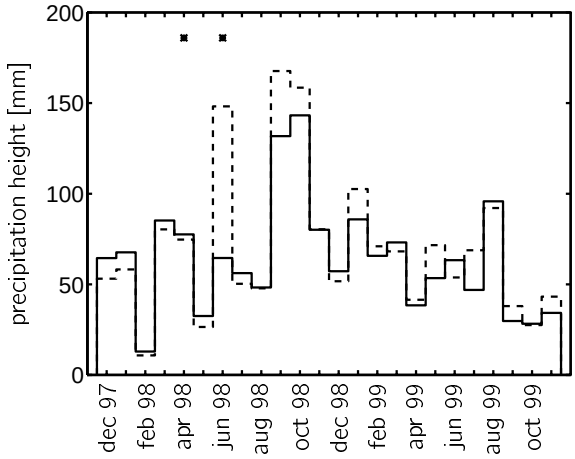

Figure 5.5: Monthly precipitation heights at Eindhoven Airport (measured (KNMI 1997–99): ----) and at the Auditorium (at position P2, based on 5-min clock periods: ——). Period: 1-12-1997 to 30-11-1999. Asterisks indicate that the monthly percentage of available clock periods of the TUE data is below 80%.

weather reports (KNMI 1997–99), the monthly number of days with snowfall was approximately normal. (Normally, snow occurs during the months of November to April and the largest number of monthly snow days (8) occurs in February.) So, the monthly precipitation heights are often close to the actual rain amounts. Thirty-year normals of monthly rain amounts at Eindhoven Airport are not presented in the table, because the meteorological institute did not yet publish them. An asterisk in table 5.2 indicates that the number of available clock periods of the TUE data is below 80%. We recall here that horizontal rain is measured at two positions on the roof of the Auditorium, namely P2 and P3 (figure 3.4). Figure 5.5 depicts the monthly rain amounts measured at Eindhoven Airport and at position P2 on the Auditorium.

Striking in the table and figure are the very large rain amounts measured in June, September and October 1998. Unfortunately, due to a 2-day malfunction of the data acquisition system in June 1998, a large amount of rain was not registered at the Auditorium. The high rainfall during September and October 1998 is considered in section 5.2.7, along with the corresponding wind and driving rain data. In general, the rain amounts measured at Eindhoven Airport and the Auditorium are in good agreement. There is no reason to consider systematic deviations due to topography, because the distance between these two measurement sites is not very large and the exposure of both sites is very open.

The distribution of 5-min horizontal rain amounts over twelve wind direction intervals is listed in table 5.3. Clock periods with $U_h < 0.3$ m s^{-1} are listed separately. Obviously, most rain is coming with wind from the south-west ($\Phi \approx 225°$). The horizontal rain

Table 5.3: Horizontal rain amounts at positions P2 and P3 at the Auditorium and driving rain amounts at P4/5 and P6 for twelve wind direction intervals. The last two columns show respectively the percentage of all available 5-min periods per wind direction interval and the percentage of only those available clock periods with rain at P2 or P3. Clock periods with $U_h < 0.3$ m s^{-1} are listed separately. Based on 5-min data from 1-12-1997 to 30-11-1999.

$\Phi \pm 15°$	horizontal rain				driving rain				number	
	P2		P3		P4/5		P6		all	rain
	[mm]	[%]	[mm]	[%]	[mm]	[%]	[mm]	[%]	[%]	[%]
0°	49.9	3	47.5	3	0.01	0	0.06	0	5	2
30°	38.2	2	37.4	3	0.00	0	0.00	0	7	1
60°	20.0	1	18.8	1	0.00	0	0.00	0	7	2
90°	13.2	1	12.9	1	0.00	0	0.00	0	3	1
120°	51.5	3	50.7	4	0.00	0	0.00	0	5	3
150°	73.9	5	71.3	5	0.00	0	0.00	0	4	5
180°	157.4	10	154.2	11	0.11	0	0.11	0	10	12
210°	403.6	26	363.9	25	11.47	16	8.31	8	21	30
240°	311.3	20	289.8	20	24.22	33	23.41	23	18	21
270°	229.3	15	212.5	15	29.04	40	44.83	45	10	13
300°	108.1	7	103.8	7	6.16	8	17.24	17	6	6
330°	77.5	5	76.1	5	1.86	3	6.15	6	4	4
$U_h < 0.3$ m s^{-1}	2.8	0	2.7	0	0.02	0	0.02	0	0	0
totals	1536.6	100	1441.7	100	72.90	100	100.13	100	100	100

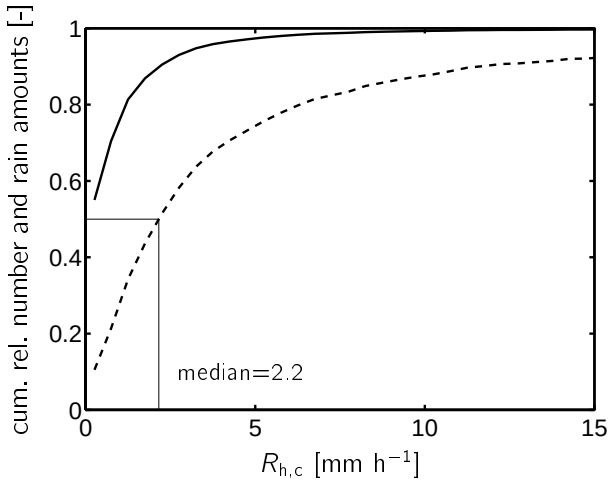

Figure 5.6: Cumulative relative distributions of horizontal rain intensities, in terms of the number of 5-min clock periods with that intensity (——) and the horizontal rain amount (----). Based on 5-min data measured at position P2 from 1-12-1997 to 30-11-1999. The median 5-min horizontal rain intensity (according to rain amounts) is also indicated.

amount for wind directions 195°–255° is approximately 45% of the total rain amount over all wind directions, and occurs during approximately 50% of the total 5-min clock periods with rain. So, the average rain intensity for wind directions 195°–255° is only slightly lower than the rain intensity averaged over all wind directions. On the other hand, the average rain intensity for wind directions 15°–115° is almost equal to the overall average rain intensity.

Figure 5.6 shows two distributions of horizontal rain intensities measured at the Auditorium during the 24-month measuring period. One distribution (the solid line) is the cumulative relative distribution of the number of 5-min clock periods with a particular rain intensity. The other distribution (the dashed line in the figure) is the cumulative relative distribution of the rain amount contributed by all clock periods with a particular rain intensity. The dashed line increases less with the horizontal rain intensity than the solid line, because there are less clock periods with a high rain intensity than with a low rain intensity and because clock periods with a high rain intensity contribute more to the total rain amount than clock periods with a low rain intensity. The cumulative relative distribution in terms of the rain amount (dashed line) is hence more useful. The median indicated in the figure represents the rain intensity below which half of all rain water is collected. At position P2 on the Auditorium the median 5-min rain intensity is 2.2 mm h^{-1}.

Figure 5.7 shows the relative number distribution of daily amounts of horizontal rain at De Bilt presented by Buishand and Velds (1980, p. 93), and at the Auditorium (P2). The

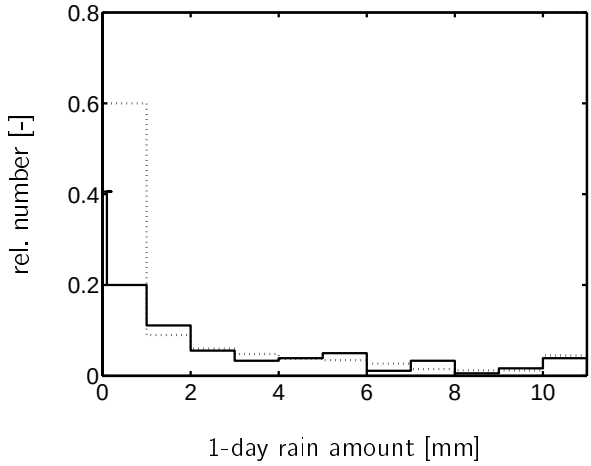

Figure 5.7: Relative number distribution of daily amounts of horizontal rain, measured at the Auditorium (P2) for the winter months December 1997 to February 1998 and December 1998 to February 1999 (——), and measured at De Bilt (Buishand and Velds 1980, p. 93) for the winters (December–February) from 1906 to 1977 (.....). The most right bar denotes daily amounts of 10 mm and more. The most left bar of the solid line denotes zero daily amounts.

data of De Bilt were taken from winters from 1906 to 1977. Therefore the TUE data were taken from the winter months December 1997 to February 1998 and December 1998 to February 1999. The data of Buishand and Velds (1980) do not indicate zero daily amounts separately: so approximately 60% of the days had a daily amount of less than 1 mm. Our data show that approximately 40% of the days had no rain and approximately 20% had a rain amount between 0 and 1 mm. Apart from this possible difference, the figure shows quite a good agreement between the TUE rain data and the De Bilt rain data. We cannot state whether this agreement is fortuitous or not, because similar data for the weather station at Eindhoven Airport for a period of many years ($\geq$30 years) have not yet been published.

5.2.3 Horizontal rain measurements by two gauges and a disdrometer

On the roof of the Auditorium two tipping-bucket rain gauges were installed at positions P2 and P3, respectively (figure 3.4). The distance between these two positions is 33 m. The purpose of the two rain gauges is to investigate spatial differences in rain intensity on the roof. Figure 5.8 shows the horizontal rain amounts measured at P2 and P3 (normalised to the total rain amount) corresponding to relative differences of the rain

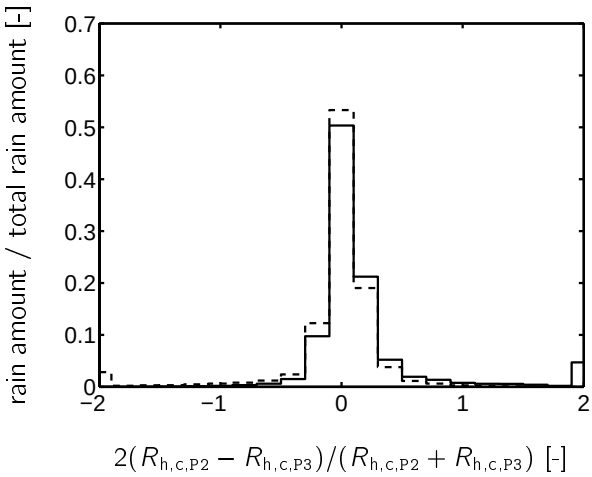

Figure 5.8: Relative horizontal rain amounts measured at position P2 (——) and P3 (----) corresponding to intervals of relative differences (formula 5.2) between 5-min rain intensities at these two positions. Period: 1 December 1997 to 30 November 1999.

intensity measured by the two gauges. These relative differences are defined as the difference in rain intensity divided by the mean rain intensity:

$$2\frac{R_{h,c,P2} - R_{h,c,P3}}{R_{h,c,P2} + R_{h,c,P3}}. \tag{5.2}$$

From the figure one can deduce that the rain intensity difference is within 10% (30%) for approximately 52% (83%) of the total rain amount. These results are quite satisfactory, form which we conclude that the two positions P2 and P3 represent the same situation.

At approximately 1.5 m from the rain gauge at position P3 a disdrometer was installed. The disdrometer was operational from 1-10-1999 to 7-1-2000. Figure 5.9 presents the cumulative horizontal rain amounts measured by the three devices during this period. Differences are within 30% on monthly basis. Remarkably, the amounts collected by the disdrometer seem larger than those collected by the two rain gauges.

A distribution of rain amounts over intervals of relative differences (cf. formula 5.2) between the gauge at P2 and the disdrometer for every 5-min clock period is plotted in figure 5.10. Almost 18% (46%) of the total horizontal rain amount is measured with less than 10% (30%) difference between the 5-min values of the rain gauge and the disdrometer. The figure also shows that the disdrometer measures quite a large rain amount during clock periods when the rain gauge measures no rain (i.e. when the relative difference equals −2). This explains figure 5.9, where we observed that the total amount of rain measured by the disdrometer is larger than the total amount of rain measured

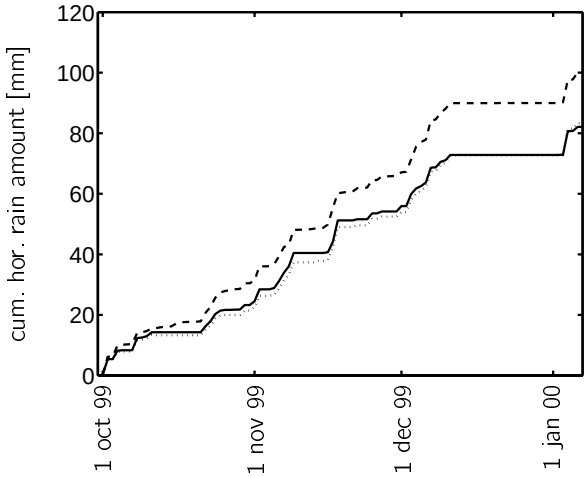

Figure 5.9: Cumulative horizontal rain amounts measured by a rain gauge at position P2 (——), a rain gauge at position P3 (.....), and a distrometer (close to P3) (----). Based on 5-min data from 1-10-1999 to 7-1-2000.

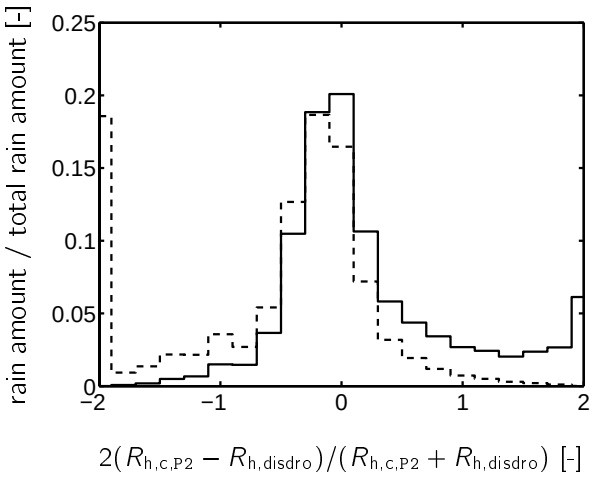

Figure 5.10: Relative horizontal rain amounts measured by the rain gauge at P2 (——) and by the disdrometer (----) corresponding to intervals of relative differences between 5-min rain intensities by these two devices. Period: 1-10-1999 to 7-1-2000.

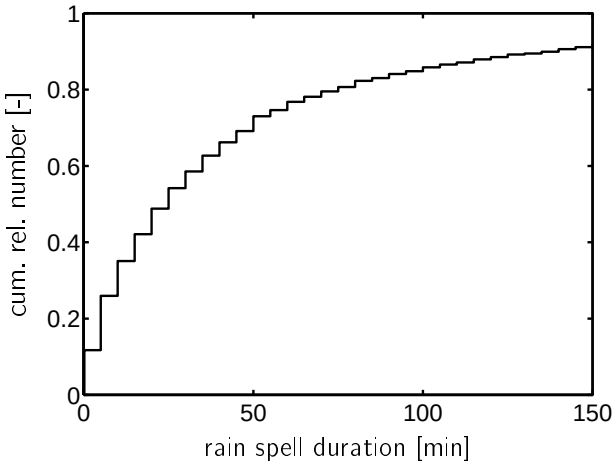

Figure 5.11: Cumulative relative distribution of rain spell durations measured at the Auditorium (position P2). Based on 5-min clock periods from 1-12-1997 to 30-11-1999.

by the rain gauges. The implications of this observation are not clear, because the considered period comprises only almost three months (during which disdrometer data are missing from 12–20 December 1999) and because we do not have much experience with the disdrometer. It is possible that the disdrometer does not function totally well and its performance should be investigated in more detail.

Nevertheless, we conclude that the differences in reading between the rain gauge and the disdrometer are generally not so bad, because, as said before, the rain intensity difference is within 30% for approximately 46% of the total rain amount.

5.2.4 Rain spells

A rain spell is defined here as a period consisting of consecutive 5-min clock periods with $R_{\mathrm{h,c}} > 0.02$ mm h^{-1}. In figure 5.11, the cumulative relative distribution of rain spell durations measured at the Auditorium is plotted. Almost 50% of the rain spells take less than 25 min. In section 5.1, we noted that hourly rain intensity data should be applied with care, because they will give a poor indication of actual rain intensities, especially maxima. Figure 5.11 supports for this conclusion: rain spells are often shorter than an hour.

From our measurements, we can also calculate the percentage of the time that rain occurs. This is approximately 8%. Buishand and Velds (1980) mention a percentage of 7% for the Netherlands.

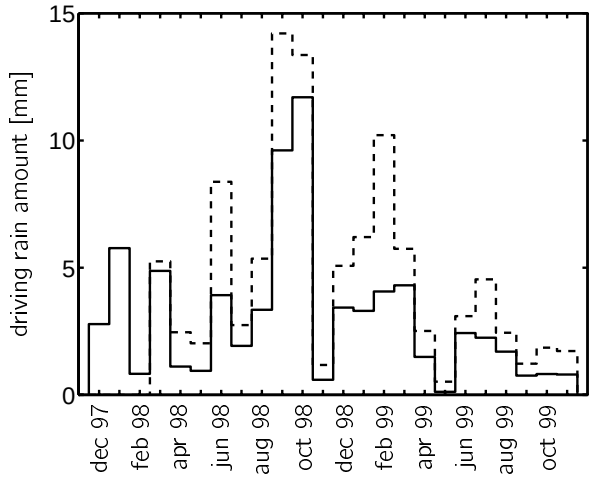

Figure 5.12: Monthly driving rain amounts at position P4/5 (——) and P6 (----) measured by TUE-II type driving rain gauges. Based on 5-min clock periods during 1-12-1997 to 30-11-1999. Note that the gauge at P6 was operational from 2 March 1998.

5.2.5 Driving rain amounts and intensities

Driving rain measurements were performed by two TUE-II type gauges. One of these gauges was placed at a central position on the west façade of the Main Building (positions P4 or P5; in short: P4/5), and the other TUE-II gauge was installed at the north edge of the façade (position P6). The reader is referred to figure 3.6 for a drawing of the exact positions.

Figure 5.12 shows the monthly driving rain amounts collected by the driving rain gauges at P4/5 and P6, respectively. The same information is listed in table 5.2. The driving rain gauge at the edge (P6) catches 1.1 to 4.3 times the driving rain amount of the central gauge (P4/5), and on average about 1.5 times as much.

Figure 5.13a gives a distribution of driving rain measured by the TUE-II gauge at position P4/5 from December 1997 to November 1999, over intervals of reference wind speed and wind direction measured at the top of the mast on the Auditorium. Figure 5.13b shows the driving rain distribution for the north-edge west façade position P6. The edge catches especially more rain for wind speeds between 3 and 10 m s^{-1} and for wind directions of NW and W.

Figure 5.14 shows 5-min driving rain intensities as a function of the wind velocity component perpendicular to the façade (U_y) for two narrow horizontal rain intensity intervals ($R_{\mathrm{h,c,P2}}$) and for the two positions P4/5 and P6. Note that the x axis of the graphs represents $-U_y$ (with the minus) because only negative values of U_y correspond to wind

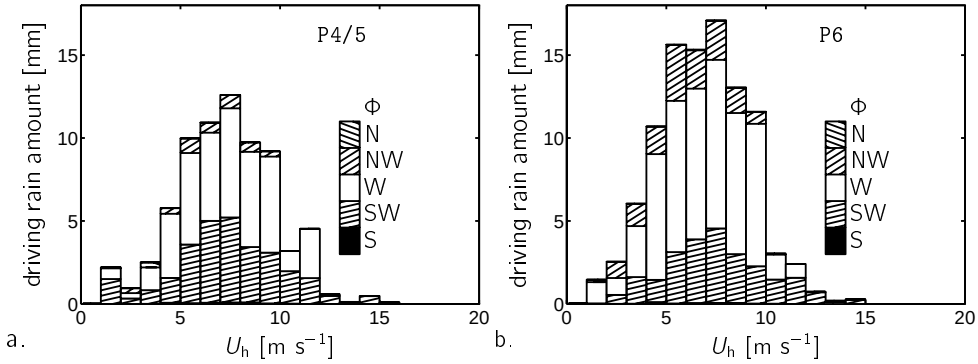

Figure 5.13: Driving rain amounts for various horizontal wind velocity intervals (U_h) and various wind direction (Φ) intervals. Based on 5-min data measured from 1-12-1997 to 30-11-1999. Driving rain was measured by the TUE-II gauges at position P4/5 (fig. a) and position P6 (fig. b), respectively.

blowing towards the façade (see the axis definition in figures 2.4 and 3.4). As we expect, driving rain intensity increases with wind speed and horizontal rain intensity. However, one also concludes from these plots that driving rain intensities even show large variations for a particular wind speed and horizontal rain intensity. A factor which has not been measured and therefore is not taken into account here, is the raindrop spectrum. Variations of the raindrop spectrum might be the cause of a part of the variation in driving rain intensities. In section 5.3 the relation between wind speed, wind direction, horizontal rain intensity and driving rain intensity will be described in more detail.

Distributions of driving rain intensities are drawn in figures 5.15a for P4/5 and 5.15b for P6. Every figure has two lines and is similar to figure 5.6 (for horizontal rain). The solid line represents the cumulative relative distribution of 5-min clock periods with a particular driving rain intensity. The dashed line represents the cumulative relative distribution of the total driving rain amount contributed by all clock periods with a particular rain intensity. The medians at positions P4/5 and P6 are 0.67 and 1.0 mm h^{-1}, respectively. This suggests that the driving rain intensities at the façade edge (P6) are higher than at the central façade position (P4/5). The discussion on the differences between the two façade positions is continued in the following section.

5.2.6 Driving rain at two positions

Table 5.4 lists the results of least-squares fits ($y = cx$) of correlations between the driving rain intensities measured at P4/5 and P6, respectively. The correlations are obtained from the data selected according to various wind direction intervals and horizontal rain

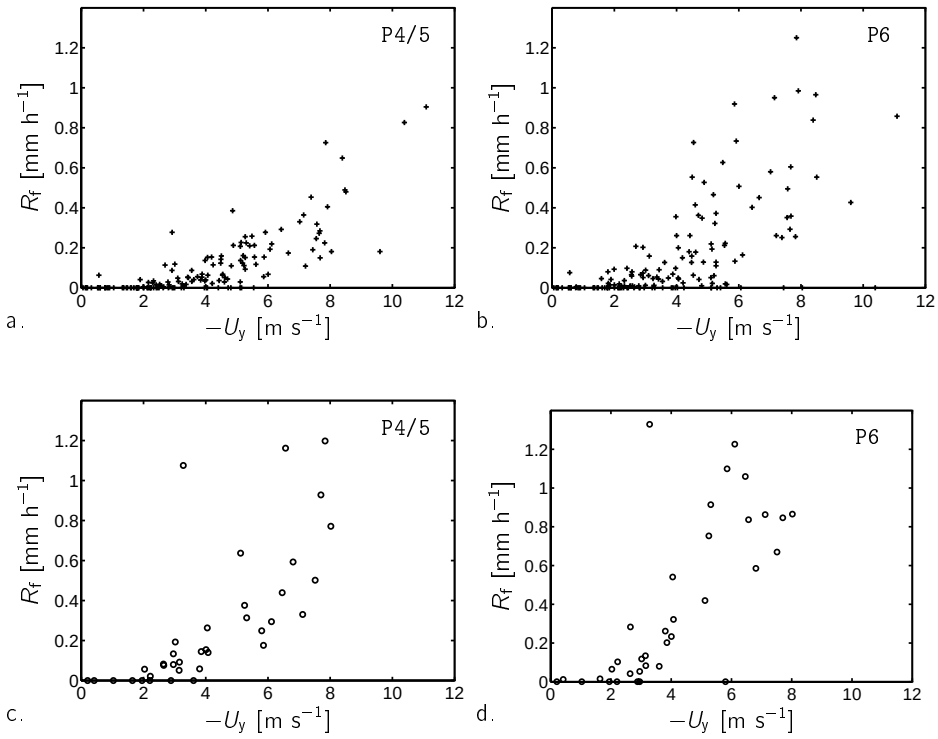

Figure 5.14: Driving rain intensities at P4/5 (fig. a&c) and P6 (fig. b&d) as a function of the wind velocity component perpendicular to the façade (U_y), for horizontal rain intensities $R_{h,c,P2}$ = 2.0–2.1 mm h^{-1} (+) and 4.0–4.1 mm h^{-1} (o). Based on 5-min data from 1-12-1997 to 30-11-1999.

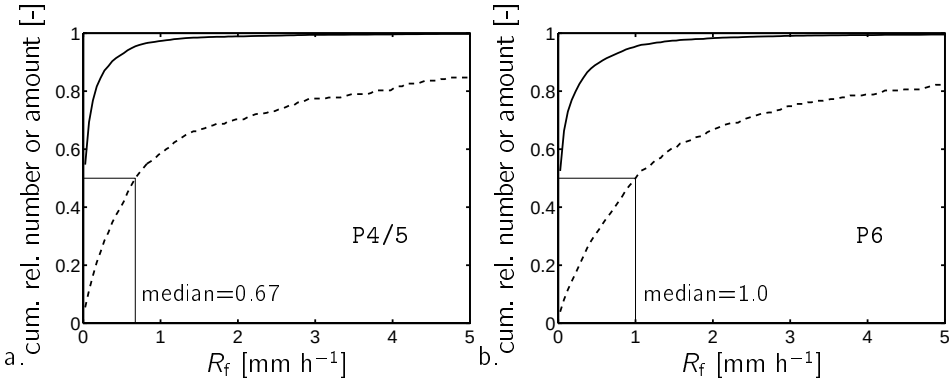

Figure 5.15: Cumulative relative distribution of driving rain intensities, in terms of the number of 5-min clock periods with that intensity (——) and the driving rain amount (----). Based on 5-min data measured by driving rain gauge TUE-II at positions P4/5 (fig. a) and P6 (fig. b) from 1-12-1997 to 30-11-1999. The median 5-min driving rain intensity (according to rain amounts) is also indicated.

intensity intervals (table 5.4a) and according to various wind direction intervals and wind speed intervals (table 5.4b). The intervals cannot be taken too small, because in that case the number of data points would be too low. For this reason, the data are not selected by the three parameters (wind direction, wind speed and rain intensity) together. Correlations with a selection based on the horizontal rain intensity and the wind speed component perpendicular to the façade (U_y) are not shown here, because these lead to very dispersed correlation plots.

Four correlations of table 5.4a are plotted in figure 5.16. From the figure and table 5.4a, one concludes that south-western wind (i.e. between 210° and 240°) yields a ratio $R_{f,P6}/R_{f,P4/5}$ of approximately 1, and this ratio increases for western and north-western winds. The coefficient of determination (r^2) is worse for wind directions of 330° than for wind directions of 210° or 240°. This is mainly due to a low number of data points, and perhaps also due to more variation caused by the turbulence at the façade edge near P6. Table 5.4a also shows that, generally, an increase of the horizontal rain intensity for a particular wind direction interval does not change the ratio $R_{f,P6}/R_{f,P4/5}$ much. At the wind direction interval of 330° the ratios are different for lower and higher rain intensities; this is due to the large scatter (and the small number of data) at the higher rain intensities. Table 5.4b lists the correlations of $R_{f,P6}/R_{f,P4/5}$ for various wind direction intervals and wind speed intervals. The ratios reveal no particular tendency for increasing wind speeds. Our data indicate that the wind direction has a much larger influence on the ratio, than wind speed and horizontal rain intensity.

Table 5.4: Correlations of $R_{f,P6}/R_{f,P4/5}$ for various wind direction intervals and horizontal rain intensity intervals (table a), and various wind direction intervals and horizontal wind speed intervals (table b). The last column lists the number of data points. Some of the correlations of table a are plotted in figure 5.16. Based on 5-min data from 1-12-1997 to 30-11-1999.

a.

$\Phi \pm 15°$	$R_{h,c,P2}$ [mm h^{-1}]	$R_{f,P6}/R_{f,P4/5}$	r^2	number	
210°	0.1–2.0	0.81	0.70	795	
	2.0–4.0	0.97	0.85	223	
	4.0–6.0	0.83	0.88	73	
240°	0.1–2.0	1.00	0.76	1106	→fig. 5.16a
	2.0–4.0	1.14	0.73	278	→fig. 5.16b
	4.0–6.0	1.22	0.42	70	
270°	0.1–2.0	1.62	0.68	814	→fig. 5.16c
	2.0–4.0	1.75	0.59	224	→fig. 5.16d
	4.0–6.0	1.71	0.54	43	
300°	0.1–2.0	2.59	0.43	398	
	2.0–4.0	2.50	0.28	96	
	4.0–6.0	2.63	0.16	27	
330°	0.1–2.0	4.21	0.53	123	
	2.0–4.0	2.87	0.21	70	
	4.0–6.0	2.43	0.20	20	

b.

$\Phi \pm 15°$	$U_{h,P1}$ [m s^{-1}]	$R_{f,P6}/R_{f,P4/5}$	r^2	number
210°	3.0–5.0	2.72	0.82	170
	5.0–7.0	0.70	0.75	437
	7.0–9.0	0.97	0.90	328
240°	3.0–5.0	1.29	0.73	325
	5.0–7.0	1.05	0.69	623
	7.0–9.0	1.18	0.79	325
270°	3.0–5.0	1.66	0.65	342
	5.0–7.0	1.66	0.80	386
	7.0–9.0	1.71	0.80	265
300°	3.0–5.0	2.26	0.55	223
	5.0–7.0	3.04	0.79	210
	7.0–9.0	2.03	0.87	44
330°	3.0–5.0	2.05	0.83	80
	5.0–7.0	2.84	0.51	63
	7.0–9.0	2.28	0.71	55

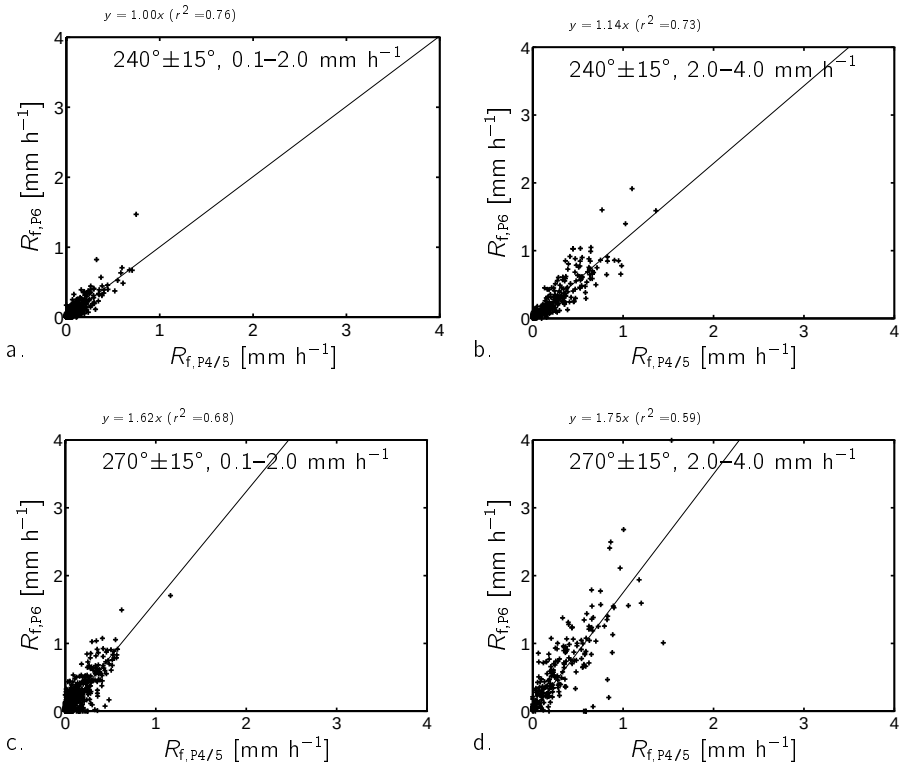

Figure 5.16: Correlations between 5-min driving rain intensities at position P4/5 and P6, for various wind direction intervals (Φ, figures a&b versus c&d) and horizontal rain intensity intervals ($R_{\mathrm{h,c,P2}}$, figures a&c versus b&d). Period: 1-12-1997 to 30-11-1999.

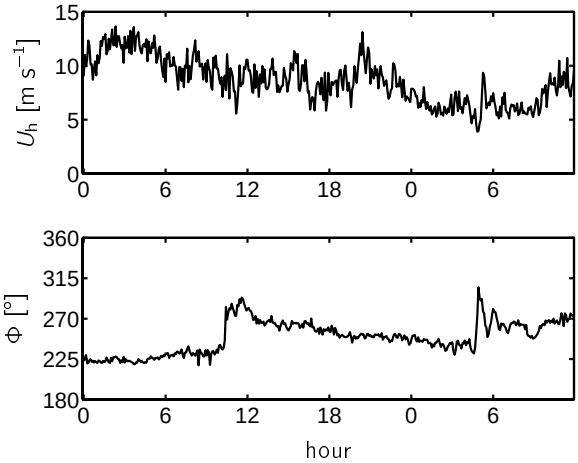

Figure 5.17: Five-minute wind speeds and directions from 28-10-1998 (0h00) till 29-10-1998 (12h00).

5.2.7 Example of rainfall with high driving rain intensities

The year 1998 was an extremely wet year, so even the 1998 annual report of the KNMI was dedicated to rain (KNMI 1999). The rain amounts of March, April, June, September, October and December 1998 were almost twice of the normal rain amounts. The yearly total was 1239.6 mm (normally 803 mm). At Eindhoven Airport the yearly total was 955.1 mm. At the Auditorium we measured 857.2 mm at P2 and 809.4 mm at P3. The Auditorium total is approximately 100 to 150 mm less than the Airport total, of which approximately 80 mm can be attributed to the malfunction of our devices during June 1998.

We measured a series of high driving rain intensities in September 1998 and October 1998. The driving rain gauge at P4/5 collected 6.1 mm of driving rain during 20 hours continuously on 14 and 15 September 1998 (the monthly driving rain amount was 8.5 mm). The reservoir of the driving rain gauge was emptied once during rain; this may have led to an error of 0.1 mm. Also much of the driving rain amount in October 1998 was collected in a short time. During 20 h on 27 and 28 October 1998 the gauge at P4/5 measured 6.0 mm. Unfortunately, the reservoir had to be emptied twice during rain, which may have led to an error of 0.4 mm. The total driving rain amount of October 1998 was 10.3 mm. Note that these mentioned errors relate to the exceptional cases in September and October 1998, when the reservoirs were (almost) overflowed. Of course, these errors are not typical for the normal functioning of the driving rain gauges.

For merely illustrative purposes, figures 5.17–5.19 show the wind speeds, wind directions, horizontal rain and driving rain (intensities as well as cumulative amounts) measured on

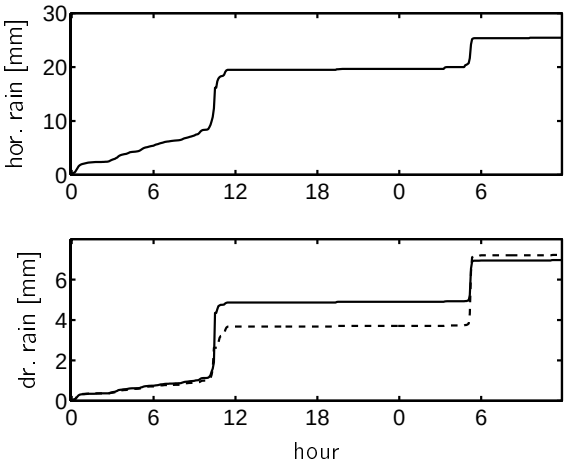

Figure 5.18: Cumulative horizontal rain amounts (at P2) and driving rain amounts (at P4/5, ——, and at P6, ----), from 28-10-1998 (0h00) till 29-10-1998 (12h00).

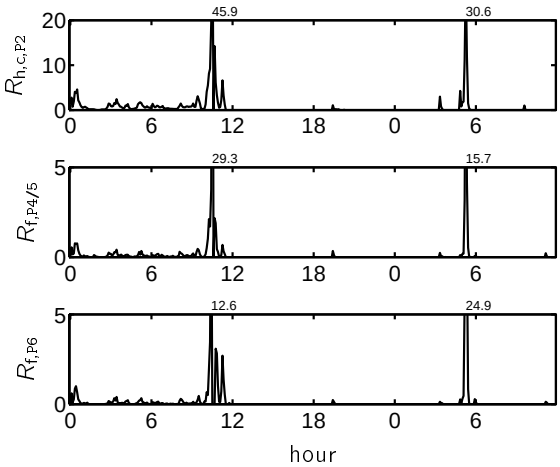

Figure 5.19: Five-minute horizontal rain intensities (at P2) and driving rain intensities (at P4/5 and P6), from 28-10-1998 (0h00) till 29-10-1998 (12h00).

28-10-1998 and 29-10-1998. Remarkable for the presented rain events is that a sudden wind direction change towards 270° goes along with increasing horizontal rain and driving rain intensities, which reach very high peek values at 28-10-1998 on 10h25 and 29-10-1998 on 05h15. The dynamics of the horizontal rain and the driving rain were so high that the lower rain intensities in figure 5.19 are hardly visible.

5.2.8 Maximum horizontal rain and driving rain

Tables 5.5 and 5.6 list the ten 5-min clock periods with the highest driving rain intensities measured at position P4/5 and P6, respectively. The tables also list the horizontal rain intensities, wind speeds, wind directions and dates corresponding to the ten largest driving rain intensities. For every value of a quantity, except for the wind direction, its rank and its number of occurrence is indicated. A rank of 1 means that the value is the highest value. To avoid many ranking levels, the quantities were rounded to a tenth or to one. If the number of occurrence of a particular value is more than one, this means that the same value occurred several times. If the number of occurrence of a driving rain intensity value is more than one, the indicated date is the date of the first occurrence. The indicated dates (and times) give the start of the 5-min clock periods.

The ten largest 5-min driving rain intensities at P4/5 are all unique occurrences (except for the 8th in rank, which occurred twice), and range from 6.0 to 29.3 mm h^{-1}. The corresponding horizontal rain intensities range from 22 to 53 mm h^{-1}, and are very high compared to the median of 2.2 mm h^{-1} (see figure 5.6). The corresponding wind speeds range from 1.7 (!) to 11.1 m s^{-1}. One would expect that higher wind speeds and horizontal rain intensities would yield higher driving rain intensities, but this is not obvious for the events in table 5.5. Only the values of the wind speed components perpendicular to the façade (U_y) show a more distinct increasing tendency. Remarkable is that the second highest driving rain intensity occurred when the wind speed was only 1.9 m s^{-1}. A close inspection of the data of 7-1-1998 14h00 reveals that the previous clock period had a wind speed U_y of 5.9 m s^{-1} and a rain intensity of 1.2 mm h^{-1}. The next clock period had a wind speed U_y of 8.5 m s^{-1} and a rain intensity of 7.8 mm h^{-1}. It is therefore possible that the wind speed indicated in the table for 7-1-1998 14h00–14h05 is an error due to a time lag between the clocks in the two data acquisition systems (one for the rain measurements, the other for the wind measurements, see figure 3.19).

Table 5.5 also shows driving rain intensities at P6 corresponding to the ten highest driving rain intensities at P4/5. Note that the driving rain gauge at P6 was not operational at the time of the 5-min clock periods starting at 7-1-1998 14h00 and 3-1-1998 15h25. At 28-10-1998 10h30 the reservoir of the P6 driving rain gauge was emptied to prevent it from overflowing and thus the actual driving rain intensity at P6 could not be registered.

Table 5.6 shows the 10 highest driving rain intensities measured at position P6. The 10 highest driving rain intensities at P6 correspond to the 20 highest driving rain intensities

Table 5.5: The ten highest 5-min driving rain intensities at P4/5 from from 1-12-1997 to 30-11-1999, with the other parameters corresponding to the same 5-min clock period. The rank and the number of occurrence (#) of the actual values are also indicated. The indicated dates (and times) give the start of the 5-min clock periods. The units are mm h^{-1} for rain intensities, m s^{-1} for wind speeds and degrees from north for wind directions.

$R_{f,P4/5}$	29.3	17.8	15.7	13.0	10.5	9.6	7.2	6.7	6.4	6.0
rank	1	2	3	4	5	6	7	8	9	10
#	1	1	1	1	1	1	1	2	1	1
$R_{f,P6}$	–	–	24.9	17.5	9.9	16.5	8.6	–	10.3	4.9
rank	–	–	1	2	6	3	10	–	5	22
#	–	–	1	1	1	1	1	–	1	1
$R_{h,c,P2}$	46	31	31	41	45	28	50	33	22	34
rank	4	13	13	7	5	15	3	11	18	10
#	1	3	3	1	1	1	1	2	1	1
$R_{h,c,P3}$	53	29	30	40	48	27	50	30	20	25
rank	2	11	10	7	4	13	3	10	18	15
#	2	1	3	1	1	1	1	3	3	1
U_h	11.1	1.9	9.3	6.2	5.9	9.7	7.6	9.5	4.8	5.7
rank	47	139	65	96	99	61	82	63	110	101
#	43	2691	192	1600	1930	175	666	185	3184	2160
Φ	269	245	278	260	253	263	221	208	256	223
U_y	11.1	1.7	9.3	6.1	5.7	9.7	4.9	4.5	4.7	3.9
rank	26	120	44	76	80	40	88	92	90	98
#	12	2778	61	498	684	52	1238	1458	1382	2084
year	1998	1998	1998	1998	1998	1998	1999	1998	1999	1999
month	10	1	10	9	8	6	6	1	2	8
day	28	7	29	9	26	2	3	3	21	18
hour	10	14	5	16	14	15	21	15	17	11
minute	30	0	15	55	35	55	55	25	40	20

Table 5.6: The ten highest 5-min driving rain intensities at P6 from from 1-12-1997 to 30-11-1999. See further the caption of table 5.5.

$R_{f,P4/5}$	15.7	13.0	9.6	3.8	6.4	10.5	3.8	4.2	3.7	7.2
rank	3	4	6	18	9	5	18	15	19	7
#	1	1	1	2	1	1	2	2	1	1
$R_{f,P6}$	24.9	17.5	16.5	12.6	10.3	9.9	9.6	9.4	9.3	8.6
rank	1	2	3	4	5	6	7	8	9	10
#	1	1	1	1	1	1	1	1	1	1
$R_{h,c,P2}$	31	41	28	19	22	45	17	59	20	50
rank	13	7	15	21	18	5	23	1	20	3
#	3	1	1	3	1	1	6	1	7	1
$R_{h,c,P3}$	30	40	27	18	20	48	17	58	18	50
rank	10	7	13	20	18	4	21	1	20	3
#	3	1	1	5	3	1	6	1	5	1
U_h	9.3	6.2	9.7	7.7	4.8	5.9	6.6	1.7	7.3	7.6
rank	65	96	61	81	110	99	92	141	85	82
#	192	1600	175	598	3184	1930	1291	2431	824	666
Φ	278	260	263	283	256	253	292	262	294	221
U_y	9.3	6.1	9.7	7.5	4.7	5.7	6.2	1.7	6.7	4.9
rank	44	76	40	62	90	80	75	120	70	88
#	61	498	52	225	1382	684	489	2778	369	1238
year	1998	1998	1998	1998	1999	1998	1998	1999	1998	1999
month	10	9	6	10	2	8	8	7	8	6
day	29	9	2	28	21	26	22	4	24	3
hour	5	16	15	10	17	14	14	23	1	21
minute	15	55	55	25	40	35	50	30	40	55

Table 5.7: Horizontal rain amounts [mm] measured by the tipping-bucket rain gauges at P2 and P3 and by the disdrometer, and driving rain amounts [mm] at P4/5 and P6, per wind direction interval. The last column shows the number of 5-min periods with rain. Clock periods with $U_h < 0.3$ m s^{-1} are listed separately. Based on 5-min data from from 1-10-1999 to 7-1-2000. Cf. table 5.3.

	hor. rain			dr. rain		
$\Phi \pm 15°$	P2	P3	disdro	P4/5	P6	number
0°	4.2	3.9	4.9	0.00	0.01	187
30°	0.0	0.0	0.6	0.00	0.00	151
60°	0.0	0.0	1.3	0.00	0.00	404
90°	0.0	0.0	0.5	0.00	0.00	210
120°	1.8	1.8	2.8	0.00	0.00	167
150°	1.3	1.1	1.9	0.00	0.00	142
180°	4.9	4.9	6.5	0.00	0.00	382
210°	28.6	29.6	31.3	0.33	0.33	1488
240°	20.0	20.5	24.8	1.25	1.60	1224
270°	13.0	12.8	17.3	2.06	4.25	491
300°	5.2	5.5	6.1	0.32	1.15	214
330°	2.5	2.8	3.0	0.00	0.05	188
U_h <0.3 m s^{-1}	0.8	0.7	0.1	0.02	0.01	27
totals	82.2	83.5	101.0	3.97	7.38	5275

at P4/5 (see the ranks in the second row in table 5.6). Similar to P4/5, one can conclude that the circumstances for very high driving rain intensities at P6 vary quite a lot and there is no evident correlation between the wind speed, the horizontal rain intensity and the driving rain intensity. Note that a two year measurement period is too short for decisive conclusions with respect to rain events with extreme driving rain, although the measurements were carried out during an extremely wet year. Nevertheless, the driving rain intensity values of tables 5.5 and 5.6 can be used as a guide for driving rain gauge design (cf. section 4.4).

5.2.9 Raindrop spectra

As was mentioned in section 5.2.3, the disdrometer was only operational from 1-10-1999 to 7-1-2000. Although this is a rather short period and only a small part coincides with the general 24-month measurement period, some (exemplary) results are presented here to demonstrate the temporal variability and the parameterisation of raindrop spectra. Table 5.7 lists the horizontal and driving rain amounts measured during the period when the disdrometer was operational. It shows that the driving rain amounts during this period were small.

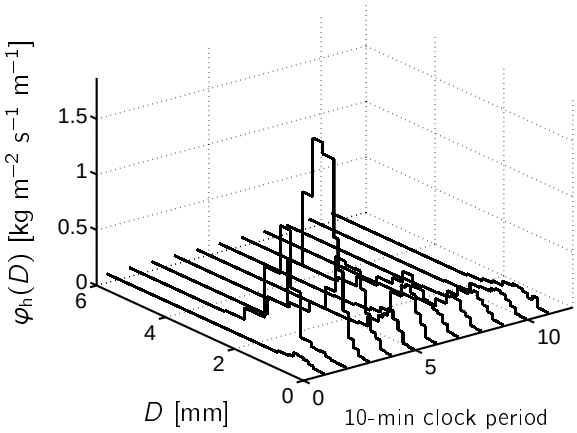

Figure 5.20: Horizontal raindrop mass flux spectra $\varphi_h(D)$ as a function of time from 2-10-1999 13h00.

Figure 5.20 shows the measured horizontal raindrop mass flux spectra of an arbitrarily chosen period of rain. The plotted sequential 10-min spectra show the evolution of a rain period with its large changes of raindrop spectra and rain intensity.

In chapter 6 we will use the raindrop spectrum parameterisation of Wessels (1972). He obtained a range of the parameter A of the Best spectrum formula (eq. 2.24). Ninety percent of his 533 observations at De Bilt (NL) had a value of A ranging from 0.88 to 1.77. Here, we compare raindrop spectra measured with our disdrometer with raindrop spectra calculated with $A = 0.88$ and $A = 1.77$. The calculated raindrop spectra have the same horizontal rain intensity as the measured spectra. The purpose is to investigate how much the calculated spectra differ from actual spectra. Figure 5.21c shows a raindrop spectrum measured by the disdrometer during an arbitrary 5-min clock period. The asterisk indicates the median drop size. Figures 5.21a and 5.21b show the corresponding raindrop spectra calculated with $A = 0.88$ and 1.77, respectively. They are obviously different from the measured spectrum.

Figure 5.22 shows the correlation between the median drop size of the measured spectra ($D_{50,\mathrm{disdro}}$) and the median drop sizes of the two calculated raindrop spectra (with $A = 0.88$, □, and 1.77, ◇). The median drop size was chosen to make differences in the spectra visible (yet to some extent). Figure 5.22 shows that generally the measured median drop size is between the two calculated median drop sizes (i.e. the straight line is between a □ and a ◇ at the same $D_{50,\mathrm{disdro}}$). However, for larger median drop sizes the measured median drop size becomes larger than the calculated median drop sizes. This indicates that the measured drop spectra contain more larger drops than the spectra calculated with the given parameters (cf. figure 5.21). From the figure we

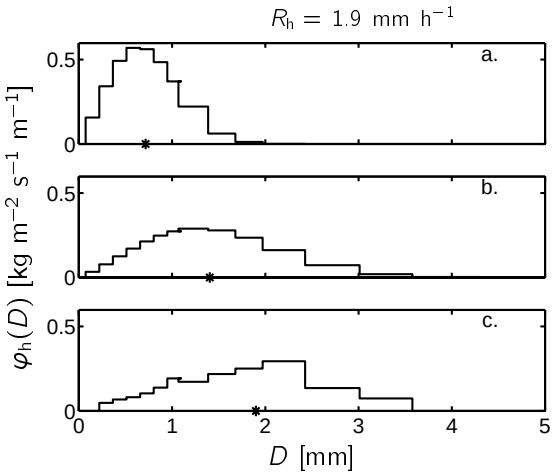

Figure 5.21: Horizontal raindrop mass flux spectra $\varphi_h(D)$ with the same horizontal rain intensity (1.9 mm h^{-1}), (a) calculated from the parameterisation of Wessels (1972) with $A = 0.88$, (b) with $A = 1.77$, and (c) measured by the disdrometer during an arbitrary 5-min clock period. The asterisk indicates the median drop size.

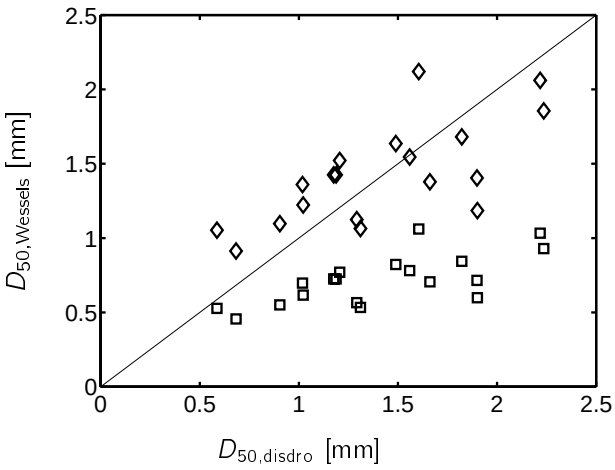

Figure 5.22: Correlation of median drop sizes measured by the disdrometer ($D_{50,\mathrm{disdro}}$) and calculated according to the parameterisations of Wessels (1972), i.e. with $A = 0.88$ (□) and $A = 1.77$ (◇). The measurements are based on 5-min data from 1-10-1999 to 7-1-2000 selected for $U_h = 3.5$–11.2 m s^{-1} and $\Phi = 270° \pm 15°$.

conclude that the measured raindrop spectra come close to the two parameterisations of Wessels (1972), but that the parameterisations have a tendency to underestimate the number of large drops. Schönhuber et al. (2000) measured raindrop spectra of a few storm events in a moderate climate with a two-dimensional video-disdrometer. These few measurements revealed a considerable number of large drops up to 8 mm (more than one expects from the Marshall and Palmer (1948) spectra) and seem to support our suggestion that the number of large drops is underestimated by relations like those of Marshall and Palmer (1948) and Best (1950).

5.3 Driving rain models

In the present section, the measurements of wind speed, wind direction, horizontal rain and driving rain are used to develop a model which estimates (predicts) driving rain intensities on the façade with given reference wind speeds, wind directions and horizontal rain intensities. Four steps will be made: definition of the model (section 5.3.1), obtaining the parameter values by fitting to the measurement data (section 5.3.2), estimating the driving rain with the measured reference quantities and, finally, comparison of the driving rain estimates with the measured driving rain amounts (section 5.3.3). Two models based on the empirical model described in section 2.3.2 will be formulated.

5.3.1 Model definitions

Model 1. The first model is a very traditional model, based on Lacy (1965), which is similar to the approach implemented in the British Standard 8401 (BSI 1992). In section 2.3.2 we mentioned equations 2.29 and 2.35, which can be put together as:

$$R_{\mathrm{f}} = \kappa\, \alpha\, R_{\mathrm{h}}^{\beta}\, U_{\mathrm{r}}, \tag{5.3}$$

where the obstruction factor κ is meant to account for the position on the façade, the building geometry and the building environment. The parameters α and β are fixed to their values given by Lacy (1965), i.e. 0.22 and 0.88, respectively (see also eq. 2.33). For R_{h} we will use $R_{\mathrm{h,c,P2}}$.

U_{r} is defined as the wind velocity component perpendicular to the façade at roof height in the undisturbed approaching flow. In the case of the Main Building of the TUE, U_{r} equals $-U_y$, measured on the mast on the Auditorium. Note that only negative U_y will be taken into account, i.e. when the wind is blowing towards the façade. See the y axis definition in figures 2.4 and 3.4.

The obstruction factor κ is obtained by division of the total sum of measured driving rain amounts by the total sum of 5-min products of $\alpha(-U_{\mathrm{y}})R_{\mathrm{h,c,P2}}^{\beta}$. The total sums relate to total measurement period of 24 months, or to a year.

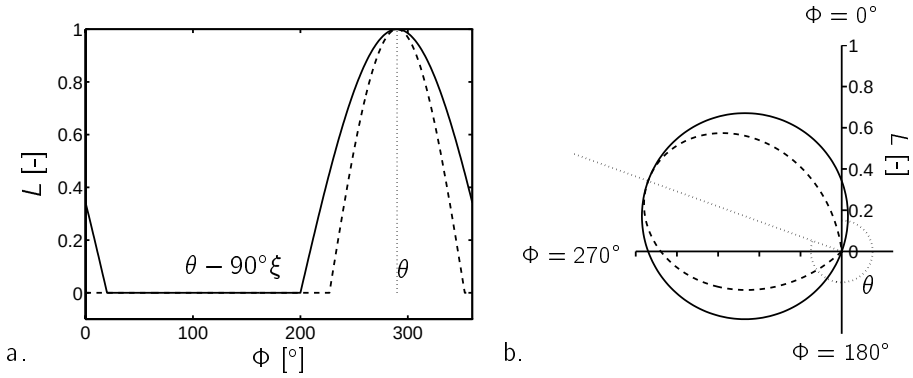

Figure 5.23: Function $L(\Phi, \theta, \xi)$. Figure a depicts the function L as a function of angle Φ for a given θ and two given values of ξ (1, ——, and 0.7, - - - -). Figure b gives a polar representation of figure a, where L is the radius from the origin and Φ is the angle in clockwise direction (cf. the axis definition in figures 2.4 and 3.4).

Model 2. The second model is basically similar to the first model. It also comprises horizontal rain intensity and wind speed, but wind direction is now a distinct variable. Moreover, the values of the parameters will be obtained by fitting the 5-min data points. The formula is:

$$R_{\mathrm{f}} = \alpha \, R_{\mathrm{h}}^{\beta} \, U_{\mathrm{h}}^{\gamma} \, L(\Phi, \theta, \xi), \tag{5.4}$$

where α, β and γ are empirical parameters, and θ (in degrees) and ξ are empirical parameters related to the function L, defined and explained in the next two paragraphs.

The function $L(\Phi, \theta, \xi)$ is defined as $\cos((\Phi - \theta)/\xi)$ for $-90°\xi \leq \Phi - \theta \leq 90°\xi$ and as 0 for the other values of Φ. The values of L range from 0 to 1 inclusive and the values of ξ are restricted from 0 to 1, see figure 5.23a. The polar diagram of the function L yields a lobe-like curve (figure 5.23b). The angle θ determines the angle of the axis of the lobe; the factor ξ determines its width. When eq. 5.4 is fitted to the data, the angle θ will roughly correspond to the normal of the façade. Note that $-U_{\mathrm{y}} = U_{\mathrm{h}} L(\Phi, 270°, 1)$, and therefore formula 5.3 of model 1 is a special case of formula 5.4 of model 2 with $\gamma = 1$, $\theta = 270°$ and $\xi = 1$. An advantage of model 2 is that θ follows automatically from the fitting of the data, and the a priori setting of θ (as in model 1) is not necessary.

Now the form of the function L is given, we can explain its meaning in equation 5.4. Both α and L are meant to account for the position on the façade. On a particular position on the façade, driving rain can only come from a particular range of wind directions. Within this range the driving rain intensity will not be equal for every direction (e.g. the driving rain intensity will go towards zero when the wind blows more and more parallel to the façade). At a particular wind direction (i.e. at $\theta°$) the driving rain intensity is maximal. In a horizontal plane, one can therefore assume a function like $L(\Phi, \theta, \xi)$. Therefore, this function is intended to describe differences in driving rain intensities on a horizontal

Table 5.8: Parameter values of model 1, obtained from the measured data (see eq. 5.3).

position P4/5

period	κ	r^2
1997-12-01 → 1999-11-31	0.097	0.47
1997-12-01 → 1998-11-31	0.109	0.49
1998-12-01 → 1999-11-31	0.078	0.60

position P6

period	κ	r^2
1998-03-02 → 1999-11-31	0.147	0.53
1998-03-02 → 1998-11-31	0.155	0.50
1998-12-01 → 1999-11-31	0.136	0.67

line on the façade. Differences depending on the height on the façade can be described in a similar way, but in that case the function L has a three-dimensional form. We will only consider the two-dimensional form for the horizontal plane, because we only have two measurement positions, which are on the same height on the west façade of the Main Building (P4/5 and P6). Our approach was inspired by Snape and Atkinson (1999) who drew lobe-shaped diagrams indicating the amount of driving rain on a building face as a function of wind direction. Moreover, in section 5.2.6 we observed from our measurements that wind direction is an important factor for the ratio of driving rain intensities on two façade positions.

The difference between models 1 and 2 is not only the applied formulae, but also the manner of obtaining the parameter values. Unlike model 1, the values of the parameters of model 2 are obtained by fitting 5-min data of reference wind speed (U_{h}), reference wind direction (Φ), reference horizontal rain intensity ($R_{\mathrm{h,c,P2}}$) and driving rain intensity ($R_{\mathrm{f,P4/5}}$ and $R_{\mathrm{f,P6}}$).

5.3.2 Parameterisation

Tables 5.8 and 5.9 list the values of the parameters of model 1 and 2, respectively. The parameter values are listed for three time 'blocks', namely the whole 24-month period (December 1997 to November 1999), the first 12-month period (December 1997 to November 1998) and the second 12-month period (December 1998 to November 1999). For position P6 the time blocks start at 2-3-1998 instead of 1-12-1997. An additional data selection criterion is $R_{\mathrm{h,c,P2}} > 0.5$ mm h^{-1}.

The parameter values of model 1 corresponding to the 24-month block are the average of those corresponding to the first and second 12-month blocks (table 5.8). For model 1,

Table 5.9: Parameter values of model 2 and their 95% confidence intervals, obtained from fits to the measured data (see eq. 5.4).

position P4/5

period	α [$\times 10^{-2}$]	β	γ	θ [°]	ξ	r^2
1997-12-01	0.683	1.31	1.39	266	0.79	0.82
→ 1999-11-31	0.608–0.759	1.29–1.33	1.34–1.44	265–268	0.77–0.81	
1997-12-01	1.49	1.38	0.93	265	0.81	0.84
→ 1998-11-31	1.29–1.69	1.36–1.41	0.87–0.98	263–266	0.78–0.84	
1998-12-01	0.351	1.20	1.75	266	0.85	0.84
→ 1999-11-31	0.298–0.405	1.17–1.22	1.69–1.82	264–267	0.82–0.87	

position P6

period	α [$\times 10^{-2}$]	β	γ	θ [°]	ξ	r^2
1998-03-02	6.56	1.00	0.78	281	0.87	0.62
→ 1999-11-31	5.69–7.43	0.97–1.02	0.71–0.84	279–284	0.84–0.91	
1998-03-02	14.2	0.98	0.46	281	0.75	0.61
→ 1998-11-31	11.6–16.7	0.95–1.02	0.37–0.55	278–283	0.71–0.79	
1998-12-01	0.915	1.15	1.62	284	0.92	0.85
→ 1999-11-31	0.794–1.036	1.13–1.17	1.57–1.68	282–286	0.89–0.95	

Table 5.10: Parameter values of model 2 and their 95% confidence intervals, obtained from fits to the measured data (see eq. 5.4) with predefined, fixed values for β, γ and ξ. Cf. table 5.9.

position P4/5

period	α [$\times 10^{-2}$]	β	γ	θ [°]	ξ	r^2
1997-12-01	0.679	1.30	1.40	269	0.85	0.82
→ 1999-11-31	0.669–0.689			268–270		
1997-12-01	0.704	1.30	1.40	267	0.85	0.83
→ 1998-11-31	0.691–0.717			265–269		
1998-12-01	0.530	1.30	1.40	266	0.85	0.82
→ 1999-11-31	0.516–0.544			265–267		

position P6

period	α [$\times 10^{-2}$]	β	γ	θ [°]	ξ	r^2
1998-03-02	1.79	1.00	1.40	281	0.85	0.58
→ 1999-11-31	1.74–1.84			279–283		
1998-03-02	1.79	1.00	1.40	286	0.85	0.52
→ 1998-11-31	1.70–1.87			283–289		
1998-12-01	1.94	1.00	1.40	278	0.85	0.82
→ 1999-11-31	1.89–1.98			277–279		

this is obvious because the parameter κ is calculated from a division of the total sum of driving rain amounts by the total sum of $\alpha(-U_y)R^{\beta}_{h,c,P2}$. The ratio between $\kappa_{P4/5}$ and κ_{P6} is approximately 1.5 and resembles the average ratio $R_{f,P6}/R_{f,P4/5}$ presented in sections 5.2.5 and 5.2.6. The qualities of the fits, expressed by the coefficient of determination r^2 in table 5.8, are not very good.

The parameter values of model 2 in table 5.9 were obtained from fitting (by a least-squares method) the measured data. The table also lists the 95% confidence intervals and the coefficients of determination. The values of the parameters α and γ of model 2 vary much between the 24-month block, the first 12-month block and the second 12-month block. The coefficient of determination for position P4/5 is good. Contrary to the second 12-month period, the coefficient of determination for position P6 is poor for the 24-month block and the first 12-month period. In order to relate the parameters of the two positions and to decrease the arbitrariness of the parameter values, we refitted the data with predefined, fixed values for some of the parameters. The results of this operation are tabulated in table 5.10. Only the parameters α and θ were kept free during the refitting, and the parameters β, γ and ξ had the fixed values of 1.30 (or 1.00 for P6), 1.40 and 0.85, respectively. The value of β was derived from the previous fit (table 5.9). We suggest that its value depends on the position on the façade: the more the position is near to the edge, the more it tends to 1. In section 6.4 (results of driving rain calculations with CFD) we will see that towards the edge the catch ratio $\eta(D)$ becomes more and more constant for varying drop diameters. Therefore the driving rain intensity will become proportional to the horizontal rain intensity, and therefore β goes to 1. The fixed value of γ (1.4) was taken from the average in table 5.9. We chose this value for γ of P6 too, because the second 12-month block for P6 yields a high value of γ (1.6) in combination with a high value of r^2 (0.85) in the previous fit, whereas the average of γ over the three blocks is about 0.95. The value of ξ varies very much in the previous fits (table 5.9), but it seems not so critical and we fixed it to an average value of 0.85. Altogether, we cannot be very certain about the actual values of the parameters now, because we have measured data of only two positions on one particular building.

In the previous section 5.3.1 we asserted that θ accounts for the influence of wind direction on driving rain. At position P4/5 the value of θ is approximately 268°. This is only 2° away from the normal of the façade (i.e. 270°). Position P4/5 is on the southern half of the west façade, and therefore θ is (should be) inclined to the south-west. The value of θ at position P6 is approximately 282°. In other words, θ at P6 is directed to the north-west because position P6 is at the northern half of the west façade.

Figure 5.24 shows how the parameterisation varies with the selected measurement data. The graphs are polar diagrams (as figure 5.23b) and depict 5-min driving rain intensities (R_f at P4/5 and P6) per wind direction (Φ). The measured data were selected for two horizontal rain intensity intervals and for a certain wind speed interval. In the graphs, the area between the two lobe-shaped solid curves represents all possible driving rain intensities calculated with equation 5.4 of model 2 and with the parameterisation cor-

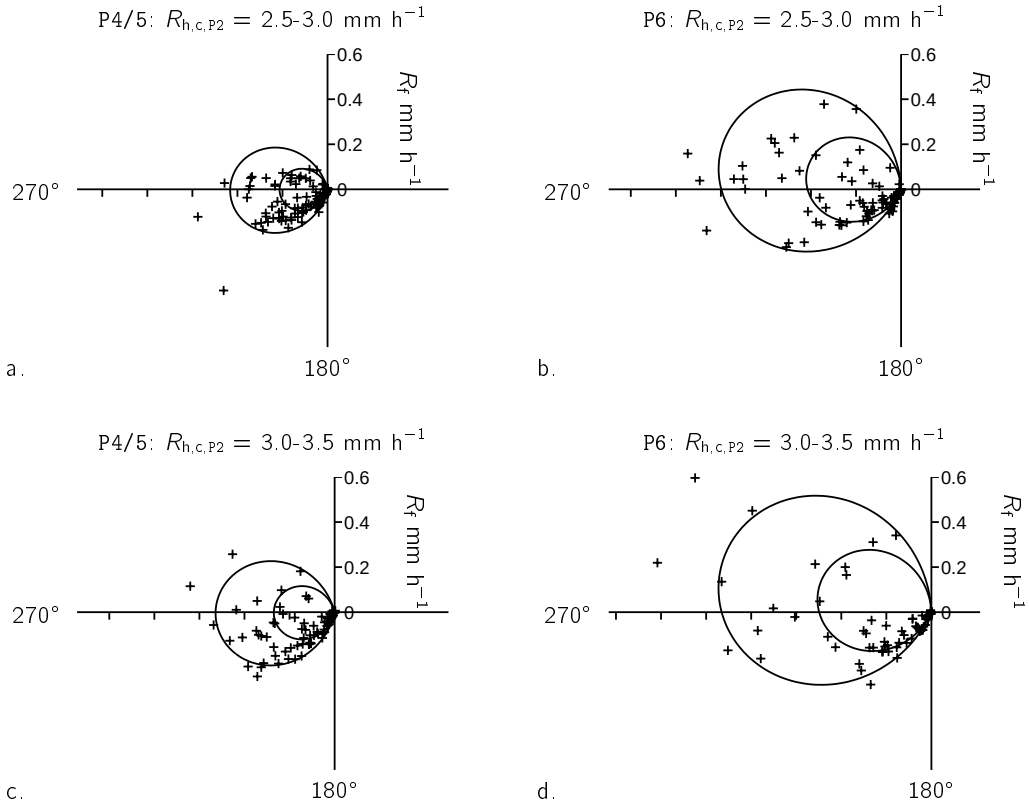

position	α [$\times 10^{-2}$]	β	γ	θ [°]	ξ
P4/5	0.7	1.3	1.4	269	0.85
P6	1.8	1.0	1.4	281	0.85

Figure 5.24: Driving rain intensities R_f as a function of wind direction Φ plotted in a polar diagram, for two selected horizontal rain intensities (figures a&b versus c&d) and selected wind speeds (U_h = 5.0-7.0 m s^{-1}). Figures a&c relate to position P4/5 and figures b&d to P6. The origin of the plot corresponds with $R_f = 0$; Φ and θ rotate clockwise from the north (north is upwards in the graphs). The measurements are indicated by + and are based on 5-min data from 1-12-1997 to 30-11-1999. The boundaries of the corresponding fits (model 2) are indicated by ——; the applied parameter values are tabulated below the graphs.

responding to the 24-month block for the given horizontal rain intensity intervals and a wind speed interval (table 5.10). The figure shows that most of the data points of the measured driving rain intensity fall within the larger lobe. Many measured data points, however, fall also within the smaller lobe, which should ideally contain no data. Despite of this, the measurement points do not seem to form a circle (i.e. $\xi = 1$), and the obtained lobe-like shape ($\xi \approx 0.8...0.9$) seems to fit better. Moreover, the difference between the two positions P4/5 and P6, i.e. the sizes of the outer lobe comprising the measurement points, is quite well described by the model.

5.3.3 Estimations and measurements

Estimates of 5-min driving rain intensities according to model 1 are calculated with equation 5.3, the parameter values of table 5.8 and the 5-min measurements of wind speed, wind direction and horizontal rain intensity. The estimates according to model 2 are calculated with eq. 5.4, the parameter values of table 5.10 and the same measurement data.

To compare the driving rain amounts estimated from the two models with the actually measured driving rain amounts, three representations will be considered:

- monthly driving rain amounts,
- histogram of the difference between measured and estimated 5-min driving rain intensities, and
- a list of the ten highest 5-min driving rain intensities.

The first representation is useful for a general comparison between the estimated and measured results. The histogram of differences and the list of the ten highest 5-min driving rain intensities give more detailed information.

Figure 5.25a shows the monthly estimated and measured driving rain amounts at position P4/5, cumulatively over time. The models obviously tend to overestimate the real driving rain amount. The three parameterisations of model 2 yield more accurate results than the three parameterisations of model 1. At the end of the 24-month period, the total driving rain amount estimated by model 1 deviates 29, 46 and 4%, respectively, from the measured total. The deviation of the results of model 2 is 17, 23 and 6%, respectively. Only one of the parameterisations yields a (slight) underestimation (-6%). This is the parameterisation of the second 12-month period of model 2, in which α is lower than the other values of α (table 5.10) and in which r^2 is better.

The measured and estimated cumulative driving rain amounts at position P6 are depicted in figure 5.25b. Here, the deviation of model 1 is 27, 34 and 17%, respectively. Model

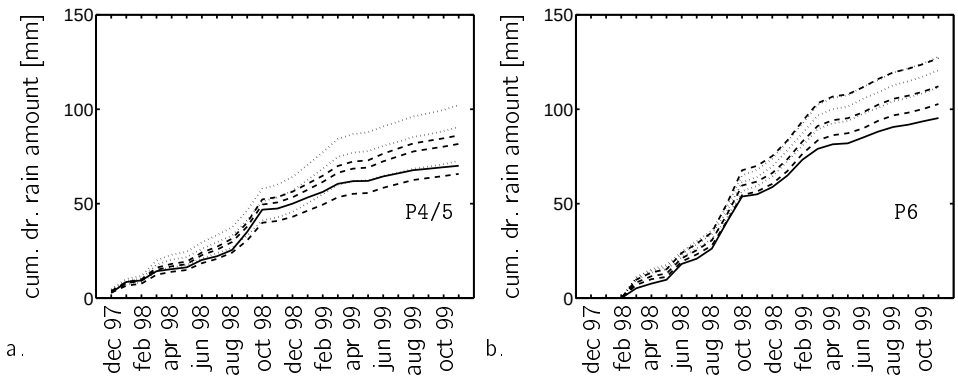

Figure 5.25: Cumulative driving rain amounts at P4/5 (figure a) and P6 (figure b), according to the measurements (——), model 1 (.....) and model 2 (----). Each model is represented by 3 curves according to the 3 parameterisations listed in tables 5.8 and 5.10. Based on 5-min measured data from 1-12-1997 to 30-11-1999.

2 yields deviations of 18, 8 and 33%, respectively. So, the estimates of model 1 at P6 tend to deviate generally more from the measurements than those of model 2.

Histograms of differences between measured and estimated 5-min driving rain intensities ($R_{\mathrm{f,m}}$ and $R_{\mathrm{f,e}}$ respectively) are shown in figure 5.26. Only clock periods with non-zero horizontal rain intensities ($R_{\mathrm{h,c,P2}}$) are taken into account. In other words, the histogram indicates the percentage of clock periods with rain with a particular absolute difference between $R_{\mathrm{f,m}}$ and $R_{\mathrm{f,e}}$. From figure 5.26, we conclude that the estimates of model 2 for the two positions P4/5 and P6 are closer to the measurements than the estimates of model 1. Apart from this, the estimates for position P4/5 are closer to the measurements than the estimates for position P6. Approximately 75% (55%) of the driving rain intensities at P4/5 estimated with model 2 (model 1) differ less 0.02 mm h^{-1} from the measurements. At position P6, the percentage is about 60% for model 2 (and about 50% for model 1).

Tables 5.11 and 5.12 list the ten highest measurements of 5-min driving rain intensities at P4/5 and P6, respectively, with the corresponding estimates from model 1 and model 2. The rank (« 1 » means « the highest ») and the number of occurrence of an actual value are also indicated. To avoid many ranking levels, the quantities were rounded to a tenth. If the number of occurrence of a particular value is more than one, this means that the same value occurred several times. Table 5.11 shows that the highest driving rain intensity measured at P4/5 was 29.3 mm h^{-1} on 28-10-1998 at 10h30–10h35. The estimates according to model 2 for the same clock period are 23–29 mm h^{-1}, which is a good result. The corresponding estimates of model 1 are very much lower, namely 5–8 mm h^{-1}, and this model did not predict any higher values at all ! An other good result

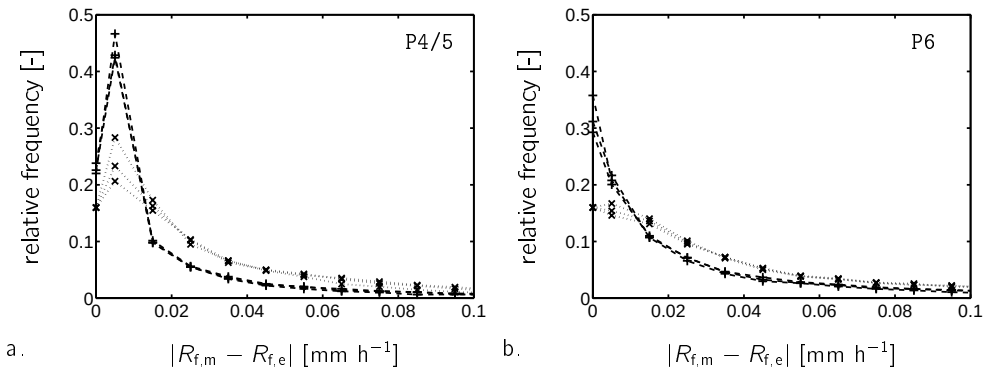

Figure 5.26: Histogram of the differences between measured 5-min driving rain intensities ($R_{f,m}$) and estimated 5-min driving rain intensities ($R_{f,e}$), for the two positions P4/5 (fig. a) and P6 (fig. b). Each model (model 1: ....., model 2: ----) is represented by 3 curves according to the 3 parameterisations listed in tables 5.8 and 5.10. Based on 5-min measured data of 1-12-1997 to 30-11-1999. Only clock periods with non-zero horizontal rain intensity are taken into account.

of model 2 is the fact that the 5 highest estimates of driving rain intensities (7.2–28.7 mm h^{-1}) fall within the range of driving rain intensities of the 7 highest measurements (7.2–29.3 mm h^{-1}).

Table 5.12 shows that the highest 5-min driving rain intensity measured at P6 was 24.9 mm h^{-1} on 29-10-1998 at 05h15–05h20. None of the corresponding estimates comes close to this value. Unfortunately, a rank of 1 is not present in the table for any of the estimates. An inspection of all results reveals that the overall highest estimated driving rain intensities are 10.5, 11.1, and 9.7 (model 1), 23.1, 22.3 and 25.4 (model 2). The estimates of model 1 are unsatisfactory; the highest estimated values of model 1 are only half of the highest measured value and the second highest estimated values (i.e. rank=2) are even below the 10th highest measured value. The results of model 2 are obviously better.

Altogether, from the comparison between the measured and estimated driving rain intensities it follows that model 2 gives more realistic results than model 1. Model 2 yields realistic data with respect to both cumulative driving rain amounts and 5-min driving rain intensities (see the histograms of driving rain intensity differences and the list of the ten highest intensity values). The estimated cumulative driving rain amounts after 24 months according to model 1 deviate 4–46% from the measurements at P4/5 and 17–34% at P6. The respective figures for model 2 are 6–23% at P4/5 and 8–33% at P6. Model 1 gives similar results with respect to cumulative driving rain amounts as model 2, but performs clearly worse in estimating actual 5-min driving rain intensities.

Table 5.11: The ten highest 5-min driving rain intensities at P4/5, according to the measurements (« meas. »), together with the corresponding estimates from model 1 and model 2. The entries « m. n/m » stand for model n with the parameterisation listed in the mth line of table 5.8 or 5.10. The rank and the number of occurrence (#) of the actual values are also indicated. The indicated dates (and times) give the start of the 5-min clock periods. The unit of the driving rain intensity is mm h^{-1}. Based on 5-min measured data of 1-12-1997 to 30-11-1999.

meas.	29.3	17.8	15.7	13.0	10.5	9.6	7.2	6.7	6.0	5.0
rank	1	2	3	4	5	6	7	8	9	10
#	1	1	1	1	1	1	1	2	1	1
m. 1/1	6.9	0.7	4.0	3.4	3.5	3.8	3.3	2.1	1.9	1.5
rank	1	22	2	5	4	3	6	8	10	14
#	1	41	1	1	1	1	1	1	3	6
m. 1/2	7.8	0.8	4.6	3.9	3.9	4.3	3.7	2.4	2.1	1.7
rank	1	23	2	4	4	3	5	7	10	14
#	1	38	1	2	2	1	1	1	3	5
m. 1/3	5.6	0.6	3.2	2.8	2.8	3.1	2.7	1.7	1.5	1.2
rank	1	18	2	4	4	3	5	7	9	12
#	1	47	1	2	2	1	1	1	3	8
m. 2/1	28.5	1.2	13.0	10.7	10.9	12.1	10.2	4.7	4.5	3.2
rank	1	38	2	5	4	3	6	10	11	19
#	1	12	1	1	1	1	1	2	1	2
m. 2/2	29.3	1.3	13.3	11.1	11.3	12.5	11.2	5.5	4.9	3.3
rank	1	38	2	6	4	3	5	7	10	22
#	1	8	1	1	1	1	1	1	1	3
m. 2/3	22.2	1.0	10.0	8.4	8.6	9.5	8.7	4.3	3.8	2.4
rank	1	34	2	6	5	3	4	7	9	21
#	1	14	1	1	1	1	1	1	2	3
year	1998	1998	1998	1998	1998	1998	1999	1998	1999	1998
month	10	1	10	9	8	6	6	1	8	8
day	28	7	29	9	26	2	3	3	18	21
hour	10	14	5	16	14	15	21	15	11	14
minute	30	0	15	55	35	55	55	25	20	0

Table 5.12: The ten highest 5-min driving rain intensities at P6, according to the measurements («meas.»), together with the corresponding estimates from model 1 and model 2. See the further explanation at table 5.11.

meas.	24.9	17.5	16.5	12.6	9.9	9.6	9.3	8.6	8.5	8.2
rank	1	2	3	4	5	6	7	8	9	10
#	1	1	1	1	1	1	1	1	1	1
m. 1/1	6.1	5.2	5.8	3.3	5.2	2.5	3.0	5.0	2.6	2.3
rank	2	4	3	6	4	14	9	5	13	16
#	1	2	1	1	2	3	1	1	2	5
m. 1/2	6.5	5.5	6.2	3.5	5.5	2.6	3.2	5.3	2.8	2.5
rank	2	4	3	6	4	14	8	5	12	15
#	1	2	1	1	2	3	1	1	1	2
m. 1/3	5.7	4.8	5.4	3.1	4.8	2.3	2.8	4.6	2.4	2.1
rank	2	4	3	6	4	13	8	5	12	15
#	1	2	1	1	2	2	2	1	3	4
m. 2/1	12.5	8.5	11.1	6.0	8.1	4.3	5.6	5.0	4.7	3.7
rank	2	4	3	6	5	11	7	8	10	16
#	1	1	1	1	1	1	2	2	1	1
m. 2/2	12.3	8.0	10.6	6.0	7.5	4.3	5.7	3.5	4.6	3.8
rank	2	4	3	6	5	12	7	17	11	16
#	1	1	1	1	1	1	1	1	2	2
m. 2/3	13.6	9.5	12.3	6.5	9.1	4.6	5.9	6.3	5.1	4.0
rank	2	4	3	6	5	14	9	7	13	19
#	1	1	1	1	1	1	1	1	1	3
year	1998	1998	1998	1998	1998	1998	1998	1999	1998	1998
month	10	9	6	10	8	8	8	6	10	8
day	29	9	2	28	26	22	24	3	29	21
hour	5	16	15	10	14	14	1	21	5	14
minute	15	55	55	25	35	50	40	55	20	0

An explanation of the latter observation may be the higher degree of turbulence at the building corner close to P6, and therefore the driving rain intensity may be more sensitive to changes in wind speed, wind direction and horizontal rain intensity than the applied models can cope with. In section 5.2.6 we already observed that the driving rain intensity correlation between the two positions is quite complicated.

5.4 Summary

In section 1.1, a general two-step approach was introduced for the translation of weather station data to driving rain data on a building envelope. Figure 1.1 depicts this approach. In the present chapter, parts of the steps were reported:

- weather station → site:
  - the correlation between the hourly wind speed at the weather station of Eindhoven Airport ($U_{\mathrm{h,EA}}$) and at the TUE site ($U_{\mathrm{h,P1}}$) seems to be quite independent of the wind direction in the range 180°–360°, namely $U_{\mathrm{h,P1}} = 0.90 U_{\mathrm{h,EA}}$,
  - the monthly horizontal rain amounts at the weather station and at the TUE site are in good agreement, see table 5.2 and figure 5.5,
- site:
  - the spatial variation of the wind speed and direction at the site was not investigated,
  - the spatial variation of the horizontal rain amounts was investigated with the two rain gauges on the roof of the Auditorium. The measured 5-min rain intensities of the two gauges differ less than 10% (30%) for approximately 52% (83%) of the total collected rain amount,
  - raindrop spectra were measured by our disdrometer during approximately three months. The measured spectra vary much over time. Generally, the measured median drop size is between the two median drop sizes calculated from the parameterisations of Wessels (1972) with $A = 0.88$ and $A = 1.77$, respectively, which encompass 90% of his measurements in the Netherlands,
- site → building:
  - driving rain intensities vary much at a façade position and on a small time-scale (5 min), even for narrow ranges of reference wind speed, wind direction and horizontal rain intensity (see e.g. figure 5.14 and section 5.2.5). Moreover, the correlation between the two measurement positions P4/5 and P6 is very complex and depends to a great degree on wind direction (section 5.2.6),

- two empirical models, yet to some extent similar, were formulated to describe the driving rain intensity as a function of wind speed, wind direction and horizontal rain intensity (section 5.3). The same measurement data set was used for parameterisation as well as for checking the driving rain estimates from the models with the driving rain measurements. Model 1, based on the simple empirical formula 5.3 according to Lacy (1965), yields less realistic estimates of (especially maxima of) 5-min driving rain intensities than model 2, which is our improvement by taking wind direction and position on the façade more explicitly into account (eq. 5.4). However, the models overestimate the cumulative driving rain amounts after 24 months by up to 35–45%,
- the influence of the raindrop spectrum on driving rain quantities was not investigated.

Chapter 6

CFD simulations

The CFD calculations of wind and rain are described in this chapter. A literature survey on CFD simulations was already reported in section 1.3. In this chapter we first describe the applied models for the CFD calculations of wind and raindrop trajectories (sections 6.1 and 6.2 respectively). The Main Building and its direct surroundings are implemented in the model. Subsequently, wind simulations are carried out for several reference wind speeds and wind directions. Finally, driving rain intensities on the west façade of the Main Building are calculated from the wind simulation results and the raindrop spectra obtained from literature and our measurements. The results are presented in sections 6.3 (wind) and 6.4 (driving rain). The results of the calculations are compared to the full-scale measurements.

The main goal of the chapter is an investigation of the suitability of CFD for driving rain calculations, and especially of the aspects which should be dealt with to obtain reliable results.

6.1 Wind calculation method

Numerical simulations of the wind around the Main Building were performed by the commercially available CFD package *Fluent*. We used versions 4.4 and 4.5 and the differences between these two versions are not relevant for our purpose. The used turbulence model is a standard K-ϵ model (Fluent 1995, or see e.g. Launder and Spalding 1974 and Rodi 1980).

Model constants The applied values for the K-ϵ model constants are: $C_\mu = 0.032$, $C_{1\epsilon} = 1.44$, $C_{2\epsilon} = 1.92$, $\sigma_k = 1$ and $\sigma_\epsilon = 1.3$. Except for C_μ, the standard values of the

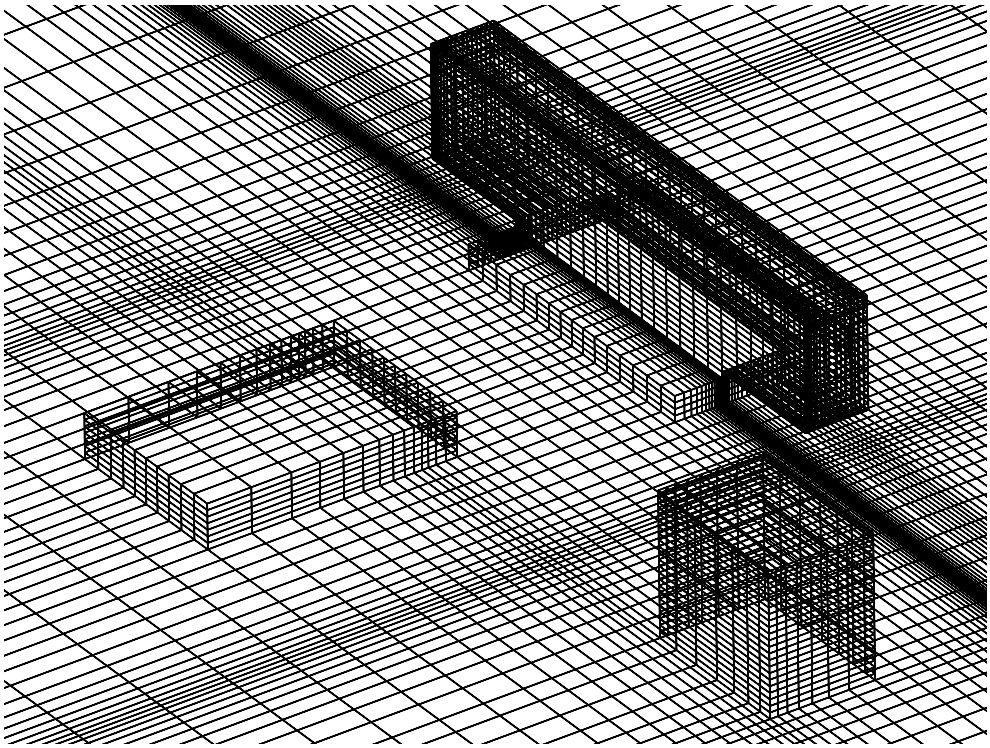

Figure 6.1: Computational grid. View from south-west. From left to right: the Auditorium, the Main Building and Building T.

K-ϵ model have been applied (the model and the constants are described in Launder and Spalding 1974). The C_μ constant was adapted according to the findings of Bottema (1993b), who also compared the results of his simulations favourably with wind tunnel measurements.

Grid The applied grid is a so-called structured grid. The size of the three-dimensional computational domain was determined by the rules of thumb given by Bottema (1993a) and based on general estimates of the influence zone in which wind speeds deviate by more than 10% due to the presence of the building. The reader is also referred to section 2.1.4. For the description of this zone the dimension $\mathcal{L}_g$, i.e. the smaller of $2\mathcal{H}$ and $\mathcal{W}$, is used. The upstream influence zone is about $5\mathcal{L}_g$ and its downstream counterpart extends to $16\mathcal{L}_g$. The influence zone in lateral and vertical directions extends to $2\mathcal{L}_g$. The boundaries of the computational domain should be outside the influence zone, although for the downstream influence zone one may make an exception and put the boundary at only $8\mathcal{L}_g$ (Bottema 1993a).

As $\mathcal{L}_g$ is 90 m (=$2\mathcal{H}$) in our case, the computational domain should be about $(5+8)\mathcal{L}_g$ (=1170 m) long along the wind direction. To be able to simulate wind flow around the Main Building at oblique angles, the chosen computational domain is rectangular with the Main Building situated in the south-west corner, at $\sim 5\mathcal{L}_g$ from the south and the west domain boundaries.

The actual three-dimensional computational domain is 1190 m long in east-west direction, 1477 m long in north-south direction and 225 m high. It consists of 95, 96 and 47 cells, respectively. Figure 6.1 shows the computational grid with the three buildings (Auditorium, Main Building and Building T) in it. Two variants of the shown configuration will be applied: with and without Building T. There are two reasons for this. Firstly, the influence of Building T on winds from south-west to south can be presented. Secondly, the grid without Building T is symmetric with respect to the east-west plane. This implies that winds from directions $270° - \theta$ and $270° + \theta$ (where θ is a value from 0° to 90°) can be studied using one simulation.

The grid cells become progressively smaller near building boundaries. The first grid cells on the façade of the Main Building have a thickness of 0.25 m. Care is taken to keep the grid expansion factor of two successive grid lines between 0.7 and 1.3. However, since the grid is structured, undesired large expansion factors and cell aspect ratios are inevitable in some parts of the grid.

Wind profile The profile of the wind entering the domain is described by:

$$u_{<20}(z) = \frac{u_{*,1}}{k} \ln\left(\frac{z}{z_{0,1}}\right) \quad \text{for } z < 20\text{m}, \tag{6.1}$$

and:

$$u_{\geq 20}(z) = \frac{u_*}{k} \ln\left(\frac{z-d}{z_0}\right) \quad \text{for } z \geq 20\text{m}, \tag{6.2}$$

with $u(z)$ = longitudinal wind velocity [m s^{-1}] at height z [m] above ground level, z_0 = roughness length [m] for $z > 20$ m, $z_{0,1}$ = roughness length [m] for $z < 20$ m, u_* = friction velocity [m s^{-1}], $u_{*,1}$ = friction velocity [m s^{-1}], resulting from the requirement that $u(z)$ is continuous at $z = 20$ m, k = von Kármán constant (0.4), and d = displacement height [m].

The applied values of $z_0 = 1.0$ m and $d = 10$ m were taken from results of measurements at the site by Geurts (1997). The division of the wind profile in two parts is necessary to account for the displacement height d of 10 m; otherwise, the wind profile below 10 m height would be undetermined. Moreover, the fetch consists of a park up to a distance of 400 m from the Main Building (therefore an estimated $z_{0,1}$ of 0.1 m) and buildings west from the park with a height of ~20 m. The choice of $z_{0,1}$ and the choice that the boundary between the two parts of the profile is at 20 m height, are relatively

arbitrary, but the simulation results are not very sensitive to the precise values of these parameters.

The friction velocity u_* is based on the wind speed U_{10} at Eindhoven Airport (~7.5 km westward from the Main Building, with $z = 10$ m, $z_0 = 0.03$ m and $d = 0$ m). See section 5.2.1 for a discussion on the measurements of $u(45)/U_{10}$.

Turbulent kinetic energy The profiles of the turbulent kinetic energy and its dissipation rate, for wind coming into the domain are described by:

$$K = \frac{u_*^2}{\sqrt{C_\mu}}, \tag{6.3}$$

and:

$$\epsilon = \frac{u_*^3}{kz}, \tag{6.4}$$

respectively, with K = turbulent kinetic energy per unit of mass [m^2 s^{-2}], and ϵ = energy dissipation rate [m^2 s^{-3}].

Terrain roughness In *Fluent* the roughness of surfaces is modelled by the following formula:

$$u(z) = \frac{u_*}{k} \ln\left(\frac{E u_* z}{\nu}\right) \tag{6.5}$$

where E is a roughness parameter [-] and ν is the kinematic viscosity [m^2 s^{-1}] of air.

The roughness parameter is empirically determined. Its value is 9.8 for a smooth wall. Equation 6.5 corresponds to the wind profile (eqs. 6.1 and 6.2) if:

$$E = \frac{\nu}{u_* z_{0,1}}. \tag{6.6}$$

Façade roughness Equations 6.5 and 6.6 are also applied to model the surface roughness of the building façades. As the façade consists of a smooth glass cladding, a value of 0.0005 m is assumed for its roughness length z_0,

Separation modelling Separation of the airflow at corners has been modelled by so-called « link-cuts » (i.e. a feature of *Fluent* by which the wall-function in a computational cell is disabled).

Chosen wind speeds and directions The following reference wind speeds and directions at the mast on the Auditorium were chosen for the wind calculations:

- U_h = 3.5, 5.7 and 11.2 m s^{-1},
- Φ = 210°, 240°, 270°, 300° and 330°.

Not every combination was simulated, see table 6.2 for the simulations which were actually performed. Recall that we use two geometrical models, namely with and without the inclusion of Building T, and because of symmetry, the simulations with $\Phi = 240°$ will be used to represent $\Phi = 300°$ too. The validity of these 'double simulations' will be discussed in section 6.3.

6.2 Driving rain calculation method

The calculations of the drop trajectories were performed with the same CFD package *Fluent* (versions 4.4 and 4.5). The trajectories were calculated after the wind flow calculation for a chosen geometry, reference wind speed and wind direction.

Drop trajectory The motion of a drop is modelled in *Fluent* with equation 2.10. In *Fluent*, the drag coefficient C_d as a function of the Reynolds number of Morsi and Alexander (1972) was implemented (figure 2.6).

The turbulent dispersion of drop trajectories is not easily modelled because the K-ϵ model does not provide detailed information on small scale eddies or fluctuating velocity

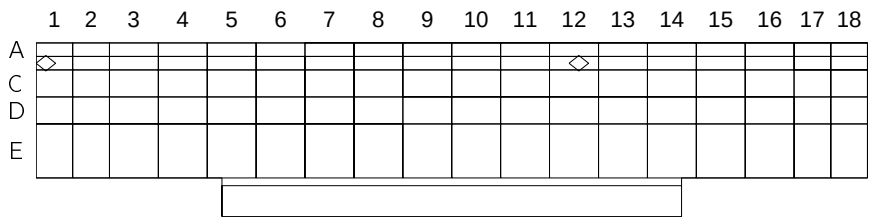

Figure 6.2: Façade sections on the west façade of the Main Building, with section numbering. The diamonds indicate the measurement positions of the full-scale experiment; position P6 is in façade section B1, and position P4/5 in B12. See also figure 3.6.

components. In *Fluent* it is possible to obtain the fluctuating velocity components by solving the Langevin equation, which results in filtered white noise. This is called the « continuous random walk » model (Fluent 1997). This model requires more computational effort (because the time steps are smaller during the integration of the particle trajectory equations) than the other model implemented in *Fluent*, the « random walk model », in which the fluctuating velocity components are random values which are kept constant over an interval of time given by the characteristic lifetime of eddies. An advantage of the continuous random walk model is that it can include the effects of crossing trajectories.

The Langevin equation of the continuous random walk model is the following (Fluent 1997):

$$du_i = \frac{-1}{T} u_i dt + \left(\frac{2\overline{u_i' u_i'}}{T} \right)^{\frac{1}{2}} dw, \tag{6.7}$$

with u_i = the wind velocity [m s^{-1}] along the coordinate axis i (= x, y or z), T = the so-called integral time [s], and w = a Gaussian distributed random number.

The integral time T is estimated by the assumption that it is equal to the Langrangian integral time T_L, which is proportional to K/ϵ. For the K-ϵ model, the Langrangian integral time is approximately $0.15K/\epsilon$ (Fluent 1997). The model in *Fluent* applies a correction of the integral time T to account for the effects of crossing trajectories, depending on the turbulent kinetic energy and the difference between wind and drop speeds (Fluent 1997):

$$\frac{T}{T_\mathrm{L}} = \frac{1}{\left(1 + 6\beta^2 \left(\overline{\vec{u} - \vec{u_\mathrm{D}}}\right)^2 / K\right)^{\frac{1}{2}}} \tag{6.8}$$

with β = a user-definable constant (default 0.5). The mean of $\vec{u} - \vec{u_\mathrm{D}}$ is obtained from averaging the instantaneous values over the period $3T_\mathrm{L}$.

In our calculations we will use two schemes: (1) the calculation of drop trajectories *without* turbulent dispersion, i.e. straightforward calculation according to eq. 2.10, and (2) the calculation *with* turbulent drop dispersion according to the continuous random walk model including trajectory crossing effects. The user-definable and other constants mentioned above are kept at their default values.

Grid The trajectory calculation has also implications for the computational grid: the dimensions of the grid cells in which drop trajectory deviations are expected to occur, should be smaller than the stopping distance of the smallest drop. This implies a maximum dimension of 0.5 m near the façade, i.e. the approximate stopping distance of 1 m for a 0.5 mm drop at 2 m s^{-1} (figure 2.8).

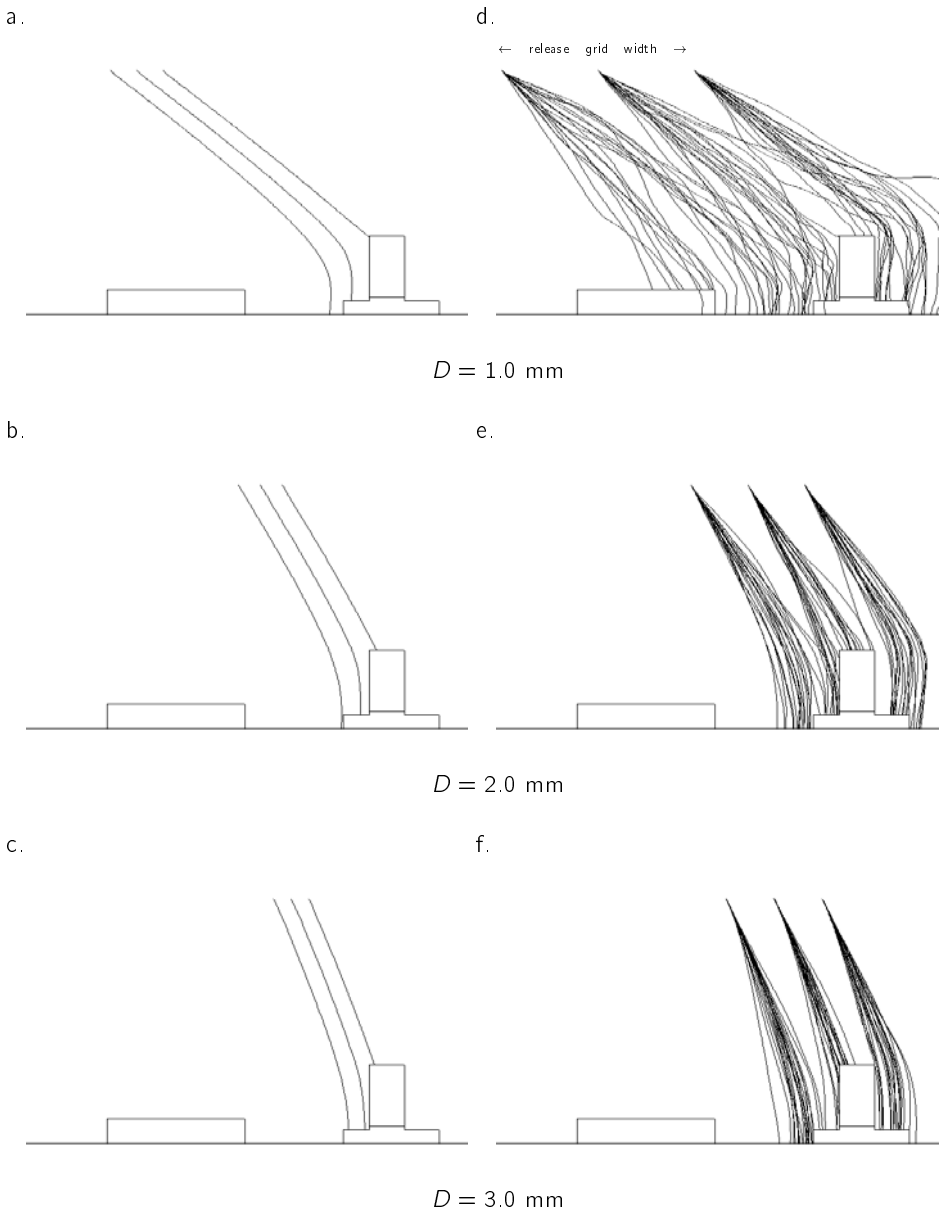

Figure 6.3: Simulated drop trajectories for $U_h = 3.5$ m s^{-1} and $\Phi = 270°$. In figures a–c, turbulent drop dispersion was *not* taken into account; in figures d–f it was included. Every graph shows the Auditorium (left) and Main Building (right), seen from the south.

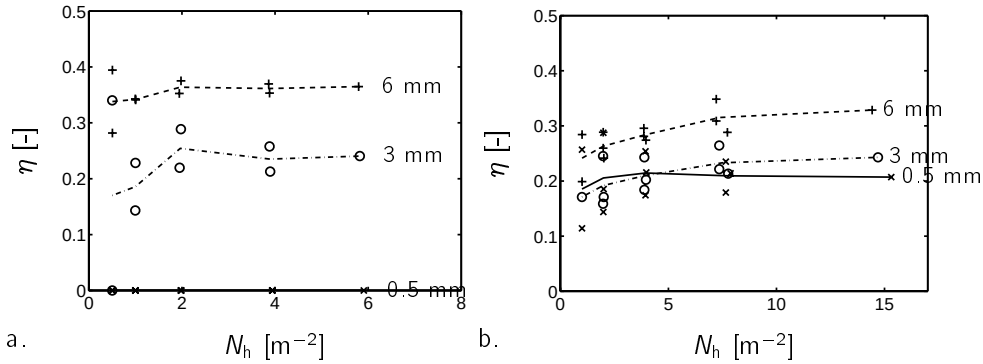

Figure 6.4: Catch ratio η as a function of N_h for three drop diameters (—— (average), ×: $D = 0.5$ mm; —·—·, ○: $D = 3$ mm; ----, +: $D = 6$ mm), at façade section B12 (see figure 6.2), $U_h = 5.7$ m s^{-1}, $\Phi = 270°$. Figure a and b results from simulations without and with turbulent drop dispersion, respectively.

Façade sections For the calculation of catch ratios $\eta(D)$, the façade is divided into smaller areas, which we call here « façade sections ». The applied division with a numbering scheme is shown in figure 6.2. The measurement positions for driving rain and wind are located at B1 (position P6) and B12 (P4/5).

Calculation of catch ratios $\eta(D)$ In a wind field calculated for a given geometry, wind speed and direction, raindrops with a chosen diameter are released from a 'release grid'. This grid forms a horizontal plane with a certain length and width, positioned such that the whole façade is covered with drops. The dimensions of the release grid are not determined automatically but interactively by trial. For the trajectory calculations with turbulent dispersion the release grid sizes were taken larger than strictly necessary. This means that drops from the extremities of the release grid are released at such a distance that they —with their dispersed trajectories— do not hit the building. The release grid is positioned at 2–3.5 times the Main Building height. Figure 6.3d shows an example of the width of a release grid for a simulation at a particular wind speed, wind direction and drop diameter, in which turbulent drop dispersion is included. The other graphs of figure 6.3 show example drop trajectories for the same wind speed and direction, but different drop diameters and with/without turbulent drop dispersion.

After the trajectory calculations, the catch ratio η for a particular raindrop diameter on a particular area on the façade (façade section) is computed by (cf. eq. 2.26):

$$\eta = \frac{N_f}{N_h}, \tag{6.9}$$

with N_f and N_h the number of drops per unit of area on a façade section and in the release grid, respectively.

Figure 6.4 shows an example of the calculated catch ratio η as a function of N_h for several raindrop diameters. The curves indicate an average of the respective data points, which were obtained by reducing the number of released drops by a factor of two. (More data points are available for lower N_h, because dividing a set of released drops in two sets (with half of the original N_h) leads to two new data points. This division should only be repeated a few times, of course.) By evaluating the convergence of η as a function of N_h, we determined the minimum number of drops to be released for a reliable $\eta(D)$.

The drop diameters for which drop trajectories are calculated, are $D = 0.5$, 1.0, 1.5, ... 6.0 mm. The calculated $\eta(D)$ functions for a particular façade area based on the mentioned series of drop diameters are smoothed by interpolation. The resulting smoothed $\eta(D)$ functions are used for further driving rain calculations. These will be presented in section 6.4.

Table 6.1 presents the number of released drops in a particular simulation. For the trajectory calculations without turbulent drop dispersion, a total of 25.8×10^5 drops were released; these calculations took 131 hours (~5.5 days) of CPU time on a Sun Entreprise Server with two 400 MHz UltraSparc-II processors, 1 Gbyte RAM and the Solaris 2.7 operating system (the CPU time was ~75% of the elapsed clock time). For the trajectory calculations *with* turbulent drop dispersion, the numbers were 68.3×10^5

Table 6.1: The number of drops released for a simulation with $U_h = 5.7$ m s^{-1}, $\Phi = 270°$.

	without turb. disp.		with turb. disp.	
D [mm]	number in release grid	N_h [m^{-2}]	number in release grid	N_h [m^{-2}]
0.5	5.4×10^5	5.9	1.4×10^6	15.3
1.0	4.8×10^5	5.9	1.3×10^6	15.3
1.5	3.1×10^5	5.9	8.1×10^5	15.1
2.0	1.9×10^5	5.8	5.1×10^5	14.8
2.5	1.9×10^5	5.8	5.1×10^5	14.8
3.0	1.6×10^5	5.8	4.2×10^5	14.7
3.5	1.5×10^5	5.8	3.9×10^5	14.6
4.0	1.2×10^5	5.8	3.1×10^5	14.5
4.5	1.2×10^5	5.8	3.1×10^5	14.5
5.0	1.2×10^5	5.8	3.1×10^5	14.5
5.5	1.0×10^5	5.8	2.8×10^5	14.4
6.0	1.0×10^5	5.8	2.8×10^5	14.4

Table 6.2: Wind calculations and raindrop trajectory calculations that were performed. « N.t.d. » stands for « no turbulent drop dispersion » and « w.t.d. » for « with turbulent drop dispersion ».

wind		Building T	drop trajectories	
Φ	U_h [m s^{-1}]	included	n.t.d.	w.t.d.
210° (330° ⋆)	3.5 m s^{-1}	–	–	–
210°	3.5 m s^{-1}	+	+	–
240° (300° ⋆)	3.5 m s^{-1}	–	+	+
	5.7 m s^{-1}	–	+	–
	11.2 m s^{-1}	–	+	–
240°	3.5 m s^{-1}	+	–	–
270°	3.5 m s^{-1}	–	+	+
	5.7 m s^{-1}	–	+	+
	11.2 m s^{-1}	–	+	–

⋆ Because of symmetry, the indicated simulation represents two wind directions. Note that $\Phi = 270°$ is wind blowing perpendicular to the west façade of the Main Building.

released drops and 414 hours of CPU time (∼17 days) respectively. Of course, the number of released drops and the time involved with the drop trajectory calculations depend on the reference wind speed and direction.

Raindrop spectra As we have a rather limited number of raindrop spectrum data measured with the disdrometer, we will use the parameterisation of raindrop spectra reported by Wessels (1972). He measured raindrop spectra at De Bilt (NL) during 1968 and 1969 and obtained a range of the parameter A of the Best spectrum formula (eq. 2.24). Ninety percent of his 533 observations had values of A ranging from 0.88 to 1.77 (with $a = 0.21$, $b = 2.25$, $C = 67$, and $q = 0.846$). We will apply these two values of A to calculate two 'extreme' raindrop spectra: one with relatively many small drops and one with relatively large drops.

Table 6.2 lists the simulations which were performed. Because of their long computation times, the number of drop trajectory simulations is rather small.

6.3 Results of wind calculations

In this section, the simulation results are evaluated in three ways: (a) by comparison of simulated wind velocities with full-scale measurements, (b) by comparison of mean pressure coefficients with full-scale and wind tunnel measurements, and (c) qualitatively.

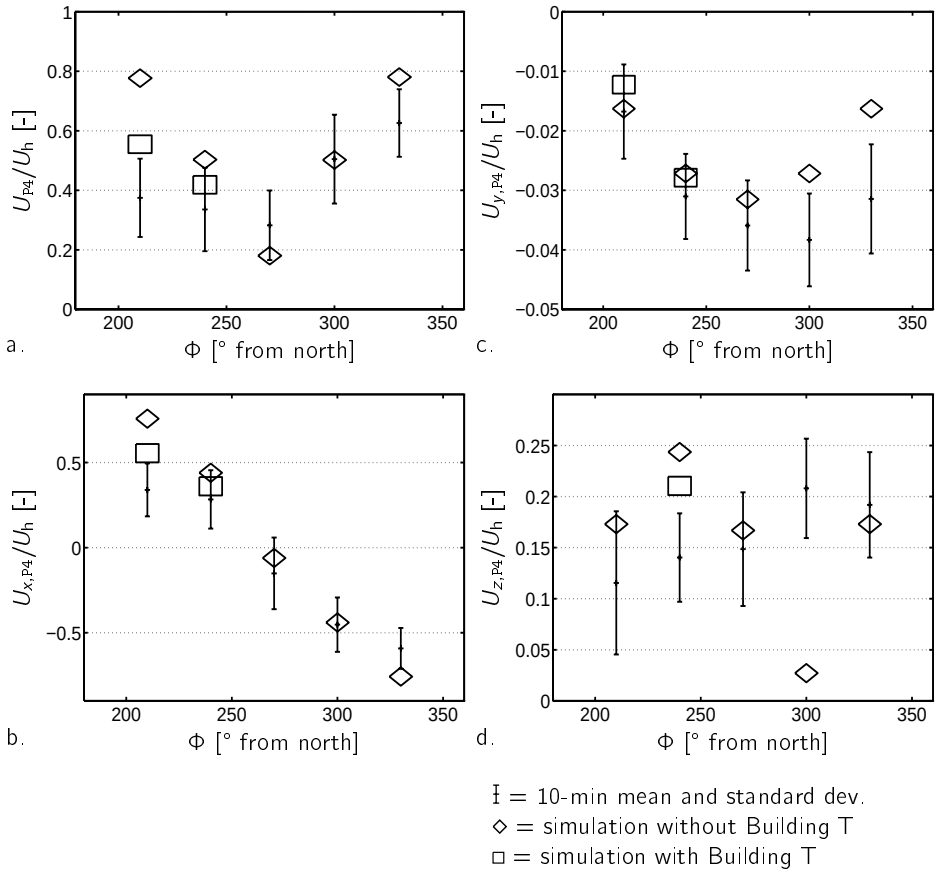

Figure 6.5: Measured and simulated wind velocities at 50 cm from the façade at position P4, normalised by the reference wind speed U_h, as function of the reference wind direction Φ. Figure a: the normalised wind speed U_{P4}. Figures b–d: the normalised velocity components $U_{x,P4}$, $U_{y,P4}$ and $U_{z,P4}$, respectively. Based on 10-min averages from 16-9-1998 to 14-9-1999.

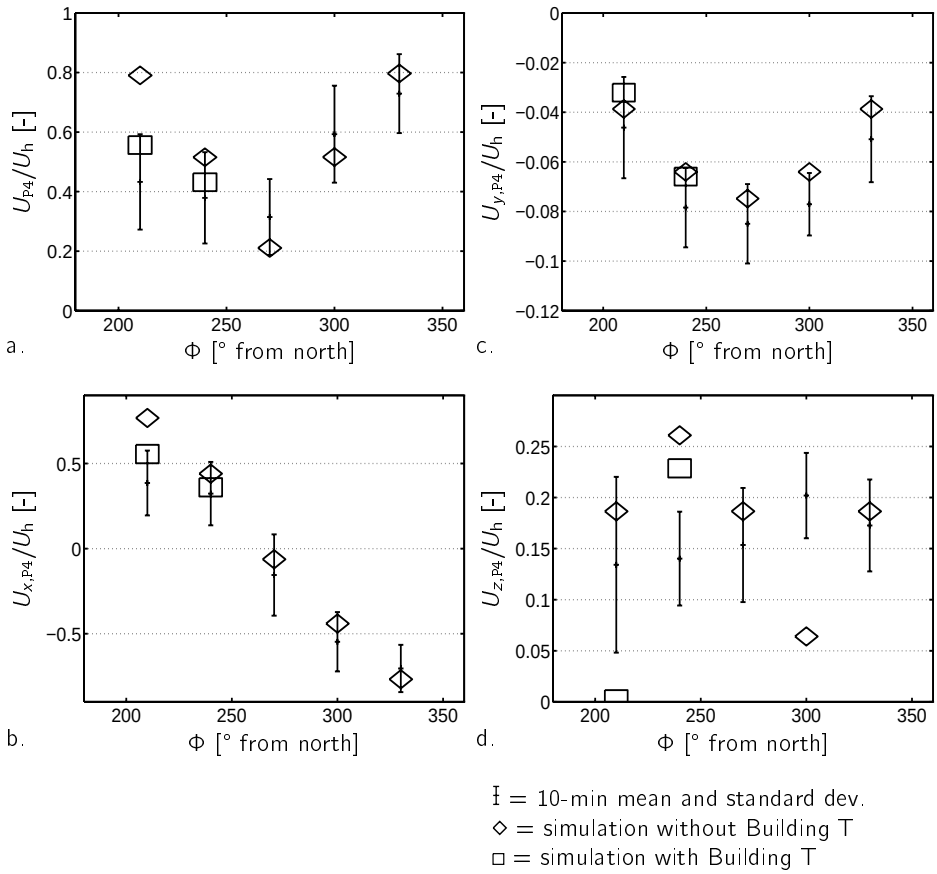

Figure 6.6: Similar to figure 6.5, but for wind speeds measured at 125 cm from the façade at position P4. Based on 10-min averages from 17-7-1998 to 16-9-1998 and from 14-9-1999 to 30-11-1999.

Normalised wind velocities Figure 6.5a shows the simulated and measured wind speeds at 50 cm from the façade at position P4, U_{P4}, normalised by the horizontal wind speed U_{h} at position P1.

The simulated wind speeds $U_{\mathrm{P4}}/U_{\mathrm{h}}$ (figure 6.5a) are (just) within the standard deviation of the measurements. The largest deviations are found at wind directions of less than 240°. This is due to the wake of Building T. Building T (figure 6.1) has the same height as the Main Building. When Building T is included in the computational domain, the results for $\Phi < 240°$ compare better with the measurements.

Figures 6.5b-d show the normalised velocity components at 50 cm from the façade at position P4. See figures 2.4, 3.4, 3.5 and 3.6 for the definition of the x-y-z axis system. The predictions from the simulations (with inclusion of Building T in the grid) for $U_{x,\mathrm{P4}}$ are within the standard deviation of the measurements. This does not apply for the vertical component $U_{z,\mathrm{P4}}$, which is the second most important contribution to the wind speed at P4. In this case, however, one should be careful interpreting the measured data: the ultrasonic anemometer at P4 is positioned vertically, and in this direction, the vertical wind is mostly obstructed by the housing of the anemometer.

Figure 6.6 is similar to figure 6.5, but with the P4 position wind speed measured at 125

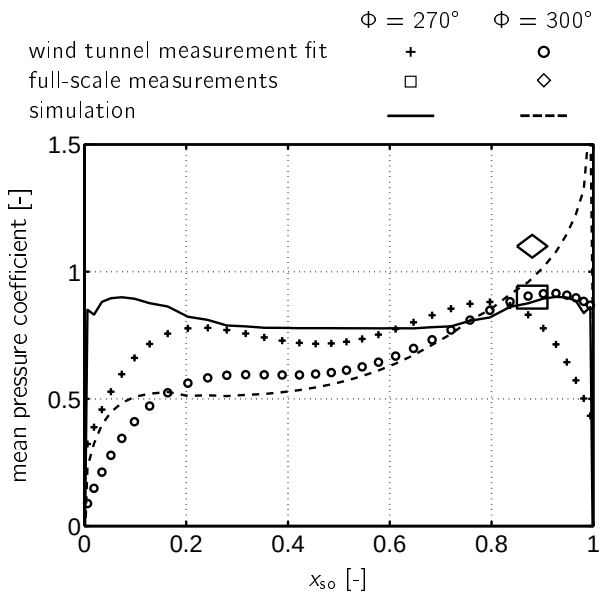

Figure 6.7: Measured (Geurts 1997) and simulated (current study) mean pressure coefficients as function of the position on the façade, at 72% of the building height. The north edge of the west façade is represented by the relative position $x_{\mathrm{so}} = 1$, the south edge by $x_{\mathrm{so}} = 0$.

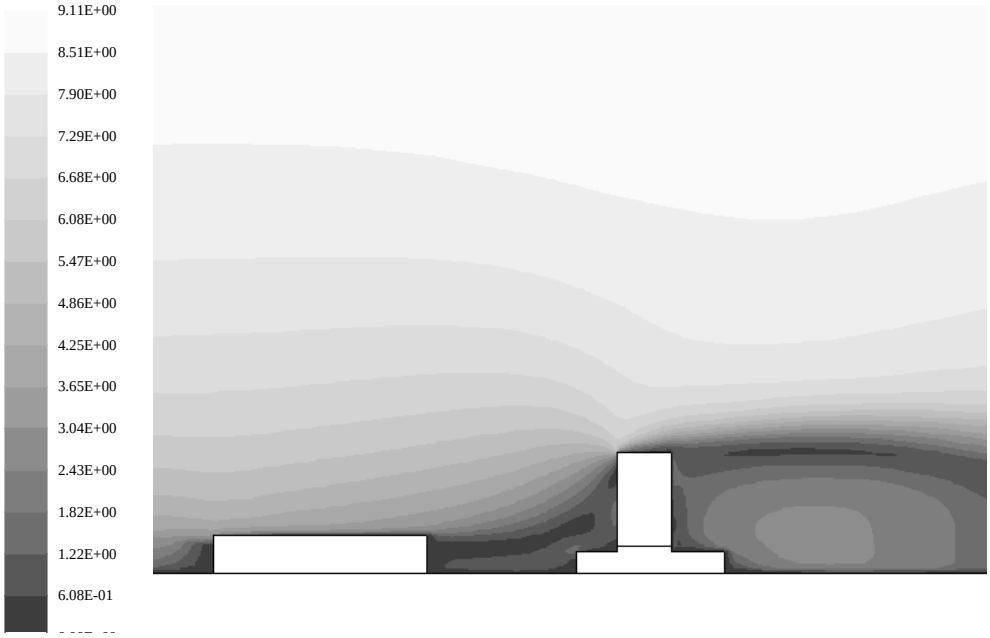

Figure 6.8: Contours of simulated velocity magnitudes [m s^{-1}] in the y-z plane through the middle of the Main Building. Reference parameters are U_h = 5.7 m s^{-1} and Φ = 270°.

cm from the façade surface. The differences between these two figures are small. The most important difference is that the absolute values of $U_{y,\mathrm{P4}}/U_\mathrm{h}$ at 125 cm (figure 6.6c) are larger than than the respective values at 50 cm. This means that, as expected, the wind velocity component perpendicular to the building façade ($U_{y,\mathrm{P4}}$) is relatively more reduced towards the façade than the wind velocity components parallel to the façade ($U_{x,\mathrm{P4}}$, $U_{z,\mathrm{P4}}$).

Mean pressure coefficients Data from previous wind tunnel and full-scale measurements of mean pressure coefficients on the west façade of the Main Building (Geurts 1997) are compared with the simulation results of the current study in figure 6.7. The simulation, wind tunnel and full-scale results for Φ = 270° are in good agreement. However, towards the building edges, the wind tunnel measurements reveal strongly decreasing pressure coefficients. This is in contrast to the full-scale measurements and simulations, which both suggest more or less the same value. Large differences between the wind tunnel measurements and the other results are also visible towards x_so = 1 for Φ = 300°, where the full-scale measurements and the simulations seem to give

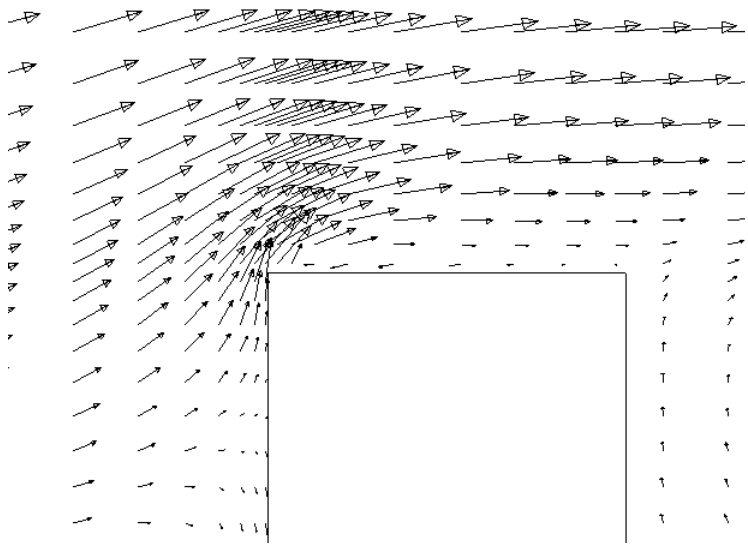

Figure 6.9: Simulated velocity vectors in the y-z plane through position B12 of the Main Building (figure 6.2). Reference parameters are $U_h = 5.7$ m s^{-1} and $\Phi = 270°$. An arrow with the length of the building width corresponds to 32 m s^{-1}.

the same increase in pressure coefficients. For both wind directions, measurements and simulations in the middle part of the façade are in good agreement.

Qualitative evaluation It is not practical to present all data and graphs for a qualitative evaluation of the simulation results. We restrict ourselves by presenting a contour diagram of velocities in a plane through the Main Building (figure 6.8) and a graph of velocity vectors at the Main Building roof (figure 6.9). The latter figure clearly shows a reattachment on the roof, which we may expect according to literature (see e.g. Bottema 1993b). Figure 6.8 shows (among others) that the recirculation zone in the building wake extends up till the expected distance of $4\mathcal{L}_g$ behind the Main Building ($4\mathcal{L}_g = 8\mathcal{H}$ in our case). For the definition of $\mathcal{L}_g$ one is referred to section 6.1, and for an overview of flow patterns around buildings to Bottema (1993b).

Conclusion The general difficulties of the standard K-ϵ model with the simulation of recirculation on the leeward sides of a building and the (over-)production of turbulent kinetic energy at the windward edges of a building have been pointed out in the literature (see e.g. Murakami et al. 1992). Nevertheless, in the literature it is also pointed out that generally the simulated wind speed values at the windward side of a building are in good agreement with (wind tunnel) measurements. In view of this, the mentioned

general difficulties, and the use of a structured grid with inevitably non-ideally shaped grid cells, the wind simulations of the present study seem to compare well enough with the measurements to proceed to the driving rain calculations.

6.4 Results of driving rain calculations

Results of rain simulations are presented and discussed in the same order as the calculations, i.e. firstly catch ratios $\eta(D)$ on the west façade of the Main Building and, secondly, driving rain amounts on the façade. Finally, the driving rain simulations are compared with driving rain measurements.

Catch ratios $\eta(D)$ Figure 6.10 shows simulated catch ratios $\eta(D)$ on the west façade of the Main Building for $U_h = 3.5$ m s^{-1} and wind from the west. The calculations included turbulent dispersion of drops. From the figure one can observe that, for a given drop diameter, the upper part of the façade has higher catch ratios than the lower part. This applies also for the sides of the west façade in comparison to the middle part. Besides, the catch ratio on a façade section increases with drop diameter (figure 6.10) and with wind speed (cf. figures 6.10 and 6.12).

When the turbulent drop dispersion is not included in the calculations, the results are as shown in figure 6.11. Compared to the calculations with dispersion, these results show lower values of $\eta(D)$. The relative differences are larger for smaller D. It seems that drops more easily hit the façade when turbulent dispersion is included in the calculations. Turbulence can be seen as an extra mechanism which drives drops out of their 'mean paths' which are determined by the mean wind velocity and the drop's inertia. However, the calculation of the turbulent drop dispersion in the K-ϵ model assumes isotropic turbulence, which is not realistic near surfaces. This means that the simulated turbulent velocity component perpendicular to the façade might be too large and the lateral turbulent component too small. Because of their smaller inertia, larger drops are less sensitive to turbulence than smaller drops, and therefore the difference in η of larger drops with and without turbulent dispersion is smaller.

Exemplary drop trajectories in figure 6.3 also illustrate the differences between smaller and larger drops, and between calculations with and without turbulent drop dispersion.

The simulated catch ratios $\eta(D)$ at several façade sections as a function of drop diameter are depicted in figures 6.13 (with drop dispersion) and 6.14 (without drop dispersion). In figures 6.13a and 6.14a, solid lines refer to façade sections A1, B1, etc. to E1, whereas the dashed lines refer to façade sections A18, B18, etc. to E18, which are their symmetric counterparts. Figures 6.13b and 6.14b present the results of façade sections A7 to E7 and A12 to E12, respectively. By showing the symmetrical counterparts of the

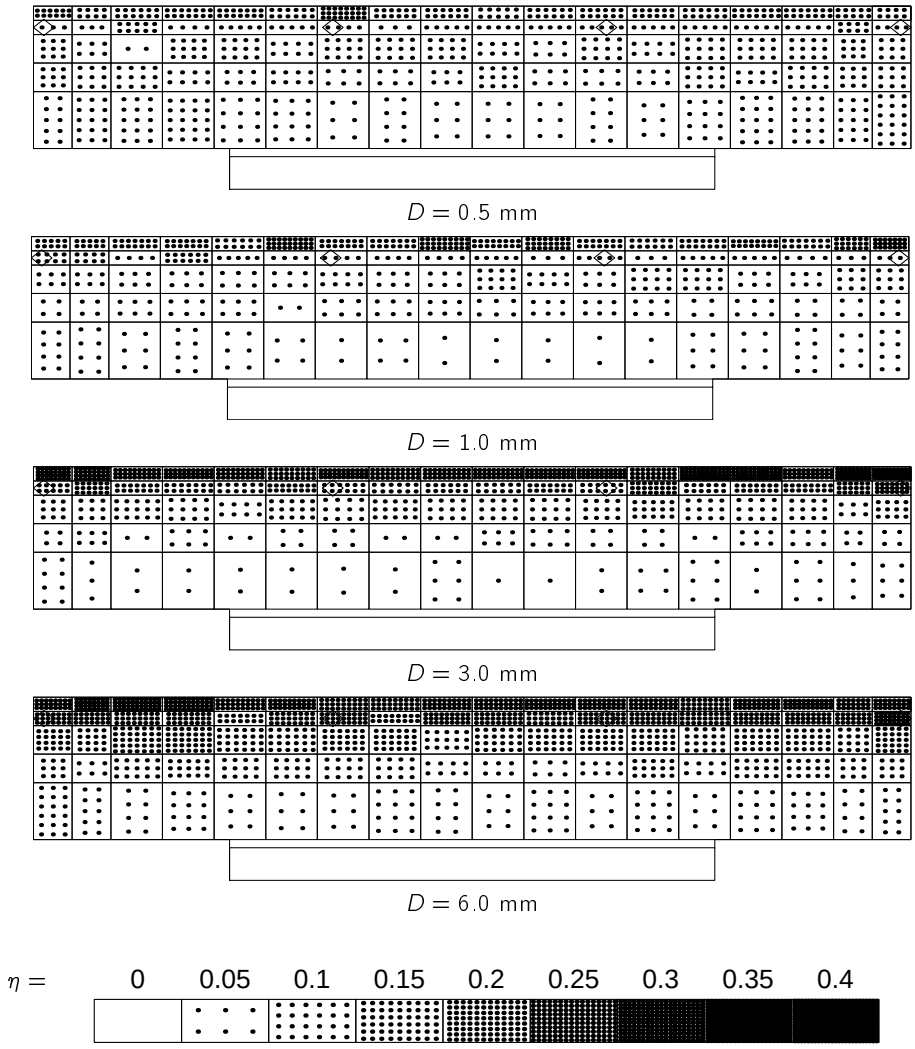

Figure 6.10: Simulated catch ratios $\eta(D)$ on the west façade of the Main Building, for $U_h = 3.5$ m s^{-1} and $\Phi = 270°$. Calculations with turbulent dispersion of drops.

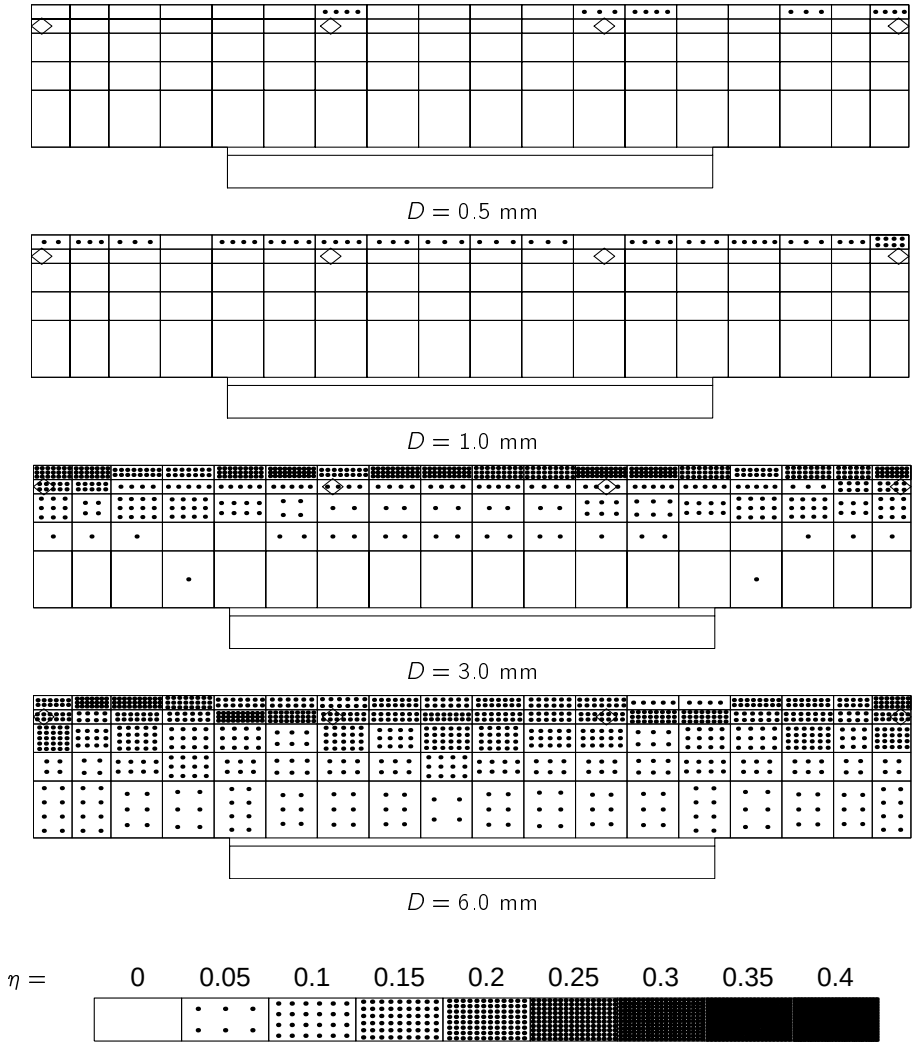

Figure 6.11: As figure 6.10, but without turbulent dispersion of drops.

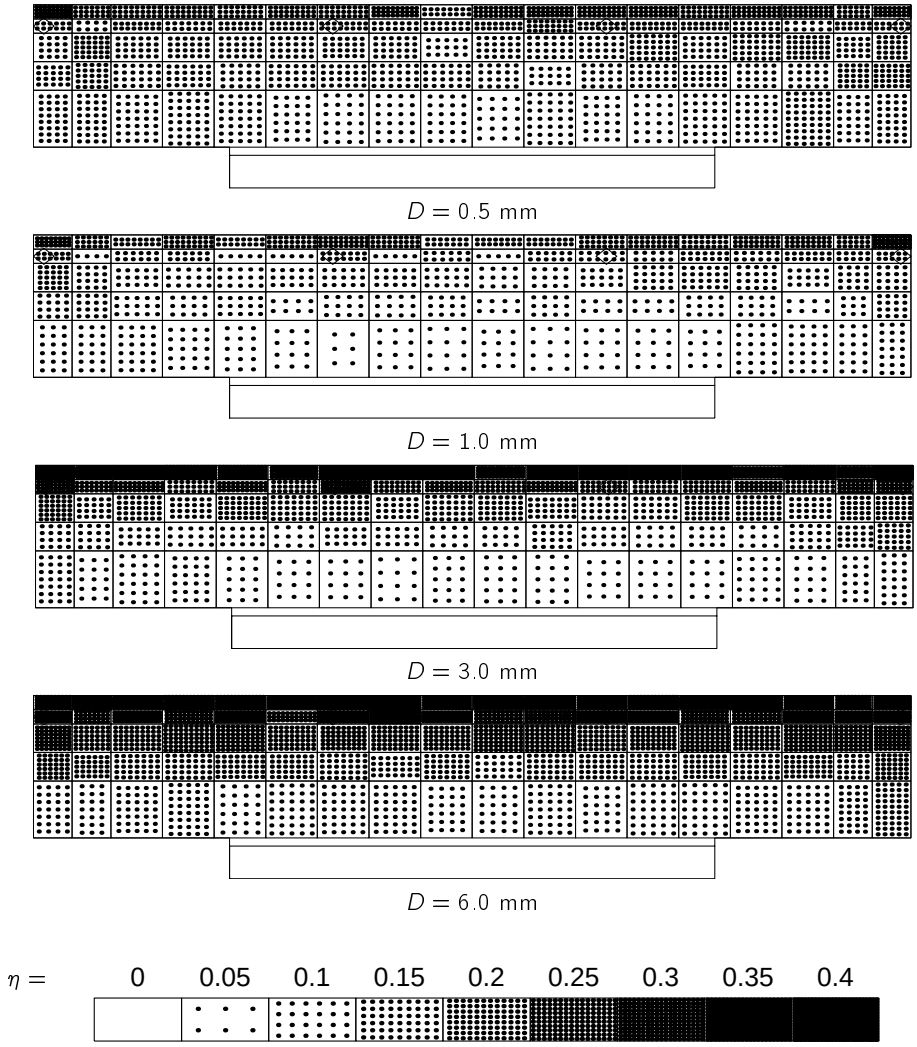

Figure 6.12: As figure 6.10, but with $U_h = 5.7$ m s^{-1}.

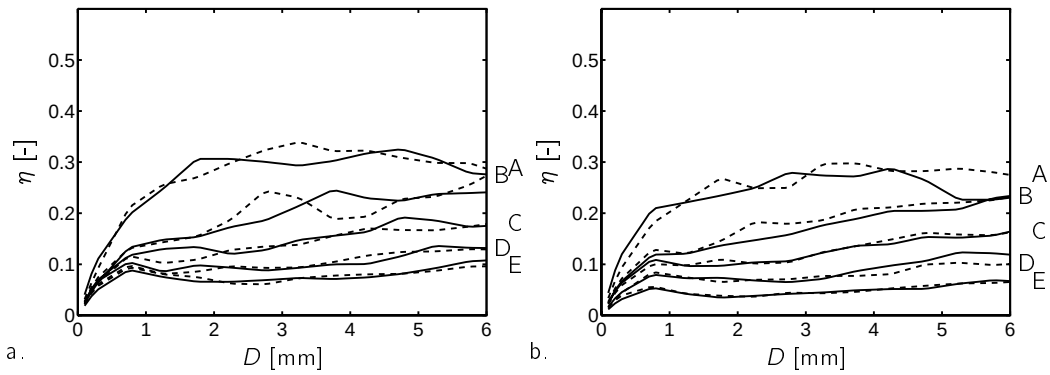

Figure 6.13: Simulated catch ratios $\eta(D)$ at façade sections A1–E1 (solid lines in figure a), A18–E18 (dashed lines in a), A7–E7 (solid lines in b) and A12–E12 (dashed lines in b). Cf. figure 6.10. Configuration: $U_h = 3.5$ m s^{-1} and $\Phi = 270°$, with turbulent drop dispersion. See figure 6.2 for the positions of the façade sections.

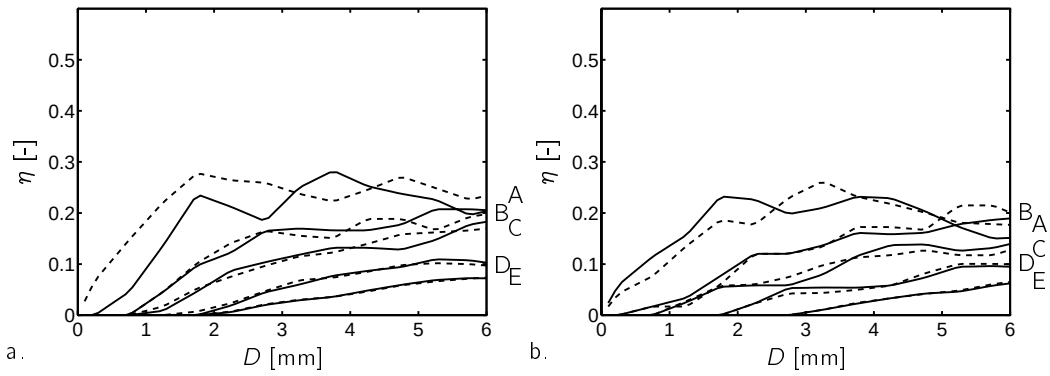

Figure 6.14: As figure 6.13, but without turbulent drop dispersion. Cf. figure 6.11.

façade sections in one figure, we can see the variations in $\eta(D)$ at symmetrical façade sections. These variations are larger when a façade section is located more to the edges, and can be explained by the higher degree of turbulence at the edges of the building, and by computational errors in the wind and drop trajectory simulations.

Comparing the results of the calculations with and without turbulent drop dispersion, one can see that especially drops of smaller sizes do not hit the façade on the lower façade sections at all when drop dispersion is not included. Moreover, $\eta(D)$ is generally lower without drop dispersion than with drop dispersion.

Driving rain ratio k The chosen raindrop spectra for the calculation of driving rain ratios ($k = R_f/R_h$) are depicted in figure 6.15. As mentioned in section 6.2, the parameterisation of Wessels (1972) is used. Figures 6.16 to 6.19 show the driving rain ratios k for the various façade sections and the two values of A. As one can expect from the above observations on $\eta(D)$, the driving rain ratio is higher at the upper and side edges of the building, and for rain spectra with relatively more larger drops. Moreover, the differences in η resulting from the inclusion of turbulent dispersion are also apparent in k.

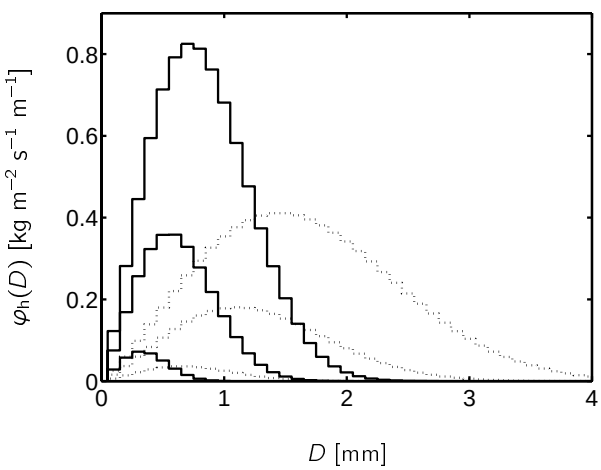

Figure 6.15: Raindrop mass flux spectra with rain intensities of 0.1, 1.0 and 3.0 mm h^{-1} respectively, according to the parameterisation of Wessels (1972): $A = 0.88$ (——) and 1.77 (.....), $a = 0.21$, $b = 2.25$, $C = 67$, and $q = 0.846$ (eq. 2.24). $\Delta D = 0.1$ mm.

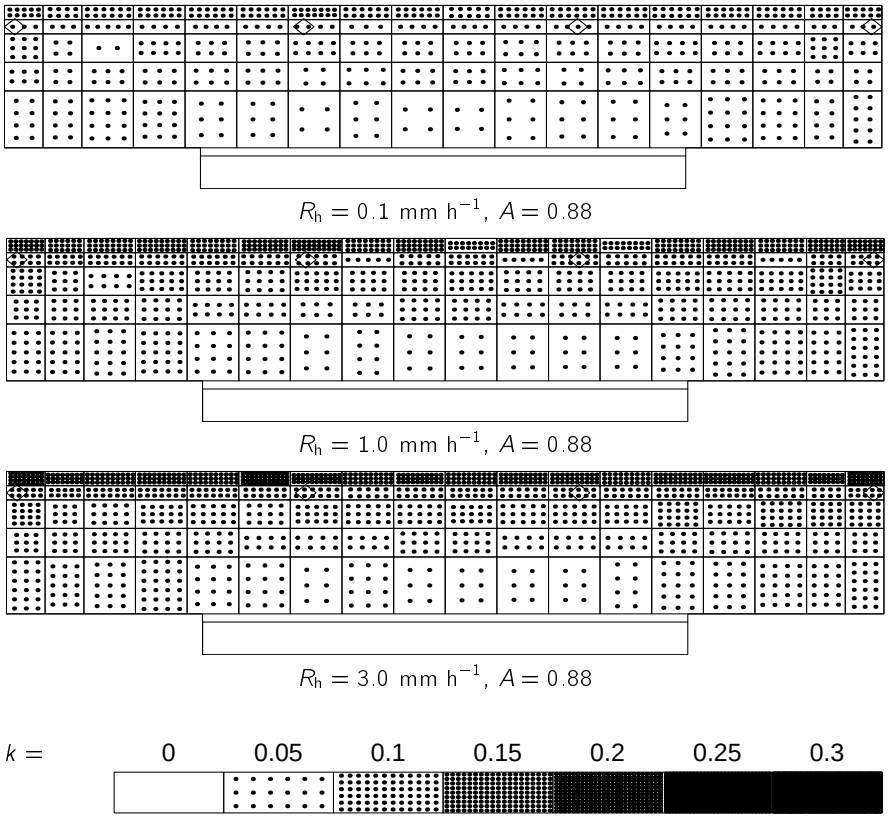

Figure 6.16: Simulated driving rain ratio k on the west façade of the Main Building, for $U_h = 3.5$ m s^{-1}, $\Phi = 270°$, trajectory calculations with turbulent drop dispersion, and the raindrop spectrum of Wessels (1972) with $A = 0.88$ (see ——— in figure 6.15).

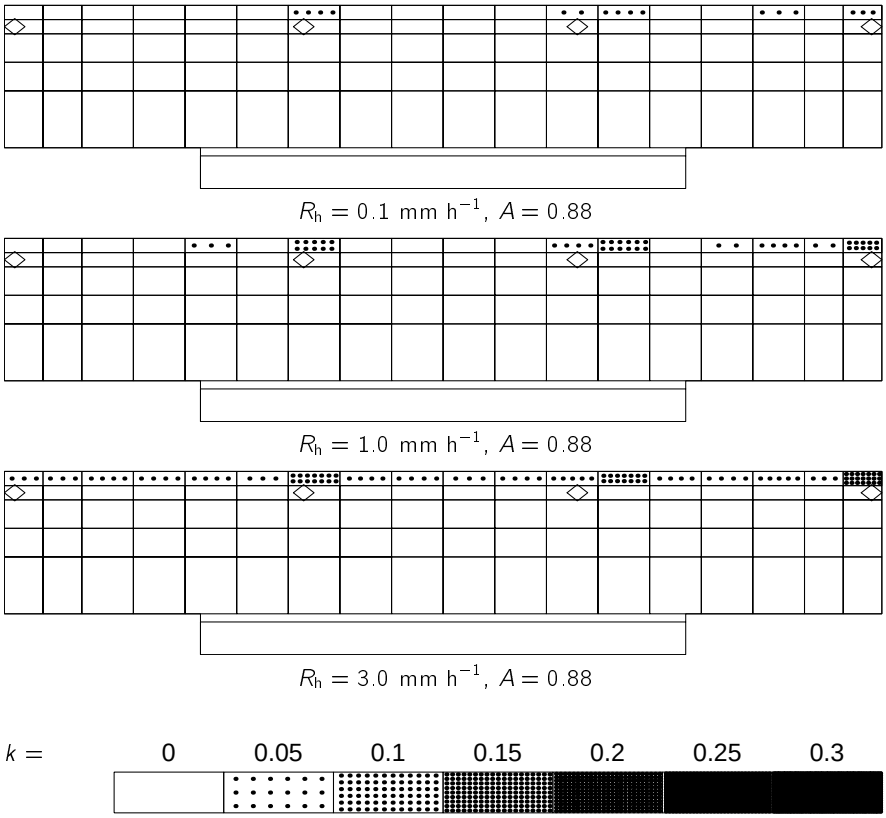

Figure 6.17: As figure 6.16, but without turbulent drop dispersion.

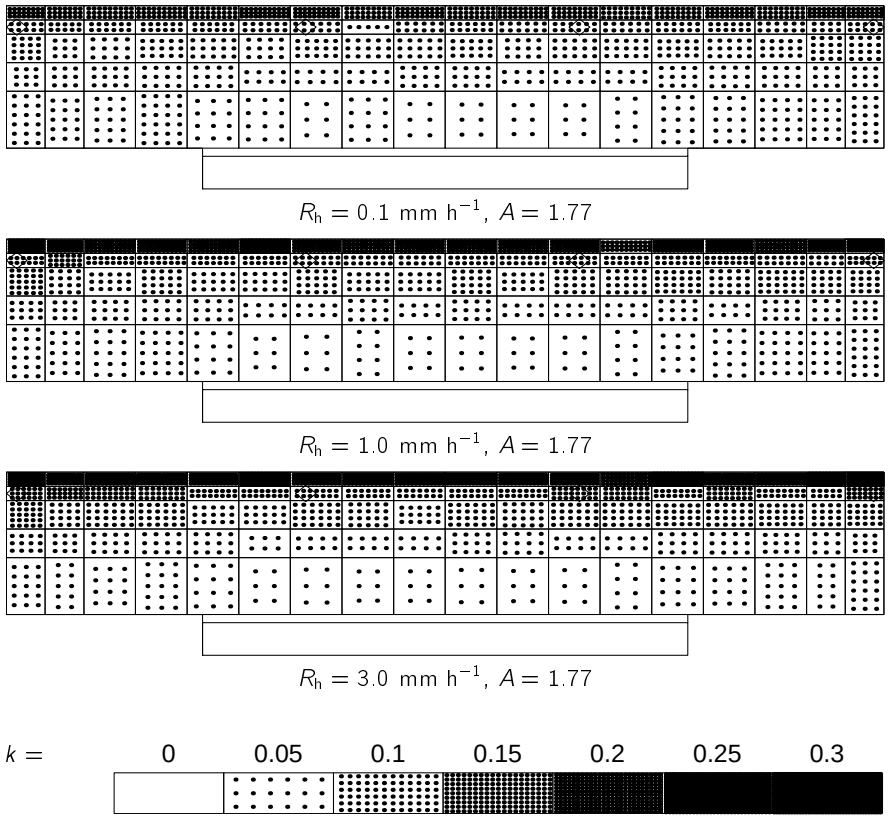

Figure 6.18: As figure 6.16 but based on raindrop spectra with $A = 1.77$ (see ..... in figure 6.15).

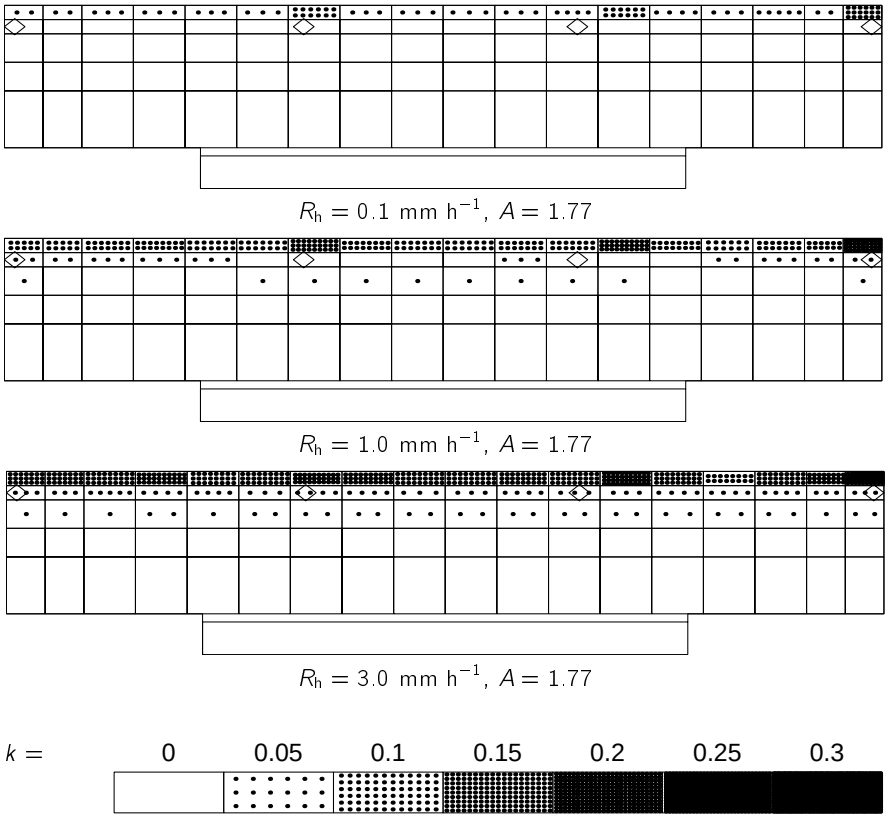

Figure 6.19: As figure 6.17 but based on raindrop spectra with $A = 1.77$.

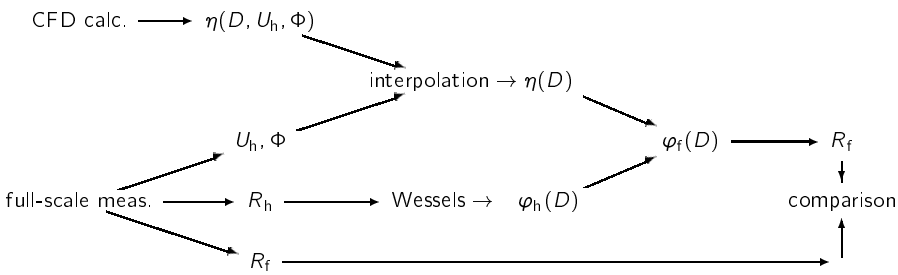

Figure 6.20: Simulation of driving rain intensities based on CFD calculations of drop trajectories and based on data of full-scale measurements. The resulting driving rain intensity is compared with the corresponding measured values in figures 6.21–6.23.

Comparison with measured driving rain intensities A scheme of the driving rain intensity calculations is presented in figure 6.20. Using the Wessels (1972) parameterisations, the raindrop mass flux spectra ($\varphi_h(D)$) are calculated from the horizontal rain intensity obtained from the full-scale measurements. Catch ratios ($\eta(D)$) for a particular façade section, reference wind speed and direction are obtained by interpolation of the catch ratios obtained by the raindrop trajectory (CFD) calculations. As these calculations were not performed for every possible reference wind speed and direction, we can only calculate $\eta(D)$ and, subsequently, $\varphi_f(D)$ for limited ranges of wind speeds and directions. (The actually performed CFD calculations are listed in table 6.2.) The results presented below are obtained by the method described in this paragraph and depicted in figure 6.20.

The plots in figure 6.21 show measured and simulated driving rain intensities at position P4/5 as a function of horizontal rain intensity. The full-scale measurement data in figure 6.21a result from selection for $\Phi = 270° \pm 15°$ and $U_h = 4$–5 m s^{-1}, while the simulated data were obtained from calculations with turbulent drop dispersion. The simulated data show that different raindrop spectrum parameters result in different driving rain intensities for a given horizontal rain intensity, wind speed, wind direction and façade position. Moreover, a given spectrum parameterisation yields an almost linear relation between horizontal and driving rain intensities. This relation can be expressed by the following formula:

$$R_f = \int \eta(D)\varphi_h(D, A, R_h)dD \approx k(A)R_h, \tag{6.10}$$

where $\varphi_h(D, A, R_h)$ is the raindrop mass flux spectrum as a function of the Best (1950) raindrop spectrum parameters A and R_h (eq. 2.24).

Figure 6.21a and equation 6.10 show that the driving rain ratio (k) for given façade position, wind speed and wind direction is a function of parameter A, which determines the shape of the raindrop spectrum. In other words, raindrop spectra with the same

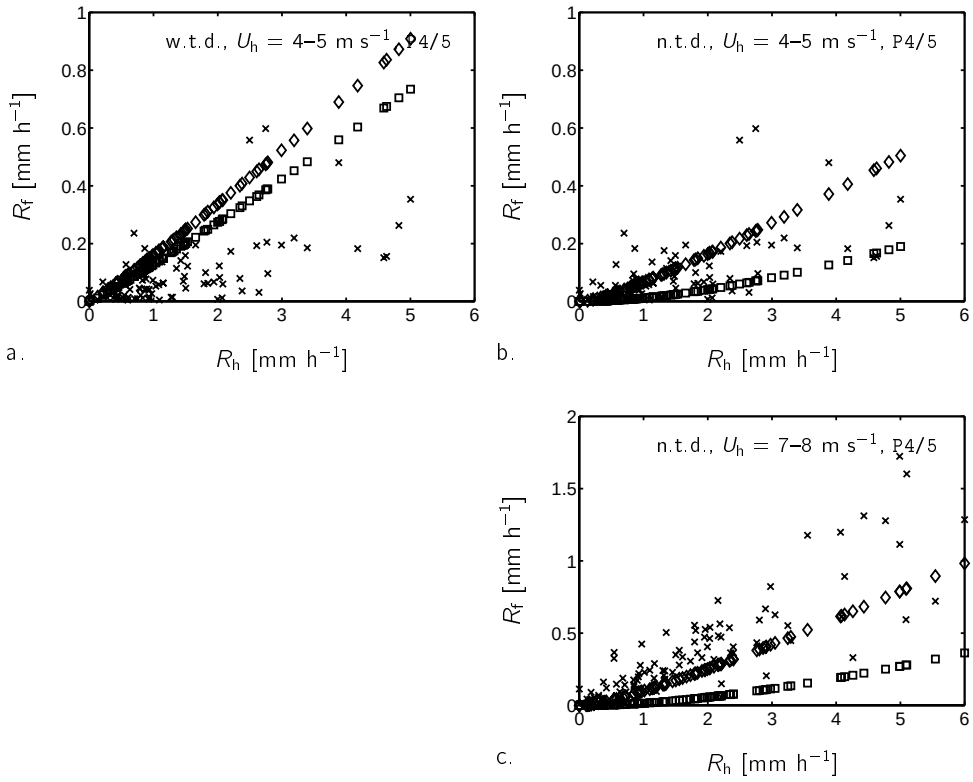

Figure 6.21: Driving rain intensities as a function of horizontal rain intensities, at position P4/5; for $\Phi = 270° \pm 15°$, and for U_h = 4–5 m s^{-1} (figures a&b) or 7–8 m s^{-1} (figure c). The measurements are indicated by × and based on 5-min values from 1-12-1997 to 30-11-1999. The simulations are indicated by □ and ◇ and based on measured R_h and Wessels' spectra with $A = 0.88$ and $A = 1.77$, respectively. In figures b&c, the simulations do not include turbulent drop dispersion (n.t.d.), whereas in figure a it is included (w.t.d.). Note the different scale of the y coordinate in figure c.

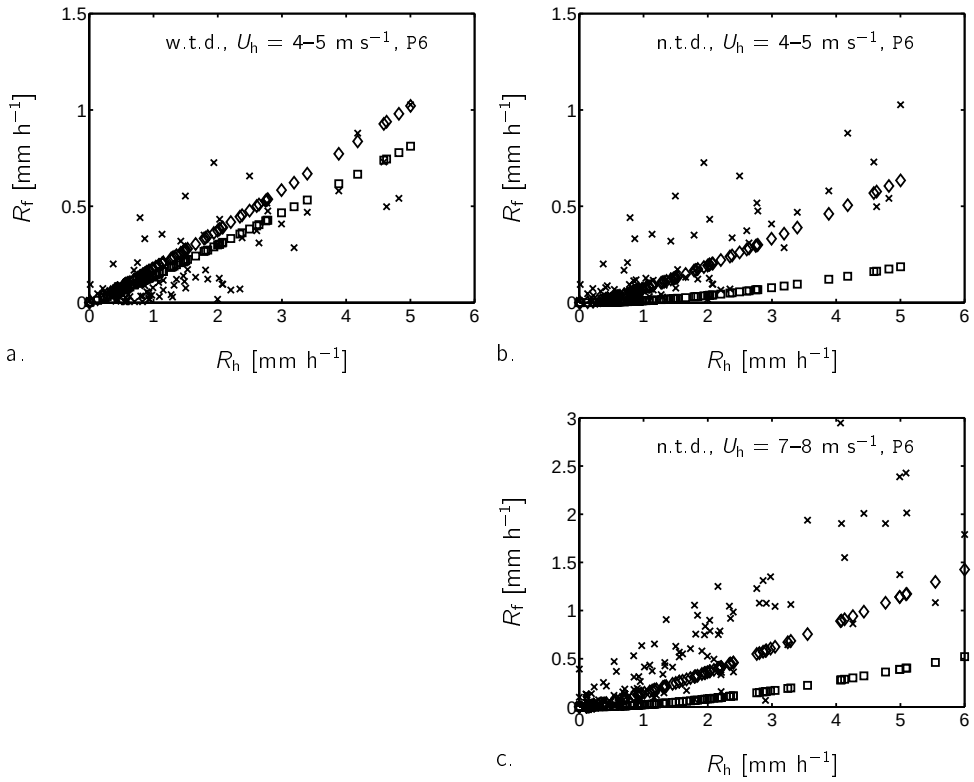

Figure 6.22: As figure 6.21, but for position P6.

horizontal rain intensity but with different shapes yield different driving rain intensities. The measured data are very scattered and differ often much from the simulated data. Of course, the real raindrop spectra are unknown, and hence could not be used in the calculations. We know that it is very likely that measured raindrop spectra differ much from relations like those given by Best (1950) (see section 5.2.9). Hence, we cannot yet conclude whether the relation of equation 6.10 corresponds to reality. Moreover, it is possible that the simulated catch ratio $\eta(D)$ do not correspond to the actual situation because of errors in the simulation of wind speeds and raindrop trajectories. Other causes for the scatter may be, for instance, the applied clock period, the temporal evolution of rain events, and the neglect of raindrop coagulation in the model. At the end of this section we will show results of driving rain intensities calculated directly from measured raindrop spectra.

The simulation shown in figure 6.21b differs only from the one in figure 6.21a by the fact that no turbulent drop dispersion is used. The difference between the two simulation results in figure 6.21b, i.e. corresponding to the two parameterisations of the raindrop spectra, is now much larger. Thus, without turbulent drop dispersion, the influence of differences in drop spectra (i.e. in A) has a larger effect than with turbulent drop dispersion. This is explained by differences in the catch ratios $\eta(D)$ (e.g. figure 6.13 and 6.14 respectively). Small drops have a smaller tendency to fall onto the façade in calculations without turbulent drop dispersion, and therefore the ratio between the number of smaller and bigger drops, which is quite large in the chosen raindrop spectrum parameterisations (see figure 6.15), results in larger differences in the simulated driving rain intensities.

The simulation shown in figure 6.21c differs only from the one in figure 6.21b by the reference wind speed, namely 7–8 m s^{-1}. As expected, higher wind speeds result in higher driving rain intensities. Comparing the results of the measurements with the results of the simulations presented in figures 6.21a–c, we see that many measurements fall outside the region enclosed by the simulated data which represent 90% of all drop spectra in the Netherlands according to Wessels (1972). The simulation may even systematically overestimate (figure 6.21a) or underestimate (figure 6.21c) the measurements by a factor of 2.

Figure 6.22 shows the results for position P6 in the same way as figure 6.21 for position P4/5. More or less the same conclusions as given above hold position P6.

The results of simulations without and with turbulent drop dispersion for a given position, wind speed and wind direction can be compared by comparing figure 6.21a with figure 6.21b, and figure 6.22a with figure 6.22b. The figures show that the simulations with turbulent drop dispersion result in higher driving rain intensities than those without turbulent drop dispersion. If one projects all results presented in the figures 6.21a and b (and in the figures 6.22a and b respectively) into one figure, many measured data fall within the region comprised by the simulated data. As we also have seen before,

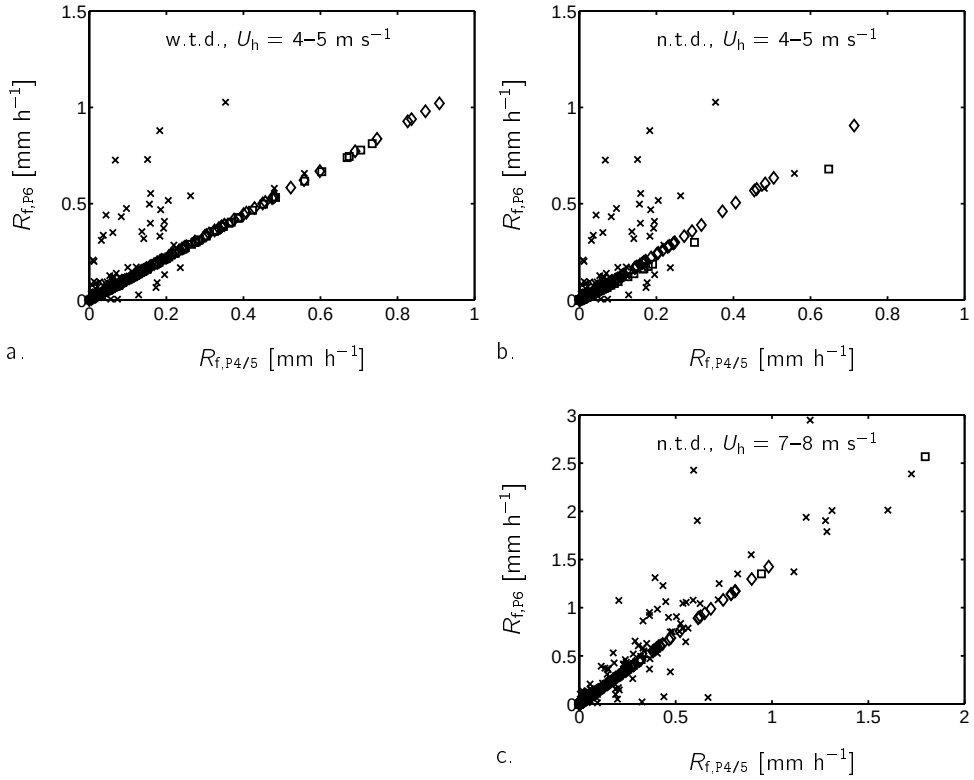

Figure 6.23: Correlation of driving rain intensities at positions P4/5 and P6; for $\Phi = 270° \pm 15°$, and for U_h = 4–5 m s^{-1} (figures a&b) and 7–8 m s^{-1} (figure c). The measurements are indicated by × and based on 5-min values from 1-12-1997 to 30-11-1999. The simulations are indicated by □ and ◇ and based on measured R_h and Wessels' spectra with $A = 0.88$ and $A = 1.77$, respectively. In figures b&c, the simulations do not include turbulent drop dispersion (n.t.d.), whereas in figure a it is included (w.t.d.).

a simulation with turbulent drop dispersion yields larger driving rain intensities than without turbulent drop dispersion. Due to the fluctuating velocity components, more drops impinge on the façade than in simulations without turbulent drop dispersion, and hence the driving rain intensity is higher. Moreover, the trajectory model with the turbulent drop dispersion may likely overestimate the number of drops on the façade because it is based on isotropic turbulence, and therefore on too high estimates of fluctuating velocity components perpendicular to the façade. Comparing the simulations with the measurements, it seems indeed that the two raindrop trajectory models yield an upper and lower limit.

Comparison between P4/5 **and** P6 A correlation of the measured and simulated driving rain intensities at positions P4/5 and with those at P6 is plotted in figure 6.23. Figure 6.23a corresponds to figures 6.21a & 6.22a and, likewise, figure 6.23b with 6.21b & 6.22b and figure 6.23c with 6.21c & 6.22c. As we have observed that the relation between horizontal rain intensity and simulated driving rain intensity is almost linear (eq. 6.10 and figs. 6.21 and 6.22), it is obvious that the simulated data in figure 6.23 form a straight line too. The ratio between the simulated driving rain intensities at P4/5 and P6 is therefore almost independent of raindrop spectrum parameterisation. The measured data are, however, very much scattered. The measured ratios $R_{\mathrm{f,P6}}/R_{\mathrm{f,P4/5}}$ (compare also with table 5.4b) are generally larger than the simulated ratios. Here again, it is difficult to trace back where inaccuracies were introduced in the simulations.

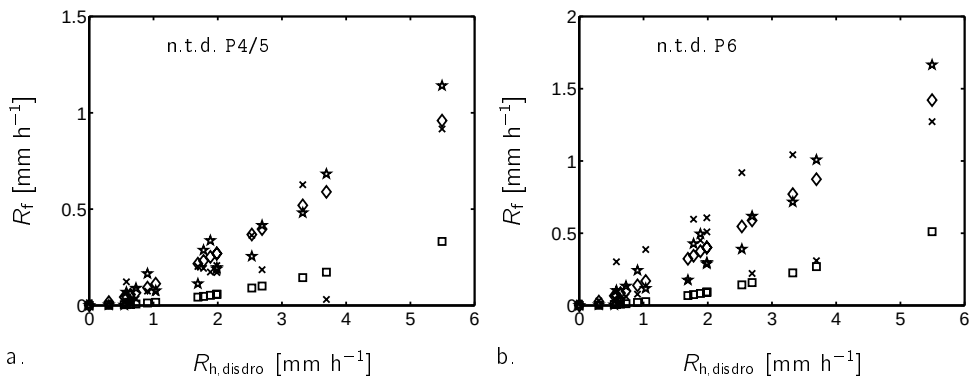

Figure 6.24: Driving rain intensities at positions P4/5 and P6: □ & ◇, simulated with $R_{\mathrm{h,disdro}}$ and Wessels' parameterisations with $A = 0.88$ and $A = 1.77$ respectively; ★, simulated with measured raindrop spectra ($\varphi_{\mathrm{h,\ disdro}}(D)$); and ×, measured. The horizontal rain intensity $R_{\mathrm{h,disdro}}$ is based on 5-min measurements by the disdrometer from 1-10-1999 to 7-1-2000, selected for $\Phi = 270° \pm 15°$ and for $U_{\mathrm{h}} = 3.5$–11.2 m s^{-1}. The simulations do not include turbulent drop dispersion (n.t.d.).

Measured raindrop spectra Figure 6.24 shows the results of driving rain intensities calculated from our measured raindrop spectra. The disdrometer was only operational during a short period (1-10-1999 to 7-1-2000). Therefore the range of the selected wind speeds was extended to 3.5–11.2 m s^{-1} to obtain enough data. The data indicated by □ and ◇ represent the calculations based on Wessels' spectra with $A = 0.88$ and $A = 1.77$, respectively, and with horizontal rain intensities measured by the disdrometer ($R_{\mathrm{h,disdro}}$). The calculations indicated by ★ are based directly on the measured raindrop spectra ($\varphi_{\mathrm{h,\ disdro}}(D)$), so not totally similar to figure 6.20. Important to note is that the simulation results based on the measured raindrop spectra (★) show much more scatter than the other simulation results (□ and ◇). The measured driving rain intensities are indicated by ×. The figure shows that the simulated driving rain intensities differ from the measured driving rain intensities. However, in the case of position P4/5 the simulations based on the measured raindrop spectra and those based on the Wessels' parameterisation with $A = 1.77$ are quite close to the measurements. In the case of position P6 almost all simulated data are lower than the measured driving rain data. Although the number of measurements with the disdrometer is small, we intend to conclude that the best parameterisation of the raindrop spectrum by Wessels is the one with $A = 1.77$.

6.5 Summary

Figure 1.1 depicts the general two-step approach for the translation of weather station data to driving rain data on a building envelope. In the present chapter, the second step (from site to building) was investigated by means of CFD simulations and by comparing the simulation results with the results of the measurements:

- modelling (sections 6.1 and 6.2):
  - the simulation of wind around the Main Building was carried out by the standard K-ϵ model as provided by *Fluent*. Except for $C_\mu = 0.032$ (Bottema 1993a), the standard model constants were applied,
  - the applied grid was a structured grid, which unfortunately creates undesired large grid expansion factors and cell aspect ratios in some parts of the grid. The size of the computational domain was determined by the rules of thumb given by Bottema (1993a). The domain included the Main Building, Auditorium and, optionally, Building T,
  - the size of the grid cells should be smaller than the stopping distance of the smallest considered raindrop. This implied a maximum dimension of 0.5 m near the façade, which is smaller than would be necessary for wind simulations alone,

- it was assumed that raindrop trajectories do not influence wind flow. Consequently, raindrop trajectories were calculated for a previously calculated wind field. We also assumed that the lifetime of a drop is not affected by drop interaction (collision and break-up) nor by evaporation,
- two models for drop trajectory calculations were applied: (1) *without* turbulent drop dispersion (resulting in 'mean trajectories') and (2) *with* turbulent drop dispersion (« continuous random walk model »),
- catch ratios $\eta(D)$ per façade section, reference wind speed and wind direction were obtained from the trajectory calculations. Driving rain intensities were calculated by assuming a certain raindrop spectrum: we used Wessels' (1972) parameterisation of the Best (1950) spectrum,
- by doubling the number of released drops, we evaluated the convergence of the calculated values of $\eta(D)$ and thus determined the minimum number of drops to be released for a reliable $\eta(D)$ (figure 6.4);

• simulations versus measurements (sections 6.3 and 6.4):

- the wind velocity simulations compare well with the full-scale wind measurements at position P4. Simulated mean pressure coefficients over the west façade compare quite well with wind tunnel and full-scale measurements of Geurts (1997),
- catch ratios $\eta(D)$ calculated with turbulent drop dispersion have higher values than without turbulent drop dispersion. Due to the (extra) turbulent velocity component, drops are more easily driven towards the façade when they come close to it. The smaller the drops are, the easier they are driven onto the façade. Moreover, the longer a drop flies closely to a façade, the higher is the probability that it is driven onto the façade. Figure 6.3 illustrates drop trajectories resulting from the two drop trajectory models; figures 6.10 to 6.14 show simulated catch ratios $\eta(D)$,
- results of simulated driving rain intensity distributions over the façade are depicted in figures 6.16 to 6.19,
- as $\eta(D)$ calculated with turbulent drop dispersion is more constant with drop diameter D than without turbulent drop dispersion, differences in raindrop spectra with the same horizontal rain intensity have a smaller effect on the eventual driving rain intensities,
- a comparison between the measurements and the simulations (based on the raindrop spectrum parameterisation of Wessels 1972) reveals that the results calculated with turbulent drop dispersion are likely to overestimate the measured driving rain intensities. The results calculated without turbulent drop dispersion are likely to underestimate the measurements,
- the driving rain intensities simulated for a given façade section, reference wind speed and wind direction, and based on Wessels' raindrop spectrum

parameterisation, result in an almost linear relation with horizontal rain intensity: $R_f \approx k(A)R_h$, where k depends only on the shape (in our case, parameter A) of the raindrop spectrum,

- in contrast to the previous item, the measured driving rain intensities for a given façade section, reference wind speed and wind direction show large variations. When measured raindrop spectra are used in the simulations, these simulated driving rain intensities show scatter too. Because the number of measured raindrop spectra during driving rain is rather small, we can not yet decisively conclude whether the relation mentioned in the previous item is actually valid.

Chapter 7

Conclusions

This chapter summarises the main conclusions from the previous chapters (indicated by •) and gives suggestions for further research (indicated by ▹).

Theory (chapter 2)

In chapter 2 we demonstrated that driving rain is a complex phenomenon of falling raindrops in the turbulent flow of wind around a building. Every individual drop has its individual drop trajectory. The lifetime of a drop is affected by drop interaction (collision and breakup) and the environment (wind and evaporation). However, in our « theoretical model » the onslaught of individual raindrops on a façade depends only on the wind field nearby the building. In our « empirical model » we define the onslaught in terms of driving rain intensities, i.e. amounts of driving rain water onto the building envelope per time interval. The empirical model is useful for analyses of our full-scale measurements. For both models we concentrated on the second step (from site to building façade) of the general two-step approach (figure 1.1).

Site and measurement set-up (chapter 3)

The objectives of the experiments were (a) the development and testing of driving rain gauges, and (b) the acquisition of driving rain data simultaneously with relevant weather data (in real circumstances, in full scale). The measured data should also be suited for the validation of CFD simulations of wind and driving rain in the same situation.

We chose the Main Building of the TUE mainly because of the relative simplicity of its geometry and the site topography. This simplicity relates to the following aspects. The

Main Building is obviously higher than nearby buildings. Its height surpasses $20 \times z_0$. Its wind field is hardly affected by other buildings and obstacles for south-west to west winds. Another important aspect is that a suitable location for site reference measurements of wind and rain was easily defined at the west side of the Main Building. Moreover, the large west façade is oriented towards the prevailing direction for wind and rain.

The instrumentation is described extensively in section 3.2. Recommendations, which do not relate to the driving rain gauges, are:

- ▹ The output of the disdrometer used by us has two disadvantages for our purposes. Firstly, the disdrometer gives the raindrop number concentration spectrum, which is derived from the quantity which we are interested in, namely the raindrop mass flux spectrum. Secondly, the interval of the size classes increases with the diameter, which results in larger absolute errors of the real mass flux at larger diameters. The two disadvantages can be solved by outputting every detected raindrop with its diameter and velocity. It is recommended to adapt the software of the disdrometer in this way.
- ▹ The two-dimensional video-disdrometer of Schönhuber et al. (1994) is able to register details of raindrops. It could be used to verify actual raindrop spectra with those measured by the optical disdrometer of Löffler-Mang and Joss (2000) which we used.

  The video-disdrometer can also be mounted in a façade in order to validate simulated catch ratios $\eta(D)$ (eq. 2.26) directly from measurements of $\varphi_{\mathrm{h}}(D)$ and $\varphi_{\mathrm{f}}(D)$.
- ▹ The measurement set-up at the TUE site may be continued and extended with instruments for the measurement of outdoor air temperature, relative humidity, solar irradiation etc., so that every important climatological parameter can be included to the benefit of heat-air-moisture studies.

Driving rain gauges (chapter 4)

The conclusions of the international full-scale driving rain gauge comparison test are listed in section 4.4 (and were partially presented in Högberg et al. 1999).

Adding some suggestions, we repeat the most important conclusions here:

- The experiments resulted in the formulation of design rules for driving rain gauges. These design rules relate to the catchment area, the prevention of drops from remaining stuck on the surface of the driving rain collector, the temporal resolution of the water flux gauge and the finish of the collector surface.

- The TUE-II gauge, which was developed at the TUE and is equipped with a rotating wiper (figure 3.14), accurately registers driving rain intensities. It has a good resolution for shorter time intervals (0.001 mm h^{-1} for 10-min periods). Its wiper keeps the surface clean and forces impinged raindrops to coagulate and drip down (hence less evaporation). Moreover, it is not sensitive to wind.

- The TUE-I gauge, which is similar to TUE-II except that it is not equipped with a rotating wiper (figure 3.13), registers approximately half of the monthly driving rain amount measured by the TUE-II gauge (table 4.1). This is also valid for 10-min periods (figure 4.1c).

- The monthly driving rain amounts of the CTH, DTU and TUE-II gauges deviate within 30% from each other (table 4.1). On much smaller time bases, such as 10-min intervals, gauge responses can deviate significantly (figures 4.1–4.4). This applies especially for small time bases of the used tipping-bucket driving rain gauge (CTH): during a 10 min period it tips only once at a driving rain intensity of 0.18 mm h^{-1}.

▹ Given the results of the CTH gauge for driving rain measurements, we suggest that for short-time intervals (like 5- or 10-min intervals) one should apply a continuous measuring principle instead of the tipping-bucket principle.

  Indeed, given the necessary yet cumbersome correction of the tipping-bucket gauge data (sections 3.4.3 and 5.1), the suggestion also applies to horizontal rain measurements.

- The effect of size and shape of the catchment area cannot clearly be deduced from the experiments. A comparison of the CTH gauge (0.032 m^2) and the TUE-I gauge (0.5 m^2) does not give a straightforward conclusion, because of the differences in measuring principle.

▹ It is recommended for further research to compare simultaneously the readings of driving rain gauges with different catchment areas but with the same continuous measuring principle. One could, for instance, add the CTH gauge and the TUE-II gauges as references. Further measurements with the disdrometer (with which we measured during a too short period) may be useful for explaining the differences between the readings of driving rain gauges.

  Another line of research are calculations with a model for raindrops sticking, coagulating and running off on a driving rain collector, as mentioned in Blocken et al. (2001).

- Lower driving rain intensities (measured with the TUE-II gauge) are overestimated by the DTU gauge (figures 4.1b–4.4b). The scatter in the DTU/TUE-II correlations is larger than in the TUE-I/TUE-II correlations. This is probably due to the noise caused by the wind acting on the freely suspended collector. The applied

signal-processing method (see section 3.4.6) was kept simple and (▹) can perhaps be improved.

▹ The possibility of splashing and the effects of protruding rims and other projections were not investigated. With our full-scale measurement set-up, it is possible to mount at least three gauges with different protruding rims at P4/5/7. An investigation on splashing effects is less easy; perhaps one may use video cameras.

▹ As it occurred that the reservoirs of the TUE-II and TUE-I gauges overflowed during heavy driving rain, it is recommended to investigate other types of continuous water flux measurements. We have done some laboratory experiments with a drop-counting device (Bijsterbosch 2000). Combined with a collector of $A_{\text{catch}} = 0.5$ m^2, it has a resolution of 0.0006 mm h^{-1} for 10-min periods and an accuracy of approximately 5% for driving rain intensities ranging at least from 0.12 to 1.20 mm h^{-1} (one drop equals 0.05 g $\pm$ 5%). We recommend to test it in full scale first.

Full-scale measurements (chapter 5)

The full-scale experiments at the TUE site resulted in a unique series of continuous measurements during 24 months of driving rain on the west façade of the Main Building and wind and rain at the well-defined site reference location. Raindrop spectra with a disdrometer were measured during 3 months too. The measurements are detailed (data at 5-minute intervals were provided) and are available for future research (at the website http://sts.bwk.tue.nl/drivingrain/).

Section 5.4 gives a summary of the measurement results. The present study introduces the following new items to our knowledge on driving rain:

- a time series of detailed measurements of driving rain on a façade on a particular building in an urban surrounding with well-defined site reference measurements,
- the readings of different types of driving rain gauges were compared with each other in a full-scale comparison test (see chapter 4),
- raindrop spectra were measured with a disdrometer of Löffler-Mang and Joss (2000). Unfortunately, the number of measured spectra during driving rain was rather small.

  ▹ Further raindrop spectrum measurements are recommanded, because we could not conclude our investigation on the influence of raindrop spectrum on driving rain quantities,

- driving rain intensities vary much at a façade position and on small time-scales (5 min), even for narrow ranges of reference wind speed, wind direction and horizontal rain intensity (see e.g. figure 5.14 and section 5.2.5). Moreover, the correlation between the two measurement positions P4/5 and P6 is very complex and depends to a great degree on wind direction (section 5.2.6),

- the traditional empirical model (model 1, eq. 5.3), based on Lacy (1965) and implemented in the British Standard 8401 (BSI 1992), is improved by taking the wind direction and the position on the façade more explicitly into account (model 2, eq. 5.4). Model 1 yields less realistic estimates of (especially maxima of) 5-min driving rain intensities than model 2. However, the models overestimate the cumulative driving rain amounts after 24 months by up to 35–45%.

  ▹ In order to validate models 1 and 2 further, we recommend measurements of the distribution of driving rain intensity over the façade on more than two façade positions. Probably a better line of research are driving rain measurements on other buildings; below we will suggest some conditions for such experiments.

We investigated a large part of the two-step approach (figure 1.1) in chapter 5, but we did not show every possible analysis of the measurement data, such as:

▹ an investigation on the relation between hourly values and 5-min (10-min) values, as generally only hourly values of measured wind and rain parameters are available at a weather station,

▹ an analysis of the temporal development of horizontal and driving rain intensities during rain spells.

CFD simulations (chapter 6)

Section 6.5 summarises our CFD simulations of wind and driving rain at the TUE site. Figures 6.16 to 6.19 depict the results of simulated driving rain intensity distributions over the west façade of the Main Building. The main conclusions are:

- In spite of the known limitations of the applied K-ϵ model (e.g. Murakami et al. 1992), the practically limited number of grid cells and the use of a structured grid with inevitably non-ideally shaped grid cells, the simulated wind speed at the façade is within the standard deviation of the full-scale wind speed measurements at position P4. Simulated mean pressure coefficients over the west façade compare quite well with wind tunnel and full-scale measurements of Geurts (1997).

- Catch ratios $\eta(D)$ calculated with turbulent drop dispersion have higher values than without turbulent drop dispersion. Due to the (extra) turbulent velocity component, drops are more easily driven towards the façade when they come close to it. The smaller the drops are, the easier they are driven onto the façade. Moreover, the longer a drop flies closely to a façade, the higher is the probability that it is driven onto the façade. Figure 6.3 illustrates drop trajectories resulting from the two drop trajectory models; figures 6.10 to 6.14 show simulated catch ratios $\eta(D)$.
- A comparison between the measurements and the simulations (based on the raindrop spectrum parameterisation of Wessels 1972) reveals that the results calculated with turbulent drop dispersion are likely to overestimate the measured driving rain intensities. The results calculated without turbulent drop dispersion are likely to underestimate the measurements.

▹ To validate our CFD driving rain simulations more precisely, it is needed to measure wind speed and driving rain intensities at more positions close to and on the façade.

- As concluded before, the *measured* driving rain intensities for a given façade section, reference wind speed and wind direction show large variations. The driving rain intensities *simulated* without turbulent drop dispersion and based on the raindrop spectrum parameterisation of Wessels (1972), yield an almost linear relation with horizontal rain intensity: $R_f \approx k(A)R_h$, where k depends only on the shape (in our case, parameter A) of the raindrop spectrum. However, when measured raindrop spectra are used in the simulations, these simulated driving rain intensities show scatter too. Because the number of measured raindrop spectra during driving rain is rather small, we can not yet decisively conclude whether the relation $R_f \approx k(A)R_h$ is actually valid.

▹ It is therefore recommended to elaborate the problem of the previous item with more measurements of raindrop spectra and driving rain.

- Altogether, the following aspects for reliable CFD results of wind and driving rain are important:
  - experience with the CFD program, useful references, like Bottema (1993a), and validations of simulated data with measured data will make one conscious about the possibilities and limitations of the applied models. Standards on CFD simulations of wind nearby buildings are still in development though,
  - the building geometry and the surrounding topography should be simple enough for CFD modelling. An important condition for the surrounding topography is the presence of a site reference location and an unobstructed fetch for a certain range of wind directions. These will determine the values of the displacement height d and the roughness length z_0. The larger region around the site should also be considered for these parameters. Preferably, the considered building has distinct dimensions compared to its surroundings (e.g. $\mathcal{H} \geq 20 \times z_0$),

- the grid and the size of the computational domain depend on the expected wind flow and raindrop trajectories. For instance, the stopping distance of the smallest considered raindrop determines the grid size nearby the building envelope,
- the modelling of turbulent drop dispersion is still an issue for research,
- reliable results depend on realistic values of climatological parameters, namely wind speeds, wind directions, horizontal rain intensities and raindrop spectra. For a climate like that of the Netherlands, the raindrop spectrum parameterisations of Wessels (1972) are very useful.

Further measurements and simulations

In most of the previous suggestions we addressed further studies for our own site. More general suggestions are formulated in the following items:

▹ From the start of the present study in 1996, only few comparisons between full-scale measurements and simulations of driving rain on a particular building in a particular topography have been reported (van Mook 1999a and Blocken et al. 2001). However, the number of studies on CFD simulations without the validation with full-scale measurements is larger (section 1.3).

Important for the advance of the knowledge on driving rain are several further studies in which CFD simulations are validated with full-scale measurements. Of course, one should carefully select another situation (i.e. a particular building and its environment), given the limitations of CFD simulations. One should also pay attention to the instrumentation and the measurement method. In order to make a comparison between our situation and other situations feasible, we recommend to carry out measurements and simulations in situations which are comparable to our situation. This means:

- The geometry of buildings is considered comparable if it has a simple shape, i.e. without many or complex protrusions or recesses. Given the Main Building, it would be interesting to investigate e.g. two-dimensional situations of two blocks of flats or two rows of terraced houses, and three-dimensional situations of a tower, a building with a large indentation in the middle of the roof or a building with a large canopy.

  With regard to the surrounding topography we refer to our above-mentioned considerations for reliable CFD results.
- The climate of the site is nearly the same as that at the TUE site, as the driving rain onslaught in moderate maritime climates are very different from the onslaught in e.g. tropical thunderstorms (cf. Choi 1999a).

- A full-scale experiment is designed with the approach described in chapters 3 and 4 and with the recommendations resulting from these chapters borne in mind. We recommend especially to obtain measured data at small time bases (of the order of 1–5 min), to measure continuously during at least 6 months, not to use tipping-bucket gauges, to measure raindrop spectra, and —of course— to use a driving rain gauge as accurate as TUE-II.

The comparison between our situation and other situations may relate to: the validation of model 1 (eq. 5.3) and model 2 (eq. 5.4), the validation of the turbulent raindrop dispersion modelling in CFD and the influence of raindrop spectra on driving rain.

▹ Within the context of the previous item, collaboration between driving rain research projects at different locations, like by Blocken et al. (2001), should be stimulated.

▹ Pictures of façades which were just exposed to driving rain, may give a nice overview on the wetting of a façade, and help in acquiring qualitative data for validation of CFD simulations. Such pictures may also serve to understand the influence of façade details (e.g. projections) on driving rain onslaught and run-off. Moreover, small projections and canopies are difficult to implement in a CFD model. It is recommended to take photographs (before, during and after rain), such as done by El-Shimi et al. (1980) and Snape and Atkinson (1999).

▹ The TUE-II gauges were suitable for our driving rain measurements, but they are not easily installed due to the size of their collectors and the space needed for the reservoirs and balances. A 'portable' gauge is needed when one would like to do more in situ driving rain measurements. Perhaps a driving rain gauge equipped with a drop-counting device (see above) could serve for this.

Samenvatting

Slagregen op de gebouwschil

Hoofdstuk 1

De duurzaamheid van een gebouwschil (gevels en daken) is beperkt door degradatie zoals vanwege warmte- en vochttransport, depositie van chemische stoffen, ontwerpfouten en fouten tijdens de bouw. Voor een duurzaam ontwerp is kennis van de blootstelling van het gebouw aan de atmosfeer een vereiste. Een van de belangrijke micro-klimatologische parameters is slagregen (« driving rain » ofwel « wind-driven rain »). Deze is gedefinieerd als de regen die door de wind op de gebouwschil terecht komt.

Wanneer we de literatuur over slagregen overzagen, bleek dat de kennis over de kwantificering van de slagregen als funktie van gebouwvorm, wind en regen veel leemtes bevatte. Zo bestonden er geen ontwerpregels voor slagregenmeters en waren er geen resultaten van zowel metingen als simulaties van slagregen in dezelfde situatie gepubliceerd. Ons onderzoek heeft de volgende doelen: (1) het ontwikkelen en testen van slagregenmeters, (2) het gedetailleerd meten van slagregen op de gevel van een gebouw samen met de relevante meteorologische grootheden, (3) het ontwikkelen en toepassen van simulaties en rekenmethodes voor de slagregen op de gebouwschil, met verificatie met metingen in dezelfde situatie.

Hoofdstuk 2

In dit hoofdstuk worden de toe te passen grootheden voor wind, regen en slagregen gedefinieerd. In een « theoretisch model » beschrijven we slagregen als funktie van de wind nabij het gebouw en de druppelgrootte. Dit model wordt in hoofdstuk 6 voor onze computersimulaties uitgewerkt en toegepast. De hoeveelheid water die per tijdsinterval op de gebouwschil terecht komt, is de som van individuele regendruppels in dat tijdsinterval. Deze som wordt normaliter gemeten en daarvoor wordt een « empirisch model » beschreven, dat in hoofdstuk 5 voor onze metingen wordt uitgewerkt en toegepast.

Hoofdstuk 3

In dit hoofdstuk worden het testobjekt en de meetinstrumenten uitgebreid beschreven.

Als testobjekt is het 45 m hoge Hoofdgebouw op het TUE-terrein gekozen. Het gebouw en zijn omgeving (figuren 3.1–3.6) zijn redelijk eenvoudig van vorm. Een bruikbare referentie van het lokale klimaat kan men bovendien aan de westkant van het Hoofdgebouw, op het Auditorium, meten. De referentiewindsnelheid en -windrichting worden op 45 m hoogte, op een mast op het dak van het Auditorium, gemeten; Geurts (1997) heeft reeds de eigenschappen van de wind in deze situatie bestudeerd. De referentieregenintensiteit wordt op het dak van het Auditorium gemeten.

Slagregen wordt gemeten op twee posities op eenzelfde hoogte op de westgevel van het Hoofdgebouw (figuren 3.7–3.9). Op een middenpositie (P4/5/7) zijn vier verschillende slagregenmeters vlak naast elkaar geïnstalleerd. Ook wordt daar de windsnelheid vlak aan de gevel (50 tot 125 cm) gemeten. De andere meetpositie (P6) is aan de noordelijke rand van de gevel.

Twee slagregenmeters, een traditioneel ontwerp (TUE-I, figuur 3.13) en een verbeterd ontwerp met een draaiende wisser (TUE-II, figuur 3.14), zijn aan de TUE ontwikkeld. De twee andere slagregenmeters zijn aan de Chalmers Universiteit in Göteborg (CTH, figuur 3.17) en respektievelijk aan de Technische Universiteit Denemarken (DTU, figuur 3.18) ontwikkeld. De vier slagregenmeters verschillen in opvangoppervlakte en meetprincipe (tabel 3.5).

Hoofdstuk 4

De registraties van de vier slagregenmeters op de gevel van het Hoofdgebouw worden in dit hoofdstuk met elkaar vergeleken, teneinde ontwerpregels voor slagregenmeters op te stellen. De ontwerpregels zijn in paragraaf 4.4 samengevat.

De maandelijkse slagregensommen volgens de CTH-, DTU- en TUE-II-meter verschillen binnen 30% van elkaar (tabel 4.1). De TUE-I-meter (zonder wisser) meet ongeveer de helft van de slagregensom; dit geldt ook voor registraties op 10-minutenbasis (figuur 4.1c). Hieruit concluderen we dat een slagregenmeter met een groot opvangoppervlak (ca. 0,5 m^2) een grote systematische meetfout heeft indien men niet alle opgevangen slagregenwater laat registeren: de wisser van de TUE-II-meter voorkomt immers afdoende dat opgevangen regendruppels verdampen en daarom ongemeten blijven. Het toepassen van een tipping bucket voor het meten van de opgevangen regenflux, zoals bij de CTH-meter, is niet aan te raden voor het bepalen van slagregenintensiteiten op 5- of 10-minutenbasis, omdat de meetnauwkeurigheid voor zulke tijdsbasissen te klein is. Overigens geldt deze aanbeveling ook voor gewone regenmeters, waarmee men regenintensiteiten door een horizontaal vlak meet. Twee andere aanbevelingen zijn (i) het

nader onderzoeken van de invloed van de grootte en vorm van het opvangoppervlak met slagregenmeters met hetzelfde meetprincipe, en (ii) het in volle schaal testen van een slagregenmeter met een druppelteller voor het meten van de flux van het opgevangen regenwater (Bijsterbosch 2000). Hieruit, samen met de bevindingen uit dit proefschrift, kan een in situ eenvoudiger toe te passen slagregenmeter worden ontwikkeld.

In het vervolg worden uitsluitend de resultaten van de goed gebleken TUE-II-meter gebruikt.

Hoofdstuk 5

Dit hoofdstuk begint met een beschrijving van de dataverwerking en -selektie. Tijdens een periode van 24 maanden hebben de volle-schaalmetingen continu plaatsgevonden. Vervolgens komt een algemene presentatie van deze unieke wind-, regen- en slagregenmetingen in de vorm van statistieken, correlaties tussen grootheden en correlaties tussen meetposities aan bod. De meetgegevens zijn beschikbaar via website http://sts.bwk.tue.nl/drivingrain/ .

Een belangrijk resultaat is de grote spreiding in de gemeten slagregenintensiteiten voor nauwe intervallen van de referentiewindsnelheid, -windrichting en -regenintensiteit (zie bijvoorbeeld figuur 5.14). Het verband tussen de twee meetposities aan de gevel is ingewikkeld (tabel 5.4). De grote spreiding wordt verklaard met de dispersie van regendruppels door turbulentie van de wind en met de grote variatie in regendruppelspektra (grootteverdelingen van regendruppels). Dit laatste blijkt uit de metingen van de regendruppelspektra met een disdrometer (figuren 5.20–5.22; onze metingen van regendruppelspektra beslaan slechts 3 maanden). Tevens blijkt dat parameterisaties van druppelspektra uit de literatuur (Wessels 1972) het aantal grote druppels ($D > 1{,}5$ mm) onderschatten (figuur 5.22).

Vervolgens komen in het hoofdstuk twee empirische modellen aan bod voor de slagregenintensiteit als funktie van referentiewindsnelheid, -windrichting, -regenintensiteit en positie op de gevel. Model 1 is een eenvoudige empirische formule (vgl. 5.3) volgens Lacy (1965), waarop de Britse norm BS 8104 (BSI 1992) voor het schatten van slagregensommen op gevels is gebaseerd. Model 1 gaat uit van totalen van de afzonderlijke 5-minutenwaardes over een langere periode (1 of 2 jaar). Uit onze metingen worden de waardes van de parameters van model 1 bepaald, en deze worden vervolgens gebruikt om de slagregenintensiteiten te schatten. De cumulatieve slagregensom over 24 maanden wordt op de middenpositie P4/5 met 4–46% en op de randpositie P6 met 17–34% overschat. De slagregenintensiteiten op 5-minutenbasis en hun maxima worden slecht geschat: 5–8 mm h^{-1} voor de gemeten maxima van 25–29 mm h^{-1}.

Model 2 is een door ons voorgesteld verbeterd empirisch model dat preciezer rekening met windrichting en positie op de gevel houdt (vgl. 5.4). Bovendien gaan we uit van

afzonderlijke 5-minutenwaardes. Zowel de cumulatieve slagregensom over 24 maanden (afwijkingen van 6–23% voor P4/5 en 8–33% voor P6) als de slagregenintensiteiten op 5-minutenbasis en hun maxima (afwijkingen tot ca. 2 mm h^{-1}) worden redelijk tot goed geschat.

Model 2 is dus geschikter voor slagregenintensiteiten op kleine tijdschaal dan model 1. Voor het berekenen van slagregensommen over langere tijd zijn beide modellen bijna even geschikt.

Hoofdstuk 6

In dit hoofdstuk worden de methodes en de resultaten van de computersimulaties van wind en regen rond het Hoofdgebouw en slagregen op de westgevel besproken.

Een standaard K-ϵ-model van het programma *Fluent* (versies 4.4 en 4.5) wordt voor de simulaties gebruikt. Het rekendomein wordt als een « structured grid » in cellen opgedeeld, wat helaas op sommige plaatsen tot ongewenste celverhoudingen leidt. Ondanks de beperkingen van het model (zie ook bijvoorbeeld Murakami et al. 1992), valt de gesimuleerde windsnelheid vlak voor de gevel bij de middenpositie P4/5 binnen de standaarddeviatie van de gemeten windsnelheid. Verder zijn de gesimuleerde gemiddelde drukcoëfficiënten positief met in situ- en windtunnelmetingen van dezelfde situatie (Geurts 1997) vergeleken.

In de simulatie van slagregen wordt uitgegaan van het reeds berekende windveld nabij het Hoofdgebouw. Bij het berekenen van de banen van de druppels veronderstellen wij dat de regen het windveld niet beïnvloedt en dat regendruppels niet verdampen, niet met elkaar botsen en niet uiteenvallen. We hanteren twee modellen voor het berekenen van de regendruppelbanen, namelijk zònder en mèt turbulente dispersie van druppels (figuur 6.3). Simulaties van slagregen met turbulente dispersie geven duidelijk grotere slagregenintensiteiten dan simulaties zonder turbulente dispersie (figuren 6.16–6.19). Dit komt doordat druppels door de (extra) component van de turbulente windsnelheid makkelijker naar de gevel worden gedreven. Bovendien: hoe langer een druppel langs een gevel vliegt, hoe groter de kans is dat deze door de turbulentie tegen de gevel komt. Tegelijkertijd kan men beargumenteren dat simulaties met turbulente dispersie de slagregen overschatten omdat het K-ϵ-model van isotrope turbulentie uitgaat. De gemeten slagregenintensiteiten vallen inderdaad voornamelijk tussen de gesimuleerde slagregenintensiteiten met en die zonder turbulente dispersie. Hierbij gaat het overigens om simulaties die op de parameterisaties van regendruppelspektra door Wessels (1972) zijn gebaseerd. Duidelijke conclusies aan de hand van de door ons gemeten regendruppelspektra zijn niet mogelijk omdat het aantal spektrametingen met slagregen te beperkt is (een te korte meetperiode).

Hoofdstuk 7

In het laatste hoofdstuk wordt het onderzoek aan de hand van conclusies en aanbevelingen samengevat. Aan de orde komt de vraag onder welke voorwaardes verdere metingen en simulaties kunnen worden gedaan om de kennis over slagregen uit te breiden. Onder andere om onze bevindingen met model 1 en 2 en onze simulaties van turbulente dispersie van regendruppels te controleren, menen we dat het nodig is zodanig verder met in situ-metingen en computersimulaties van andere situaties te gaan dat een redelijke vergelijking met onze resultaten mogelijk is. Hierbij spelen de keuze van het testobjekt (gebouw) met zijn omgevingstopografie, de beperkingen van computersimulaties en de keuze (nauwkeurigheid) van meetinstrumenten een zeer belangrijke rol.

References

Basart, A. (1946). *Verhandeling inzake de regenval op het verticale vlak met betrekking tot de bouwconstructie*. Technical report, Instituut voor Warmte-Economie TNO & Keramisch Instituut TNO, 's-Gravenhage (NL).

Beranek, W. (1994a). Wind environment around building configurations. *Heron 29*(1), 33–70.

Beranek, W. (1994b). Wind environment around single buildings of rectangular shape. *Heron 29*(1), 4–31.

Best, A. (1950). The size distribution of raindrops. *Q. J. R. Meteorol. Soc. 76*, 16–36.

Bijsterbosch, K. (2000). *Slagregenmeting met behulp van een druppelteller*. T9-project report, Building Physics group, Eindhoven University of Technology.

Blocken, B. and J. Carmeliet (2000a). Driving rain on building envelopes – (I) numerical estimation and full-scale experimental verification. *Journal of Thermal Envelope and Building Science 24*, 61–85.

Blocken, B. and J. Carmeliet (2000b). Driving rain on building envelopes – (II) representative experimental data for driving rain estimation. *Journal of Thermal Envelope and Building Science 24*, 89–110.

Blocken, B., J. Carmeliet, and H. Hens (1999). A numerical and an experimental approach for estimating driving rain loads on building envelopes. In *10th International Symposium for Building Physics and Building Climatology, Dresden (DE), September 1999*.

Blocken, B., F. van Mook, C.-E. Hagentoft, and J. Carmeliet (2001). A status report of numerical-experimental driving rain studies on 3 full-scale buildings. In *Third European and African Conference on Wind Engineering, Eindhoven (NL), 2–6 July 2001*, pp. 133–140.

Bookelmann, J. and J. Wisse (1992). Numerical estimate of driving rain. In *Inaugural Conference of the Wind Engineering Society, Cambrigde (UK), 28–30 September 1992*. Wind Engineering Society.

Bottema, M. (1993a). Numerieke simulatie met K-ϵ modellen en ASM; betrouwbaarheid, mogelijkheden en onmogelijkheden. In *Workshop computational fluid dynamics toepassingen voor de windtechnologie: theorie en praktijk, 25 November 1993*. Stuurgroep Windtechnologie, KIVI.

Bottema, M. (1993b). *Wind climate and urban geometry*. Ph. D. thesis, Eindhoven University of Technology.

Brocken, H. J. (1998). *Moisture transport in brick masonry: the grey aera between bricks*. Ph. D. thesis, Eindhoven University of Technology.

Brown, B. (1988). *Field measurements to gauge catch ratios of free-space driving rain on house walls at exposed estates in Dorset*. BRE Note N 127/88, Building Research Establishment, Watford (UK).

BSI (1992). *BS 8104: Code of practice for assessing exposure of walls to wind-driven rain*. British Standards Institute.

Buishand, T. and C. Velds (1980). *Neerslag en verdamping*. De Bilt (NL): KNMI.

Choi, E. (1993). Simulation of wind-driven-rain around a building. *Journal of Wind Engineering and Industrial Aerodynamics 46/47*, 721–729.

Choi, E. (1994a). Characteristics of the co-occurrence of wind and rain and the driving-rain index. *Journal of Wind Engineering and Industrial Aerodynamics 53*, 49–62.

Choi, E. (1994b). Determination of wind-driven-rain intensity on building faces. *Journal of Wind Engineering and Industrial Aerodynamics 51*, 55–69.

Choi, E. (1994c). Parameters affecting the intensity of wind-driven rain on the front face of a building. *Journal of Wind Engineering and Industrial Aerodynamics 53*, 1–17.

Choi, E. (1995). Numerical modelling of gust effect on wind-driven rain. In *9th International Conference on Wind Engineering, New Delhi (IN), 9–13 January 1995*, pp. 214–215. International Association for Wind Engineering.

Choi, E. (1999a). Characteristics of wind and wind-driven rain during tropical thunderstorms. In *Wind engineering into the 21st century: Proceedings of the 10th International Conference on Wind Engineering. København (DK), 21–24 June 1999*, pp. 729–736.

Choi, E. (1999b). Wind-driven rain on building faces and the driving-rain index. *Journal of Wind Engineering and Industrial Aerodynamics 79*, 105–122.

Choi, E. (2001). Wind-driven rain and driving rain coefficient during thunderstorms and non-thunderstorms. *Journal of Wind Engineering and Industrial Aerodynamics 89*, 293–308.

Couper, R. (1974). Factors affecting, the production of surface runoff from wind-driven rain. In *2nd International CIB/RILEM Symposium on Moisture problems in buildings, Rotterdam (NL), 10–12 September 1974*.

Crowe, C., M. Sommerfeld, and Y. Tsuji (1998). *Multiphase flows with droplets and particles*. London: CRC Press.

de Wit, M., T. Stathopoulos, and J. Wisse (2002). Airport wind speeds used for the design in urban environments: the Eindhoven case. *Journal of Wind Engineering and Industrial Aerodynamics 90*(11), 1289–1298.

El-Shimi, M., R. White, and P. Fazio (1980). Influence of façade geometry on weathering. *Canadian Journal of Civil Engineering/ Revue canadienne de génie civil 7*, 579–613.

Etyemezian, V., C. Davidson, M. Zufall, W. Dai, S. Finger, and M. Striegel (2000). Impingement of rain drops on a tall building. *Atmospheric Environment 34*, 2399–2412.

Flori, J.-P. (1988). *Conditions de mouillage et de séchage des façades verticales: Étude bibliographique*. Technical Report EN-CLI 88-17 L, Centre Scientifique et Technique du Bâtiment, Nantes (FR).

Flori, J.-P. (1990). *Mouillage et séchage d'une façade verticale: analyse expérimentale*. Technical Report EN-CLI 90.2 L, Centre Scientifique et Technique du Bâtiment, Nantes (FR).

Fluent (1995). *Fluent user's guide; Version 4.3*. Fluent Inc.

Fluent (1997). *Fluent 4.4 user's guide*. Fluent Inc.

Frank, W. (1973). Einwirkung von Regen und Wind auf Gebäudefassaden. In *Berichte aus der Bauforschung*, Volume H. 86, pp. 3–13. Berlin: Wilhelm Ernst & Sohn.

Fuchs, N. (1964). *The mechanics of aerosols*. Oxford: Pergamon Press.

Gandemer, J. and G. Barnaud (1995). The Jules Verne climatic wind tunnel: innovative design for aerodynamic and climatic studies. In *9th International Conference on Wind Engineering, New Delhi (IN), 9–13 January 1995*, pp. 1740–1741. International Association for Wind Engineering.

Geurts, C. (1994). *Wind induced pressures on the main building of the Eindhoven University of Technology; configuration of the full scale experiment*. BKO-report 94-05, Eindhoven University of Technology.

Geurts, C. (1997). *Wind induced pressure fluctuations on building facades*. Ph. D. thesis, Eindhoven University of Technology.

Grossklaus, M., K. Uhlig, and L. Hasse (1998). An optical disdrometer for use in high wind speeds. *Journal of Atmospheric and Oceanic Technology 15*, 1051–1059.

Grunau, E. B. (1973). *Verhinderung van Bauschäden; Verwitterung, Erosion und Korrosion von Baustoffen — Moderne Schutzmethoden*. Köln-Braunsfeld (DE): Verlagsgesellschaft Rudolf Müller.

Grunau, E. B. (1975). *Die Außenwand; Fassade, Wasserhaushalt, bauphysikalische Funktionen*. Köln-Braunsfeld (DE): Verlagsgesellschaft Rudolf Müller.

Gunn, R. and G. Kinzer (1949). The terminal velocity of fall for water droplets in stagnant air. *Journal of Meteorology 6*, 243–248.

Hangan, H. and D. Surry (1998). Wind-driven rain on buildings: A C-FD-E approach. In *Proceedings of the 4th UK Conference on Wind Engineering, Bristol (UK), 2–4 September 1998*, pp. 23–28. Wind Engineering Society.

Henriques, F. (1992). Quantification of wind-driven rain — an experimental approach: a general review on driven rain and details of an experiment in Portugal to supplement existing research results in Norway, the UK and elsewhere. *Building Research and Information 20*(5), 295–297.

Hens, H. and F. A. Mohamed (1994). Preliminary results on driving rain estimation. In *IEA Annex 24: Heat, air and moisture transfer through new and retrofitted insulated envelope parts (Hamtie) — Task 2, Environmental Conditions, T2-B-94/02*. International Energy Agency.

Högberg, A. (1998). *Microclimate description: To facilitate estimating durability and service life of building components exposed to natural outdoor climate*. Technical Report P-98:5, Chalmers University of Techology, Göteborg (SE).

Högberg, A. (1999). Microclimate measurement focused on wind-driven rain striking building surfaces. In *5th Symposium of Building Physics in the Nordic Countries, Göteborg (SE), 24–26 August 1999*, pp. 369–375.

Högberg, A. (2002). *Microclimate load: transformed weather observations for use in design of durable buildings*. Ph. D. thesis, Dep. of Building Physics, Chalmers University of Technology.

Högberg, A., M. K. Kragh, and F. van Mook (1999). A comparison of driving rain measurements with different gauges. In *5th Symposium of Building Physics in the Nordic Countries, Göteborg (SE), 24–26 August 1999*, pp. 361–368.

Inculet, D. and D. Surry (1995). *Simulation of wind-driven rain and wetting patterns on buildings*. Technical Report BLWTL-SS30-1994, Boundary Layer Wind Tunnel Laboratory, University of Western Ontario, London (CA).

Joss, J. and E. Gori (1978). Shapes of raindrop size distributions. *Journal of Applied Meteorology 17*, 1054–1061.

Joss, J. and A. Waldvogel (1967). Ein Spektrograph für Niederschlagstropfen mit automatischer Auswertung. *Pure and Applied Geophysics 68*, 240–246.

Joss, J. and A. Waldvogel (1969). Raindrop size distribution and sampling size errors. *Journal of the Atmospheric Sciences 26*, 566–569.

Karagiozis, A. and G. Hadjisophocleous (1996). Wind-driven rain on tall buildings. In *Proceedings of the 4th symposium on Building Physics in the Nordic Countries: Building Physics '96, Espoo (SF), 9–10 September 1996*, pp. 523–532. VTT Building Technology.

Karagiozis, A., G. Hadjisophocleous, and S. Cao (1997). Wind-driven rain distributions on two buildings. *Journal of Wind Engineering and Industrial Aerodynamics 67&68*, 559–572.

Kerr, D., R. Matthews, and T. Kirmayr (1997). To develop a European standard dynamic watertightness test for curtain walling. In *Proceedings of the 2nd European and African Conference on Wind Engineering, Genova (IT), 22–26 June 1997*, Volume 2, pp. 1051–1058.

KNMI (1992). *Climatological data of stations in the Netherlands — Normals and extreme values of the fifteen principal stations for the period 1961–1990*. Publication 150-27, KNMI, De Bilt (NL).

KNMI (1997–99). *Maandoverzicht van het weer in Nederland*. MOW-bulletin vols. 94 (12) – 96 (8), KNMI, De Bilt (NL).

KNMI (1999). *Jaarverslag 1998 — in het teken van de regen*. Annual report, KNMI, De Bilt (NL).

KNMI (2000). *KNMI HYDRA project: wind climate assessment of the Netherlands*. Url: http://www.knmi.nl/samenw/hydra/ (first published on 24-2-2000), KNMI, De Bilt (NL).

Knollenberg, R. (1970). The optical array: An alternative to scattering or extinction for airborne particle size determination. *Journal of Applied Meteorology 9*, 89–103.

Kragh, M. K. (1998). *Microclimatic conditions at the external surface of building envelopes*. Ph. D. thesis (report R-027), Dep. of Building Physics, Technical University of Denmark.

Künzel, H. (1994). Bestimmung der Schlagregenbelastung von Fassadenflächen. In *IBP-Mitteilung 21(263)*. Stuttgart (DE): Fraunhofer-Institut für Bauphysik.

Lacy, R. (1965). Driving-rain maps and the onslaught of rain on buildings. In *RILEM/CIB Symposium on Moisture in Buildings, Helsinki (SF), 1965*.

Lacy, R. (1977). *Climate and building in Britain; A review of meteorological infomation suitable for use in the planning, design, construction and operation of buildings*. London (UK): Building Research Establishment.

Lakehal, D., P. Mestayer, J. Edson, S. Anquetin, and J.-F. Sini (1995). Eulero-Lagrangian simulation of raindrop trajectories and impacts within the urban canopy. *Atmospheric Environment 29*, 3501–3517.

Launder, B. and D. Spalding (1974). The numerical computation of turbulent flows. *Computer Methods in Applied Mechanics and Engineering 3*, 269–289.

Laws, J. O. and D. A. Parsons (1943). The relation of raindrop-size to intensity. *Transactions American Geophysical Union 24*, 452–460.

Löffler-Mang, M. and J. Joss (2000). An optical disdrometer for measuring size and velocity of hydrometeors. *Journal of Atmospheric and Oceanic Technology 17*, 130–139.

Marshall, J. and W. Palmer (1948). The distribution of raindrops with size. *Journal of Meteorology 5*, 165–166.

METEK (2000). *Micro Rain Radar MRR-2*. Url: http://www.metek.de (as published on 10-1-2000), METEK Meteorologische Meßtechnik, Hamburg (DE).

Middleton, W. K. (1969). *Invention of the meteorological instruments*. Baltimore: The Johns Hopkins Press.

Montgomery, D. and G. Runger (1999). *Applied statistics and probability for engineers*. New York (US): John Wiley & Sons.

Morsi, S. and A. Alexander (1972). An investigation of particle trajectories in two-phase flow systems. *Journal of Fluid Mechanics 55*, 193–208.

Mulvin, L. and J. Lewis (1994). Architectural detailing, weathering and stone decay. *Building and Environment 29*(1), 113–138.

Murakami, S., A. Mochida, Y. Hayashi, and S. Sakamoto (1992). Numerical study on velocity-pressure field and wind forces for bluff bodies by k-ϵ, ASM and LES. *Journal of Wind Engineering and Industrial Aerodynamics 41-44*, 2841–2852.

Newman, A., D. Whiteside, P. Kloss, and W. Willis (1982). Full-scale water penetration tests on twelve cavity fills — Part I. Nine retrofit fills, Part II. Three built-in fills. *Building and Environment 17*, 175–207.

Oemraw, B. (1982). *Stationsbeschrijving windwaarneming Eindhoven (VB) – periode 1949-1980*. Technical Report T.R. 29, KNMI, De Bilt (NL).

Osmond, S. (1995). *Assessment of the full scale micro-climate around buildings*. BRE Note N47/95, Building Research Establishment, Watford (UK).

Osmond, S. (1996). *Assessment of the full scale micro-climate around builings*. BRE Note N91/96, Building Research Establishment, Watford (UK).

Panofsky, H. and J. Dutton (1984). *Atmospheric turbulence, models and methods for engineering applications*. New York (US): Wiley International.

PMTech (1999). *Instruction manual: Parsivel M300, laser-optical device for measuring particle size and velocity simultaneously*. Forschungzentrum Karlsruhe & PMTech AG Karlsruhe.

PMTech (2000). *Parsivel M300*. Url: http://www.pmtech.de/deutsch/pro/parsivel.htm (as published on 24-8-2000), PMTech AG, Karlsruhe (DE).

Prior, M. (1985). *Directional driving rain indices for the United Kingdom — computation and mapping: background to BSI Draft for Development DD93*. Technical report, Building Research Establishment, Garston (UK).

Pruppacher, H. and J. Klett (1978). *Microphysics of clouds and precipitation*. Dordrecht (NL): Reidel Publishing Company.

Raasch, J. and H. Umhauer (1984). Errors in the determination of particle size distributions caused by coincidences in optical particle counters. *Particle Characterization 1*, 53–58.

Richter, C. and M. Hagen (1997). Drop-size distributions of raindrop by polarization radar and simultaneous measurements with disdrometer, windprofiler and PMS probes. *Q. J. R. Meteorol. Soc. 123*, 2277–2296.

Rodgers, G. G., G. Poots, J. Page, and W. Pickering (1974). Rain impaction on a slab type building: a theoretical approach. In *2nd International CIB/RILEM Symposium on Moisture Problems in Buildings, Rotterdam (NL), 10–12 September 1974*.

Rodi, W. (1980). Turbulence models for environmental flows. In W. Knollmann (Ed.), *Prediction methods for turbulent flows*, pp. 259–350. London: Hemisphere Publ. Corp.

Salles, C., J. Creutin, and D. Sempere-Torres (1998). The optical spectropluviometer revisited. *Journal of Atmospheric and Oceanic Technology 15*, 1215–1222.

Sandberg, P. I. (1974). Driving rain distribution over an infinitely long, high building: computerized calculations. In *2nd International CIB/RILEM Symposium on Moisture Problems in Buildings, Rotterdam (NL), 10–12 September 1974*.

Sankaran, R. and D. Paterson (1995a). Computation of rain falling on a tall rectangular building. In *9th International Conference on Wind Engineering, New Delhi (IN), 9–13 January 1995*, pp. 2127–2137. International Association for Wind Engineering.

Sankaran, R. and D. Paterson (1995b). Wind driven rain: data collection facility at CSIRO, Sydney, Australia. In *9th International Conference on Wind Engineering, New Delhi (IN), 9–13 January 1995*, pp. 2023–2033. International Association for Wind Engineering.

Schaffer, R. (1972). *The weathering of natural building stones*. Garston (UK): Building Research Station.

Schönhuber, M., H. Urban, J. P. Baptista, W. Randeu, and W. Rielder (1994). Measurements of precipitation characteristics by a new disdrometer. In *Proceedings of Atmospheric Physics and Dynamics in the Analysis and Prognosis of Precipitation Fieds, Rome (IT), 1994*.

Schönhuber, M., H. Urban, W. Randeu, and J. P. Baptista (2000). Distrometer results obtained in various climates and their applications to weather radar data inversion. In *ESA SP-444 Proceedings « Millenium Conference on Antennas and Propagation », Davos (CH), 9–14 April 2000*.

Sempere Torres, D. and J. Porrà (1994). A general formulation for raindrop size distribution. *Journal of Applied Meteorology 33*, 1494–1502.

Sheppard, B. (1990). Measurement of raindrop size distributions using a small Doppler radar. *Journal of Atmospheric and Oceanic Technology 7*, 255–268.

Simiu, E. and R. Scanlan (1996). *Wind effects on structures* (3 ed.). New York (US): John Wiley & Sons.

Simpson, J. W. and P. J. Horrobin (1970). *The weathering and performance of building materials*. Aylesbury: Medical and Technical Publ. Co. Ltd.

Snape, P. and B. Atkinson (1999). Mapping rainfall distribution characteristics on façades using surface deposit geometry. In *Proceedings of the 8th international Conference on Durability of Building Materials and Components, Volume 2, Vancouver (CA), 30 May – 3 June 1999*, pp. 943–955.

Straube, J. (1998). *Moisture control and enclosure wall systems*. Ph. D. thesis, University of Waterloo, Waterloo (CA).

Surry, D., D. Inculet, P. Skerlj, J.-X. Lin, and A. Davenport (1994). Wind, rain and the building envelope: a status report of ongoing research at the University of Western Ontario. *Journal of Wind Engineering and Industrial Aerodynamics 53*, 19–36.

Uijlenhoet, R. (1999). *Parameterization of rainfall microstructure for radar meteorology and hydrology*. Ph. D. thesis, Wageningen University.

Uijlenhoet, R. and J. Stricker (1999). A consistent rainfall parametrization based on the exponential raindrop size distribution. *Journal of Hydrology 218*, 101–127.

Ulbrich, C. (1983). Natural variations in the analytical form of the raindrop size distribution. *Journal of Climate and Applied Meteorology 22*(10), 1764–1775.

van Mook, F. (1998a). *Description of the measurement set-up for wind and driving rain at the TUE*. Technical Report FAGO 98.04.K, Building Physics group, Eindhoven University of Technology.

van Mook, F. (1998b). *Measurements of driving rain by a driving-rain gauge with a wiper*. Paper presented at CIB taskgroup 21 meeting, Gävle (SE), 5–6 June 1998, Building Physics group, Eindhoven University of Technology.

van Mook, F. (1999a). Full-scale measurements and numeric simulation of driving rain on a building fasade. In *Wind engineering into the 21st century: Proceedings of the 10th International Conference on Wind Engineering. København (DK), 21–24 June 1999*, pp. 1145–1152.

van Mook, F. (1999b). Measurements and simulations of driving rain on the Main Building of the TUE. In *5th Symposium of Building Physics in the Nordic Countries, Göteborg (SE), 24–26 August 1999*, pp. 377–384.

van Mook, F., M. de Wit, and J. Wisse (1997). Computer simulation of driving rain on building envelopes. In *Proceedings of the 2nd European and African Conference on Wind Engineering, Genova (IT), 22–26 June 1997*, pp. 1059–1066.

Verkaik, J. (1999). *Documentatie windmetingen in Nederland*. Report published at http://www.knmi.nl/samenw/hydra/ on 9 december 1999, KNMI, De Bilt (NL).

Verkaik, J. (2000). Evaluation of two gustiness models for exposure correction calculations. *Journal of Applied Meteorology 39*(9), 1613–1626.

Waldvogel, A. (1974). The N_0 jump of raindrop spectra. *Journal of the Atmospheric Sciences 31*, 1067–1078.

Wessels, H. (1967). *Druppelgroottemeter voor regen*. Verslag v 197-vi, KNMI, De Bilt (NL).

Wessels, H. (1972). *Metingen van regendruppels te De Bilt*. Technical Report W.R. 72-6, KNMI, De Bilt (NL).

Wieringa, J. (1992). Updating the Davenport roughness classification. *Journal of Wind Engineering and Industrial Aerodynamics 41-44*, 357–368.

Wieringa, J. (1996). Does representative wind information exist? *Journal of Wind Engineering and Industrial Aerodynamics 65*, 1–12.

Winkler, E. (1997). *Stone in architecture; Properties, durability*. Berlin: Springer-Verlag.

Wisse, J. (1994). Driving rain, a numerical study. In *9th Symposium for Building Physics and Building Climatology, Dresden (DE), 14–16 September 1994*.

Symbols

Latin symbols

a, A		empirical constants in Best (1950) drop spectrum (eq. 2.24)
A	[m^2]	area
A_{catch}	[m^2]	catchment area
b		empirical constant in Best (1950) drop spectrum (eq. 2.24)
c		slope of the fit function $y = cx$, in correlation plots
c_p	[-]	mean pressure coefficient
C		empirical constant in Best (1950) drop spectrum (eq. 2.24)
C_1, C_2, C_3, C_4		parameters in a general formula for raindrop spectra (eq. 2.25)
C_d	[-]	drag coefficient
C_μ	[-]	K-ϵ model constant
$C_{1\epsilon}$	[-]	K-ϵ model constant
$C_{2\epsilon}$	[-]	K-ϵ model constant
d	[m]	displacement height
D	[m]	raindrop diameter
D_{50}	[m]	median median drop size (eq. 2.20)
E	[-]	roughness parameter (eq. 6.5)
$F(D)$	[-]	fraction of liquid water in the air comprised by drops with diameters less than D (eq. 2.19)
g	[m s^{-2}]	gravitational acceleration
$h_{\text{i.b.l.}}$	[m]	internal boundary layer height
$\mathcal{H}$	[m]	building height; obstacle height

I_u, I_v, I_w	[-]	turbulence intensities
k	[-]	driving rain ratio (eq. 2.28)
k	[-]	von Kármán constant (0.4)
K	[m^2 s^{-2}]	turbulent kinetic energy per unit of mass
ℓ_{stop}	[m]	stopping distance
$\mathcal{L}$	[m]	characteristic eddy dimension (section 2.2.3)
$\mathcal{L}_g$	[m]	smaller of $2\mathcal{H}$ (two times building height) and $\mathcal{W}$ (building width), section 2.1.4
L_u	[m]	integral length scale
m	[kg]	mass
$m(D)$	[kg m^{-3} m^{-1}]	raindrop mass concentration spectrum
$n(D)$	[m^{-3} m^{-1}]	raindrop number concentration spectrum
n_0	[m^{-3} m^{-1}]	parameter in Marshall and Palmer (1948) drop spectrum (eq. 2.21)
N	[-]	number
q		empirical constant in Best (1950) drop spectrum (eq. 2.24)
r		correlation coefficient; the coefficient of determination is r^2 (eq. 3.4)
R	[mm h^{-1}]	rain intensity, also expressed in [kg m^{-2} s^{-1}] = [mm s^{-1}]
R_{f}	[mm h^{-1}]	driving rain intensity
Re	[-]	Reynolds number
t	[s]	time
t_{cl}	[s]	averaging and summation period, the periods are synchronised to clock and calendar; the first period of a day starts at 00h00.
t_{dry}	[s]	pause between rain spells
t_{s}	[s]	sample time
t_{prec}	[s]	precipitation time
T	[s]	integral time (eq. 6.7)
u_*	[m s^{-1}]	friction shear velocity
$\vec{u}$	[m s^{-1}]	wind velocity vector
u, v, w	[m s^{-1}]	longitudinal, lateral and vertical wind velocity
$\vec{u}_{\text{D}}$	[m s^{-1}]	raindrop velocity vector
$u_{\text{D}}, v_{\text{D}}, w_{\text{D}}$	[m s^{-1}]	raindrop velocity in x, y and z direction
U	[m s^{-1}]	wind speed $= \sqrt{U_x^2 + U_y^2 + U_z^2}$

U_h	[m s^{-1}]	horizontal wind speed $= \sqrt{U_x^2 + U_y^2}$
U_{10}	[m s^{-1}]	horizontal wind speed at 10 m height on open terrain with $z_0 = 0.03$ m and $d = 0$ m
U_x, U_y, U_z	[m s^{-1}]	wind velocity components (U_x is due north, U_y west, U_z upwards)
U_1, U_2, U_3	[m s^{-1}]	wind velocity vectors according to the anemometer axis system
V_{tip}	[ml]	effective volume of a rain gauge bucket
w_{term}	[m s^{-1}]	terminal drop speed
W	[kg m^3]	liquid water content (i.e. amount of liquid water per unit of air)
$\mathcal{W}$	[m]	building width
x, y, z	[m]	position coordinates (z is upwards)
x, y		x-axis quantity and y-axis quantity of the fit function $y = cx$, in correlation plots
z_0	[m]	roughness length

Greek symbols

α		coefficient in Lacy's formula 2.29
α		coefficient in model 2 (eq. 5.4)
β		exponent in Lacy's formula 2.29
β		exponent in model 2 (eq. 5.4)
β		constant in eq. 6.8
γ		exponent in model 2 (eq. 5.4)
ϵ	[m^2 s^{-3}]	dissipation rate of K
$\eta(D)$	[-]	catch ratio (eq. 2.26)
θ	[°]	constant in function L (fig. 5.23) for model 2 (eq. 5.4)
θ	[°]	angle (in chapter 6)
κ	[-]	obstruction factor, eq. 2.35
Λ	[m^{-1}]	parameter in Marshall and Palmer (1948) drop spectrum (eq. 2.21)
μ		parameter in Ulbrich (1983) drop spectrum (eq. 2.23)
μ	[kg m^{-1} s^{-1}]	dynamic viscosity (1.6–1.8 10^{-5} kg m^{-1} s^{-1} for air), $\mu = \rho\nu$
ν	[m^2 s^{-1}]	kinematic viscosity (1.3–1.5 10^{-5} m^2 s^{-1} for air), $\nu = \mu/\rho$

ν_t	[m^2 s^{-1}]	turbulent or eddy viscosity
ξ	[-]	constant in function L (fig. 5.23) for model 2 (eq. 5.4)
ρ	[kg m^{-3}]	density
σ_K	[-]	K-ϵ model constant
σ_ϵ	[-]	K-ϵ model constant
τ	[N m^{-2}]	turbulent shear stress $\rho u'w'$
τ_0	[N m^{-2}]	surface shear stress (eq. 2.2)
$\varphi(D)$	[kg m^{-2} s^{-1} m^{-1}]	raindrop mass flux spectrum (definition of $\varphi_\mathrm{h}(D)$ in eq. 2.16)
Φ	[°]	horizontal wind direction, angle from which the wind blows, clock wise from north (e.g. 270° is wind from west)

Subscripts

5, 10, 60	clock period t_cl = 5, 10 and 60 min respectively
a	air
c	corrected, esp. for rain intensity: rain intensity is obtained by combining data of a tipping-bucket rain gauge and a rain indicator (see section 3.4.3)
D	raindrop
e	estimate (eq. 3.4)
f	at façade
h	horizontal (at reference unless otherwise indicated)
m	measurement (eq. 3.4)
`P1, P2, ...`	measurement positions
r	reference
u	uncorrected, esp. for rain intensity: rain intensity is obtained by simply counting the tippings of a tipping-bucket rain gauge (see section 3.4.3)
v	vertical (at reference unless otherwise indicated)

Operators

$\bar{x}$	mean of x
x'	fluctuating component of x ($x = \bar{x} + x'$)
σ_x	standard deviation of x
$L(\Phi, \theta, \xi)$	$\cos((\Phi - \theta)/\xi)$ for $-90°\xi \leq \Phi - \theta \leq 90°\xi$, and by 0 for the other values of Φ, where ξ is limited to the interval 0–1 (fig. 5.23)

Curriculum vitae

17 November 1971	Born in 's-Hertogenbosch (NL).
1984 – 1990	Grammar school education at the *Orduynen College* in 's-Hertogenbosch. Final examination at pre-university level (*atheneum*) in June 1990.
September 1990 – January 1996	Study at the Faculty of Architecture, Building and Planning of the Eindhoven University of Technology. Specialisation in building physics at the FAGO group of the Faculty. Master's thesis on measurement and visualisation methods for low indoor air velocities. Graduation with distinction (*met lof*) as building engineer (*bouwkundig ingenieur*) in January 1996.
February 1996 – August 2001	Research assistant on the topic of the present thesis, at the aforementioned FAGO group.

Stellingen — Theses

1. Een vermindering van de slagregenbelasting of een maatregel aan een gevel in verband met slagregen begint met de beoordeling (het ontwerp) van de algehele gebouwvorm en de direkte omgeving.

   Reduction of driving rain onslaught or a measure to a façade related to driving rain starts with the judgement (the design) of the total building and its direct surroundings.

2. Metingen van wind, regen en slagregen in situaties die qua eenvoud met onze gebouwgeometrie en omgevingstopografie vergelijkbaar zijn, en die met dezelfde meetnauwkeurigheid als de onze worden uitgevoerd, zijn nodig ter contrôle van methode 2 (eq. 5.4) en de turbulente dispersie van druppelbanen in CFD (paragraaf 6.2).

   Measurements of wind, rain and driving rain in situations which are comparable in simplicity with our building geometry and surrounding topography, and which are carried out with the same accuracy as ours, are necessary in order to validate method 2 (eq. 5.4) and the turbulent dispersion of drop trajectories in CFD (section 6.2).

3. Slagregenmeters met een groot opvangoppervlak moeten met een wisser worden uitgerust (paragraaf 4.2).

   Driving rain gauges with a large catchment area should be equipped with a wiper (section 4.2).

4. Het is jammer dat er in het gebied van het TUE-terrein tot en met het NS-station in Eindhoven met zoveel ongunstig resultaat wordt verbouwd en gebouwd: de (ontstane) hoogbouw veroorzaakt een slecht windklimaat voor voetgangers en fietsers. Bovendien verandert het voorheen relatief ongestoorde voorland waar we bij onze wind- en regenmetingen veel van hebben geprofiteerd.

   It is a pity that the building and renovation activities in the area from the TUE campus to the railway station in Eindhoven have such unfavorable results: the high buildings worsen the wind climate for pedestrians and cyclists. Moreover, the previously undisturbed fetch from which we benefitted a lot for our wind and rain measurements, has been changed.

5. Goede uitwisseling van ideeën bestaat niet alleen uit meepraten maar ook uit meedoen 'in het veld' of 'met de handen'.

   Good exchange of ideas does not consist only of conversation but also of collaboration 'in the field' or 'with the hands'.

6. Het centrum kent de marge niet; de marge het centrum wel. Ruth Oldenziel, *NOS Actueel*, 13 september 2001.

   The centre does not know the margin; the margin does know the centre. Ruth Oldenziel on Dutch television on 13 September 2001.

7. Meertaligheid kan het best bevorderd worden door (1) het leren van een tweede taal vóór het 11e of 12e levensjaar, (2) het leren van (weer) een andere taal na deze leeftijd en (3) het invoeren van het vak algemene taalkunde in het middelbaar onderwijs (met name in het v.w.o.).

   Multilingualism can be best advanced by (1) learning a second language before the age of 11 or 12 years, (2) learning (again) an other language after this age and (3) introducing a course on general linguistics in secondary education (especially in grammar schools).

8. Het is misleidend de indeling van bijvoeglijke naamwoorden in de twee groepen « kwaliteiten » (« kvalitoj ») en « betrekkingen/toebehoren » (« rilatoj/apartenecoj ») in paragraaf 280-2 van *Plena analiza gramatiko de Esperanto* door K. Kalocsay en G. Waringhien (Rotterdam: UEA, 1985) een indeling naar betekenis te noemen, omdat de twee groepen elkaar qua betekenis overlappen volgens de nadere indeling in paragraaf 296, en omdat zij worden gebruikt om verschillen in woordvorming te beschrijven (paragrafen 282 en 286-II).

   It is misleading to call the classification of adjectives in the two groups « qualities » (« kvalitoj ») and « relations/belongings » (« rilatoj/apartenecoj ») in section 280-2 of Plena analiza gramatiko de Esperanto *by K. Kalocsay en G. Waringhien (Rotterdam: UEA, 1985) a semantical classification, because the two groups overlap each other semantically according to the further classification in section 296, and because they are used to describe differences in word formation (sections 282 and 286-II).*

9. Sms is selfservice-telegrafie.

   Sms is selfservice telegraphy.

10. Het maken van stellingen is net zo nutteloos als het maken van puzzels.

    Making theses is as useless as making puzzles.